LIGHT ACTIVATED SHAPE MEMORY POLYMER COMPOSITE BASED SMART STRUCTURES: A FRAMEWORK FOR MATERIAL DEVELOPMENT AND ACTIVATION METHODOLOGIES

A Thesis submitted by

Herath Mudiyanselage Chathura Madhubhashitha Herath

BSc Eng (Hons), MEng

For the award of

Doctor of Philosophy

2020

Abstract

Shape memory polymers (SMPs) are evolving intensively in smart materials research. SMPs can undergo large deformations, hold a temporary shape and then recover their original shape upon exposure to a particular external stimulus. The emerging development of fibre reinforced shape memory polymer composites (SMPCs) has improved SMPs' mechanical properties to be comparable to modern fibre reinforced composites. Moreover, the inclusion of nanoparticles has enhanced the diversity in activation mechanisms and improved structural properties and durability.

Today, the SMPCs are generally viewed as promising substances for engineered applications that have raised intensive interest among the scientists and engineers. Interestingly, stimulation by light enables unique and advanced shape memory effects (SMEs) in SMPCs that can fulfill the sophisticated demands of engineering. The ability to vary the light wavelength, intensity, periodicity, polarization and the irradiated position on the SMP component enables wavelength selective, reversible, sequential and multiple SMEs. Furthermore, light travel long distances in a vacuum, can be focussed onto a certain area, is safe to humans and, can be a control signal carrier and most notably, can be sent through optical fibres to extremely inaccessible areas.

Incorporation of metallic, carbon and organic based photothermal fillers into a SMP matrix is a convenient proven method to prepare light activated shape memory polymer composites (LASMPCs). These photothermal fillers convert electromagnetic radiation into thermal energy that triggers the SMP matrix. The current study comprehensively reviewed the performances, mechanisms, challenges and limitations of the existing LASMPC systems and associated optical technologies. Predominantly this research was intended to develop reinforced LASMPC systems and allied optical technologies applicable for large scale structural engineering applications.

In this study, styrene and bisphenol A epoxy based thermosets and polylactic acid (PLA) based thermoplastic SMPs were used as polymer matrix materials. Carbon fibre, glass fibre, multiwalled carbon nanotube (MWCNT) and rare earth organic complexes of $Nd(TTA)_3Phen$ and $Yb(TTA)_3Phen$ were used as reinforcement and photothermal fillers. The samples were produced by means of vacuum bagging, mould casting and 4D printing. Morphological investigations were conducted to identify the microstructure and

manufacturability of the LASMPCs. The samples' mechanical and physical properties were tested by standard test methods for polymer matrix composites. Dynamic mechanical analysis was carried out to determine the thermomechanical characteristics. The photothermal effect was investigated through thermal imaging and associated shape memory behaviours were studied through shape fixing and recovery experiments. A finite element analysis was performed with ABAQUS to simulate the photothermal heating behaviour.

The current study established a material development framework for LASMPC materials and presented apt manufacturing methods for structural and large scale engineering applications. Different modes of light diffusion such as scattered low intensity light, focussed laser beams and light delivery through fibre optics were proved for structural LASMPCs. Sequential and selective wavelength activation of structural LASMPCs are presented. The FEA simulation provided additional understanding on light exposed LASMPCs' 3-dimensional heating behaviour. Embedding a D-shaped optical fibre in an LASMPC created a single unit smart actuator, which was remotely activated by light. It was proven that flexible radiation shields can reduce the unanticipated shape recovery of LASMPCs components and protect the LASMPCs from polymer degradation due to radiation.

The improvements to their structural properties and innovative remote activation methodologies have justified LASMPCs' aptness for space engineering applications. This study has proven its successful completion by three selected case studies of space applications. An LASMPC solar panel array model was sequentially deployed in four recovery steps. In a vacuum, a space habitat structure model was compressed to a third of its volume and then recovered its original shape. A 4D printed boom structure model was tested, proving customized LASMPC structures for sophisticated space equipment fabrication. The deployable LASMPC structures can reduce the occupied room in spacecraft. The improvements to the structural properties of LASMPCs while keeping the SME, understanding on thermomechanical and photothermal behaviours, remote actuation through optical fibres, radiation shields and the insight to space applications are the most significant novel outcomes of this study. This thesis opens up windows of opportunity for the scientific and engineering communities to provide innovative solutions to realize the sophisticated large scale engineering demands in aerospace and space applications and beyond.

Certification of Thesis

This Thesis is entirely the work of Herath Mudiyanselage Chathura Madhubhashitha Herath except where otherwise acknowledged. The work is original and has not previously been submitted for any other award, except where acknowledged.

Principal Supervisor: Associate Professor Jayantha Ananda Epaarachchi

Associate Supervisor: Associate Professor Mainul Islam

Student and supervisors signatures of endorsement are held at the University.

Acknowledgements

Pursuing a PhD has been one of the most amazing experiences in my life and I am truly grateful for all those who have supported me throughout this journey. There are several individuals and organisations without whom this thesis might not have been attainable in its current form. First and foremost, I would like to acknowledge the University of Southern Queensland (USQ) and the Australian Government for providing me this great opportunity.

I would like to express my special appreciation and sincere gratitude to my principal supervisor, Associate Professor Jayantha Epaarachchi, for his tremendous academic support, valuable guidance and constant encouragement throughout this journey. The experience and expertise I have gained would not have been possible without his sound knowledge, positive attitude, technical support, cooperative behaviour and valuable suggestions. His prompt responses, easy access and open-door policy helped me to carry out my research smoothly. He played a major role in building up my research foundation.

Also, I would like to extend my sincere thanks to Associate Professor Mainul Islam, the associate supervisor of my PhD project. I am grateful for his experience and providing numerous suggestions, valuable comments, thoughtful guidance and motivation.

For offering me the USQ International Stipend Research Scholarship and the USQ International Fees Research Scholarship, I am highly indebted to the University of Southern Queensland. Also, I would like to express my gratitude to all supportive staff at the Faculty of Heath Engineering and Sciences (HES), USQ Library, Graduate Research School, Information and Communications Technology, Human Resources, Travel Office Student Life and Student Services.

I am also indebted to the Centre for Future Materials Research (CFM) and the Institute for Advanced Engineering and Space Sciences (IAESS) for providing me a world class research environment. I am thankful to the executive director and all staff members. My special appreciation goes to the skilled and cooperative technical staff of CFM and HES.

My deepest thanks go to my fellow postgraduates at CFM and IAESS, who worked cooperatively during my PhD journey. I want to give a big shout-out to my senior and junior colleagues, Wessam, Ayad, Sartip, Nazar, Chris and Janitha.

This study might not have been possible without the financial support from the Asian Office of Aerospace Research and Development (AOARD), Air Force Office of Scientific Research (AFOSR), and U.S. Air Force [Grant Number FA2386-16-1-4043]. Taking part in such an inspiring project was a great privilege for me. I would like to extend my sincere thanks to Lt Col (Dr) Scott Robertson and Dr. Jeremy Knopp at AOARD.

I would like to appreciate the support provided by all research collaborators in Australia and China. I am indebted to the Harbin Institute of Technology (HIT), Professor Jinsong Leng and his research group for providing the materials used in this study and accommodating me during my stay in HIT. I appreciate the technical inputs from Associate Professor Liang Fang at Nanjing Tech University, Professor Gang Ding Peng at the University of New South Wales and Professor Cheng Yan at the Queensland University of Technology.

I am indebted to Dr. Barbara Harmes at the Language Centre, University of Southern Queensland, Australia for the support given on proofreading my journal publications. Moreover, I appreciate the professional service of Ms Julie Martyn at Grammar Fun (ABN 12 524 859 099) for proofreading this thesis.

I am indebted to the Student Village for providing me a comfortable accommodation. A huge appreciation goes to my friends in Toowoomba Indika, Prabuddha, Prasanna, Dananjali, Sachindra and Professor Saman. Also, I appreciate the valued support of the USQ Sri Lankan Cultural Club and Toowoomba Sri Lankan Association.

I am truly grateful to all my peers, teachers, supervisors, mentors and bosses throughout my career from preschool to grad school. My deepest thanks go to Dr. Nandita Hettiarachchi for recommending me to this PhD position.

My heartfelt love and appreciation go to my dear parents and sister who have been by my side throughout my long academic journey. Moreover, I am thankful to my loving wife and her family. I extend my sincere thanks to all my supportive and caring relations and friends in Sri Lanka and Australia. Without their love and encouragement, I would not have finished my thesis successfully.

For me, this PhD journey was a life-changing experience. I deeply treasure every single minute of it and I am truly grateful for all the well-wishers and the people who supported me to turn this big dream into a reality.

Table of Contents

List of Figures

List of Tables

Abbreviations

AB	Aniline black
3D	Three-dimensional
4D	Four-dimensional
BADGE	Bisphenol A diglycidyl ether
BN	Boron nitride
CB	Carbon black
CCD	Charge coupled device
CFR	Carbon fibre reinforced
CIE	Crystallization induced elongation
CNC	Cellulose nanocrystal
CNT	Carbon nanotubes
DGEBA	Bisphenol A diglycidyl ether
DMA	Dynamic mechanical analysis/analyser
DSC	Differential scanning calorimetry
EVA	Ethylene-vinyl acetate
FDM	Fused deposition modeling
GFR	Glass fibre reinforced
GNP	Gold Nano Particles / Graphene nanoplatelets
HEP	Hydro epoxy
IR	Infrared
LASMP	Light activated shape memory polymer
LASMPC	Light activated shape memory polymer composite
LC	Liquid crystal
LCE	Liquid crystalline elastomer
LCN	Liquid crystal network
LED	Light emitting diode
MIC	Melting induced contraction
MIR	Mid infrared
MWCNT	Multiwalled carbon nanotubes
NIR	Near infrared
NP	Nano particle

NR	Nanorod
NS	Nanosphere
NW	Nano wire
OEG	Oligo(ethylene glycol)
PAA	Polyacrylic acid
PAM	Pneumatic artificial muscle
PANi	Polyaniline
PCL	Poly(e-caprolactone)
PCL–PU	Polycaprolactone-co-poly(urethane/urea)
PDMS	Polydimethylsiloxane
PEG	Polyethylene glycol
PEGDA	Polyethylene glycol diacrylate
PEO	Poly(ethylene oxide)
PLA	Polylactic acid
PVA	Poly(vinyl alcohol)
SCP	Shape changing polymers
SMA	Shape memory alloy
SME	Shape memory effect
SMP	Shape memory polymer
SMPC	Shape memory polymer composite
SWCNT	Single walled carbon nanotube
Tc	Crystallization temperature
TECS	Technology enhanced clad silica
Tg	Glass transition temperature
Th	Upper temperature limit of the glass transition region
Tl	Lower temperature limit of the glass transition region
Tm	Melting temperature
TPP	Tetraphenylporphyrin
TTA	Thenoyltrifluroacetone
UTS	Ultimate tensile strength
UV	Ultraviolet

Chapter 1

Introduction

1.1 Background

Shape memory polymers (SMPs) and their composites (SMPCs) have been evolving intensely since their discovery in the1980s [1]. These intelligent materials have the ability to keep a temporary shape and then recover the original shape when subjected to an external stimulus such as heat, electricity, magnetic field, moisture, chemical stimulus, microwave or light, of which the most common activation method is by heat [2-4]. Compared to shape memory alloys (SMAs), SMPs and SMPCs represent a significant share of smart materials research because of their advantages: manufacturability, large recoverable strains, biodegradability, biocompatibility, tailorable glass transition temperature, wide range of stimuli, low density, recyclability and multifunctional nature [4-6].

Neat SMPs are not applicable for many practical applications that require particular functions such as high strength and high recovery force. Therefore, shape memory polymer composites have been produced by incorporating reinforcing materials, i.e. particles [7, 8], nano fibres [9, 10], short fibres [11, 12] and long fibres [13-15], all of which have been studied to meet the various requirements in practical applications. Furthermore, researchers have investigated the effects of UV and γ radiation, and impact mitigation techniques, cycle life and service environment-based performances of shape memory polymer composites [16-19]. Smart materials, SMPs and SMPCs facilitate numerous applications, ranging from the micro scale to the large scale [2]. They have potential in the areas of biomedicine [20, 21], smart textiles [22, 23] and self-healing applications [24, 25]. Interestingly, SMPCs are being developed and qualified especially as deployable components and structures for aerospace and the space engineering sector. These applications include hinges, trusses, booms, antennas, optical reflectors and morphing skins [26, 27]. Figure 1.1 presents an overview of the recent SMPC research.

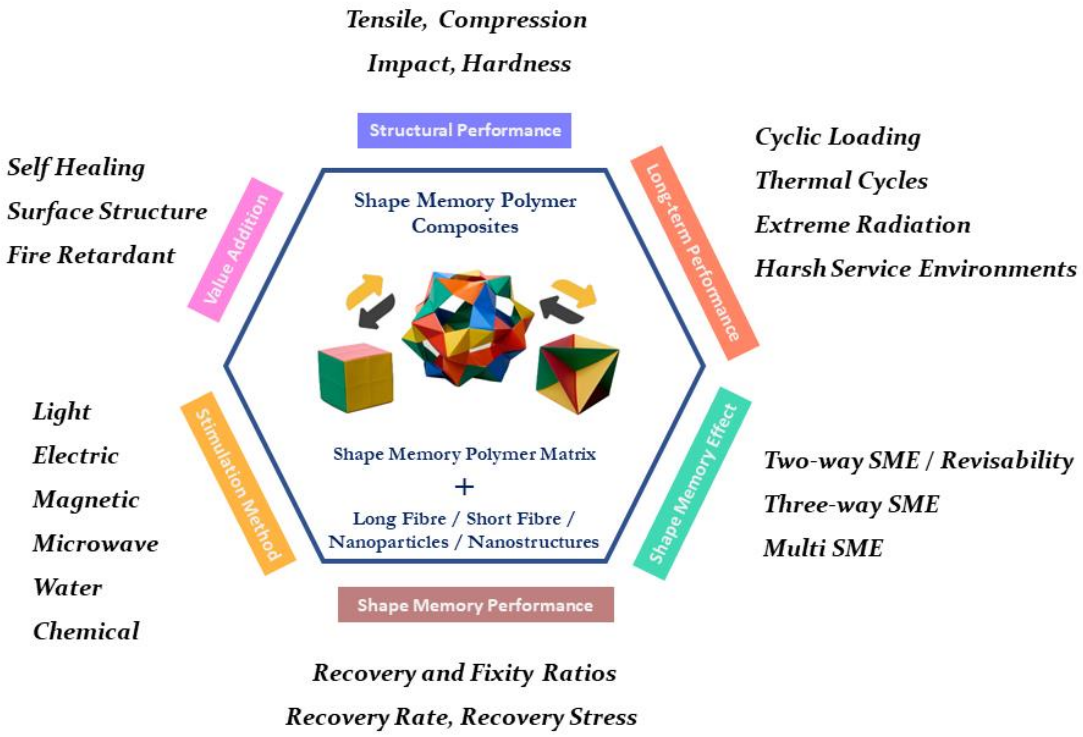

Figure 1.1: An overview of the recent shape memory polymer composite research.

In particular, the unique characteristics of light activated shape memory polymers (LASMPs) and their composites (LASMPCs) make these the foremost candidates in the world of innovative materials [28-30]. In the field of light activated shape memory materials, the stimulus light is considered as the optical radiation of any wavelength from 1 to 10^6 nm. Table 1.1 illustrates the spectral bands for the optics and photonics [31]. The stimulus of light holds exceptional abilities: it acts as a source of energy, is a control signal carrier, travels long distances in a vacuum, has the ability to focus on a certain area, is safe to human tissues and has the ability to disperse through optical fibres. These abilities enable LASMPs and LASMPCs to be suitable in a wide range of applications: biomedical applications [32-35], micro and small scale applications [30, 36], and space and large scale engineering applications [37].

Liquid crystal elastomers (LCE) [38, 39], hydrogels [40, 41], LASMPs [28] and LASMPCs [30, 37, 42] have been widely reported as light induced shape changing materials. Bidirectional or multi directional shape changing functionalities of photo responsive LCEs and hydrogels can be controlled by light irradiation, without any external work [39, 41]. In contrast, LASMPs and LASMPCs require an additional shape programming step by applying an external load. Subsequently, the programmed SMP materials undergo light triggered shape recovery [28, 43].

Table 1.1: Spectral bands for the optics and photonics [31].

Designation of the radiation		**Short designation**		**Wavelength (nm)**	**Photon energy (eV)**
Ultraviolet radiation (UV)	Extreme UV	EUV		1 to 100	1024 to 12.4
	Vacuum UV	UV-C	VUV	100 to 190	12.4 to 6.5
	Deep UV		DUV	190 to 280	6.5 to 4.4
	Mid UV	UV-B		280 to 315	4.4 to 3.9
	Near UV	UV-A[b]		315 to 380	3.9 to 3.3
Visible radiation		VIS		380 to 780	3.3 to 1.6
Infrared radiation (IR)	Near IR	IR-A	NIR	780 to 1400	1.6 to 0.9
		IR-B		1400 to 3000	0.9 to 0.4
	Mid IR	IR-C	MIR	3000 to 50000	0.4 to 0.025
	Far IR		FIR	50000 to 10^6	0.025 to 0.001

The approaches to SMPs' light stimulation can be classified into two major categories: photo responsive LASMPs [28] and photothermal LASMPCs [30, 37, 42, 44]. Moreover, hybrid materials exist which demonstrate both the photo responsive and photothermal effects [29]. Generally, the polymers containing cinnamic groups are photo responsive LASMPs. As the SMP cross-links are directly responsive to light, no temperature variation occurs during the shape memory process of photo responsive LASMPs [28].

Photothermal LASMPCs are produced by incorporating photothermal fillers into thermally induced SMP matrixes. Metallic, carbon and organic based photothermal fillers: gold [25], silver [45], titanium [46], carbon nanotube [47], carbon black [37], graphene [48], rare earth complexes [30], aniline black [36], polypyrrole [49], and porphyrin [50], are used for photothermal LASMPCs. The complete shape memory process of photothermal LASMPs is illustrated in Figure 1.2. The photothermal effect due to light absorbance causes the temperature increase necessary for the shape recovery phase.

In the case of photothermal LASMPCs, the absorption of electromagnetic radiation causes photoexcitation of the photothermal filler material, which results in rapid nonequilibrium heating. Once the photothermal fillers are excited with resonant photons, electron-electron scattering results in a rapid increase in the surface temperature of the filler particles. Subsequently, the energy exchange between the electrons and the lattice phonons of the filler material creates equilibrium.

Afterward the lattice cools via phonon-phonon coupling, which enables heat dissipation into the surrounding shape memory polymer medium [37, 51]. When the thermally induced SMP matrix reaches its Tg due to photothermal heating, the shape recovery takes place. Incorporation of photothermal fillers into thermally induced SMP matrixes are reported as one of the widely used and proven methods to prepare LASMPCs [30, 37, 43]. Moreover, composites are the most appropriate candidates for light triggered structural engineering SMP applications.

Varying the light wavelength, intensity, irradiated position of the component, and polarization permits advanced light activated shape memory effects (SMEs). Selectively activated LASMPCs have been developed by incorporating selective wavelength triggered photothermal fillers into the SMP matrix [30, 52, 53]. Furthermore, light activated

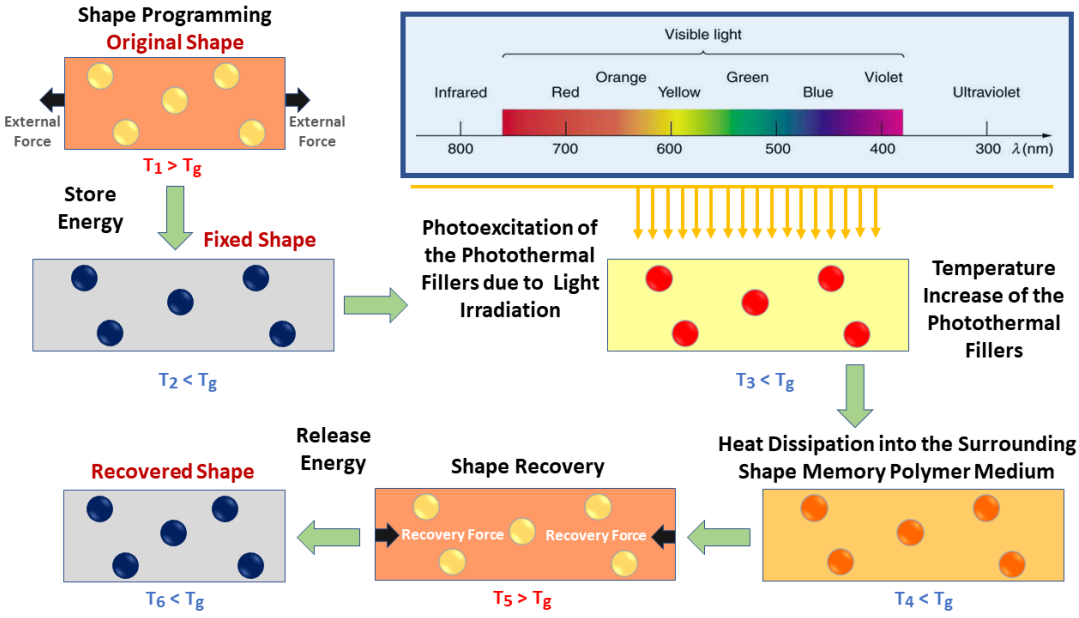

Figure 1.2: Complete shape memory process of photothermal LASMPCs. Different colours represent the material's temperature at each stage.

reversible SME and multi SME enhance the applicability of LASMPs and LASMPCs for sophisticated SMP applications [29, 53, 54].

In addition to the material developments, the advances in optical techniques have extensively changed the light activation capabilities of SMPs. Convex lenses, band pass filters and polarizing beam splitter cubes have facilitated customized light dispersions onto the SMP material [29, 55]. Surface treating of optical fibres and optical fibre-SMP joining techniques have enabled light dispersion into the SMP material [32, 56]. Furthermore, the modelling of light activated shape memory mechanisms has enhanced the knowledge and understanding of LASMPs to introduce novel polymer systems, improve functionalities and develop innovative applications [57-59].

1.2 Research Problems

- During the last four decades various LASMPs have been synthesised and LASMPCs have been developed. Most of the light stimulus SMP systems were targeted toward biomedical applications. Advantageously, light has the credentials to be the foremost stimulus for space and aerospace engineering applications. But there are challenging concerns when selecting lightweight materials for space applications i.e. endures uniquely in harsh environments, being stable in the presence of micrometeoroids traveling as fast as 60 kms^{-1}, space debris traveling at an average velocity of 10 kms^{-1}, a vacuum ($1.33322e^{-4}$ to $1.3332e^{-7}$ Pa), ultraviolet (UV) radiation, particulate radiation, plasma, atomic oxygen, temperature extremes and thermal cycling (from -120 °C to +120 °C) [60]. Therefore, the composites materials intended for space and aerospace engineering applications require excellent mechanical properties i.e. uniaxial tensile strength (100 - 2890 MPa), tensile modulus (17 - 343 GPa), tensile strain to failure (0.002 - 2.75 %), uniaxial compressive strength (147 - 871 MPa), compressive modulus (40 - 332 GPa), impact energy absorbance (5 - 16 J) [61, 62]. However, crucial aspects of LASMPs and LASMPCs such as (i) tensile strength, (ii) elastic modulus, (iii) compressive strength, (iv) impact energy, (v) hardness (vi) damping, (vii) fatigue life, (viii) stress recovery, and (ix) strain recovery have not been comprehensively investigated and quantified for structural engineering applications.

- LASMP nanocomposites based on various functional and photothermal fillers have been introduced to achieve advanced SMEs i.e. reversible SMEs, multi SMEs, wavelength selective SMEs and sequential SMEs. However, such nano fillers are relatively overpriced for the mass production of large engineering structures. Therefore, it is essential to introduce appropriate photothermal fillers for commercially viable structural engineering applications while maintaining the required shape memory effects.

- Inclusion of photothermal fillers into the thermally activated SMP matrixes enables the photothermal heating required for the light activation of LASMPCs. However, these photothermal fillers can affect the shape memory effect, thermal conductivity and structural performance of the SMP matrix. In contrast, the inclusion of fibre or particle reinforcements enhances LASMPCs' structural performances. Then again, these reinforcing materials can affect the photothermal efficiency, thermal conductivity and shape memory effect of the LASMPCs. Therefore, it is essential to study the optimum balance of the amounts of photothermal fillers and reinforcements necessary to achieve the anticipated functionalities and performances.

- Constitutive models and computer aided simulation techniques were developed to describe both thermally and light induced SMP systems under different loading conditions. However, the behaviours of photothermal LASMPCs have not been well explained numerically or analytically. Understanding about the conversion of light energy into thermal energy and the associated heat distribution in the LASMPCs is essential to improve their functionalities and develop large scale engineering applications.

- Distance and indirect activation methods represent a breakthrough in the field of smart SMP applications, where the triggering process can be remotely controlled. The existing optical fibre-based remote actuation techniques have demonstrated joule heating of a significantly small area of an SMP material, which is limited to small scale applications. However, numerous opportunities are open in the aerospace and space sectors which require large shape changing components that are required to be actuated from a distance. Therefore, it is essential to introduce

a new technique for the remote actuation of relatively large LASMPC components.

- UV and particulate radiation damages polymers by either cross-linking (hardening) or chain scission (weakening). LASMPCs are specifically designed to absorb light as much as possible. For space applications, multilayer insulations are being used to protect the equipment from radiation damage. However, it is a challenging task to insulate shape changing components. Therefore, it is essential to study the possible methods to protect LASMPC components or structures from external radiation and perform the shape recovery process on demand.

1.3 Research Objectives and Significance

The aim of this study is to investigate light activated shape memory polymer-based smart materials for structural engineering applications. This fills the remaining knowledge gap in LASMPC development for structural applications. Moreover, this project aims to develop supportive optical technologies and working models to demonstrate the applicability of LASMPCs for space and aerospace engineering applications. To realize the final outcomes successfully, the following four specific objectives has been defined during the project's implementation:

1. Review and understand the performances, mechanisms, challenges and limitations of the existing LASMPC materials.
2. Design and develop reinforced LASMPC materials that are applicable for large scale engineering applications.
3. Develop a remote-controlled actuation technique for relatively large LASMPC components.
4. Design, manufacture and demonstrate the on demand and sequential shape recovery of model space engineering applications made of LASMPCs.

Although the new findings expected by this project are complimentary to a wider field of engineering, the case studies were developed within the project to represent some critical space applications. The major reason for this was LASMPCs' inherent advantages which are indispensable for future space engineering applications.

The author of this thesis strongly believes the advancement of space technologies benefits mankind as it enhances the quality of life by improving space transportation, global communication, defence and security, meteorology, disaster management, and environmental protection. Also, space exploration produces novel knowledge about space and the discovery of distant planets and galaxies.

Deployable structures made of LASMPCs, such as hinges, trusses, booms, antennas, optical reflectors, morphing skins, release devices and wrinkled/slack control components, can shape future space technologies. Such alternative components will be lightweight and occupy small volumes in the spacecraft, which makes the best use of the deployed volume in space. Moreover, it will reduce the necessity for moving parts, assembly components and mechanical or electromechanical actuators. Ultimately, the innovative applications of LASMPCs for space exploration may provide a great scientific return on investment.

1.4 Structure of the Thesis

This thesis is composed of six chapters. A brief description of each chapter is given below.

- Chapter 1: The first chapter introduces the research study. It emphasizes the research problem, objectives and significance.

- Chapter 2: The second chapter provides a comprehensive literature review to identify the research gap that addresses the first objective of this study. State-of-the-art experimental and numerical research on light activated shape memory polymers and composites are reviewed. Supportive optical technologies and light dispersion methods for the light activation of SMPs are described. Furthermore, the chapter provides an extensive review of the applications of LASMPs and LASMPCs.

- Chapter 3: The third chapter firstly describes the materials and manufacturing methods associated with this research. Subsequently the experimental methods are presented, followed by its results and a discussion on the morphology, structural performance and thermomechanical characteristics of LASMPCs. This chapter partially addresses the second objective of this study.

- Chapter 4: The fourth chapter includes the experimental and simulation methods, results and discussion on the light absorbance, photothermal effect and light triggered shape recovery behaviours of LASMPCs. This chapter also partially addresses the second objective of this study.

- Chapter 5: The fifth chapter provides details of the experimental and simulation methods, results and discussion on remote actuation through optical fibres, radiation shielding and model space applications of LASMPCs. The chapter addresses the third and fourth objectives of this study.

- Chapter 6: The sixth chapter concludes the thesis with a discussion of the new scientific knowledge produced and the innovative outcome of this research. Moreover, the chapter provides recommendations and future directions for this field of research.

1.5 Summary

At present, most LASMP and LASMPC systems have been developed for biomedical applications. However, the inherent advantages of LASMPCs can make them the foremost candidate for a wider range of engineering applications, including space engineering, which could provide quite a long term scientific return on investment.

Materials use in space engineering applications faces several exacting demands. There are central challenges to developing LASMPCs for large scale engineering applications: enduring uniquely robust environments, maintaining their structural permanence together with large shape deformations, and being cost-effective to produce. Moreover, the sequential and remote actuations on demand of relatively large components are problematic.

Overcoming these challenges is the global objective of this study to promote the widespread acceptance and use of LASMPCs for structural applications. Accordingly, this thesis presents six chapters deliberating on the background and literature, materials and methods, results and discussion, conclusion and recommendations for future work.

Chapter 2

Literature Review

2.1 Introduction

Nearly four decades of continuous growth of research into shape memory polymers and their composites has inspired engineers and scientists to seek numerous opportunities in many branches of fundamental research and technological innovation. These polymers and composites are smart materials that can memorize their original shape after having been changed by an external stimulus such as heat, light, magnetism and an electric field. Relative to pristine SMPs, fibre and particle reinforced SMPCs facilitate enhanced structural performance and durability. Interestingly the stimulus of light has a significant potential in developing breakthrough technological advancements in biomedical, aerospace and space industry since shape can be remotely controlled by light. Light induced shape changing polymer materials can be classified as liquid crystal elastomers, hydrogels, photo responsive LASMPs and photothermal LASMPCs.

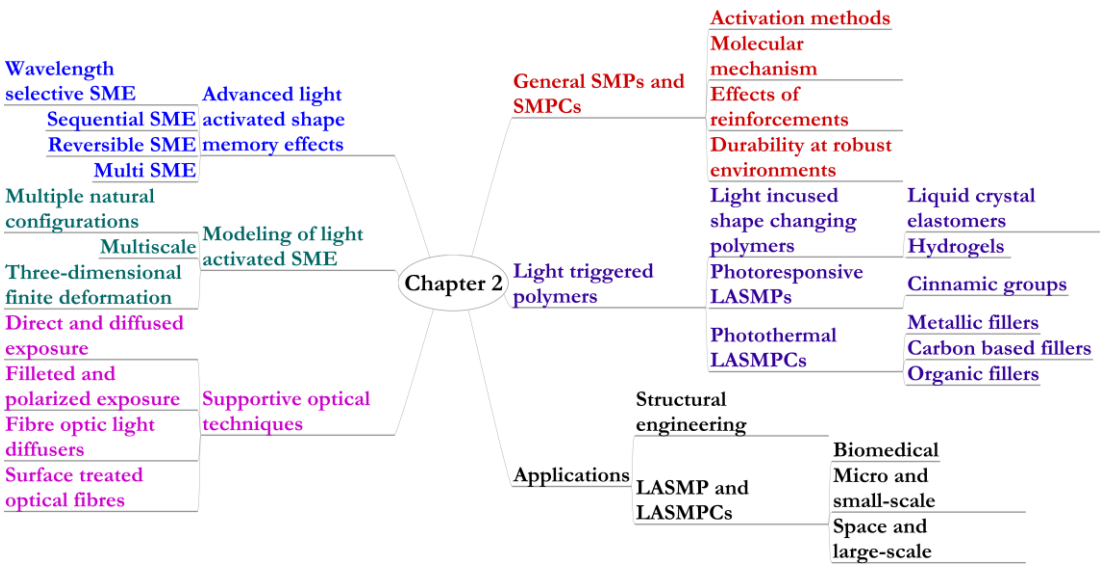

Figure 2.1: Overview of the technical content of Chapter 2.

In this chapter, relevant recent research concerning the state-of-the-art light activated shape memory polymers and their composites is presented. Figure 2.1 gives the overview of this chapter. Advanced material systems with selective triggering capability, and revisable and multi SMEs are considered. Moreover, various modeling approaches to light activated shape memory mechanisms are explained. The supportive optical technologies and light dispersion methods that are advantageous for the light activation of SMPs are described. The structural engineering applications of SMPCs and the inimitable applications of LASMPs and LASMPCs are presented. Most importantly, future research opportunities and directions are emphasized. This paves the way for the context of the current research and gives a background for its motivation. The content of this chapter is presented in the publications B1 and J1 as detailed in the appendix A of this thesis.

2.2 Shape Memory Polymers and Composites

Shape memory polymers are a class of stimuli-responsive shape changing polymers (SCPs) for which shape shifting behaviour can be programmed. This is the single most important feature that distinguishes SMPs from other stimuli-responsive SCPs [63]. Specifically, a SMP can be programmed into a temporary shape and subsequently recover to its permanent shape upon stimulation. The incorporation of functional fillers has become a popular strategy to enhance SMPs' capabilities. The incorporation of fibres, mesoporous bioactive nanoparticles, nanotubes, nanocellulose, and nanocomposite facilitates shape memory polymer composites. The functional elements within SMP nanocomposites not only provide an opportunity to improve the strength and modulus of the SMPC material but can also be utilized to impart the materials with stimuli-responsive characteristics. Figure 2.2 (a) presents the actuation methods, and mechanisms for indirectly induced SMPCs, i.e., chemo-responsive, electrically resistive Joule heating activated, light activated, microwave heating triggered and magnetically sensitive SMPCs [3].

Below the glass transition temperature (Tg), a thermally induced SMP material is at the dominant frozen phase and above Tg the SMP material is at the dominant active phase. At a certain temperature range around Tg a thermally induced SMP material demonstrates the combined properties of both phases, where the shape changes occur [64, 65]. At a temperature greater than Tg, the thermally induced SMP material is programmed to the desired shape. Then, the structure is held fixed and the material is cooled down until the material turns into a frozen polymer at a low temperature. Due to the relatively higher

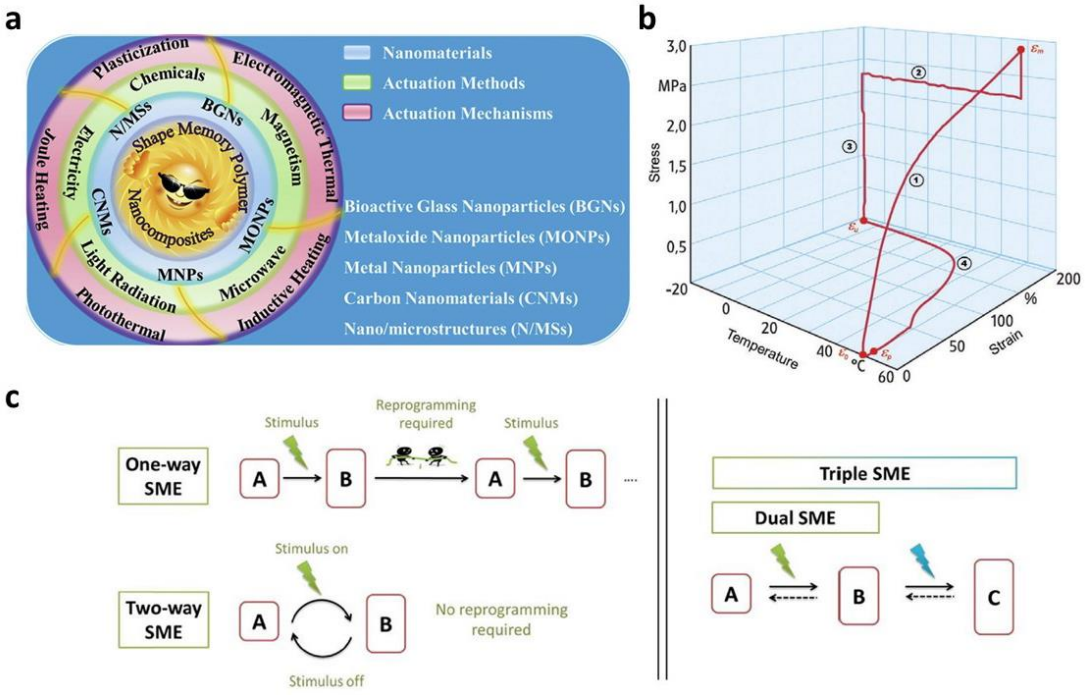

Figure 2.2: General SMP and SMPCs (a) Actuation methods and mechanisms of SMPCs [3] (b) Stress-strain-temperature diagram of thermally induced SMP [66] (c) Types of shape memory effects [67].

stiffness of the glassy phase compared to the rubbery phase, the strain drops slightly, and the material acquires the fixed shape. This is the typical and most common (one-way) shape memory effect which is activated by heat. Finally, increasing the temperature to over Tg, the strain relaxes and the shape recovers [13, 66].

This cycle is called the stress-free strain recovery of SMP and is illustrated in Figure 2.2 (b) [66]. Furthermore, a strain-free stress recovery cycle can also exist, where the programmed shape remains the same and stress in the SMP changes during the recovery. In addition to the typical shape memory effect, as described in the paragraph above, researchers are interested in two-way and multi shape memory effects which are beneficial for the advancement of future SMP applications. Figure 2.2 (c) illustrates the one-way (typical) and two-way SMEs. Moreover, dual SME and triple SME, which are the basics of the multi shape memory effect, are shown in Figure 2.2 (c) [67].

2.2.1 Molecular Mechanism

As illustrated in Figure 2.3, SMPs are polymer networks with integrated, stimuli sensitive switches. SMP network architectures consist of chain segments and netpoints. Since the

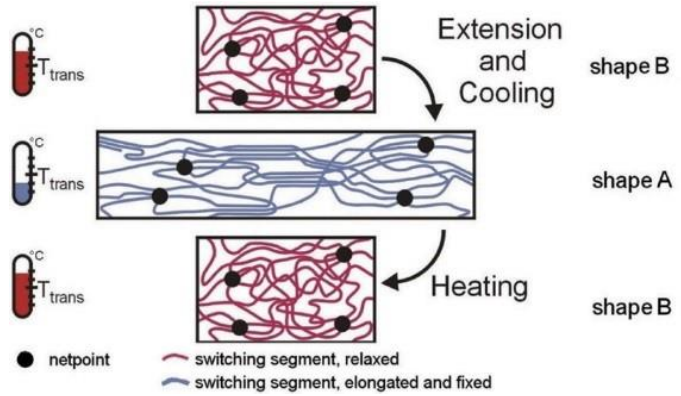

Figure 2.3: Molecular mechanism of the thermally induced shape memory effect [66].

netpoints cross-link the chain segments, they determine the permanent shape of the polymer. The cross-links can be either of a chemical nature (covalent bonds) or a physical nature (intermolecular interactions like crystals and chain entanglements); they prevent the flow of the molecular chains under deformation [68]. SMPs can be classified into thermosets and thermoplastics. Thermoset SMPs have chemical cross-links, which soften, but do not melt at elevated temperatures; instead they either start to burn or decompose. In general, thermoset SMPs have a higher stiffness and lower strain capability than thermoplastic SMPs, which are easy to reshape, since they have no covalent bonds between the chains (no chemical cross-links) [69].

Physical cross-linking is commonly found in block copolymers, whose morphologies consist of at least two segregated domains. In such cases, domains related to the phase with the highest thermal transition temperature are called "hard domains" and act as physical netpoints [70]. The hard segments constitute the permanent shape of an SMP, but to obtain shape memory functionality, a second phase is required. The chain segments associated with the second highest thermal transition temperature (Ttrans) are called "switching segments" and form a reversible phase, which can be first used for fixing a temporary shape in an SMP through polymer chain immobilization (crystallization or vitrification) and later to accomplish molecular motions during shape or stress recovery due to passing the glass transition threshold (Ttrans = Tg). Chemical cross-linking is achieved by the reaction of functional groups, which are attached to chain segments. These functional groups are be reversible [68].

2.2.2 Reinforced SMPCs

Neat SMPs are not appropriate for many practical applications that require particular functions such as high strength and high recovery force. Therefore, shape memory polymer composites (SMPCs) have been produced by incorporating reinforcing materials, i.e., particles [7, 8], nanofibres [9, 10], short fibres [11, 12] and long fibres [13-15], have been studied to meet the various requirements in practical applications. However, the improvement in mechanical properties is quite limited in SMPCs filled with particles or short fibres and such SMPCs could not be used as a structural material due to their low strength and stiffness [14]. By contrast, a continuous fibre reinforced SMPC represents excellent mechanical properties [13-15]. As both functional and structural material, continuous fibre reinforced SMPCs show potential for many advanced applications [14, 26, 71, 72].

Ohki et al. studied the mechanical and shape memory behaviour of glass fibre reinforced polyurethanes [15]. Their results revealed that the tensile strength of the developed materials become higher with the increment of fibre weight fraction under different temperature conditions. Furthermore Ohki et al. concluded that the resistance to both cycle loading and crack propagation in the developed composite materials were evidently improved due to the reinforcement fibres. It was predicted that an optimum fibre weight fraction of between 10% and 20% would demonstrate an extremely low residual strain during the cycle loading. Azzawi et al. investigated the effect of glass fibre reinforcement on mechanical properties and geometrical shape stability. Their findings revealed that, below the Tg, the addition of glass fibre improved the mechanical characteristics of the SMP. The SMPCs with a 20% fibre fraction exhibited increased storage modulus which was 1.75 times more than the neat SMP, and for the 25% fibre fraction SMPC samples, the improvement was 2.35 times that of the neat SMP [13].

However, the dimensional stability of the SMPC samples was negatively affected due to the inclusion of the reinforcement fibres. A noticeable deformation of SMPCs was observed during the thermomechanical cycle due to two reasons: i) significant variation in the mechanical properties of the SMP between high and low temperatures; ii) mismatch of the expansion coefficient of the fibre and the matrix. The unanticipated deformation was found to be dependent on the fibre volume fraction [13]. Also, a difference in storage modulus was identified between the glassy and rubbery phases, which caused the reduction in shape fixity of the material [13]. To achieve higher recovery stresses,

asymmetric glass fibre reinforced SMPC was produced by Ivens et. al [73]. The results revealed a 30-fold increase in recovery stress, compared to the neat SMP resin.

Guo et al. studied the SMP nanocomposite with short carbon fibres and alumina nanoparticles. The test results demonstrated that the SMP hybrid nanocomposites with 7% chopped carbon fibre and 1% alumina nanoparticles exhibited superior mechanical and thermal properties compared with other samples, and an enhanced shape memory property was obtained in the developed nanocomposites [11]. Gall et al. showed that carbon fibre reinforced SMPCs can be bent to a local radius of 1.6 mm and fully recovered with negligible local damage [74]. Microscopic investigations revealed that the dominant local deformation mode of the composites was a buckling of the carbon fibres on the inner surface of the bend. Localized buckling out of the material plane led to detrimental interfacial matrix failure while dispersed in-plane buckling was elastic and non-damaging [74]. Lan et al. also shown that microbuckling is the primary mechanism in the bending deformation of carbon fibre reinforced SMPCs, which provides a higher bending strain than that in a traditional structural composite [14].

Xie et al. developed a series of EVA based composites showing enhanced recovery stresses both in free state and resistant conditions by incorporating different amounts of a stiff filler carbon fibre [75]. Compared to pristine EVA, carbon fibre SMPCs containing 5-30 wt% carbon fibre possessed a 100-650% increase in enhanced recovery stress. Interestingly, the SMPC exhibited a robust shape recovery performance under loaded conditions, while the recovery capability of pristine EVA was nil [75].

2.2.3 Durability of SMPCs

Researchers have investigated the effects of UV and γ radiation, impact mitigation techniques and cycle life for different shape memory polymer composites [16-19]. Leng et al. exposed epoxy based shape memory polymers to a simulated γ-radiation (1×10^5 Gy and 1×10^6 Gy) environment for up to 140 days to investigate the effects of accelerated irradiation [16]. The influence of γ-radiation on thermal and mechanical properties was evaluated by differential scanning calorimetry, dynamic mechanical analysis, and tensile test. The results revealed that the Tg did not decrease by more than 10%. The tensile strength and elastic modulus were 26 MPa and 1.36 GPa respectively after being exposed

to 1 x 10^6 Gy radiation. Moreover, the shape recovery rate was improved once exposed to a γ-radiation of 1x10^5 Gy [16].

Xu et al. investigated the durability of a close-celled syntactic foam based SMP, under the environmental attack of accelerated ageing of up to 90 days' exposure to ultraviolet (UV) radiation [76]. Accordingly, UV exposure resulted in discolouration on the exposed surface with yellowing increasing with the duration of exposure. UV exposure resulted in cracks on the foam surface along the compression direction. Also, the UV radiation caused a decrease in mechanical strength and ductility, and an increase in modulus. Cracks in the foam have a lesser effect on tensile strength than that on compressive strength but have a greater influence on ductility.

Combined UV radiation and water immersion (rainwater and saturated saltwater) were also investigated. The combined effects of UV and water led to a larger decrease in strength and ductility than that of UV alone. The decrease for foam immersed in saltwater was less than that in rainwater. Water immersion also caused a reduction in Tg of the foam [76].

Xie et al. performed vacuum outgassing and ultraviolet (UV) radiation exposure tests on a cyanate-based SMP. The irradiation induced an instability of the molecular structure within the material, and the effect was gradually strengthened with the increase of exposure time [18]. It was revealed that this degradation resulted in the breaking of weak bonds and formation of more stable chemical bonds which may be involved in the complex photochemical process. In addition, UV radiation was found to have no effect on the thermal stability of cyanate based SMPs, including the thermal decomposition rate [18].

Wong et al. investigated discolouration, UV absorbability, surface hardness, dynamic mechanical properties and shape memory effects under UV degradation of styrene based and epoxy based SMPs filled with different percentages of nano-ZnO particles [77]. The samples were kept under accelerated UV ageing at an intensity that was eleven times higher and a temperature three times higher than those of the ambient environment. This was equivalent to the samples being exposed to 22 days of sunlight, in terms of UV intensity. After accelerated UV ageing, all styrene based samples were hardened while that of all epoxy-based samples was softened. These findings implied all styrene based samples behaved more alike amorphous thermoplastics in that they formed cross-links and became a thermoset plastic while all epoxy-based samples behaved like thermoset plastics

in that their cross-links were broken and became more flexible and less strong and stiff after UV degradation.

Al-Azzawi et al. investigated the effect of UV exposure on the thermomechanical properties and shape memory effect of a styrene based SMP and its glass fibre SMPCs (20 wt.% and 25 wt.%) [17]. Stress-free strain recovery results showed no significant effect of UV exposure on the shape fixity of the neat SMP sample. However, a small improvement was shown in the fixity ratio, from 93% to 95% for the 20 wt.% glass fibre SMPC, and from 91% to 93% for the 25 wt.% glass fibre SMPC. Conversely, the exposure reduced the shape recovery rate in the neat SMP, 20 wt.% SMPC and 25 wt.% glass fibre SMPC samples by 25%, 34% and 77% respectively. Moreover, a constrained strain stress recovery test revealed that UV exposure reduced the programming stress by 57.1%, 43.5% and 21.2% for the neat SMP, 20 wt.% SMPC and 25 wt.% glass fibre SMPC samples respectively. Furthermore, it significantly reduced the recovery stress, particularly in the neat SMP sample [17].

Jang et al. studied carbon fibre reinforced epoxy-based SMPCs under a high vacuum condition and UV irradiation [19]. The storage modulus of the carbon fibre SMPCs increased with the duration of UV exposure due to UV-induced cross-linking of the SMP matrix. However, their storage modulus decreased due to relaxation and degradation phenomena as the exposure time increased further. The study characterized these two phenomena separately using the time-temperature superposition principle to predict the long term behaviour of carbon fibre SMPCs [19].

Tandon et al. conducted a baseline assessment of the durability of styrene based (VF62) and epoxy based (VFE2-100) thermosetting shape memory polymer resin materials being considered for morphing applications when exposed to the service environment [78]. The approach for the experimental evaluation was a measurement of the shape memory properties and elastomeric response before and after separate environmental exposures to i) immersion in water at room temperature (25 °C) and 49 °C for 4 days, ii) immersion in lube oil at room temperature (25 °C) and at 49 °C for 24 h, and iii) xenon arc (63 °C, 18 min water and light/102 min light only) and iv) spectral intensity of 0.3-0.4 watts/m^2 for 125 cycles (250 h exposure time). Two shape memory cycles were performed on each specimen in order to get a preliminary estimate of repeated cycling on the shape memory behaviour. For VF62 resin under the service environment, a decrease was noticed in the stress recovery ratio for UV-exposed samples, while water immersion resulted in a small

increase. Moreover, the stress recovery ratio seemed to improve slightly during the second shame memory cycle, except for UV-conditioned specimens. Almost complete unconstrained recovery (97-100%) was possible under all conditions studied for VF62. For VFE2-100 there was some decrease in the recovery stress ratio for samples immersed in water at room temperature, while the recovery ratio remained relatively unchanged with heated water and UV exposure. Furthermore, lube oil conditioning at 25 °C and 49 °C resulted in a small knockdown in the stress recovery ratio compared with the control samples kept under room condition. With the exception of samples immersed in the heated lube oil, the stress recovery ratio reduced slightly during the second shape memory cycle. Also, for VFE2-100, almost full shape recovery (97-100%) was possible under all conditions studied. Kong and Xiao investigated the behaviour of a shape memory polyimide over 1000 shape memory cycles [79]. The SMP exhibited a shape fixity ratio of 98-100% and a recovery ratio of 100% during all the 1000 bending deformation cycles at 250 °C. The storage modulus was almost the same for all different shape memory cycles, which may be the cause for a 100% recovery [79].

Nji and Li proposed a 3D woven fabric reinforced shape memory polymer composite for impact mitigation [24]. The shape memory functionality of SMPs was utilized to self-repair (healing) impact damage in 3D woven fabric reinforced SMP based syntactic foam composites under repeated impact loadings. It was found that self-repair had a significant effect on the impact energy. Control specimens impacted with 32 J of impact energy were perforated at the 9^{th} impact while healed specimens lasted until the 15^{th} impact; control specimens impacted with 42 J of impact energy were perforated at the 5^{th} impact while healed specimens lasted until the 7^{th} impact. This result was thought to be because some unrecoverable damage such as microballoon crushing and fibre fracture increases as impact energy increases and the non-healable damage accumulates under repeated impacts. The appearance of non-healable damage was represented by a considerable reduction in either the peak impact load or the initiation energy, or an increase in propagation energy. Perforation was signified by a sharp drop in peak load, total energy, initiation energy and propagation energy [24].

2.3 Light Induced Shape Changing Polymers

Current study specifically looks in to the LASMPCs which are a subclass of light induced shape changing polymers. Smart materials such as photo responsive polymers and

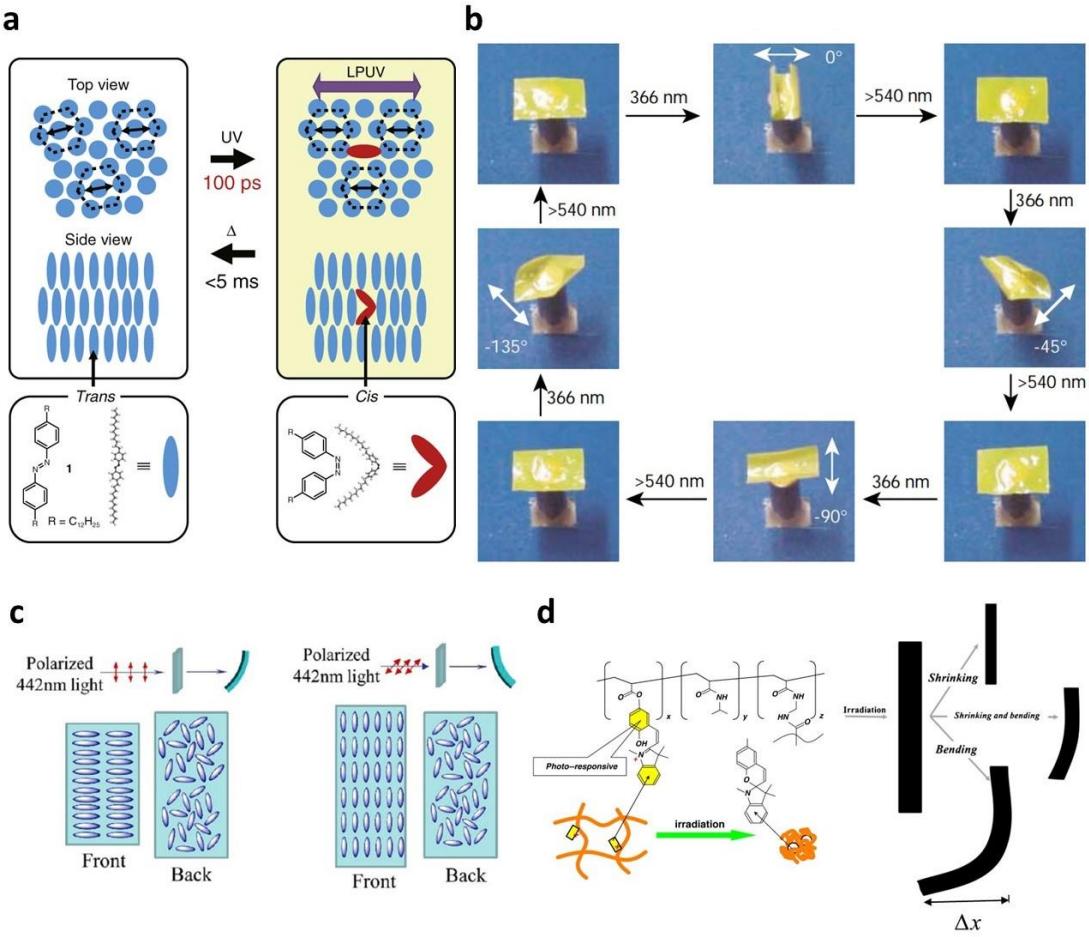

Figure 2.4: Light induced shape changes of photo responsive polymers (a) Schematic illustration of trans-cis isomerization. Azobenzene molecules are aligned with the laser polarization axis. The red bent spheroids represent azobenzene molecules in the cis-form. LPUV is linearly polarized UV light, and the direction of the angle is the polarization axis [39] (b) Directional bending and recovery of an LCN by linearly polarized light [44] (c) Mechanism of bidirectional bending of an LCN [8] (d) Isomerization (left) and schematic representation of the bending and shrinking (right) of a pSPNIPAAm hydrogel due to light irradiation [40].

composites have the ability to undergo light induced shape changes. These light induced shape changing polymer materials can be classified as liquid crystal elastomers (LCE) [39, 80], hydrogels [41, 81], light activated shape memory polymers [28] and composites [30, 37, 42]. The photo responsive LCE and hydrogels diversely form the LASMPs and LASMPCs. Photo responsive LCEs and hydrogels do not require the shape programming step that LASMPs and LASMPCs require. Research into the most salient features known to date of photo responsive shape changing LCEs and hydrogels is presented in this section.

The first efforts were made to prepare photo responsive polymers on the basis of their photomechanical mechanisms. The accumulation of light induced structural variations finally contributes to a macroscale shape deformation. Interestingly, the liquid crystal network based photo responsive polymers demonstrate bidirectional shape changes due to light, without any external load requirement for shape programming. Moreover, these polymers are capable of high frequency shape changes. A liquid crystal network (LCN) linked with an azobenzene chromophore can be repeatedly and precisely manipulated along any chosen direction by using linearly polarized light, since the light sensitive molecules undergo photo contraction and convert the light energy into mechanical energy [82-85]. The transformation between two geometrically different (orientation wise) azobenzene isomers upon light irradiation causes this energy transformation. As illustrated in Figure 2.4 (a), absorbance of the light linearly polarized in a specific direction leads to a trans-cis isomerization of the azobenzene moieties in specific domains where the azobenzene moieties are aligned along the direction of light polarization [39, 82].

A film having photoactive azo mesogens, which are initially aligned parallel to the light (homeotropic) can be bent away from the UV light source, whereas the initial alignment that is normal to the light (homogeneous) can be bent towards the UV light source [86]. Figure 2.4 (b) illustrates the ability of LCN containing an azobenzene chromophore, to bend in a single direction and recover under the illumination of $\lambda = 366$ nm and $\lambda > 540$ nm respectively [82]. Moreover, as illustrated in Figure 2.4 (c), bidirectional bending can be accomplished by the exposure to polarized light with wavelength $\lambda = 442$ nm [29].

Hydrogels are a type of soft material comprising a three-dimensional network which contains a high percentage of water. In recent years, photo responsive hydrogels have been investigated as emerging shape changing materials due to light irradiation [40, 41, 87, 88]. In general, photo responsive hydrogels consist of a polymeric network and a photoreactive moiety, with usually a photochromic chromophore as the functional part. Initially the photochromic molecules capture the optical signal and then the chromophores in the photoreceptor convert the photoirradiation to a chemical signal through a photoreaction such as isomerization, cleavage and dimerization [87, 89]. Subsequently, the signal is transferred to the functional part of the hydrogel and controls its properties. The change of the chromophores upon photoirradiation strongly depends on their molecular structures, which determine the required light irradiation [87]. The isomerization of a novel pNIPAAm based gel (abbreviated as pSPNIPAAm) containing spirobenzopyran as a photochromic chromophore is presented in Figure 2.4 (d). The

hydrogel demonstrates both shrinking and bending behaviours due to light irradiation [40].

2.4 Light Activated Shape Memory Polymers

The complete shape changing process (shape memory cycle) of an SMP contains two major components: shape programming and shape recovery. At first, the shape programing step needs to be done by applying an external load. Subsequently, the programmed SMP returns to its original shape, once exposed to the corresponding external stimulus. The polymers containing cinnamic groups are proficient to program into predetermined shapes and recover to the original shape by exposure to light illumination [28]. The unique characteristics of the photo responsive SMPs enable shape recovery at ambient temperatures such as room temperature, which could eliminate the strict temperature constraints applied on thermo responsive SMPs. Such photo responsive SMPs are being used for medical and other applications that are not generally exposed to external heating. However, photo responsive SMPs do not have the adequate structural properties for many engineering applications. Moreover, photo responsive SMPs have never previously been used to produce fibre reinforced LASMPCs.

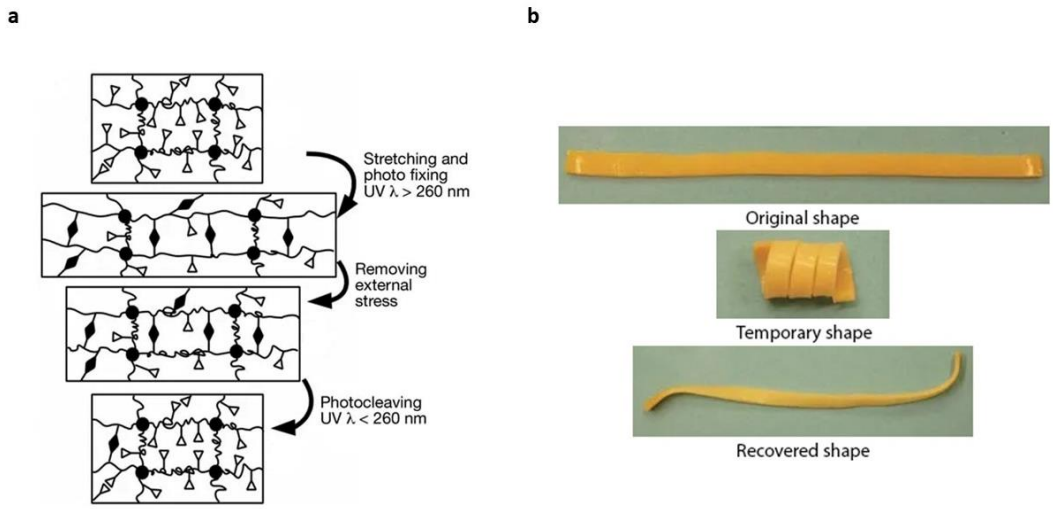

Figure 2.5: Shape memory effect of photo responsive polymers with cinnamic groups (a) Molecular mechanism of light activated shape memory effect (b) Polymer film programmed into a spiral shape and respective recovery behaviour due to 260 nm UV light [28].

As illustrated in Figure 2.5, photo responsive molecular switches, such as cinnamic acid or cinnamylidene acetic acid, are able to undergo efficient photo reversible cycloaddition reactions when exposed to UV wavelengths, i.e., photo fixing at $\lambda > 260$ nm for 60 min and photo cleaving at $\lambda < 260$ nm for 60 min [28]. It has been reported that the cinnamic acid based photo responsive SMPs show a relatively lesser shape fixity ratio and a nearly similar recovery ratio compared to thermo responsive SMPs [28]. In line with the mechanism shown in Figure 2.5 (a), the amorphous permanent network has long and coiled segments between two netpoints. The coiled segments of the chains are stretched and elongated during the shape programming process. Formation of new chemical netpoints causes the strain fixation via light irradiation, unlike the freezing of the stretched chains in thermo responsive SMPs. The elastic contraction of the stretched chain segments accounts for the lesser strain fixity ratio [28].

2.5 Light Activated Shape Memory Polymer Composites

Incorporation of photothermal fillers into a thermally induced SMP matrix is widely reported as a convenient and proven method to prepare LASMPCs [30, 37, 90-92]. The photothermal effect is a phenomenon which produces thermal energy from electromagnetic radiation. Several nanoparticles [30, 37, 90, 92, 93] and dye [32-35] based on photothermally activated LASMPCs have been introduced. Unlike the photo responsive LASMPs, photothermal LASMPCs are able to be used in a wider range of applications, ranging from the microscale [30] to the large scale [37].

2.5.1 Photothermal Effect

Metallic nanoparticles can produce heat through a surface plasmonic effect. Organic compounds and carbon based composite materials also have a photon to thermal conversion ability due to their strong light absorbance [94]. Figure 2.6 illustrates the schematic representation of the principle underlying the photothermal characteristics of gold nanostructures [51]. When metal nanostructures are excited with resonant photons, the photoexcitation of the electron gas results in rapid non-equilibrium heating. The initial electronic excitation is followed by relaxation at sub-picosecond timescales by means of electron-electron scattering which results in a rapid increase in the surface temperature. This rapid heating is followed by cooling to equilibrium by energy exchange between the

electrons and the lattice phonons. In the first several hundred picoseconds following excitation, the lattice cools via phonon–phonon coupling, resulting in heat dissipation into the medium surrounding the nanostructure.

Table 2.1 summarizes the existing photothermal fillers, their triggering wavelength ranges and their general applications. In general, the photothermal heating technique has been initially used for biomedical diagnostics, targeted therapeutics and solar thermal generation [95]. Interestingly, the photothermal materials presented in Table 2.1 have the potential to be used in future SMP developments. The photothermal fillers that are being used for targeted therapies and clinical imaging are appropriate for SMP based biomedical applications [25, 96]. Carbon-based photothermal materials are applicable for large scale engineering applications, as such types of fillers demonstrating higher photothermal efficiency and enhanced structural performances [93].

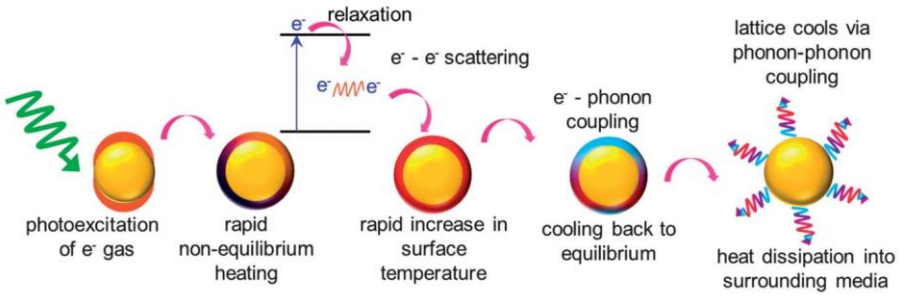

Figure 2.6: Schematic diagram of the principle of photothermal light to heat energy conversion [51].

Table 2.1: Potential photothermal fillers for future LASMPCs' development. Existing photothermal materials their triggering wavelength range and general applications.

Photothermal materials	**Light absorbance**	**Current applications**
Gold nanostructures / nanoparticles / nanorods [25, 51, 90]	UV, visible and NIR	Shape memory Self healing Biomedical diagnostics Photothermal therapy
Silver nanoparticles / dye [96-98]	UV, visible and NIR	Shape memory Solar collectors Photothermal therapy

Platinum nanoparticles / dye [32, 99]	NIR	Shape memory Photothermal therapy
Titanium oxides (TiO2, Ti_2O_3 and Ti_8O_{15}) nanoparticles [94, 100, 101]	UV, visible and IR	Solar thermal systems Photothermal therapy
Titanium nitride (TiN) [46, 102, 103]	UV, visible and IR	Shape memory Photothermal therapy Solar thermal systems
Zinc oxide (ZnO) [104-107]	UV, visible and NIR	Electronics and optoelectronics Solar energy utilization Hydrogen production Photothermal therapy
Copper oxide (CuO) [105, 108]	UV, visible and IR	Solar thermal systems
Copper sulfide (CuS) [109, 110]	NIR	Photothermal therapy
Ferrous oxide (Fe_2O_3) [111, 112]	NIR	Photothermal therapy
Palladium nanoparticles [113, 114]	Visible and NIR	Photothermal therapy
Molybdenum disulfide (MoS_2) [115, 116]	NIR	Photothermal therapy Drug delivery
Tungsten disulfide (WS_2) [83, 117]	NIR	Photothermal therapy Clinical imaging
Tungsten oxide ($W_{18}O_{49}$) [118]	UV and NIR	Shape memory
Metal ions (Fe^{3+}, Cu^{2+}, Ni^{2+}, Co^{2+}, Cd^{2+}, Cr^{2+}, Al^{3+}) [119]	NIR	Shape memory
Indocyanine green [120, 121]	NIR	Clinical imaging Photothermal therapy
Polypyrrole nanoparticles [49, 122, 123]	NIR	Shape memory Photothermal therapy
Porphyrin [50, 124]	UV, visible and NIR	Shape memory Photothermal therapy Biological imaging
Aniline black [36, 125]	UV, visible and NIR	Self healing Shape memory

Boron nitride [93, 126]	Visible and IR	Shape memory Self healing
Germanium nanoparticles / nanocrystals [127-129]	UV, visible and NIR	Photothermal therapy Biological imaging
Graphene and Graphene oxide [44, 107, 130, 131]	NIR	Shape memory Photothermal therapy
Carbon black [37, 95, 132, 133]	UV, visible and IR	Shape memory Solar thermal systems
Carbon nanotubes [44, 47, 93, 134]	UV, visible and IR	Shape memory Photothermal therapy
Carbon fibres [135]	UV, visible and IR	Photothermal therapy

2.5.2 LASMPCs with Metallic Photothermal Fillers

2.5.2.1 Gold

Gold nanoparticles (AuNPs) [25, 136-139], nanorods (AuNRs) [42, 43, 90] and nanospheres (AuNSs) [52] are widely employed as photothermal materials for LASMPCs. SMPs such as poly(ethylene oxide)(PEO) [25], branched oligo(ε-caprolactone) (bOCL) cross-linked with hexamethylene diisocyanate (HMDI) (referred to as XbOCL) [136], polyurethane [52, 137], poly(e-caprolactone)(PCL) [90], poly(vinyl alcohol) (PVA) [42] and bisphenol A diglycidyl ether (BADGE / DGEBA) [43, 139] are reported as matrix materials for AuNPs and AuNRs based LASMPCs. The AuNPs and AuNRs have been modified for improved cross-linking and homogeneous dispersion in the SMP matrix [25, 90]. The visible light of 530 nm [52] and 532 nm [25, 43, 136, 139] and NIR light of 785 nm [42, 137], 805 nm [90] and 860 nm [52] have been occupied to trigger the gold photothermal filler based LASMPCs.

Zhao et al. developed AuNPs based LASMPCs and studied their associated strain and stress recovery behaviours [25, 136, 138]. As illustrated in Figure 2.7 (a), an XbOCL with AuNPs LASMPC demonstrated spatially selective shape recovery behaviour when at 532 nm wavelength, 1.1 W/cm^2 light was irradiated onto four sections of the LASMPS film, from bottom to top. Interestingly the film recovered up to 95 % of the original length with an attached load of 3.5 g, which was 350 times higher than the weight of the

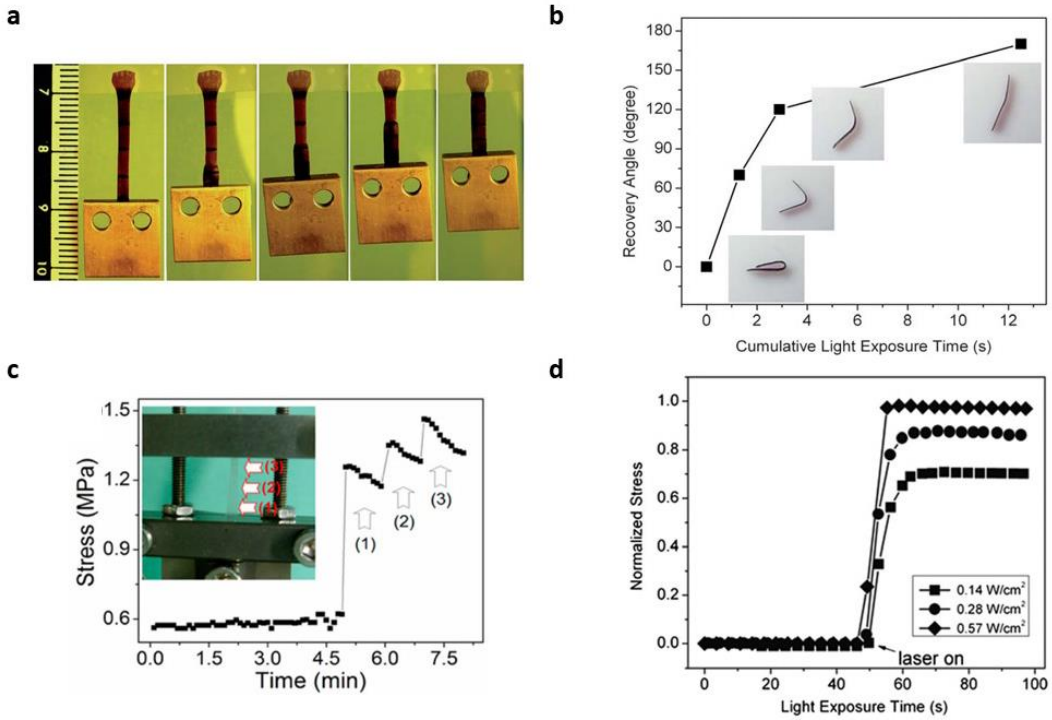

Figure 2.7: Light activated shape memory behaviour of a gold nanoparticle based LASMPCs (a) Spatially selective shape recovery process by separate laser exposures (532 nm, 1.1 W/cm^2) on four sections from bottom to top, with the LASMPC film lifting a load 350 times its weight [136]. (b) Multiple intermediate shape recovery steps by switching on and off the laser (532 nm) intermittently [136]. (c) Contraction stresses generated by a strained and fixed film due to stepwise laser (532 nm, 7 W/cm^2) exposure at three different locations of the film [25]. (d) Contraction stresses generated by a strained and fixed film due to different power densities of the laser (532 nm) exposure [136].

LASMPC film [136]. Figure 2.7 (b) demonstrates the temporal control of the light triggered recovery process that allowed the same XbOCL with AuNPs LASMPC to obtain multiple intermediate states between the temporary and permanent shapes, by turning on and off the laser as required [136].

Unlike heat, light enables a localized shape memory effect by focusing the light beam onto a particular area. In other words, light allows the release of the strain energy stored only in a specific part of an LASMPC sample. Figure 2.7 (c) shows the contraction stresses generated by a strained and fixed AuNP mixed PEO LASMPC film due to a stepwise laser exposure at three different locations of the film [25]. A laser with 7 W/cm^2 power density was initially irradiated onto Location 1 and then moved to Locations 2 and 3

consecutively. A contraction force was quickly generated as a result of the photothermally induced shape recovery in the laser exposed part of the film. When the laser spot was moved to the next location, a new contraction force was generated upon release of the strain energy stored in that region [25].

The contraction forces generated by a strained and fixed AuNPs mixed XbOCL LASMPC film increase with respect to the increase of the irradiated power density of the laser. Figure 2.7 (d) shows the normalized stress as a function of the irradiated power density of the laser, where the LASMPC film was strained up to 20% and fixed. It is clear that a higher laser power also results in a faster increase of contraction forces [136]. This is understandable because a higher laser power means more absorbance of photons by photothermal fillers and more heat release to the polymer matrix, which heats the polymer rapidly above Tg. Proving this fact, Figure 2.8 (a) depicts the temperature increase of an AuNRs mixed PCL LASMPC due to different laser intensities. The results indicate precise control over the sample heating through changes in the light intensity.

The findings of Zhao et al. on AuNRs mixed PVA LASMPC revealed that, by changing the polarization direction of the incident laser with respect to the film stretching direction, the magnitude of the longitudinal surface plasmon resonance (SPR) of AuNRs can be varied continuously. As presented in Figure 2.8 (b), the absorbance spectrum of a stretched LASMPC film depends on the direction of the light polarization, where the polarization parallel to the stretching direction is referred to as 0°. Initially, a longitudinal absorbance at 760 nm and a transverse absorbance at 515 nm were found. With the polarization parallel to the stretching direction, only longitudinal absorbance was observed while the transverse absorbance was absent. In contrast, when the polarization was set to be perpendicular to the stretching direction, the longitudinal absorbance disappeared and only the transverse absorbance was visible [42].

Interestingly, for AuNRs based LASMPCs, the amount of heat generated upon laser exposure depended on the direction of polarization. Figure 2.8 (c) shows the results that confirm the control of shape memory behaviour by using the light polarization of a 785 nm laser. Accordingly, with the polarization perpendicular to the film stretching direction, no shape recovery occurred, even after 2 min laser exposure. In contrast, by rotating the light polarization to be parallel to the stretching direction under same conditions, the film recovered to the original shape within 10 seconds of laser exposure [42].

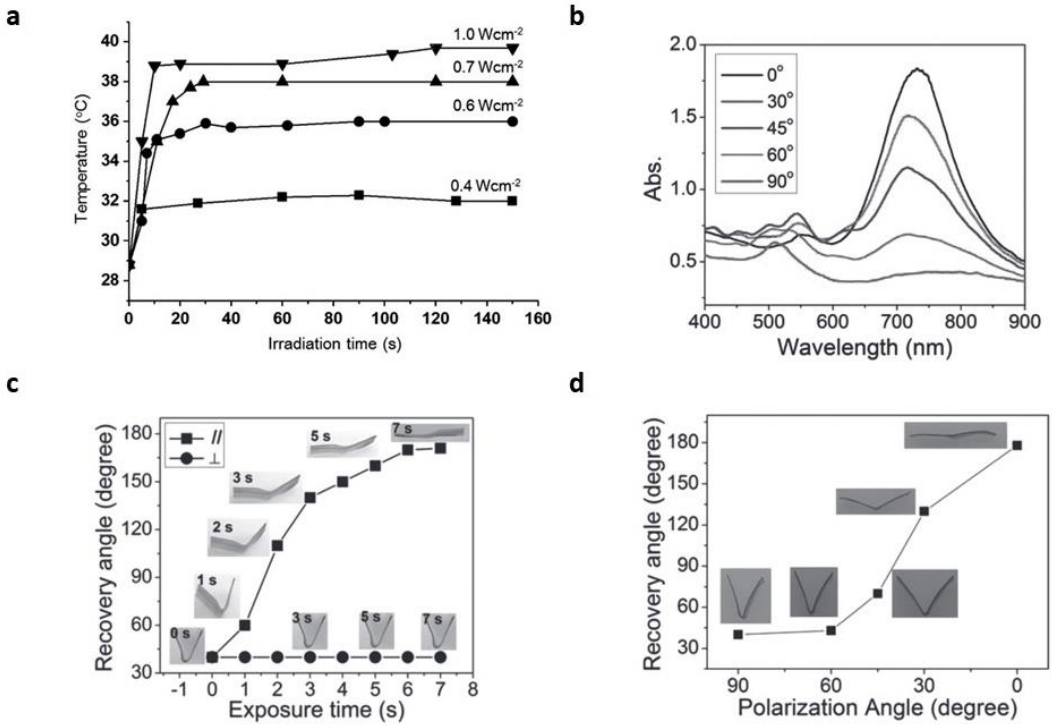

Figure 2.8: Photothermal and light activated shape memory behaviour of a gold nanorod based LASMPCs (a) Photothermal behaviour of a 0.3 wt% AuNRs LASMPC due to different power densities of 805 nm NIR light [90]. (b) Polarized light (785 nm) absorbance by a stretched LASMPC film, five different angles between the polarization direction of the incident light and the film stretching direction [42]. (c) Recovery angle from unbending versus laser exposure time with parallel and perpendicular polarization (0.2 W/cm^2 785 nm NIR) [42]. (d) Recovery angle versus laser polarization angle (1 min of 0.2 W/cm^2 785 nm NIR) [42].

With perpendicular polarization of 785 nm laser, there was no longitudinal absorbance of AuNRs and thus no heat release for heating up the LASMPC. Inversely, with parallel polarization, the longitudinal absorbance was at the maximum and the released heat could raise the temperature in the folded area above Tg, which enabled the shape recovery process. Furthermore, the angle between the two halves of the folded film, denoted as the recovery angle, was measured after 1 min of laser exposure and plotted as a function of the light polarization angle, as illustrated in Figure 2.8 (d) [42].

The extent of shape recovery increases with a decrease in the polarization angle. Accordingly, different localized heating levels can be obtained within the glass transition rejoin and therefore partial shape recovery with different recovery angles can be achieved

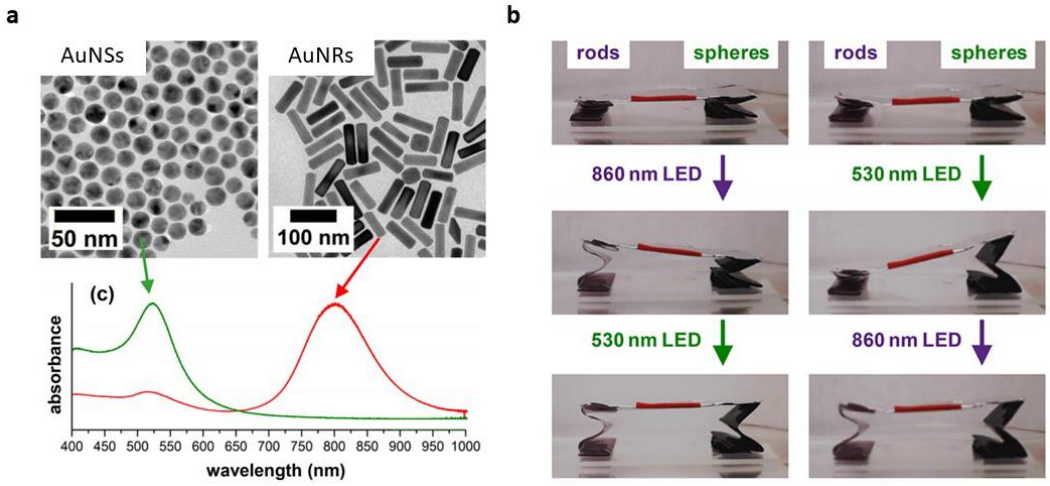

Figure 2.9: Selective wavelength shape memory behaviour of gold nanospheres and nanorods (a) transmission electron micrographs and light absorbance spectra (b) wavelength controlled shape recovery behaviour [52].

by changing the light polarization [42]. This is an added advancement to the technique demonstrated in Figure 2.7 (b).

Mishra et al. demonstrated the selective wavelength photothermal capability and associated shape recovery behaviours of thermoplastic polyurethane shape memory polymers with embedded AuNSs and AuNRs. As presented in Figure 2.9 (a), AuNSs and AuNRs showed selective absorbance peaks at 521 and 799 nm respectively [52]. Incorporation of two types of photothermal fillers into polyurethane SMP has caused an 11 nm shift in the transverse SPR for AuNSs LASMPC and a 71 nm shift in the longitudinal SPR for AuNRs LASMPC. Accordingly, 530 nm and 860 nm laser sources were occupied to trigger the AuNSs based and AuNRs based LASMPCs respectively. Figure 2.9 (b) illustrates the selective wavelength controlled shape recovery behaviour of gold photothermal filler based LASMPCs [52]. The concept of wavelength controlled photothermal heating of AuNPs with different SPRs could be extended to more than two wavelengths, using a series of AuNRs of different aspect ratios to impart more complex functions while retaining simple device architectures.

2.5.2.2 Silver

Silver nanoparticles (AgNPs) are known to produce a photothermal effect that is ten times higher than AuNPs while the cost is much less and the preparation is simple [45].

Furthermore, AgNPs act as an antibacterial agent for SMP based biomedical applications [96, 140]. However, the molecular design and synthesis of AgNPs based LASMPCs are relatively challenging as the combination of AgNPs with the switching segment and netpoints needs further consideration [45]. Toncheva et al. developed LASMPCs by incorporating 1 wt % AgNPs into poly(ε-caprolactone) (PCL). Two strategies were presented for the AgNPs generation and immobilization: (i) AgNPs adsorption on the cellulose nanocrystals' (CNCs') surface (CNC-ad-AgNPs) by direct reduction of Ag ions in the presence of NaBH4; and (ii) AgNPs grafted on the CNCs' surface (CNC-g-AgNPs) by CNCs' surface modification with thiol groups and the subsequent reduction of Ag ions in the presence of the reducing agent [96].

Figure 2.10 (a) and (b) illustrate the light absorbance capability of CNC-ad-AgNPs and CNC-g-AgNPs LASMPCs respectively [96]. For the CNC-ad-AgNPs, a single longitudinal absorbance band (centered at 400 nm) was registered, as a signature of

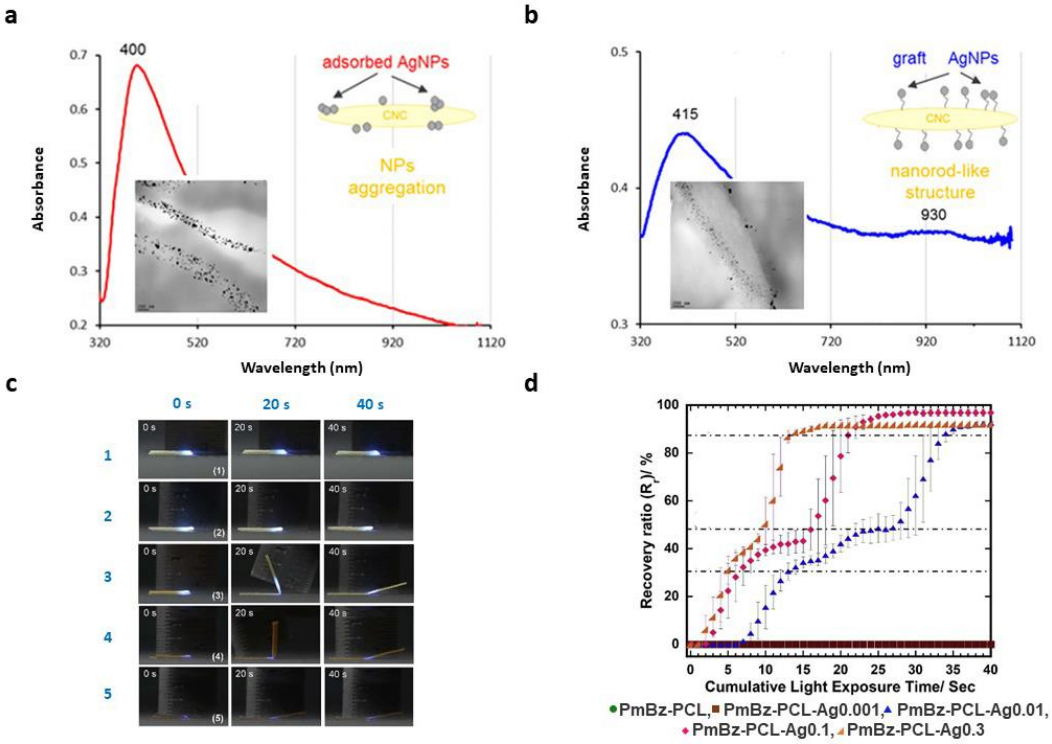

Figure 2.10: Light absorbance and shape memory behaviour of silver nanoparticle based LASMPCs (a) UV−vis and IR spectra of CNC-ad-AgNPs [96]. (b) UV−vis and IR spectra of CNC-g-AgNPs [96]. (c) Light (408 nm, 780 mW) triggered shape memory behaviour of PmBz-PCL (1), PmBz-PCL-Ag0.001 (2), PmBz-PCL-Ag0.01 (3), PmBz-PCL-Ag0.1 (4), and PmBz-PCL-Ag0.3 (5) [45]. (d) Light (408 nm, 780 mW) triggered shape recovery ratio as a function of cumulative light exposure time [45].

adsorbed spherical nanostructures. Grafting AgNPs on the nanocrystal surface resulted in a red shift of the band, plasmon excitation along the nanofiller's longer axis (415 nm), and the appearance of a second longitudinal absorbance broad band with low intensity at 930 nm. This spectral footprint provided evidence for the presence of a nanorod-like structure, where the adjacent nanoparticles (along the nanocrystal surface) were situated at a distance sufficient to interact and generate a coupling plasmonic effect. Accordingly, it is possible to increase the nanofiller longitudinal absorbance by modifying the type of nanoparticles immobilized on the nanocrystal surface [96]. The proposed design of plasmonic AgNPs grafted onto CNCs was an efficient plasmonic system for fast and remote shape memory actuation due to IR light illumination [96].

Yenpech et al. proposed an in-situ ring opening polymerization (ROP) to combine a thermoset hard segment, i.e., polybenzoxazine, and a thermoplastic soft segment, i.e., polycaprolactone and silver nanoparticles (AgNPs) for LASMPCs [45]. By varying the AgNP's percentage, four different LASMPCs were produced, termed mBz-PCL-Ag0.001 (0.001 wt%), PmBz-PCL-Ag0.01 (0.01 wt%), PmBz-PCL-Ag0.1 (0.1 wt%) and PmBz-PCL-Ag0.3 (0.3 wt%). Furthermore, an SMP film with 0 wt% of AgNPs was used as the reference (PmBz-PCL). It was revealed that the melting point and the crystallization temperatures slightly decreased when the content of AgNPs increased. Moreover, stress at yield point increased with respect to the increase of the AgNPs content.

Figure 2.10 (c) shows a series of shape recovery behaviours of PmBz-PCL films with or without AgNPs due to 408 nm, 780 mW laser light irradiation. The LASMPCs with 0 wt% and 0.001 wt% did show any shape recovery within 40 seconds. The light triggered shape recovery ratios of each test specimen were calculated and are presented in Figure 2.10 (d) as a function of laser exposed time. It is clear that the recovery time of PmBz-PCL Ag0.1 is almost equal to that of PmBz-PCL-Ag0.3. However, the recovery time of PmBz-PCL-Ag0.01 is longer than those of PmBz-PCL-Ag0.1 and PmBz-PCL-Ag0.3. The results suggest that the 0.01 wt% AgNPs content is the minimal content for such phenomenon to be visually observable.

2.5.2.3 Titanium Nitride

Titanium nitride nanoparticles (TiNNPs) were used as broadband plasmonic light absorbers to a cross-linked LASMPC of poly(ε-caprolactone) (PCL) [46]. The optical

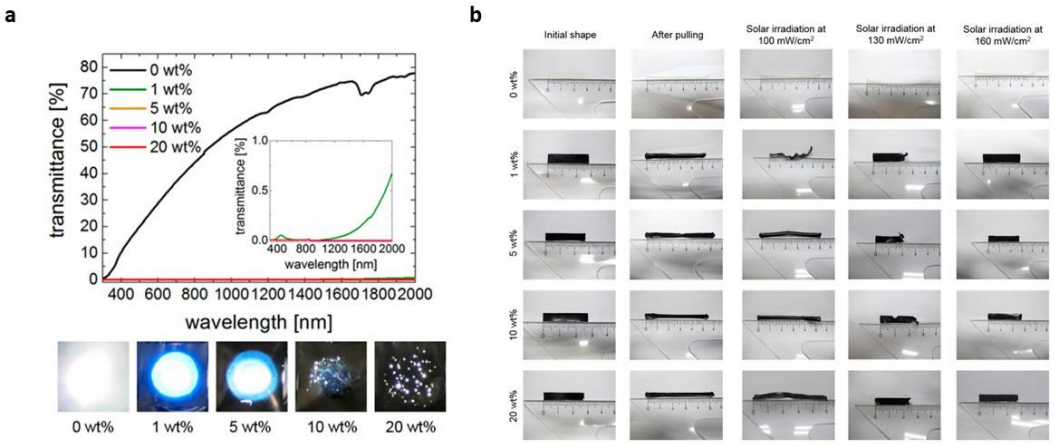

Figure 2.11: Light absorbance and shape recovery behaviour of 0, 1 , 5 , 10 and 20 wt% titanium nitride based LASMPCs (a) Transmittance spectra and top view CCD images while white light is illuminated from the bottom of the LASMPC films (b) Shape recovery due to 5 min of 100, 130 and 160 mW/cm^2 solar radiation [46].

longitudinal absorbance loss of TiN is larger than that of gold or silver, hence the line width of its plasmonic resonance is broader. Analytically and experimentally, it was found that the broad resonance of TiNNPs was advantageous for sunlight longitudinal absorbance and showed a higher longitudinal absorbance efficiency [46, 103]. Together with its chemical stability and cost effectiveness, TiNNPs has been reported as a decent light absorber. Figure 2.11 (a) presents the light absorbance behaviour of neat PCL (0 wt% TiNNPs) and 1 , 5 , 10 and 20 wt% TiNNPs mixed PCL LASMPCs [46]. Unlike the neat sample, all other LASMPC samples showed a very low transmittance, which verifies that the optical longitudinal absorbance of TiN has a broad range. Adding 1 wt % of TiNNPs into PCL made the TiN based LASMPC completely opaque. With respect to the increase of TiNNP content, the amount of white light passing through the LASMPCs was reduced. The LASMPCs with different weight ratios were elongated to a 100% strain and subsequent shape recovery was observed by exposure to 5 minutes of 100, 130 and 160 mW/cm^2 solar radiation.

In accordance with the results shown in Figure 2.11 (b), the shape fixity was identified as an independent response to TiNNP concentration [46]. The samples irradiated at 100 mW/cm^2, which is the standard irradiance of sunlight. This did not show any measurable changes. By increasing the irradiance to 130 mW/cm^2, all the TiNNPs containing samples shrank back almost to their original lengths. When the irradiance was increased to 160 mW/cm^2, all the samples except the neat sample recovered to their original shapes [46].

Importantly, PCL itself is biodegradable and TiN is chemically stable. These points, taken together with their light responsive property mean that TiNNP mixed PCL LASMPCs are suitable for biological and clinical applications. The sunlight responsive property is attractive for the sake of saving energy to activate shape memory polymers [46, 103].

2.5.2.4 Tungsten Oxide

Zhou et al. reported multi photo responsive shape memory polymer hybrids and novel chiral actuators based on $W_{18}O_{49}$ nanowires [118]. LASMPC has been produced by incorporating oligo(ethylene glycol) (OEG)-modified $W_{18}O_{49}$ nanowires into cross-linked polyethylene glycol diacrylate (cPEGDA) polymer matrices. The chemical cross-linking points formed by the acrylate group provided the shape fixity capacity, while crystalline PEG segments served as the reversible phase of shape memory. The OEG ligands on the surface of $W_{18}O_{49}$ could enhance the compatibility between $W_{18}O_{49}$ and cPEGDA through hydrogen bonds [118]. Because of this enhanced compatibility, OEG-W18O49 nanowires were well dispersed and increased the crystallinity of cPEGDA matrices, even at high loading concentrations of 4.0 wt%. Interestingly, the cPEGDA/$W_{18}O_{49}$ nanocomposites showed efficient photothermal transition and rapid shape memory behaviours. The surface temperature of LASMPC containing 2.0 wt% of cPEGDA/$W_{18}O_{49}$ nanowire films could reach up to 74 °C in 1 min due to irradiation of 365 nm UV light.

However, the photothermal effect was more efficient under the NIR irradiation than that under UV irradiation. The temperature reached to 167 °C in 20 s and 214 °C in 1 min due to the irradiation of 1.6 W/cm^2, 808 nm NIR laser. Under irradiation of 1.6 W/cm^2, 980 nm NIR laser, the temperature reached 161 °C in 20 s [118]. Furthermore, due to the oriented chain segments of the crystalline polymer and vector sum of shape recovery forces, the cPEGDA/$W_{18}O_{49}$ NW hybrid actuators exhibited stable helical deformations.

2.5.2.5 Metal Ions

Chen et al. have synthesized a series of novel NIR induced shape memory ionomers by cross-linking polyvinyl alcohol (PVA) and polyacrylic acid (PAA) with various metal ions. The PVA-PAA system was used as the framework and various metal ions (Fe^{3+}, Cu^{2+}, Ni^{2+}, Co^{2+}, Cd^{2+}, Cr^{2+}, Al^{3+}) were used as the cross-linked junctions [119]. The light

induced shape memory effect of the ionomer was freely tailored by merely adjusting the species and content of the metal ions. Figure 2.12 (a) and (b) illustrates the light absorbance and photothermal effect (due to 808 NIR light) of the pristine PVA-PAA and ionomers cross-linked by different metal ions [119]. The photothermal efficiency of the ionomers shows a direct relation to 808 NIR longitudinal absorbance intensity in the spectra.

It is well known that the longitudinal absorbance band of a metal complex in the visible or NIR window is mainly due to the d-d transition of transition metal ions induced by complex ions [119, 141]. Attributed to the electronic configuration of $4d^{10}$ and 2p6 for Cd^{2+} and Al^{3+}, no d-d transition occurs in the corresponding ionomers, leading to the low longitudinal absorbance in the NIR range. For the other ions, the increase of longitudinal absorbance intensity from Cr^{2+} to Cu^{2+} is due to the increase of d electron number and polarization of metal ions, especially for Cu^{2+}(3d9) with the highest electron number. The higher photothermal effect of Fe^{3+} relative to Co^{2+} may be attributed to its higher charge number [119].

In general, these results indicate that ionomers can be developed as a family of powerful NIR light responsive materials with a facile preparation method. Interestingly, the LASMPCs have shown a high shape recovery ratio, over 93%. Moreover, the dynamic ionic cross-linked interaction has caused light induced plasticity, leading to repeatable programming of the ionomers to new permanent shapes without reducing the shape memory performances [119].

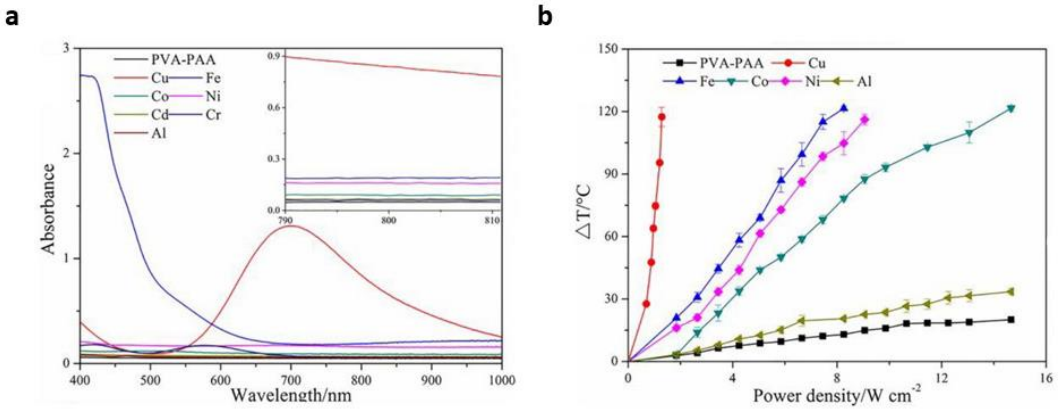

Figure 2.12: Light absorbance and photothermal abilities of the ionomers cross-linked by different metal ions (a) UV-vis-NIR spectra (b) Photothermal behaviour due to 808 nm NIR light irradiation [119].

2.5.3 LASMPCs with Carbon-based Photothermal Fillers

2.5.3.1 Carbon Nanotube

The single walled (SWCNT) and multi walled (MWCNT) carbon nanotubes were incorporated into SMP matrices not only for light activation [44, 47, 93], but also for electrical activation [142, 143], and mechanical property enhancements [7, 144]. Although SWCNTs and their exceptional properties are considered the archetypes of nanotechnology, the technological hurdles of producing and purifying them at low cost and in large scale have limited the realization of many bulk applications. In contrast, alternative gaseous fabrication routes yield MWCNTs with varying degrees of molecular perfection, which are relatively low cost [91]. Various SMP matrices, i.e., epoxy-based resin [53, 93], polyurethane [44], polydimethylsiloxane (PDMS) [47] and polylactic acid (PLA) [22] have been employed to develop CNT photothermal filler incorporated LASMPCs.

Figure 2.13 (a) compares the UV-Vis transmittance spectra of a p-aminodiphenylimide/epoxy (referred to as EADP) and MWCNT/epoxy (referred to as ECNT) composites [53]. The photothermal effect of p-aminodiphenylimide is attributed to its molecular configuration owing to the trans-cis photo isomerization of azobenzene and the photothermal effect of CNT is due to the band gap transition [53]. Unlike the EADP composite, the ECNT composite has shown a low transmission (~5%) throughout the entire wavelength range. Accordingly, it is clear that CNT shows a high light absorbance, irrespective of the wavelength. Researchers have studied the photothermal behaviour due to increasing power densities of NIR light [53].

Inclusion of CNT significantly enhances the shape recovery rate. For example, a programmable hydrogel composite with 0.75 mg/mL of SWCNTs takes ~2.7 seconds to bend into a 90º angle, whereas it takes ~14 seconds for the hydrogel composite without SWCNTs to perform the same actuation, due to 785 nm, ~30 mW laser irradiation [145]. This leads to an overall maximum response time enhancement of ~5 times through the incorporation of SWCNTs into the polymer matrix [145]. Moreover, the response time is found to be linearly changed with the SWCNT content, as illustrated in Figure 2.13 (b).

Ahir et al. studied the stresses generated by MWCNT based LASMPCs in tensile mode [47]. This revealed that the exerted stress and change to the initial length depended on both the MWCNT content and the applied pre-strain. As illustrated in Figure 2.13 (c),

samples with different nanotube loadings appear to have a crossover at the same point (around 10% pre-strain) once exposed to a 675 nm 0.008 W laser irradiation [47]. Moreover, the response increased at a higher nanotube loading, as anticipated. Interestingly, Ahir et al. concluded that the way that carbon nanotubes dispersed in an elastomer can lead to an unprecedented, reversible volume change in response to infrared irradiation. These findings have added a new dimension to LASMPCs by demonstrating a reversible photo induced mechanical response of a MWCNT elastomer nanocomposite [47].

Based on the conclusions of Ahir et al. [47], Vaia [91] explained that the direction of the actuation (expansion or contraction) depends on the extent to which the nanocomposite is strained. If the material is being slightly pulled, it will expand when exposed to infrared light. Moreover, this expansion is two orders of magnitude greater than the pristine,

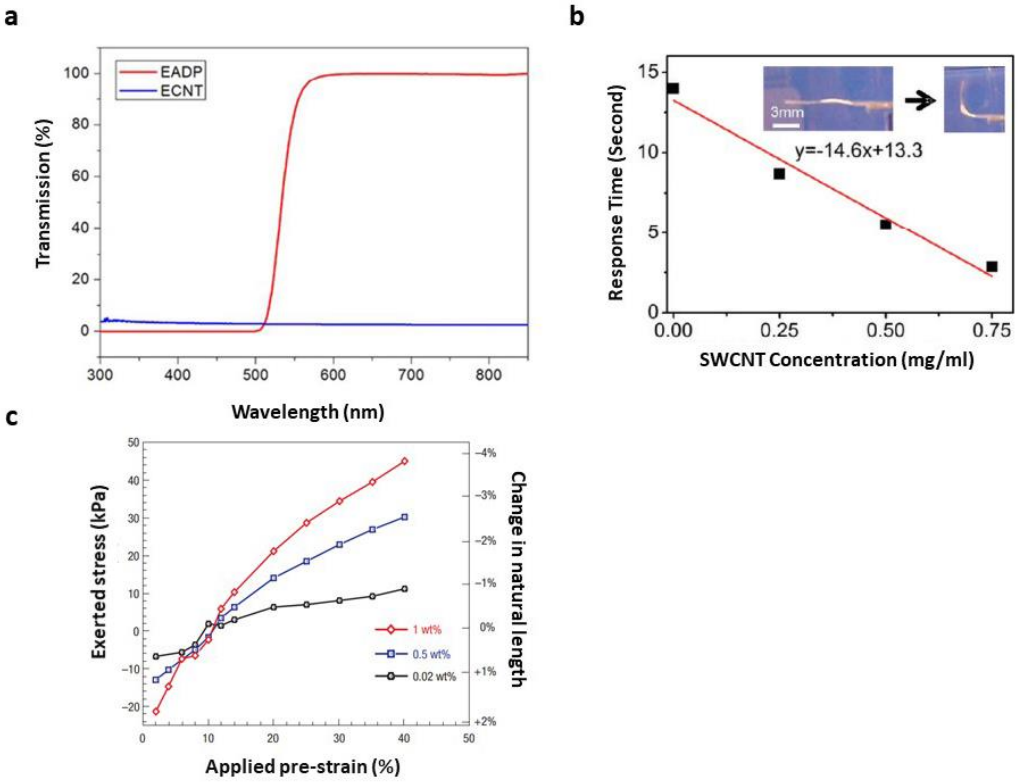

Figure 2.13: Photothermally activated shape memory properties of CNT based LASMPCs (a) Light absorbance capability [53] (b) Response time due to 785 nm, ~30 mW laser as a function of SWCNT concentration [145] (c) Exerted actuation stress and change in natural length due to 675 nm 0.008 W laser irradiation as a function of pre-strain, for samples with increasing MWCNT loading [47].

unfilled elastomer. Conversely, if the material is pulled strongly, to a strain higher than 10 %, it will contract under identical exposure to infrared light. This process is completely reversible and persists after numerous cycles.

Lu et al. found that some unique synergistic effects of CNTs and boron nitride (referred to as BN) could facilitate thermally conductive and accelerated the IR light triggered shape recovery behaviour of the SMP nanocomposites. The flexural strength of SMP nanocomposites was measured via three-point bending. Figure 2.14 (a) shows the stress strain curves of LASMPCs filled with cumulative weight concentration CNTs [93]. The results demonstrate that the mechanical strength of the nanocomposite specimens have been improved with a corresponding increase of CNT content.

DMA testing was used to characterize the elastic modulus, storage modulus and tangent delta of LASMPCs as a function of temperature. The typical size of CNTs is smaller than that of the macromolecular chains. Therefore, the mobility of macromolecular chains

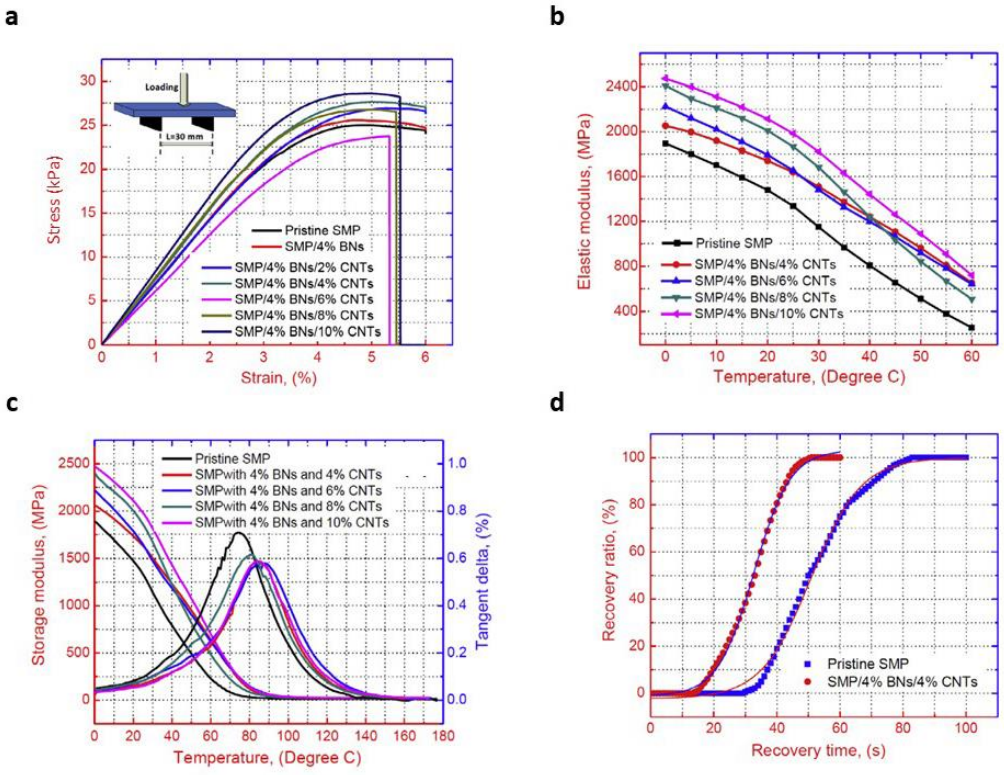

Figure 2.14: Mechanical and thermomechanical properties with respect to CNT and boron nitride content of epoxy-based LASMPCs (a) Flexural strength via three-point bending (b) Elastic modulus as a function of temperature (c) Storage modulus and tan delta curves (d) Shape recovery ratio as a function of recovery time [93].

would be restrained by CNTs. These obstacles could help the polymer matrix to resist external loading, resulting in an improved mechanical performance [93]. Experimental results imply that the addition of CNT increases both the elastic and storage modulus of nanocomposites over the whole temperature range. Furthermore, with the increase of CNT content from 0 to 10 wt.%, the Tg increases from 73.25 to 96.62 °C. IR light induced shape recovery was investigated in an IR heating oven at 120 ºC. It was identified that the LASMPC that contained 4 wt.% BN and 4 wt.% CNTs has the highest heating efficiency under IR light radiation and took 60 seconds to complete the shape recovery process. Figure 2.14 (d) presents the recovery ratio as a function of IR light exposed time for LASMPC containing 4 wt.% BN and 4 wt.% CNTs.

2.5.3.2 Graphene

Graphene, consisting of monolayers of carbon atoms arranged in a honeycomb network, is prevalent in many carbon based materials [146]. Apart from its recognized electronic properties, graphene demonstrates several other unusual attributes. In general, graphene has been incorporated into SMP matrices to enhance the electro responsive effect, thermal conductivity and mechanical stiffness [8, 147-149]. Several studies have been carried out to determine the photothermally triggered shape memory behaviour of graphene and graphene oxide incorporated LASMPCs [48, 92, 150-154]. Typically, the graphene-based LASMPCs were triggered by 808 nm NIR light [151-154], whereas activation in 450 nm visible light has also been reported [150]. Graphene-based LASMPCs also reach higher temperatures and demonstrate a higher recovery rate and recovery ratio with raised graphene content [152, 153]. Furthermore, by increasing the power density of the irradiated light, higher temperatures can be obtained [153]. Loomis et al. have shown that, by dispersing graphene nanoplatelets (GNPs) within a polydimethylsiloxane matrix, efficient light longitudinal absorbance by GNPs and subsequent energy transduction to the polymeric chains can be used to produce significant amounts of motion in a controlled way through the entropic elasticity of the pre-strained composite [48]. Figure 2.15 (a) presents the photothermal efficiency relationship as a function of GNP loading. Notably, an increase in photothermal efficiency with increased GNP loading, ranging from 0.027% (0.1 wt.% GNP) to 0.033% (2 wt.% GNP), has been found [48]. The photothermal efficiency divided by Carnot efficiency as a function of

GNP loading is presented in Figure 2.15 (b). It is clear that a minor amount of GNPs (0.1 wt%) also resulted in a substantial temperature change [48].

The storage modulus and Tg also increase as the weight percentage of graphene content increases [92, 152]. The incorporation of graphene into the SMP matrix significantly improves mechanical properties, especially enhancing toughness with a classical ductile fracture [152]. Researchers have studied the changes to the shape memory characteristics of graphene-based LASMPCs with respect to the shape memory cycles, and, importantly, no significant changes to the shape fixity and recovery ratios have been found with an increased the number of cycles (measured up to 5 cycles) [92, 152]. Long term behaviour and degradation as a function of repeated cycling for GNP incorporated composites has been studied by Loomis et al. [48]. Figure 2.15 (c) shows the measured displacement of an actuator as a function of time for 0 cycles, 1000 cycles, and 3000 cycles [48]. As revealed, even after 3000 cycles, there was only a minimum observed degradation, which

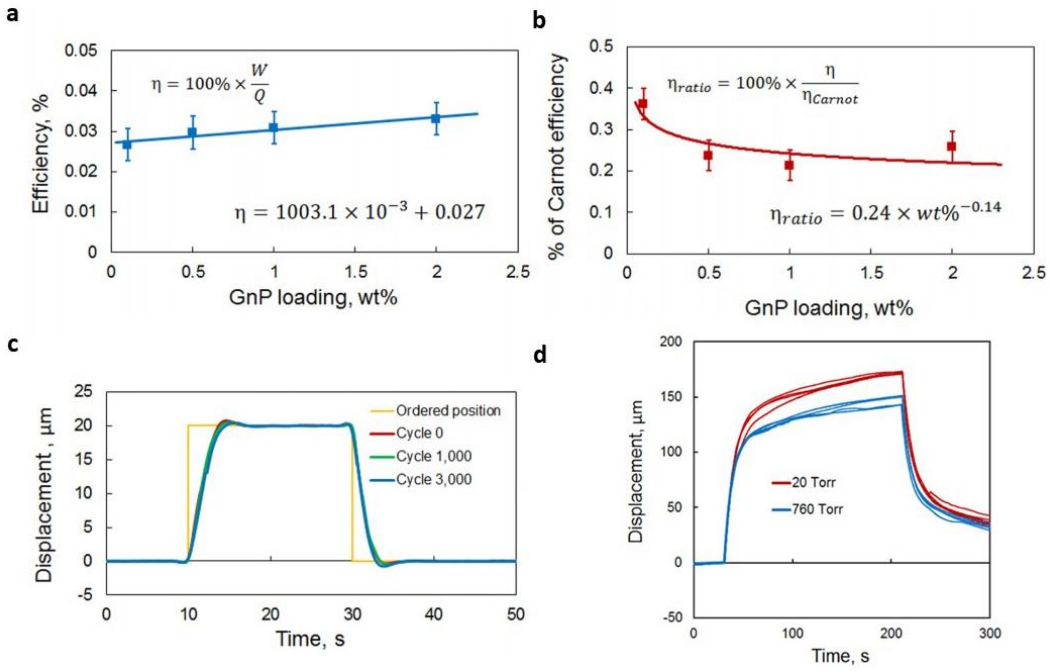

Figure 2.15: Photothermal efficiency and long term degradation of graphene-based light triggered composite (a) Photothermal efficiency as a function of GNP loading (b) Photothermal efficiency divided by Carnot efficiency as a function of GNP loading (c) Displacement as a function of time for 0 cycles, 1,000 cycles, and 3,000 cycles (d) Displacement as a function of time for a 1 wt% GNP sample at ambient pressure (760 Torr) and at medium vacuum (20 Torr) [48].

demonstrates the long lifetime and high shape recovery accuracy of graphene based composites.

Many systems to be used in the space environment utilizing micro and nano manipulation technologies require operation in a vacuum. Interestingly, light can be used to trigger such systems, as light can travel in a vacuum for long distances. In order to evaluate the feasibility of graphene-based photothermally triggered composites to work in a vacuum, the effects of pressure on displacement was investigated.

Figure 2.15 (d) illustrates the measured displacement of a 1 wt% GNP 210 mm thick composite sample as a function of time while exposing it to two environmental conditions, at ambient pressure (760 Torr) and at medium vacuum (20 Torr) [48]. Notably, at lower pressure (20 Torr), the displacement was approximately 30% higher than at atmospheric pressure, indicating that, as pressure decreases there is an associated drop in the composite heat loss due to natural convection.

2.5.3.3 Carbon Black

Carbon black (CB) is known to be a filler material for SMPCs as it enables electric triggering and enhanced mechanical properties [155]. Moreover, CB acts as a photothermal filler for LASMPCs by absorbing IR light [37, 133]. Liu et al. prepared a

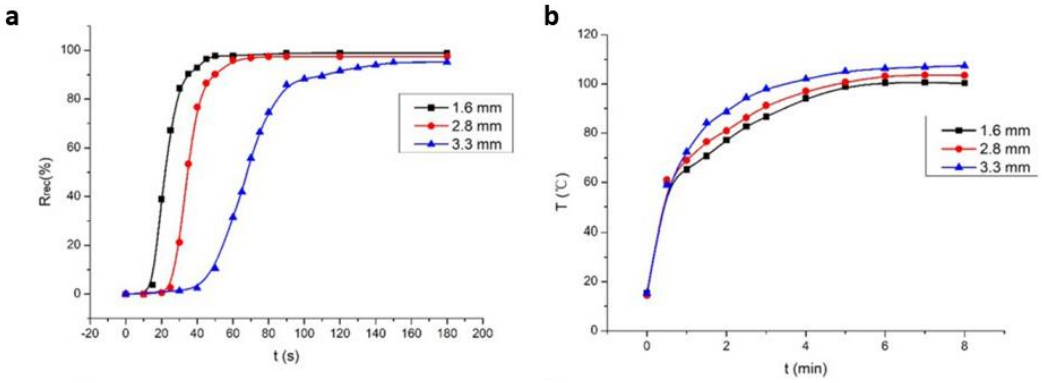

Figure 2.16: Effect of thickness and heat conductivity behaviour of carbon black based LASMPCs respectively (a) shape recovery ratio due to 1.0 W/cm^2, 10.64 μm mid IR irradiation for 1.6, 2.8 and 3.3 mm thick samples of 1.0 wt.% CB content [37] (b) Temperature increase due to 1.0 W/cm^2, 10.64 μm mid IR irradiation for 1.6, 2.8 and 3.3 mm thick samples of 1.0 wt.% CB content [37].

series of hydro-epoxy (HEP) matrix based LASMPCs with 0.5, 1.0, 1.5 and 2.0 wt% of CB [37]. The results indicated that CB particles had a better photothermal conversion effect once exposed to a 1.064 μm NIR laser, and the shape recovery ratio of CB/HEP composites was above 97%. With the increase of CB content, the growth trends of the shape recovery ratio remained unchanged, but the shape recovery ratio increased with the increase of the power density.

Moreover, the effects of composite thickness on shape recovery behaviours were investigated using 1.0 wt% CB/HEP composite [37]. According to Beer–Lambert's law, the light longitudinal absorbance of a specimen depends on three variables: extinction coefficient, path length, and concentration of the substance [156]. The path length varies with the thickness of the sample. Moreover, the light energy absorbed by the CB particles on the surface of the LASMPC converts into heat energy and passes into the underlying resin through heat conduction and transmission.

The time of heat transference is determined by the thickness of the LASMPC. Accordingly, as presented in Figure 2.16 (a), as the thickness increases, the shape recovery ratio decreases [37]. In contrast, with the increment of LASMPC thickness, the path length and the number of CB particles increase in the direction of the light incident, therefore the temperature of the LASMPC rises as presented in Figure 2.16 (b) [37].

2.5.4 LASMPCs with Organic Complex Based Photothermal Fillers

2.5.4.1 Rare Earth Organic Complexes

Rare earth materials are a special group of elements in the periodic table. The term 'rare earths' has been historically applied to the lanthanides because it was originally believed that these elements were sporadically distributed in nature. Lanthanide elements (referred to as Ln) have atomic numbers that range from 57 to 71 [157]. The rare earth organic complexes have the technical versatility for various applications such as energy harvesting, ultraviolet light detection, temperature sensing, laser and light-emitting diodes [158, 159]. Interestingly, the rare earth organic complexes containing $Yb^{3+,}$ Nd^{3+} and Sm^{3+} ions, which are being used to produce LASMPCs, respond to selective wavelengths of 980 nm, 808 nm and 1064 nm, respectively [30, 160]. Accordingly, $Nd(TTA)_3Phen$, $Yb(TTA)_3Phen$, and $Sm(TTA)_3Phen$ were incorporated into polyurethane [160],

poly[ethylene-ran-(vinyl acetate)] [30] and poly(methyl methacrylate-co-itaconic acid) [161] SMPs.

The commercial availability of the raw materials and the easy preparation approach enable such organic complexes to be cost efficient photothermal fillers for LASMPCs [30]. Furthermore, it has been reported that such organic complexes show a notable thermal stability up to 270 ºC. Initially, degradation starts at 270 ºC and continues up to 350 ºC, which can be attributed to the decomposition of ligand TTA. A further increase in temperature up to 440 ºC starts a secondary degradation and this continues up to 500 ºC, which can be attributed to the decomposition of ligand Phen [30]. However, it is noted that the photothermal efficiency of rare earth organic complexes is not comparable with conventional carbon based fillers. Therefore the mass fraction of the rare earth organic complexes is higher than that of the reported systems with carbon based photothermal fillers [30].

LAMPCs incorporating rare earth organic complexes demonstrate an increase in temperature with an increased weight percentage of photothermal fillers and irradiated power density. Poly[ethylene-ran-(vinyl acetate)] based LASMPCs with 10 phr of $Yb(TTA)_3Phen$, $Nd(TTA)_3Phen$ and $Sm(TTA)_3Phen$ have reached a temperature of 167 ºC, 120 ºC and ~105 ºC once exposed to 3.1 W/cm^2 of 980 nm, 1 W/cm^2 of 808 nm and 4 W/cm^2 of 1064 nm NIR radiation respectively [30, 160]. Furthermore, it has been found

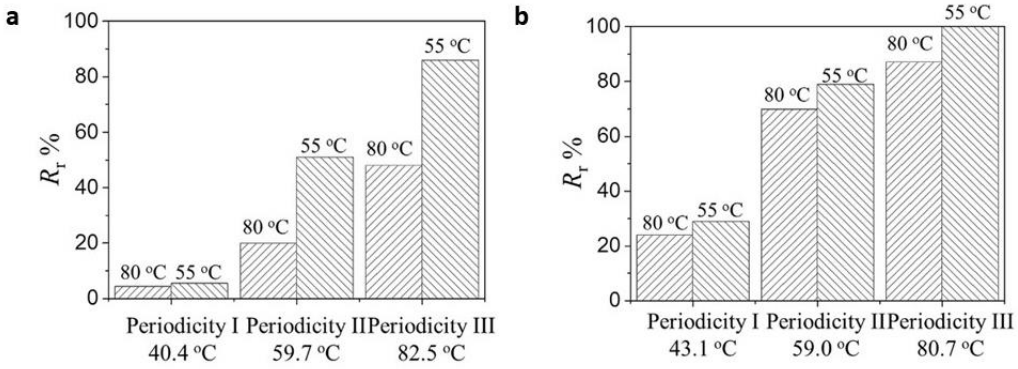

Figure 2.17: Effects of the irradiation periodicity (light on/off was set as 1/3 for Periodicity I, 1/1 for Periodicity II and 3/1 for Periodicity III) (a) Shape recovery rate of $Yb(TTA)_3Phen$ based LASMPC periodic irradiation of 1.4 W/cm^2 980 nm (irradiation frequency 3.4 Hz) [30] (b) Shape recovery rate of $Nd(TTA)_3Phen$ based LASMPC periodic irradiation of 0.65 W/cm^2 808 nm (irradiation frequency 3.4 Hz) [30].

that the temperature and shape recovery of such LASMPCs can be influenced by periodic NIR irradiation with different frequencies [30].

The irradiation periodicity can be used to control the balanced temperature, while the variation frequency only affects the range of temperature fluctuation. Figure 2.17 (a) and (b) present the periodicity dependent shape recovery rate along with photothermal temperature for $Yb(TTA)_3Phen$ (wt.% 10 phr) and $Nd(TTA)_3Phen$ (wt.% 10 phr) based LASMPC respectively [30]. The irradiation frequency was set as 3.4 Hz. By considering the ratio between light irradiation time and non-irradiation time, three periodicities were defined as Periodicity I, II, and III (light on/off was set as 1/3 for Periodicity I, 1/1 for Periodicity II and 3/1 for Periodicity III).

Furthermore, the relation between programming temperature and recovery rate has been studied by using two type of specimens programmed at 55 and 80 ºC [30]. It was clear that the recovery rate and temperature both increase with the periodicity. In addition, the specimens programmed at a lower temperature have demonstrated a higher recovery rate. It can be concluded that the four factors related to light source, i) wavelength, ii) power density, iii) periodicity, and iv) frequency, affect the light activated shape recovery behaviour of selectively triggered rare earth organic complex based LASMPCs.

2.5.4.2 Aniline Black

Polyaniline (PANi) is an electroactive synthetic polymer, originally synthesized by the oxidation of aniline by Fritzsche in 1840. PANi has been described in various forms such as aniline black, emeraldine, and nigraniline [162]. The photothermal capability of aniline black (AB) due to 808 nm NIR and sunlight has been applied in the SMP activation and self healing of polymer composites [36, 125]. The UV-Vis-NIR spectrum has shown that AB as a photothermal filler highly increases the longitudinal absorbance within both the visible and NIR range. It was reported that the incorporation of AB reduced the tensile strength of EVA based LASMPCs, where the tensile strength was 2.77, 1.77, 1.71, and 1.62 MPa for pristine EVA, EVA with 0.2 phr AB, 1.0 phr AB and 2.0 phr AB, respectively [36].

The LASMPCs programmed at 140 °C presented an excellent shape recovery, greater than 98% once exposed to 808 nm, 1.5 W/cm^2 NIR light for 3 min, while the generated temperature reached above 104 °C. Increasing the AB content from 0.5 to 2 phr reduced

the switching temperature from 85 to 74 °C. Furthermore, by changing the temperature via periodically turning on and off the irradiation, a reversible deformation of 10° was observed [36]. In addition to this light triggered activation, AB will be useful to self-repair the cracks in LASMPCs [125].

2.5.4.3 Polypyrrole and Porphyrin

Both polypyrrole and porphyrin have been investigated and reported as photothermal fillers for LASMPCs with excellent biocompatibility properties [49, 50]. A diketopyrrolopyrrole based conjugated polymer (PDPP3T) incorporated into a shape memory elastomer matrix of polycaprolactone-co-poly(urethane/urea) (PCL–PU) has shown an excellent photothermal effect under 808 nm NIR irradiation [49]. With 0.1 wt% PDPP3T polymer, the elastomer showed an obvious photothermal effect under laser irradiation with a power density of 0.5 W/cm^2. The sample temperature increased from ~22 ºC to ~45 ºC within 3 minutes. Once the power density and PDPP3T content were increased to 2.0 W/cm^2 and 0.5 wt%, the LASMPC reached a temperature of 120 ºC.

At similar conditions, the samples showed an excellent light induced shape memory performance with a shape recovery ratio of nearly 100% in recovering temporary shapes under various forms of deformations including bending, stretching and twisting. In addition, a combination of the photothermal effect and dynamic hindered urea bond in the elastomer structures has elaborated the self-healable effects. The elastomer also showed a light induced antibacterial effect due to local hyperthermia [49].

Qian et al. fabricated a tetraphenylporphyrin (TPP) loaded LASMPC by cross-linking micellar particles prepared by the co-assembly of porphyrin compounds and amphiphilic macromolecules [50]. The LASMPC was trigged by the red light of a 655 nm laser. The Tg of the SMP without TPP was 46.8 °C and the Tg has not shown any significant change due to the inclusion of TPP. The LASMPCs with TPP have shown relatively higher shape recovery and stress recovery behaviours. Furthermore, the LASMPC films were exposed to light radiation through an aqueous medium. The result showed that the aqueous medium had no effect on shape recovery behaviour [50]. This material was expected to have potential applications in the biomedical field due to the excellent biocompatibility of the porphyrin filler and the red light source, which was safe enough for biomedical treatment.

2.6 Methods of Light Diffusion

Typically, the light stimulation is being carried out by direct exposure of LASMP specimens to light radiation [28, 30, 160]. The direct exposure of LASMPC components to light is a relatively easy task. However, it limits the use of LASMPC materials to a small range of engineering applications. In addition, light diffusing, wavelength filtering and polarization enhance the LASMPC actuation capabilities [29, 42, 163, 164]. Fortunately, the recent advances in fibre optic technologies have facilitated remote activation of light sensitive materials and equipment. In particular, it has been identified that embedded optical fibres are invaluable for the remote activation of such processes for light activated SMP components [32, 33, 56, 165].

2.6.1 Irradiated Light onto the Surface of LASMPs/LASMPCs

2.6.1.1 Direct and Diffused Exposure

Generally, the LASMPs and LASMPCs are triggered by laser beams that are Gaussian in nature [55]. The laser beams can be focused onto a particular area, which enables a localized shape memory effect. Figure 2.18 (a) illustrates the widely used method of direct exposure of LASMPs and LASMPCs to a laser, where the shape memory effect is controlled by altering the wavelength, intensity and diameter of the laser beam [55]. The laser exposed area of the LASMP/LASMPC material reaches a stiff state in a short time, while the outer regions achieve the transition at progressively slower rates [55].

However, the through thickness penetration of the light intensity is non-uniform. In the case of photothermal LASMPCs, the heat is transferred along longitudinal (on surface) and transverse (through thickness) directions, which depends on the orthotopic thermal conductivity of the material [37]. Figure 2.18 (b) shows the exposure where the laser is diffused onto the LASMP material by a convex cylindrical lens [55]. Unlike the direct exposure, this diffused exposure enables light irradiation onto a larger area of an LASMP material. However, the irradiation is uneven and reduces the laser intensity due to the larger exposed area. The diffused exposure would be appropriate for non-localized LASMP activation.

Moreover, the entire area of LASMPCs with low thermal conductivity can be simulated by photothermal heating. However, due to the reduced light intensity of the diffused

exposure, the SMPs' light activated shape recovery rate will be relatively slow compared to the direct exposure.

As NIR light is safer for human tissues and the naked eye, it has been widely used to trigger LASMPCs under direct exposure. However, it is difficult to direct an invisible NIR light beam onto LASMPCs to realize the precise shape recovery of their featured areas. Fang et al. have introduced LASMPCs that present both up conversion and photothermal capabilities [166]. The modified fillers with an up conversion capability can be utilized as multifunctional fillers for LAMPCs, enabling the LASMPCs to convert the irradiated NIR light into both visible light and heat at the same time.

2.6.1.2 Filleted and Polarized Exposure

Bandpass filters are used to filter the light with a certain wavelength, from a general light source or from sunlight [29, 164]. Advantageously, a single light source with a fixed setup can be used to obtain various shape recovery behaviours, merely by changing the bandpass filter. Moreover, light polarization enables directional and reversible shape memory behaviours. Liquid crystal network based shape changing polymers and gold nanorod based LASMPCs demonstrate shape memory behaviours which are controlled by light polarization [29, 42]. Figure 2.18 (c) illustrates an experimental setup for light

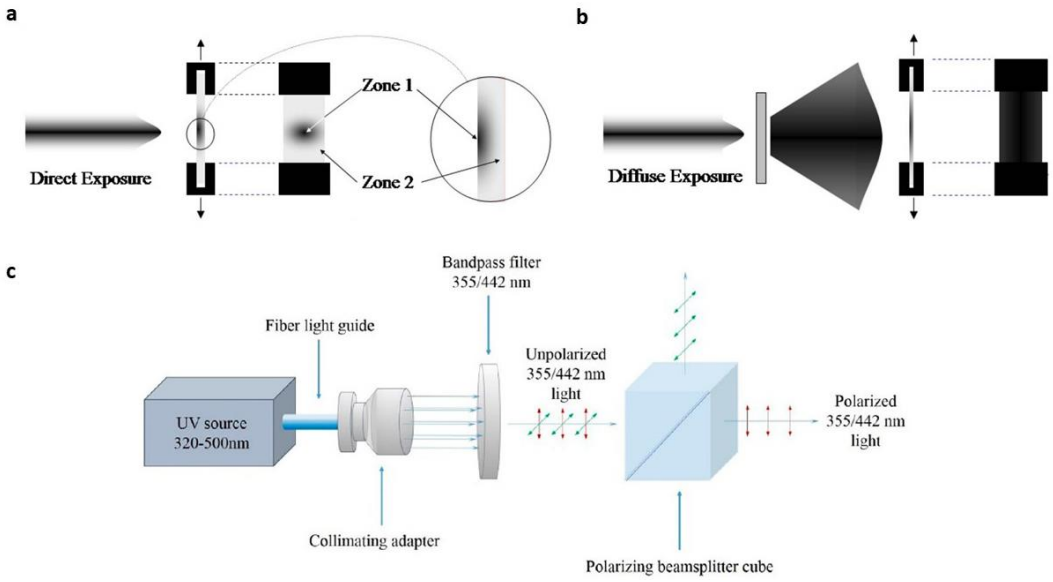

Figure 2.18: Methods of light irradiation onto LASMPs (a) Schematic diagram of the direct exposure [55] (b) Schematic diagram of the diffused exposure [55] (c) Schematic diagram of filtered and polarized light diffusion [29].

wavelength filtering with changeable bandpass filters and light polarization by a beam splitter cube [29]. In addition, light polarization rotators can be used to obtain multiwavelength light in the time domain [163]. Light filtering and polarization are being used in micro actuators with reversible and oscillating capabilities [163, 164].

2.6.2 Disperse Light into LASMPs/LASMPCs through Optical Fibres

2.6.2.1 Fibre Optic Light Diffusers Inserted into LASMP Material

Fibre optic light diffusers are being used for biomedical LASMP applications as the light can be sent into the human body in a safe manner [34, 35, 165]. Figure 2.19 (a) shows an optical fibre light diffuser used for an SMP vascular stent [165]. The diffuser was fabricated by casting an SMP formulation over the distal end of a 100 μm core diameter silica optical fibre using a tubular mold made of Teflon. To enable light diffusion, the surface of the cured SMP cylinder was abraded using a media blaster loaded with sodium bicarbonate powder. Approximately 80% of the incident laser light was emitted in the first centimeter of the diffuser. The optical fibre was sheathed with a 711 μm outer diameter stainless steel hypo tube [165]. Similar light diffusers have also been used for the devices designed for embolic treatment of aneurysms [34, 35].

2.6.2.2 Surface Treated Optical Fibres Coupled to LASMP Material

An SMP intravascular thrombectomy device consisting of an SMP micro actuator coupled to an optical fibre is shown in Figure 2.19 (b) [32]. The optical fibre is coupled by a socket joint and 810 nm laser light is dispersed into the SMP micro actuator. Initially a platinum dye photothermal filler mixed SMP rod with a 380 μm diameter was fabricated, which operated as the micro actuator. Secondly, one end of the rod was drilled coaxially along the longitudinal axis (diameter = 279 μm, depth = 1 mm). Then the drilled hole (socket) was filled with a transparent UV light curable epoxy having a refractive index of 1.49.

A step index silica core and silica clad multimode fibre with a 200 μm core diameter (240 μm diameter including the outer polyimide buffer) was cleaved on one end. The core refractive index was 1.4571 and numerical aperture was 0.22. The cleaved end of the fibre was inserted into the drilled socket of the SMP rod and then the epoxy was cured using a UV light source. The other end was coupled to a continuous wave 810 nm diode laser

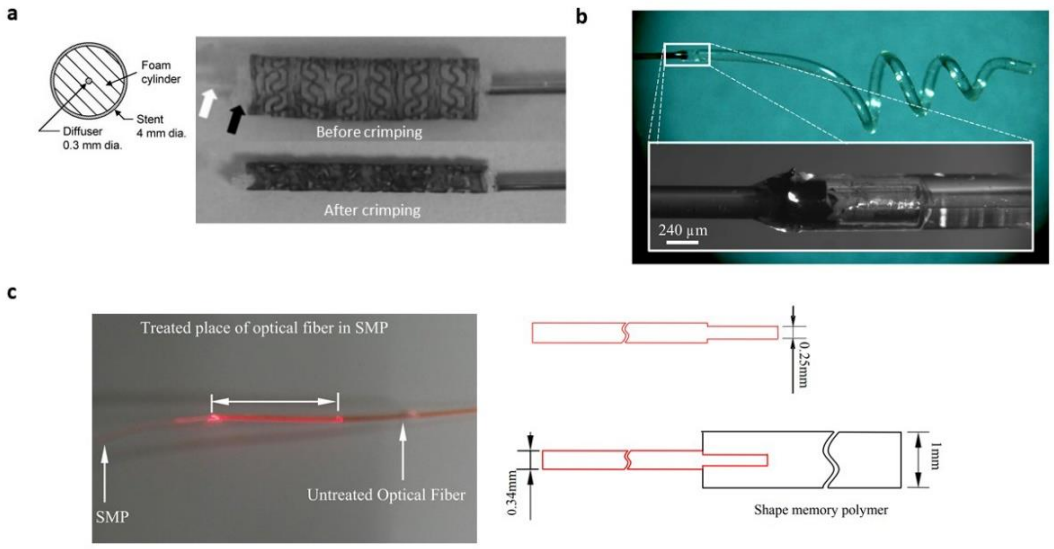

Figure 2.19: Methods of light dispersal into LASMPs/LASMPCs by optical fibres (a) Fibre optic cylindrical light diffuser [165] (b) Optical fibre connected to an LASMPC by an epoxy filled socket joint [32] (c) Surface treated (etched) optical fibre embedded into LASMP [56].

[32]. The SMP rod was programmed into a corkscrew shape by wrapping it around a custom-made conical mandrel.

The experimental results and calculations showed that more than 99.9% of the laser light was transmitted from the optical fibre into the SMP micro actuator (assuming zero longitudinal absorbance by the epoxy as noted by the manufacturer) [32]. However, the total power dropped with distance due to light leakage from the SMP corkscrew. As the SMP corkscrew turned, the light paths exceeded the critical angle for total internal reflection. Approximately 93% of the light reached the distal end of the corkscrew and 7% of the light was lost due to leakage.

Figure 2.19 (c) illustrates an etched optical fibre (340 µm diameter) connected to an LASMP [56]. The diameter of the core of was 270 µm and the refractive index of the fibre core was 2.8. The cladding of the optical fibre was etched by soaking it in a 10 wt % sodium hydroxide (NaOH) water solution for 30 seconds. After etching, the diameter of the optical fibre was reduced to 250 µm [56, 167]. Subsequently, the etched end of the optical fibre was inserted into a capillary with a 1mm diameter. Then the capillary was filled with mingled monomers cured in an oven. Next the capillary was immersed in a hydrofluoric acid solution for 24 h until the capillary was corroded. Finally, the SMP actuator was post cured in an oven. Once infrared light was sent through the optical fibre

the SMP actuator showed shape recovery in 12 seconds, where the Tg of the SMP material was 53.7 °C [56, 167].

Maitland et al. developed an optical fibre connected micro actuator for treating strokes [33]. A step index fibre with a 100 μm core diameter and a polyimide buffer were used. First the buffer was removed using a cylindrical heating element that burned it off. Then the cladding of the fibre was etched by soaking it in 100% hydrofluoric acid for 15 minutes. The acid etched fibre was dip coated by a UV-cured optical adhesive and cured. The hardened adhesive coating had a refractive index larger than the fibre core such that light transmitted efficiently into the adhesive. The SMP devices were connected by a straight fibre-SMP coupling. However, the proposed micro actuators require a well-engineered coupling of the light from the diffusing fibre through the blood into the SMP.

2.7 Wavelength Selective and Sequential Shape Memory Effect

Wavelength selective shape memory effect has been introduced for remote and sequential actuation of LASMPs / LASMPCs. There is significant interest in sequential actuation intended for sophisticated SMP applications. As discussed in Sections 2.5.2.1, 2.5.4.1 and 2.8, gold nanoparticles [52, 136], rare earth organic complexes [30, 160] and p-aminodiphenylimide [53] have the ability to facilitate wavelength selective and sequential actuation of LAMPCs. Table 2.2 presents further wavelength selective materials and respective triggering wavelengths.

Furthermore, Liu et al. have reported that printed ink on the surface of a SMP sheets discriminately absorbs light on the basis of the light wavelength and subsequently generates the photothermal heat [168]. As presented in Figure 2.20 (a), various colour patterns can be designed to absorb only specific wavelengths of light, thereby providing control of sheet folding with respect to time and space.

Such a shape memory effect may have numerous applications including actuators, sensors, implantable devices, smart packaging, reconfigurable electronics and deployable structures [168]. Figure 2.20 (b) – (e) illustrate differential light longitudinal absorbance by printed ink intended for sequential folding. For example, the yellow and cyan inks show an opposite longitudinal absorbance response to red and blue LEDs. The cyan hinge only folds in response to 660-nm light, whereas it remains unresponsive to 470-nm light even after extended exposures for 10 min. Instead, the yellow hinge only folds in response

Table 2.2: Wavelength selective shape memory and photothermal materials and respective triggering wavelengths.

SMP material / Photothermal filler	**Trigged selective wavelength**
Gold nanorods [52]	860 nm
Gold nanospheres [52]	530 nm
Gold nanoparticles [160]	520 nm
$Nd(TTA)_3Phen$ [30, 160]	808 nm
$Yb(TTA)_3Phen$ [30, 160]	980 nm
$Sm(TTA)_3Phen$ [160]	1064 nm
p-aminodiphenylimide [53]	365 nm
Polyurethane elastomer containing azobenzene groups [160]	UV light

to 470-nm light, whereas it remains unresponsive to 660-nm light irradiated for at least 10 min [168]. Figure 2.20 (f) to (h) present an application of kirigami in sequential folding to realize significant out-of-plane motion from in-plane shrinkage.

As shown in Figure 2.20 (f), a cylindrical "gripper" can be realized using a planar template of two circular rings connected with living hinges. The outer circular ring (in yellow) shrinks to generate a "closed" position using a blue LED, which is possible because of the connections of the flexible living hinges. The inner circular ring (in cyan) shrinks separately to flatten the gripper upon subsequent exposure to a red LED. Similarly, a spiral structure can be achieved, as shown in Figure 2.20 (g). The final shape appears to be a tower in which each layer can pop up one by one if each circular ring is printed in a different colour. Furthermore, as presented in Figure 2.20 (h), blue LED can generate a kirigami dome structure. The panels with black hinges fold slightly ahead of the shrinkage of the outer ring (in yellow) to promote break symmetry and thereby the formation of the raised dome shape [168].

2.8 Light Activated Reversible and Multi Shape Memory Effect

One major drawback of the general (one-way) SMPs to be applied in real life devices is the limitation of the shape change's reversibility. Once the shape recovery step is completed, a new programming step is required to rebuild the temporary shape. In each

shape memory cycle, the reprograming step needs to be performed manually [67, 169]. Advanced shape memory devices would be able to change their shape reversibly and multiple times without the necessity to apply an external load for shape programming. Reversible (two-way) SMPs are capable of switching several times between two different shapes on their own through an external stimulus [54, 170-172]. The triple shape memory polymers feature two temporary shapes [173, 174]. Usually, the intermediate temporary shape is programmed in the beginning, followed by the programming of the final temporary shape. The appropriate stimulus will lead to a transformation from the final temporary shape to the intermediate temporary shape. Subsequently, a second trigger starts the regeneration of the original permanent shape. Each of these transitions could be based on a one-way or two-way SME. Moreover, multiple (n times) shape recovery steps can be obtained by featuring one permanent shape and (n − 1) temporary shapes [53, 175, 176].

Compared to thermally induced reversible and multi shape memory effects, the use of light facilitates multiple levels of control by varying the wavelength, intensity, position, and polarization. Figure 2.21 (a) illustrates the unfolding and folding shape memory behaviours of an LCN based hybrid LASMP box exposed to UV light [29]. LCNs are able to exhibit large dimensional changes due to the macroscopic orientation of the liquid crystal (LC) domains. Advantageously, the reversible nature of the LC phase transition shown by the LC domains has been used as the switching segments of the LASMPC material. However, the LC phase transition has been mainly caused by a photothermal effect rather than a photochemical effect (trans−cis isomerization) [29].

Moreover, poly(ɛcaprolactone) copolymers and poly(ethylene-co-vinyl acetate) based LASMPCs have shown reversible two-way shape memory behaviour in respect to switching the irradiated light on and off [54, 170]. A reversible LASMPC gripper controlled by switching on and off a 365 nm UV light is shown in Figure 2.21 (b) [54]. The LASMPC was activated by the photothermal effect of p-aminodiphenylimide (p-AP).

The two-way shape memory effect reveals the crystallization-induced elongation (CIE) as the temperature decreases and melting-induced contraction (MIC) as the temperature increases [177]. During MIC, the segment melting leads to sample contraction due to entropy elasticity [178]. Accordingly, when the LASMPC undergoes cycles of photothermal heating (light on) and natural cooling (light off), the two-way reversible shape memory properties were obtained [54].

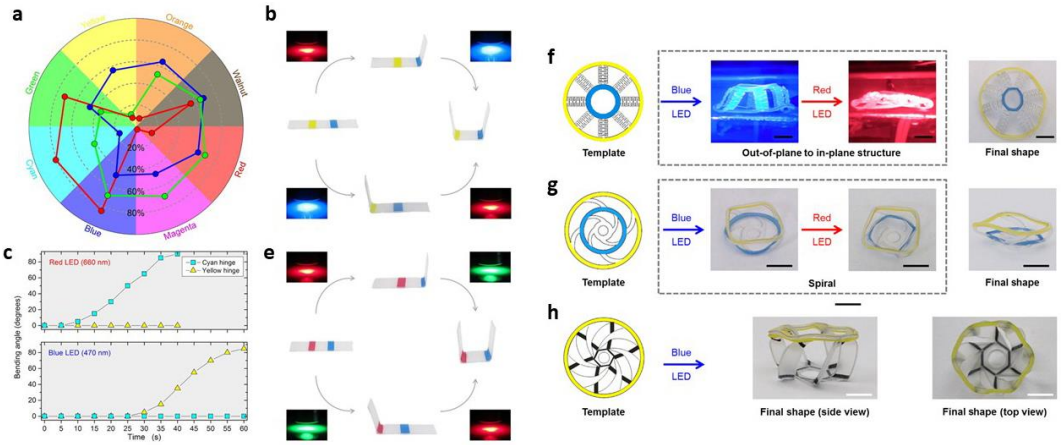

Figure 2.20: Concept of differential light longitudinal absorbance for sequential folding and sequentially actuated kirigami 3D shapes (a) Radar plot in which each wedge represents an ink colour from a laserjet printer. Data points represent the optical longitudinal absorbance of the three wavelengths of LEDs (red-660 nm, green-530 nm, and blue-470 nm). (b) Folding behaviour controlled in sequence by using hinges in yellow (in response to a blue LED) and cyan (in response to a red LED). (c) Bending angle as a function of LED exposure time for yellow and cyan hinges under the exposure of red and blue LEDs. (d) Folding behaviour controlled in sequence by using the hinges in magenta (in response to a green LED) and cyan (in response to a red LED). (f) Out-of-plane and in-plane structures are actuated sequentially by shrinking the outer ring (yellow) first to achieve out-of-plane motion and then shrinking the inner ring (cyan) to flatten the sample again. Living hinges connect the two circular rings. (g) The spiral structure forms by first pushing the bottom upward because of the shrinkage of the yellow ring and subsequently pushing the middle layer upward because of the shrinkage of the cyan ring. Images in the boxes with dashed lines show the temporary shape formed by irradiating with blue LED and then the shape formed by irradiating with a red LED sequentially. The final shape represents a side view of the spiral. (h) A dome structure results by applying inks with different optical longitudinal absorbance under a blue LED. Scale bars, 5 mm [168].

Figure 2.21 (c) - (d), illustrate the multi shape memory effect of a wavelength selective multicomposite strip consisting of three typical segments: p-Ap/epoxy (left), neat epoxy (middle) and MWCNT/epoxy (right) composites [53]. Initially, the multicomposite strip

was programmed into a cornu antelopis-like temporary shape (Shape #1). Then the multicomposite was exposed to a 365 nm light where the shape recovered to a V-type temporary shape (Shape #3) followed by heating above Tg to obtain the original shape. The respective hybrid shape memory activation- driven triple shape memory effect is shown in Figure 2.21 (c) [53]. This was achieved due to photothermal heating followed by direct heating. In addition, when the programmed multicomposite (Shape #1) was firstly exposed to a NIR light of 808 nm and secondly exposed to an UV light of 365 nm, first a pigeon-like temporary shape (Shape #2) and then V-type temporary shape (Shape #3) were obtained. In this case also, the original shape was obtained by direct heating.

The respective multi shape memory cycle with a total of three temporary shapes is shown in Figure 2.21 (d). As illustrated in Figure 2.21 (e), the shape recovery process of a wavelength selective multicomposite can be further modulated by micro localized photo induced shape memory effects through photo manipulation [53]. When 365 nm UV light or 808 nm NIR light was irradiated onto the left (p-Ap/epoxy) or right (MWCNT/epoxy) parts of the multicomposite individually, four different temporary shapes were obtained.

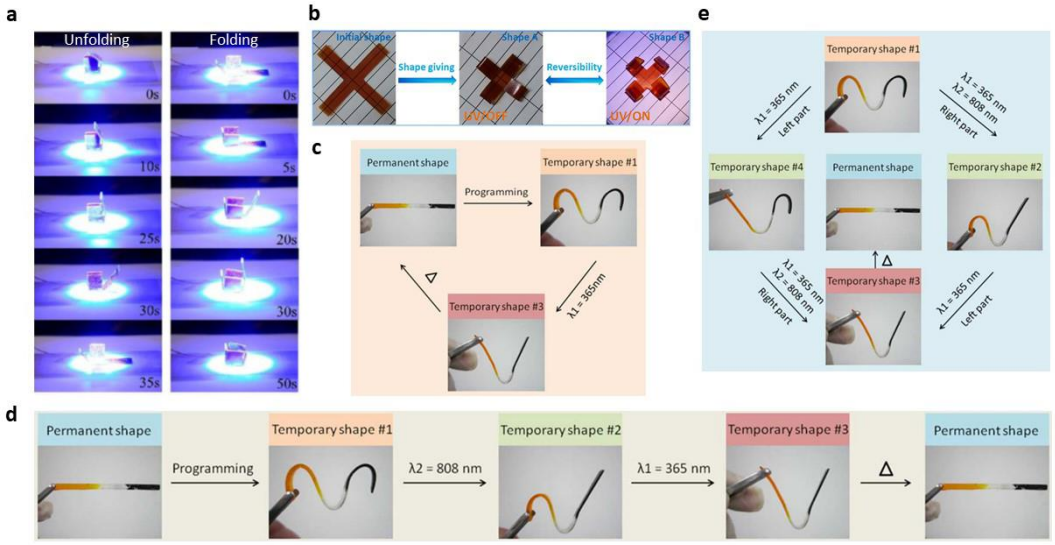

Figure 2.21: Light activated reversible and multi shape memory effect (a) Unfolding and folding shape memory behaviour of a box due to UV light [29] (b) UV light induced two-way shape memory behaviour of a gripper [54] (c) Triple shape memory effect of a wavelength selective multicomposite [53] (d) Multi shape memory effect of a wavelength selective multicomposite [53] (e) Photo manipulating shape recovery processes of wavelength selective multicomposite attributed to micro localized shape memory effect [53].

Chen et al. produced ionomers cross-linked by Cu^{2+}, Fe^{3+} and Co^{2+} to demonstrate the light induced multi shape memory effect due their large gap in photothermal conversion efficiency [119]. Fang et al. developed five photoresponsive polymers and assembled these in three manners to achieve complicated light induced shape deformation upon different light illumination sequences [160]. Assembly of the prepared five polymers in active/active, active/inert-active/inert, and active-active manners improved the spatiotemporal control over shape deformations via tuning the light irradiation sequences. Complex shapes of polymer specimens were obtained in an instantly, remotely and with no contact [160]. In future, LASMPCs with reversible and multi shape memory properties can be applicable for SMP applications such as dual acting actuators [179, 180], artificial muscles [181, 182] and morphing wings[183, 184].

2.9 Modeling of Light Activated Shape Memory Effect

The modeling of light activated shape memory mechanisms enhances knowledge and understanding of LASMPs and LASMPCs, so as to introduce novel polymer systems and to improve functionalities and develop innovative applications. Significantly, modeling techniques can be used for molecular design, shape memory programming and the prediction of shape recovery behaviour of LASMPs/LASMPCs, depending on the application of the materials. Moreover, the analyses improve the flexibility of using LASMPs/LASMPCs for real life engineering devices. Although the shape memory process of LASMPs is similar to that of thermal responsive SMPs, the external stimulus is different. Therefore, most of the models developed for thermally induced SMPs are not appropriate for describing light activated SMEs. Accordingly, various modeling approaches, i.e., multiple natural configurations modeling [57, 185, 186], multiscale modeling [58, 187] and three-dimensional finite deformation modeling [59], have been used to model light activated SMEs.

2.9.1 Multiple Natural Configurations Modeling

LASMPs are synthesized with photosensitive functional groups attached to the main polymer chain, where these photosensitive functional groups act as molecular switches [28]. As described by Sodhi and Rao [57], during the undeformed initial state, the LASMP is in a single stress-free configuration and its elastic behaviour is driven by changes in

entropy. On deformation, the coiled polymer molecules stretch. Once the LASMP is exposed to light at a specific frequency, the photoreactive molecules present in the polymer form covalent bonds with each other. These bonds form new cross-links that are formed in the deformed state. While these new cross-links are formed, the old cross-links are still active and no change in stress can be observed.

After unloading, the polymer tends to return to its original shape, which is resisted by the new photo induced cross-links. As a result, a temporary configuration in between the original and the deformed shape is obtained due to the presence of two sets of cross-links, each formed in different stress-free states. The original cross-links tend to retract to their original configuration while the photo induced cross-links prefer the deformed configuration.

The second set of cross-links is formed while the material deforms, and hence can result in anisotropic mechanical behaviour. Exposing the programmed LASMP to light will cleave its covalent bonds. As more and more of these covalent bonds break, the LASMP returns to its original shape. Accordingly, light activated SMEs are considered to be a combination of two or more networks.

Therefore, the traditional theories based on a single natural configuration (usually taken to be a stress-free state) would not be able to describe light activated SMEs. For this reason, the theory of multiple natural configurations has been used to model light activated SMEs [57, 185, 186]. This theory was introduced specifically for the materials that respond due to their multiple configurations and is closely tied to the behaviour of dissipative materials [188].

In order to model the mechanics of LASMPs, an original virgin network with a single stress-free state and two competing networks with their own stress-free states have been occupied [57]. In addition, the initiation and formation of light activated networks and the reverse transition that caused the dissolution of these networks were modeled [57]. The model was applicable for multiple networks formed by sequential deformation and exposure to UV light [57, 189]. Anisotropy in the mechanical response was also incorporated into the model and this model was used to simulate the results for specific boundary value problems, i.e., uniaxial extension and inflation of a cylinder [57].

Moreover the proposed modeling technique has been extended to study the inhomogeneous deformations of LASMPs [186]. Based on a similar framework of

multiple natural configurations, Yuan has developed a multinetwork model, wherein a new network is formed by virtue of light irradiation, which could be isotropic or anisotropic, to capture the mechanical behaviour of LASMPs [185]. Several classical boundary value problems have been studied with a view towards understanding the predictions of the models [185].

2.9.2 Multiscale Modeling

Beblo and Weiland have developed a modular, multiscale model to predict the stress strain response of LASMPs [58, 187]. The multiscale modeling approach is employed to anticipate the soft and hard state moduli, solely on the basis of a proposed molecular formulation. The approach begins with predicting polymer chain conformation using a computational approach to rotational isomeric state theory. It is considered that the backbone of the polymer comprises three groups of molecules, where only one group of molecules is responsible for photo-cross-linking.

As the molecular formula is known, the in-plane bond angles and bond lengths between each molecule have been calculated using traditional chemistry techniques. The rotational isomeric state theory builds a molecular scale model of the polymer chain, yielding a list of distances between the predicted cross-link locations, or r-values. These r-values are then fitted with Johnson probability density functions and used with Boltzmann statistical mechanics to predict stress as a function of the strain of the phantom polymer network.

Empirical adaptation for the design adds junction constraint theory to the modeling process. Junction constraint theory includes the effects of neighbouring chain interactions. Empirical fitting results in numerically accurate Young's modulus predictions. The system is modular in nature and thus lends itself well to being adapted to other polymer systems and development applications [58].

2.9.3 Three-Dimensional Finite Deformation Modeling

Once the LASMPs are exposed to light, the photochemical reactions alter the structure of the cross-linked polymer network, which result in an evolution of the polymer network and subsequent macroscopic deformation. Appropriate execution of this process enables the photomechanical shape memory effect. Based on these phenomena, Long et al. have

developed a three-dimensional finite deformation modeling framework to describe the photomechanical response of LASMP systems [59].

The proposed framework integrates four coupled phenomena that contribute to macroscopic photomechanical behaviour: photophysics, photochemistry, chemomechanical coupling, and mechanical deformation. The chemomechanical coupling consists of chemically induced structural alterations of the cross-linked network that result in subsequent deformation. Respective behaviour is described by considering a decomposition of the cross-linked network into two components consisting of an original network and a photochemically altered network, where both networks evolve during the photomechanical deformation.

Interestingly, the modeling framework has been applied to LASMP systems that are operated under various mechanisms in each of the four areas. The modeling approach has been utilized to develop constitutive models for two LASMP systems presented in the past [28, 190]. Moreover, the model was validated with experimental results of photo induced stress relaxation and bending deformation [190]. This model was also capable of predicting the effects of photomechanical parameters (applied strain magnitude, irradiation time and intensity, and photoabsorber concentration) and the behaviour of the network evolution rule on the material's response [59].

2.10 Applications

2.10.1 Structural Engineering Applications of General SMPCs

Smart materials, SMPs and SMPCs facilitate numerous applications ranging from the microscale to the large scale [2]. They show potential in the areas of the biomedical industry [20, 21], smart textiles [22, 23] and self healing [24, 25]. Interestingly, SMPCs are being developed and qualified especially for deployable components and structures for the aerospace and space engineering sector. These applications include hinges, trusses, booms, antennas, optical reflectors and morphing skins [26, 27].

Figure 2.22 (a) shows a space habitat developed by ILC Dover and Folded Structures Company, under a NASA contract [191]. Advantageously, such a deployable habitat system can minimize launch costs and maximize operational volumes. This change in volume must be fully realized for the expandable system to be worth the complexity

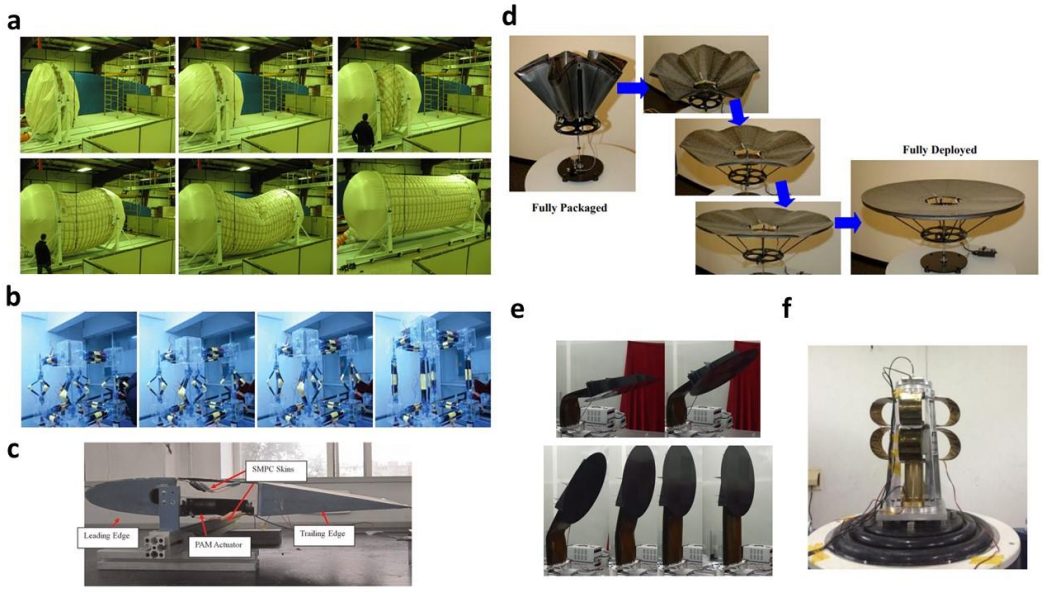

Figure 2.22: Structural applications of SMPCs (a) A space habitat developed by ILC Dover and Folded Structures Company [191] (b) A cubic deployable support structure [192] (c) A variable stiffness morphing skin for variable camber wings [193] (d) A flexible precision reflector [194] (e) An antenna reflector [195] (f) A tip-loaded deployable truss [72].

involved. A hybrid inflatable and composite floor system has been designed to demonstrate the new packing and deployment approach [191].

Li et al. have developed a cubic deployable support structure which has unique properties, such as high reliability, low cost, lightness in weight, and self-deployment without complex mechanical devices, compared with traditional deployable structures [192]. As presented in Figure 2.22 (b), this cubic deployable support structure consists of four dependent spatial cages, each cage composed of 12 three-longeron SMPC truss booms and end connections. The structure has successfully self-deployed and the average deployment time at trial was 465 seconds [192].

Figure 2.22 (c) illustrates a morphing skin for variable camber wings developed by Sun et al., by using elastic fibre reinforced SMPCs [193]. The designed structure consists of a fixed leading edge, trailing edge, a metal sheet, pneumatic artificial muscle (PAM) actuator and SMPC skins. Due to air pressure, the pneumatic actuator can be shortened, resulting in a change in the wing's camber. 2 mm thick SMPCs with 20 vol% fibres were used in the upper and lower surfaces in order to keep the surface smooth. The skins can withstand

an aerodynamic loading in a glassy state and change the shape of the wing in rubbery state. When the trailing edge flaps down, there will be a tensile strain on the upper surface and compressive strain on the bottom. The lower skin should be pre-stretched before installing it, and accordingly, it can shrink itself due to the shape memory effect [193].

Antennas are used to communicate between earth and space. The reflector aperture and precision are the two main parameters measuring the working properties of deployable antennas. Therefore, a precise recovery into the designed shape is crucial for such applications.

Figure 2.22(d) shows the deployment steps of an SMPC based solid surface radio frequency reflector, called the flexible precision reflector and developed by Harris Corporation [194]. Photogrammetry techniques were used to measure the surface shapes before packaging, after packaging and after deployment. During the test, the antenna was packaged and stored for 100 hours. The shapes of the reflector surface, before and after storage were compared, which showed satisfactory functionality [194]. Figure 2.22 (e) presents the deployment of an antenna made of SMCPs and composite spring tapes [195]. Bending and torsional stiffness tests were conducted, and structural rigidity was verified by using numerical analysis. Also, the SMPC functioned as a damper to prevent strong impact or overshooting damage of the reflector during the deployment [195].

Li et al. have developed a tip-loaded deployable truss with gusseted base and auxiliary support frame to operate under heavy tip loads. This is shown in Figure 2.22 (f) [72]. The truss was made of carbon fabric reinforced cyanate-based SMPC laminates. Swept sine vibration simulation showed that a 1.3 kg tip-loaded truss has the highest structural performance. Thus, it was manufactured to carry out a series of experiments, including swept sine vibration, acceleration and shock testing of the packaged truss, and modal testing of the deployed truss. No damage was observed, indicating the tip-loaded deployable truss has a relatively high stiffness that could withstand the predicted mechanical environment [72].

2.10.2 Applications of LASMP and LASMPCs

LASMPs and LASMPCs have unique characteristics that make the material a suitable candidate for a wider range of applications. Basically, these LASMP and LASMPC applications can be classified into three categories: biomedical applications [32-35], micro

and small scale applications [30, 36], and space and large scale engineering applications [37]. The capability of light to act as an excitation energy source and a control signal carrier is advantageous for various actuators that need a controlled SME. Furthermore, as light is fast, shape changes can be performed instantaneously and on demand [88, 118, 163]. The changes to light wavelength and polarization enable selective and directional SME, respectively [29, 42]. Optical fibre coupled LASMPs have been widely used in biomedical applications as the actuators at difficult to reach positions such as the inner human body. These can be controlled in a safer manner with light energy [32, 34, 165]. Moreover, light can travel a long distance without a medium and it can be focused onto a particular area of the device. Because of this, reinforced LASMPCs have the ability to be used for aerospace and space engineering applications [196]. Table 2.3 describes various LASMP and LASMPC applications in detail.

Table 2.3: Applications of LASMPs and LASMPCs.

Application and reference	**Materials**	**Activation method, wavelength and intensity**	**Remarks**
Biomedical			
Self-tightening knot [96]	Poly(ε-caprolactone) (PCL)* Silver nanoparticles**	Photothermal actuation due to IR light in 780 nm to 1400 nm range. Maximum power 7 W.	A rectangle cross sectioned strip has been stretched and fixed into a knot like shape. Both extremities were immobilized, and IR illumination was applied. The knot was tightened in 30 seconds and the temperature was increased from 21 ºC to 37 ºC. Possible use of the LASMPC as a biomaterial with antibacterial

			properties was investigated.
Macrophage phagocytosis [197]	Thermoplastic poly(D,L-lactic acid) (PDLLA)* Gold nanoparticles**	Photothermal actuation due to 532 nm viable light. Maximum power 2 W.	LASMPC demonstrates the capability of maintaining an anisotropic shape at body temperature and recovering to a spherical shape at a narrow temperature range above body temperature (37 to 45 °C). Entanglement based shape memory response has been achieved. LASMPC was composed of biocompatible components that could exhibit spatiotemporal controllability of its properties.
Vascular stent [165]	Thermoplastic polyurethane (MM5520)*	Photothermal actuation due to 810 nm NIR light. Maximum power 8.6 W. Light diffused through a fibre optic cylindrical light diffuser.	Tg = 55 ºC. Photothermal actuation of the stent was performed in a water-filled mock artery. At a physiological flow rate, the stent did not fully expand at the maximum laser power (8.6 W) due to convective cooling. Further studies

			are required to optimize the device and assess potential thermal tissue damage.
Intravascular thrombectomy [32]	Thermoplastic SMP (MM6520 and MM5520)* Platinum dye (Epolight™ 4121)**	Photothermal actuation due to 810 nm NIR light. Maximum power 4.5 W. Light diffused through a coupled optical fibre.	Tg of MM6520 = 65 °C, Tg of MM5520 = 55 °C. Tested in 37 °C water, similar to human body temperature. Due to cooling in water, higher laser power was required than in air. Actuation was complete within 3 seconds. Temperature rise of the blood near the device is approximately 12 °C. Tissue damage is possible with long use.
Stroke treating micro actuators (interventional ischemic stroke device and release device for embolic coil) [33]	Thermoset polyurethane (MP 5510)* Green dye (Ryvec-518)**	Photothermal actuation due to 810 nm NIR light. Power 0.1 W to 1.5 W. Light diffused through a coupled optical fibre.	Tg = 55 °C. Device actuation temperatures in the range of 65 to 85 °C. Impacts of operating the thermally activated material in a blood vessel (with and without flow) are presented.
Embolic treatment device for aneurysms [34]	LLNL SMP foam comprised of hexamethylene diisocyanate (HDI, N , N , N' , N ' - tetrakis (2-	Photothermal actuation due to 810 nm NIR light. Maximum power 8.6 W.	Tg = 45 °C. Demonstrated that SMP foams can be laser deployed in an in vitro aneurysm model. Deployment time of 60 s.

(Similar device is presented by Small et al., [35])	hydroxypropyl) ethylenediamine (HPED), and triethanolamine (TEA)* Dye (Epolight™ 4121)**	Light diffused through a cylindrical diffusing fibre.	A single device can treat a 10 mm aneurysm. Higher Tg form is required to prevent spontaneous expansion due to body temperature. Tissue damage is possible. Lower density foams with greater volume expansion are required.
Micro and small scale engineering			
Micro patterned surfaces (moveable prints) [30]	Poly[ethylene-ran-(vinyl acetate)] (EVA)* $Yb(TTA)_3Phen$** $Nd(TTA)_3Phen$**	Photothermal actuation due to 980 nm ($Yb(TTA)_3Phen$) and 808 nm ($Nd(TTA)_3Phen$) NIR light. Power density 0.1 to ~3.25 W/cm^2.	EVA/$Yb(TTA)_3Phen$ and EVA/$Nd(TTA)_3Phen$ spherical micro particles were attached onto a cured pure EVA film, forming the patterns of the letters "N" and "J" respectively. The micro particles were programmed by compressing downwards, which increased their diameters from 300 to 400 μm. Recovered by selective wavelength triggering.
Soft actuators for aqueous media (a releasing device and a gripper) [36]	Poly[ethylene- ran -(vinyl acetate)] (EVA)* Aniline black (AB)**	Photothermal actuation due to 808 nm NIR light.	Increasing AB content from 0.5 to 2 phr reduced the recovery temperature from 85 to 74 °C. Shape recovery ratio > 98%. Power density (PD) 12-16

		Power density 0.09 to ~3 W/cm^2.	times higher in water than air. Recovery time 3 min. By changing the temperature via periodically turning on and off the irradiation, a reversible deformation of 10° was observed.
Aerospace, space and large scale engineering			
Spatial four arm gripper [37]	Thermoset hydro-epoxy resin (HEP)* Carbon black**	Photothermal actuation due to 10.64 μm mid infrared light. Power density 1 W/cm^2	Tg = 60 °C. A laser can be used as an external and remote stimulus to trigger a spatially selective shape recovery process and obtain multiple intermediate shapes. Various mechanical motions can also be achieved by predetermined SMPs shape patterns and by modulating laser irradiating position, time and movement.

** Shape Memory Polymer / Matrix*

***Photothermal Filler*

††Reinforcement and Photothermal Filler

2.11 Summary

SMPs and their composites are expected to take one of the leading roles in the field of smart materials because of their inimitable characteristics: manufacturability, large recoverable strains, biodegradability, biocompatibility, tailorable glass transition

temperature, wide range of stimuli, low density, relatively low cost, recyclability and multifunctional nature. However, the major drawbacks of SMPs are their inherent low modulus, low recovery stress/forces, low cycle life and weak material stability. Reinforcement improves the applicability of SMPCs into a wider range of engineering applications.

The unique characteristics of light (acting as a source of energy, being a control signal carrier, travelling long distances in a vacuum, safety for human tissues, ability to be focused onto a certain area and ability to be dispersed through optical fibres) permit LASMPs and LASMPCs to provide long awaited smart materials and technologies for the materials engineering field. To date, two mechanisms, i.e., photo responsive LASMPs and photothermal LASMPCs, are being researched by means of experiments and numerical models. Photo responsive LASMPs have shown the ability to undergo shape recovery at ambient temperatures while photothermal LASMPCs required heat energy to recover their original shapes.

Most of the LASMP and LASMPC systems were developed for biomedical and non-structural small scale applications. It is recognized that the structural performance of the photo responsive LASMPs and photothermal LASMPCs have not been sufficiently investigated to date. Because of this, there is a large gap in the LASMP and LASMPC knowledge base. Several nanoparticles and dye based photothermally activated LASMPCs have been introduced up to now. However, most of the existing photothermal fillers would be expensive for mass production of large scale structural applications. Other potential photothermal fillers, currently used for photothermal therapies and solar thermal systems, could be adapted for future LASMPC developments.

It has been shown that varying the light wavelength, intensity, position and polarization permits advanced forms of light activated SMEs such as selective wavelength SMEs, reversible SMEs, and multi SMEs. To date, supportive optical technologies, such as light polarization, diffusing, wavelength filtering and sending light through fibre optics, are being used in order to advance the activation methods of the LASMPs and LASMPCs.

However, the existing light activation methods are limited to miniature and small scale applications and are not appropriate for the activation of large scale LASMP and LASMPC components. Moreover, the modeling of light activated shape memory mechanisms enhances current knowledge and understanding of LASMPs and LASMPCs.

Even though the shape memory process of LASMPs is similar to that of general SMPs, the external stimulus required is different.

Though precise models were developed to describe light activated SMEs, specific modeling approaches are still required to fully understand the behaviour of photothermally activated LASMPCs. This missing knowledge will be the foundation for the development of next generation of novel LASMP/LASMPC systems with improved functionalities, which is essential to develop innovative applications. To date, general SMP composites are being developed and demonstrated for structural engineering applications in the aerospace and space engineering sector. Even though the stimulus of light has advanced capabilities, LASMPCs are not widely researched at present for structural applications.

Comparable research gaps have been identified by the SMP and SMPC research community around the globe. Parallel studies showed the significance of fulfilling the corresponding research gaps i.e. structural property enhancements [75, 161], commercially viable photothermal materials [30, 160], selective light wavelength activation [52, 168], modeling and simulation [185, 198], improvements on long term behavior [17, 19] and remote actuation [119, 166]. Continued research on reinforced LASMPCs is essential to cater for future material demands aimed at sophisticated structural engineering applications.

Chapter 3

Materials Preparation and Characterization

3.1 Introduction

To date most of the LASMPCs have been developed for small scale and biomedical applications. State of the art LASMPCs for structural and large scale engineering applications were barely studied. Herein four different types of LASMPC materials and three different types of manufacturing methods for LASMPC preparation are presented. This chapter deliberates on the morphology, structural performance and thermomechanical characteristics of the LASMPC material systems. The inclusion of some reinforcements can destroy or impede the LASMPCs' thermomechanical and light absorbance properties. In contrast, photothermal fillers can weaken LASMPCs' structural and thermomechanical properties. The effects of these fibre reinforcements and photothermal fillers on numerous test parameters have been systemically studied and explicated.

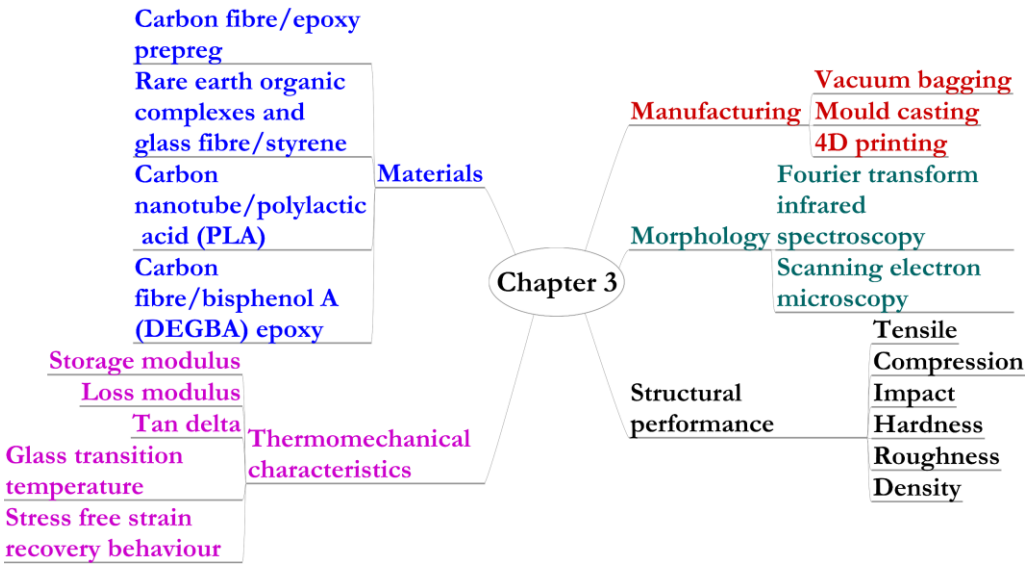

Figure 3.1: Overview of the technical contents of Chapter 3.

An overview of the technical contents of Chapter 3 is illustrated in Figure 3.1. The primary focus of this chapter is to identify the suitability of the four type of proposed LASMPC materials for non-structural, semi structural and structural applications and then filter the structural LASMPCs for further research.

The new knowledge presented in this chapter significantly contributes towards the development of LASMPC materials for structural components and large scale engineering applications. The material design, manufacturing and characterization techniques elaborated herein can be extended to develop numerous novel LASMPCs. Consequently, this chapter helps to create a materials framework for future LASMPC developments. The content of this chapter is presented in the publications J3, J4, J5, C1, C2 and C4 as detailed in the appendix A of this thesis.

3.2 Materials Preparation

In this chapter, four type of SMP/LASMPC materials are presented: i) carbon fibre/epoxy prepreg-based LASMPC, ii) rare earth organic complexes-based filler particles and glass fibre/styrene-based LASMPC, iii) carbon nanotube/polylactic acid (PLA)-based LASMPC and iv) carbon fibre/bisphenol A (DEGBA) epoxy-based LASMPC.

The first type of material, carbon fibre prepreg is a widely used material for large-scale engineering applications, because of its advantages such as provision of set weight characteristics and improvement of the work procedure during moulding of items. The second type of material included rare earth organic complexes-based photothermal fillers to stimulate the LASMPC by selective wavelength light. Also, such fillers are commercially viable and safe to use in LASMPCs, which may reach temperatures up to 270 °C during its curing or operative stages. Glass fibre reinforcements were selected to preserve the selectively triggering capability while improving the structural properties. The third type of PLA SMP material was intended for 3D printing, which is an evolving manufacturing method in the aerospace industry. It enables small quantities of customized space structures to be produced at a relatively low cost and less lead-time. The fourth material, bisphenol A based SMP is a commercially available two-part polymer which demonstrates relatively high mechanical properties. In addition, incorporation of Jeffamine can alter the Tg of the DEGBA SMP.

Table 3.1: Composition of the test samples.

LASMPC Type	Sample ID	Composition
Carbon fibre/epoxy prepreg	CFR Prepreg	4 layers of carbon fibres (~30 %) and SMP
Rare earth organic complexes-based filler particles and glass fibre/styrene	Neat Styrene	Neat SMP
	GFR Styrene	4 layers of glass fibres and SMP
	0.5Nd Styrene	0.5 % $Nd(TTA)_3Phen$ and SMP
	1.0Nd Styrene	1.0 % $Nd(TTA)_3Phen$ and SMP
	1.0Nd GFR Styrene	1.0 % $Nd(TTA)_3Phen$, 04 layers of glass fibres and SMP
	0.5Yb Styrene	0.5 % $Yb(TTA)_3Phen$ and SMP
	1.0Yb Styrene	1.0 % $Yb(TTA)_3Phen$ and SMP
	1.0Yb GFR Styrene	1.0 % $Yb(TTA)_3Phen$, 04 layers of glass fibres and SMP
Carbon nanotube/polylactic acid	Neat PLA	Neat SMP
	MWCNT PLA	7% MWCNT and SMP
Carbon fibre/bisphenol A epoxy	Neat DGEBA	Neat SMP
	CFR DEGBA	4 layers of carbon fibres and SMP

Different material preparation processes were followed for the four LASMPC materials. The sample preparation methods are described in Sections 3.2.1 to 3.2.4. Thirteen different test samples were prepared, as shown in Table 3.1. Each sample was given a sample ID according to its composition. The prepared samples were cut into standard sizes of test specimens, as shown in Table 3.1.

3.2.1 Carbon Fibre/Epoxy Prepreg-Based LASMPC

The carbon fibre reinforced shape memory epoxy prepreg used for this research was supplied by the Harbin Institute of Technology (HIT), China. The detailed chemical composition of the SMP matrix is proprietary to the Centre for Composite Materials and Structures of HIT and no chemical composition is available for disclosure. Four

Table 3.2: Specification of the test specimens.

Experiment	Dimension (mm)	
	Length	Width
DMA test	60	8
Tensile test	250	15
Compression test	140	12.8
Impact test	100	12

laminations of prepreg sheets containing 0/90 woven plain fibre mesh were cured with vacuum bagging under 70 bar for 9 hours at 80 °C, 100 °C and 150 °C respectively, with equal time spacing. The thickness of the formed sheets was 1.2 mm and the sheets were cut into standard test specimens shown in Table 3.2 by using a diamond saw cutter.

3.2.2 Rare Earth Organic Complexes and Glass Fibre/Styrene-Based LASMPC

The styrene-based shape memory resin was supplied by the Harbin Institute of Technology (HIT), China. As with the material from this manufacturer, the detailed chemical composition of the SMP matrix is proprietary to the Centre for Composite Materials and Structures of HIT. The roving plain (400 g/m^2) glass fibre was supplied by Changzhou Jlon Composite Co., Ltd., China. Sigma Aldrich, Australia supplied $NdCl_36H_2O$, $YbCl_36H_2O$, TTA and Phen.

The rare earth organic complexes of $Nd(TTA)_3Phen$ and $Yb(TTA)_3Phen$ were prepared by using a co-precipitation method. First, 1 mmol of $NdCl_3.6H_2O$ or $YbCl_3.6H_2O$, 3 mmol TTA and 1 mmol Phen were dissolved in ethanol, respectively. After that the ethanol solution of TTA was poured into a beaker and stirred at 60 °C. Successively, the ethanol solutions of $NdCl_3.6H_2O$ or $YbCl_3.6H_2O$ and the ethanol solution of Phen were added into the ethanol solution of TTA. The mixture was stirred for 15 minutes at 60 °C. Subsequently, drops of 1 mol/L sodium hydroxide ethanol solution were added into the mixture until the pH value reached 6-7. Afterwards, the mixture was left to react in a 60 °C water bath for 6 hours. Once the reaction was finished, the mixture was centrifuged at a speed of 3000 rpm for 3 hours to obtain the precipitation. Then the precipitation was dried in a vacuum oven at 50 °C for 12 hours. Finally, the complexes were powdered by using a ball mill.

After adding the photothermal fillers into the SMP resin, the solution was stirred for 15 minutes at 30 °C followed by ultrasound sonication for 10 minutes at 30 °C under 80 W ultrasound power. The neat SMP epoxy or the SMP epoxy mixed with photothermal fillers were poured into a mould, which was prepared using two glass sheets. The inside surface of the glass sheets was covered with a peel fly for easy removal of the samples. In addition, four layers of glass fibres were inserted, only for the samples with reinforcement. Subsequently, those moulds were kept in an oven for 9 hours at 80 °C, 100 °C and 150 °C, respectively, with equal time spacing, where the curing took place. Successively, eight different sheets of 300 x 300 x 2.5 mm^3 were prepared. The formed sheets were cut into standard test specimens shown in Table 3.2 by using a diamond saw cutter.

3.2.3 Carbon Nanotube/ PLA-Based LASMPC

The thermoplastic polylactic acid (PLA) SMP used in this work was supplied by the Harbin Institute of Technology (HIT), China with the detailed chemical composition of the SMP matrix being proprietary to the Centre for Composite Materials and Structures of HIT. The samples were prepared by using a 3D printing additive manufacturing technique. Two types of filaments, pristine PLA SMP and MWCNT reinforced PLA SMPC, were used for the 3D printing process. An Anycubic I3 Mega 3D printer was used to fabricate the test specimens by a fused deposition modeling (FDM) process. 3D CAD models (STL files) were developed by using Creo Parametric 4.0 software package. Ultimaker Cura 3.6.0 package was used as the slicing software. All samples were made with 100% infill density where the infill pattern was a line type. The nozzle diameter was 0.4 mm. Layer height, nozzle temperature, build plate temperature and print speed were set to 0.2 mm, 200 °C, 70 °C and 40 mms^{-1}, respectively.

3.2.4 Carbon Fibre/Bisphenol A Epoxy-Based LASMPC

Bisphenol A diglycidyl ether (DGEBA) and m-Xylylenediamine (MXDA) were supplied by Sigma Aldrich, Australia. The chemical formulas of the DGEBA resin and MXDA hardener are shown in Figure 3.2 (a) and (b) respectively. The two parts of the matrix were degassed separately before mixing and the mixing ratio of the resin to hardener was 1 to 0.5 mole (DGEBA:MXDA = 1:0.5 mol/mol). The mixed epoxy was poured into a mould prepared with two glass sheets. To easily remove the samples, the inside surface

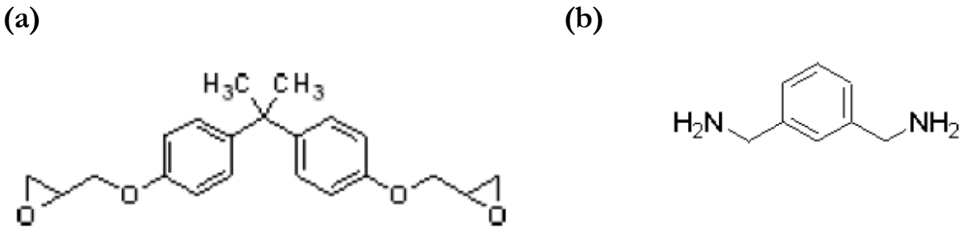

Figure 3.2: Chemical formula (a) DGEBA resin (b) MXDA hardener.

of the glass sheets were covered with a peel fly. In addition, four layers of carbon fibre fabric were inserted for the samples with reinforcement. Subsequently, those moulds were kept in the oven for 2 hours at 60 ºC, 3 hours at 100 ºC and 1 hour at 140 ºC, where the curing took place. Successively, the sheets of 300 x 300 x 2 mm^3 were prepared. The formed sheets were cut into standard test specimens as shown in Table 3.2 using a water jet cutter.

3.3 Experimental Methods

The morphology, mechanical properties, physical properties and thermomechanical characteristics of the LASMPCs were experimentally investigated. The morphology, layer formation and surface quality of the samples were observed by using a Jeol benchtop scanning electron microscope (JCM-6000 SEM). A Shimadzu Fourier transform infrared spectrometer (IRAffinity-1S FTIR) was used to obtain the infrared spectrum of transmittance of the prepared samples.

MTS 100 kN, Insight electromechanical testing system was used for the tensile testing under ISO 527-5:2009 test standard [199]. Furthermore, ASTM D6641 test standard [200] was followed to carry out the compression tests on the same MTS testing machine. The impact testing was performed by using the Instron Dynatup drop weight impact testing instrument (8200). A Barcol Impressor hand-held portable hardness tester (GYZJ-934-1) and SCHMIDT Shore Durometer HPSC equipment were used to determine the hardness of the composite materials. The Barcol hardness test procedure is described in ASTM D2583 [201] and the shore hardness test procedure is described in ASTM D2240 [202]. The surface roughness of the test samples was investigated using the MarSurf M 400 surface measuring instrument. All the experiments were conducted at the room conditions.

A TA Instruments dynamic mechanical analyzer (DMA Q800) with a double cantilever clamp was used to investigate the thermomechanical behaviour of the SMPC. The multi-frequency strain mode was used to determine the glass transitions temperature (Tg) and to characterize the storage modulus, by using a frequency of 1 Hz and a temperature ramp of 5 °C/min. In addition, the stress-free strain recovery and constrained strain stress recovery characteristics of the materials were investigated. The shape programming was performed under DMA strain rate mode as was also the stress-free strain recovery. Only for the carbon nanotube/polylactic acid SMP, a DSC experiment was conducted to identify the crystallization temperature (Tc) and melting point (Tm) by using a TA Instruments differential scanning calorimetry (DSC 25).

3.4 Morphology

3.4.1 Fourier Transform Infrared Spectra

Infrared (IR) spectroscopy plays a significant role in the physical characterization of polymers and composites. IR absorption bands are well known for their marked specificity to individual chemical functionalities. Furthermore, the unique sensitivity toward the configuration, conformation, and other local submolecular and supramolecular environments makes IR spectroscopy a very powerful probing tool for numerous scientific investigations in polymer physics.

Moreover, the interpretation of the IR spectra and the assignment of the FTIR bands are significant in monitoring the curing process, phase separation and ageing. Beyond the general use of FTIR, the spectrum of IR absorption (invert of transmittance spectrum) gives indications about energizing the material by IR rays. Figure 3.3 illustrates the FTIR spectra of SMPs/SMPCs and filler martials. Characteristic bands and the relevant assignments are shown in Table 3.3. Figure 3.3 (e) shows the FTIR spectra of the rare earth organic complexes-based photothermal fillers which were compared with the similar spectra published by Fang et al. [30]. Accordingly, the chemical structures of the Nd(TTA)3Phen and Yb(TTA)3Phen used in this research are very similar to the photothermal fillers introduced by Fang et al. [30].

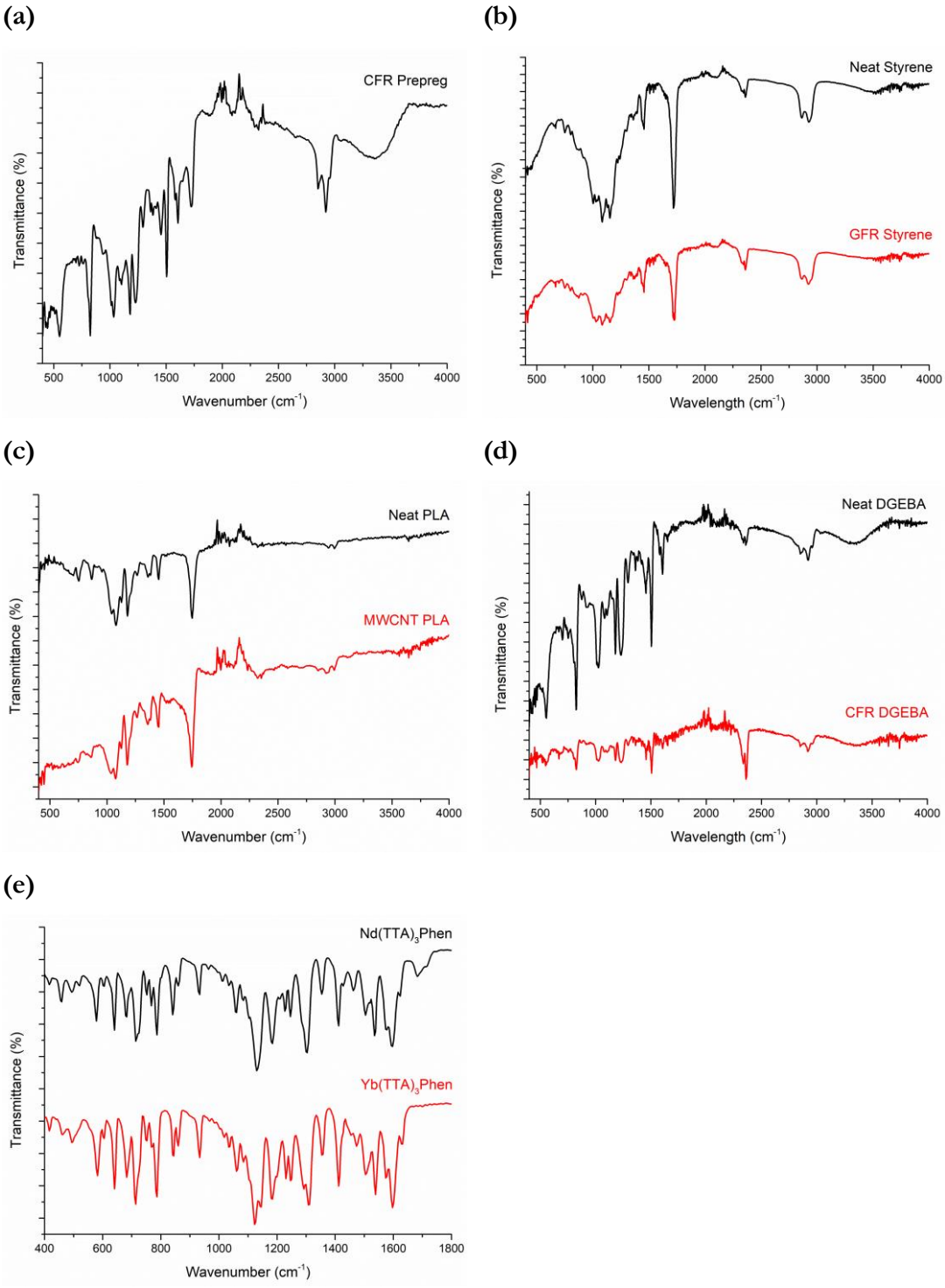

Figure 3.3: FTIR spectra of the materials (a) Carbon fibre/epoxy prepreg SMP (b) Glass fibre/styrene SMP (c Carbon nanotube/polylactic acid SMP) (d) Carbon fibre/bisphenol A SMP (e) Rare earth organic complexes-based photothermal powders.

Table 3.3: Characteristic FTIR bands of the materials

Material	Band (cm^{-1})	Assignment	Reference
Carbon fibre prepreg SMPC	823	Stretching C-O-C of oxirane group	[203]
	1036	Stretching C-O-C of ethers	
	1506	Stretching C-C of aromatic	
	1604	Stretching C=C of aromatic rings	
	1723	Stretching free C=O amide I	[204]
	2700-3000	Stretching C-H of CH and CH aromatic and aliphatic	[203]
Neat styrene SMP	1453	Ring semicircle stretch + CH_2 symmetric (scissors) deformation	[205]
	2862	C-H stretch	[206]
	2928	CH_2 asymmetric stretch	[205]
GFR styrene SMPC	1453	Ring semicircle stretch + CH_2 symmetric (scissors) deformation	[205]
	2862	C-H stretch	[206]
	2924	CH_2 asymmetric stretch	[205]
Nd(TTA)3Phen powder	1597	Due to the νc=o stretching (1642 and 1661 cm-1) of TTA	[30, 207]
	1625		
	1537	Due to the characteristic ring stretching vibration bands (1563, 851 and 736 cm-1) of Phen	
	840		
	713		
Yb(TTA)3Phen powder	1597	Due to the νc=o stretching (1642 and 1661 cm-1) of TTA	[30, 207]
	1631		
	1541	Due to the characteristic ring stretching vibration bands (1563, 851 and 736 cm-1) of Phen	
	844		
	713		
Neat PLA SMP	1077	C-O-C	[208]
	1182	Ras CH_3	
	1360	CH - CH_3	
	1451	CH_3	

	1750	Stretching C=O	
MWCNT PLA SMPC	1073	C-O-C	[208]
	1182	Ras CH_3	
	1356	CH - CH_3	
	1447	CH_3	
	1749	Stretching C=O	
Neat DEGBA SMP	821	γC-H of the 1-4 substituted benzene + $\gamma CH_{2\,r}$ of the epoxide group	[209]
	1028	δC-H of the 1-4 substituted benzene +ν_{sym}C-O-C in the case of an aromatic ether	[209]
	1180	δC-H benzenic	
	1453	δCH_2(scissoring) + $\delta_{asym}CH_3$ + νC=C of the 1-4 substituted benzene	
	1504	νC=C of the 1-4 substituted benzene	
	2926	νC-H aliphatic	
CFR DEGBA SMP	826	γC-H of the 1-4 substituted benzene + $\gamma CH_{2\,r}$ of the epoxide group	[209]
	1024	δC-H of the 1-4 substituted benzene +ν_{sym}C-O-C in the case of an aromatic ether	
	1180	δC-H benzenic	
	1457	δCH_2(scissoring) + δ_{asym}CH3 + νC=C of the 1-4 substituted benzene	
	1504	νC=C of the 1-4 substituted benzene	
	2922	νC-H aliphatic	

3.4.2 Scanning Electron Microscopy

SEM images of carbon fibre/epoxy prepreg SMP are shown in Figure 3.4. Scanning electron microscopy provided information about the surface features and delamination of the prepreg composite. Figure 3.4 (a) illustrates the top surface appearance. Accordingly, at a few locations of the top surface, voids appeared with lengths ranging up to 205 μm. Figure 3.4 (b) illustrates the cross-section. Accordingly, there were micro level gaps in between prepreg layers throughout the thickness. The maximum gap in between two prepreg layers was measured as 32.4 μm. Furthermore, the SEM image in Figure 3.4 (c) demonstrates the porous areas in the material. Figure 3.4 (d) illustrates the 0/90 woven fibre mesh and the diameters of the fibres. Accordingly, the average diameter of the carbon fibres used in this research was 14 μm.

Figure 3.5 (a) to (d) illustrate the SEM images of the cross-sections of neat styrene SMP, styrene-based SMP with rare earth organic photothermal fillers, GFR styrene and GFR

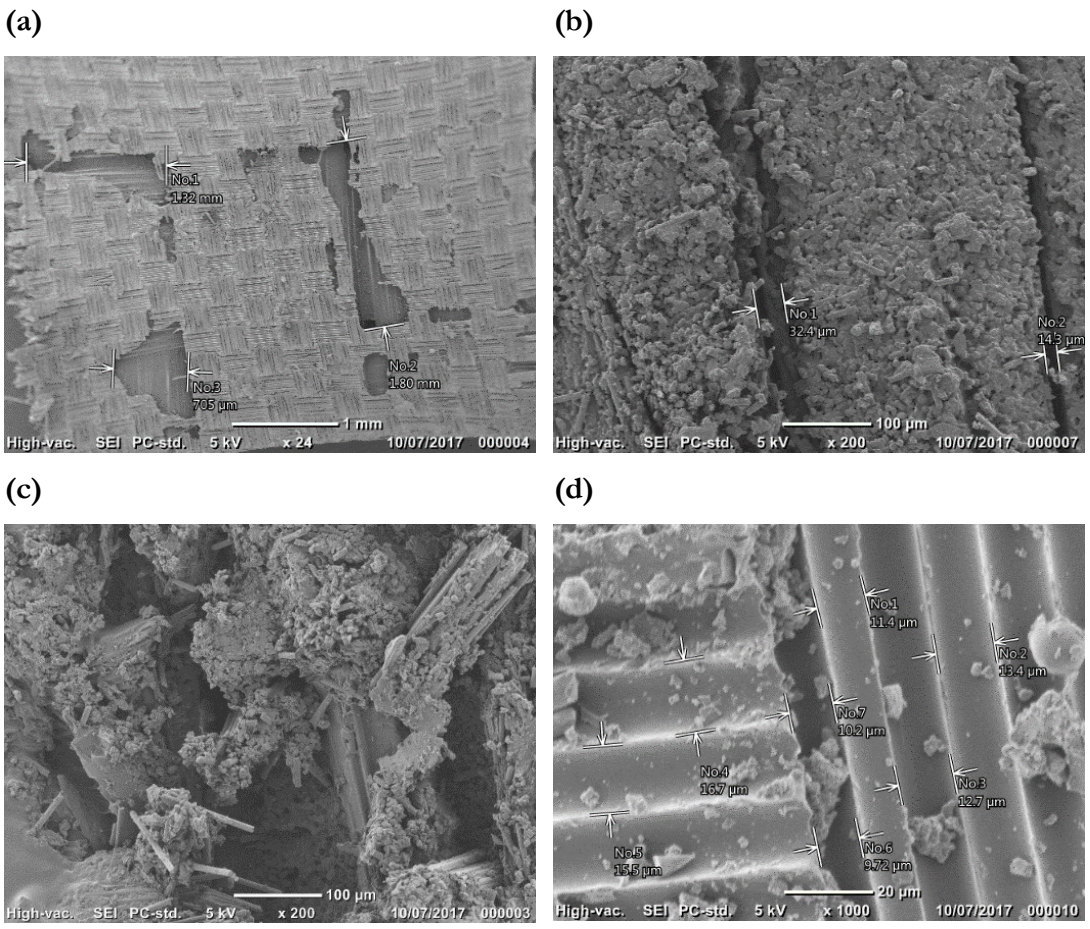

Figure 3.4: SEM images of carbon fibre/epoxy prepreg SMP (a) Voids on surface (b) Gaps between layers (c) Porous area on cross-section (d) 0/90 woven fibre mesh.

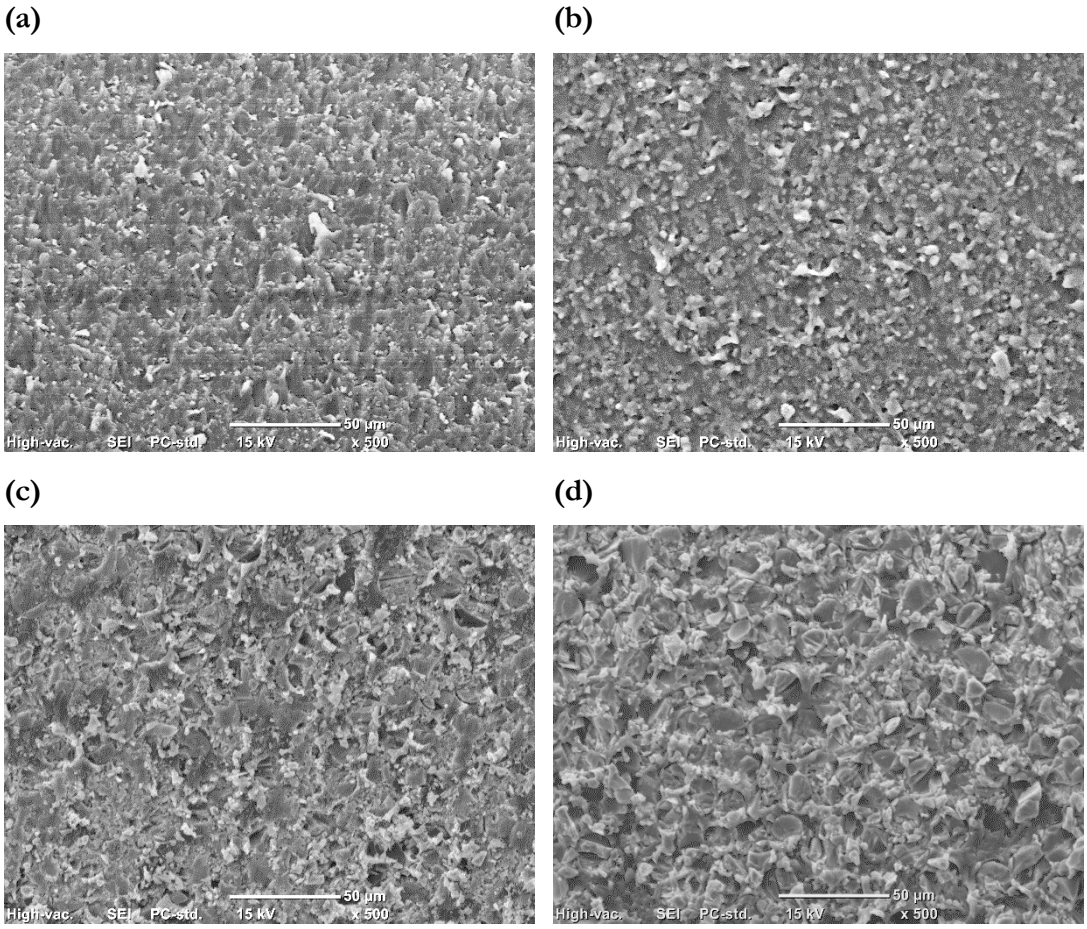

Figure 3.5: SEM images of the cross-sections of rare earth organic complexes and glass fibre/styrene-based SMP (a) neat SMP, (b) SMPC with photothermal fillers, (c) GFR SMPC and (d) GFR SMPC with photothermal fillers.

styrene with rare earth organic photothermal fillers, respectively. Accordingly, Figure 3.5 (b) shows the SMP with photothermal fillers contained microlevel voids at few locations compared to the neat SMP shown in Figure 3.5 (a). However, as shown in Figure 3.5 (d), the GFR styrene with photothermal fillers demonstrated improved aspects of fibre bonding and adhesion between the fibre and matrix. It is reported that, under loaded circumstances, the poor bonding between the fibre and matrix will cause local bending to propagate micro delamination until the failure [210]. Accordingly, the GFR styrene with photothermal fillers have less possibility for a delamination failure while operating with loads. Moreover, as shown in Figure 3.5 (b) and (d), the SMPCs with photothermal fillers and GFR styrene with photothermal fillers demonstrated uniform surface features throughout the cross-section, which indicates that the particulate photothermal fillers were incorporated into the SMP matrix in a homogeneous manner.

Figure 3.6 illustrates the SEM images of the carbon nanotube/polylactic acid SMP, where the images provided qualitative and quantitative information about the materials and the FDM additive manufacturing process. Figure 3.6 (a) and (b) illustrate the top surfaces of the SMP and SMPC samples. Accordingly, the surface of the pristine SMP made samples appears evenly and the surface of the MWCNT reinforced SMPC samples consists of micro level voids. Figure 3.6 (c) and (d) illustrate the cross sections of the neat PLA and MWCNT PLA samples. Neat PLA SMP demonstrated continuous bonding between the layers. Micro level voids were observed between the layers of MWCNT reinforced SMPC, which affected the continuous bonding between the layers.

The SEM images of carbon fibre/bisphenol A SMP are shown in Figure 3.7. Due to the manner of flow of the liquid epoxy in the mould made by two glass plates, air bubbles were trapped inside the mould which created tiny voids on the surface. However, such

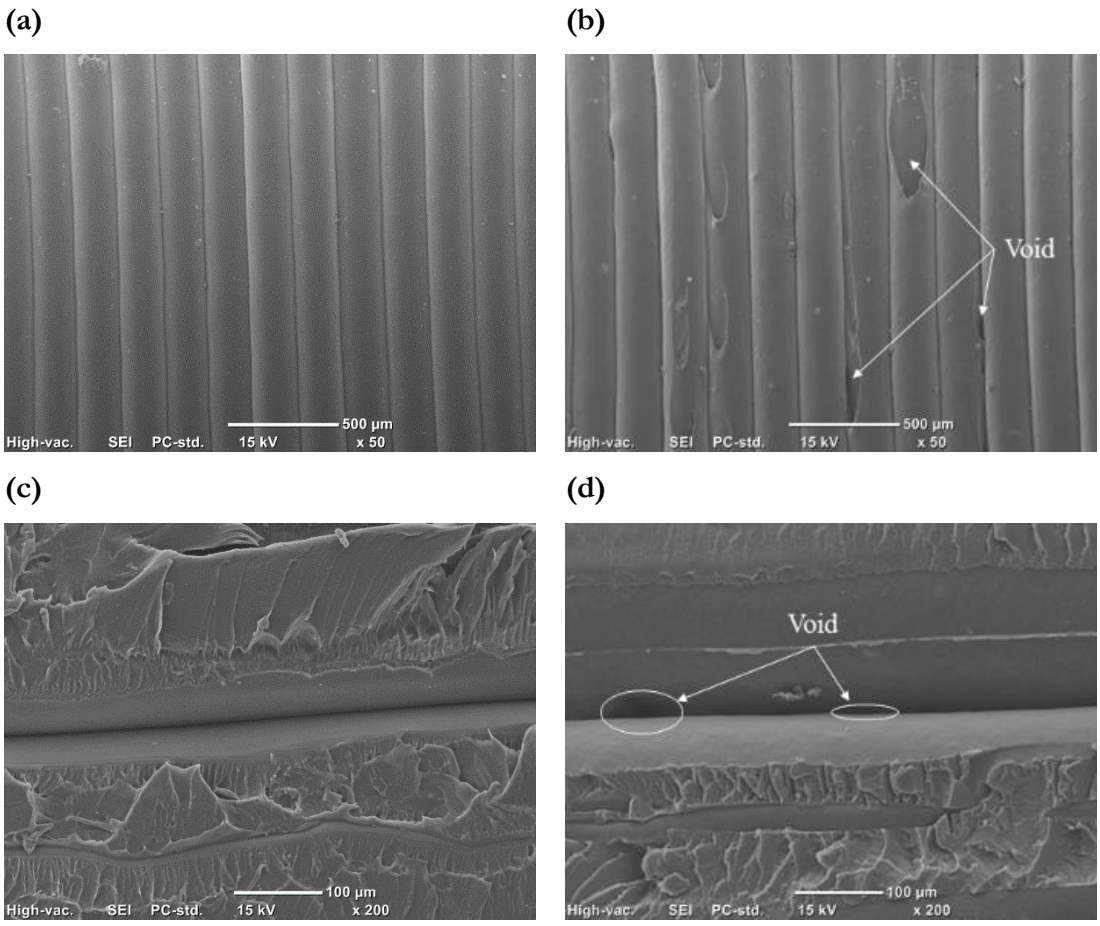

Figure 3.6: SEM images of carbon nanotube/polylactic acid SMP (a) Top surface of neat SMP (b) Top surface of MWCNT SMPC (c) Cross-section of neat SMP (d) Cross-section of MWCNT SMPC.

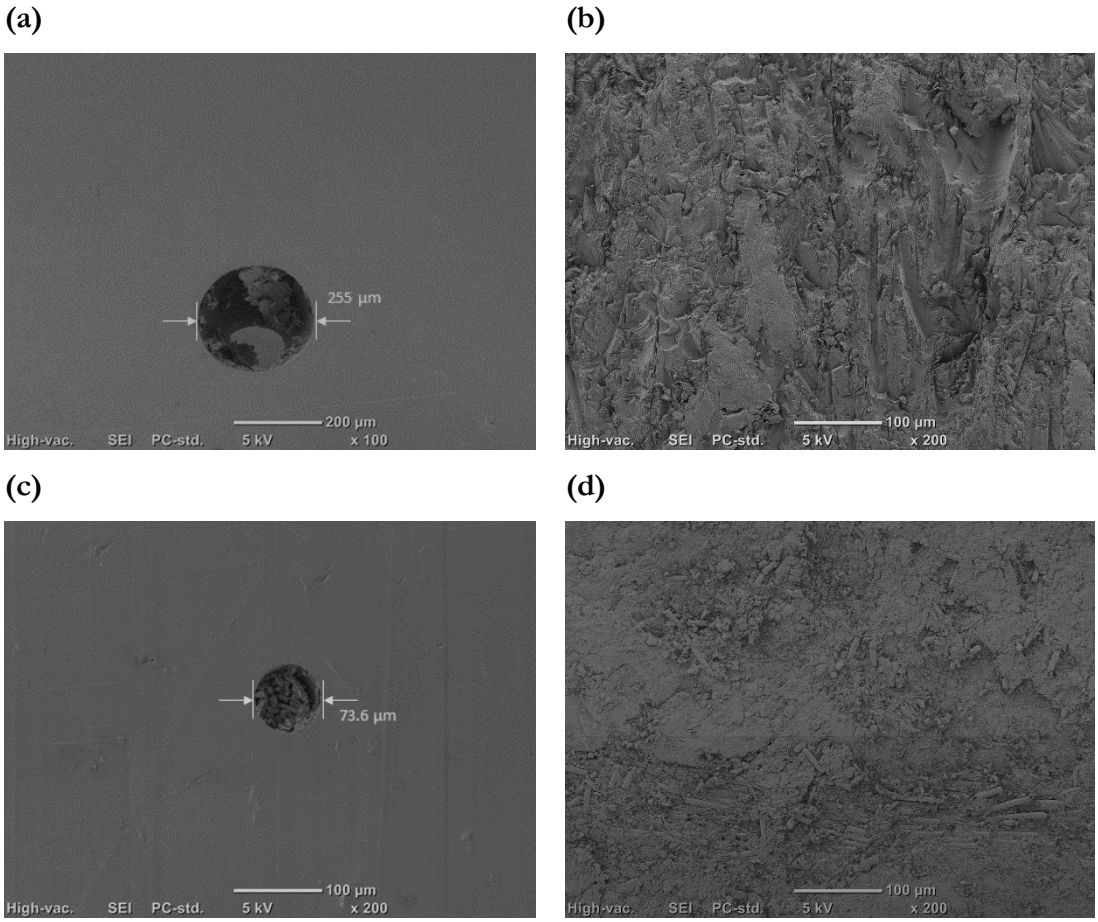

Figure 3.7: SEM images of carbon fibre/bisphenol A SMP (a) Top surface of neat DEGBA (b) Cross-section of neat DEGBA (c) Top surface of CFR DEGBA (d) Cross-section of CFR DEGBA.

voids were observed at very few locations (approx. 01 void per 10 x 10 cm^2 area). Figure 3.7 (a) and (b) illustrate that the surface voids of the neat DEGBA samples were of larger diameters than the diameters of the surface voids of the CFR DEGBA. However, the cross-sections of both neat DEGBA and CFR DEGBA did not show any significant voids due to trapped air generated during pouring into the moulds.

3.5 Structural Performance

3.5.1 Tensile Properties

The tensile stress-strain curves of four different material types are shown in Figure 3.8. Table 3.4 compares the longitudinal tensile properties of the LASMPC materials used in

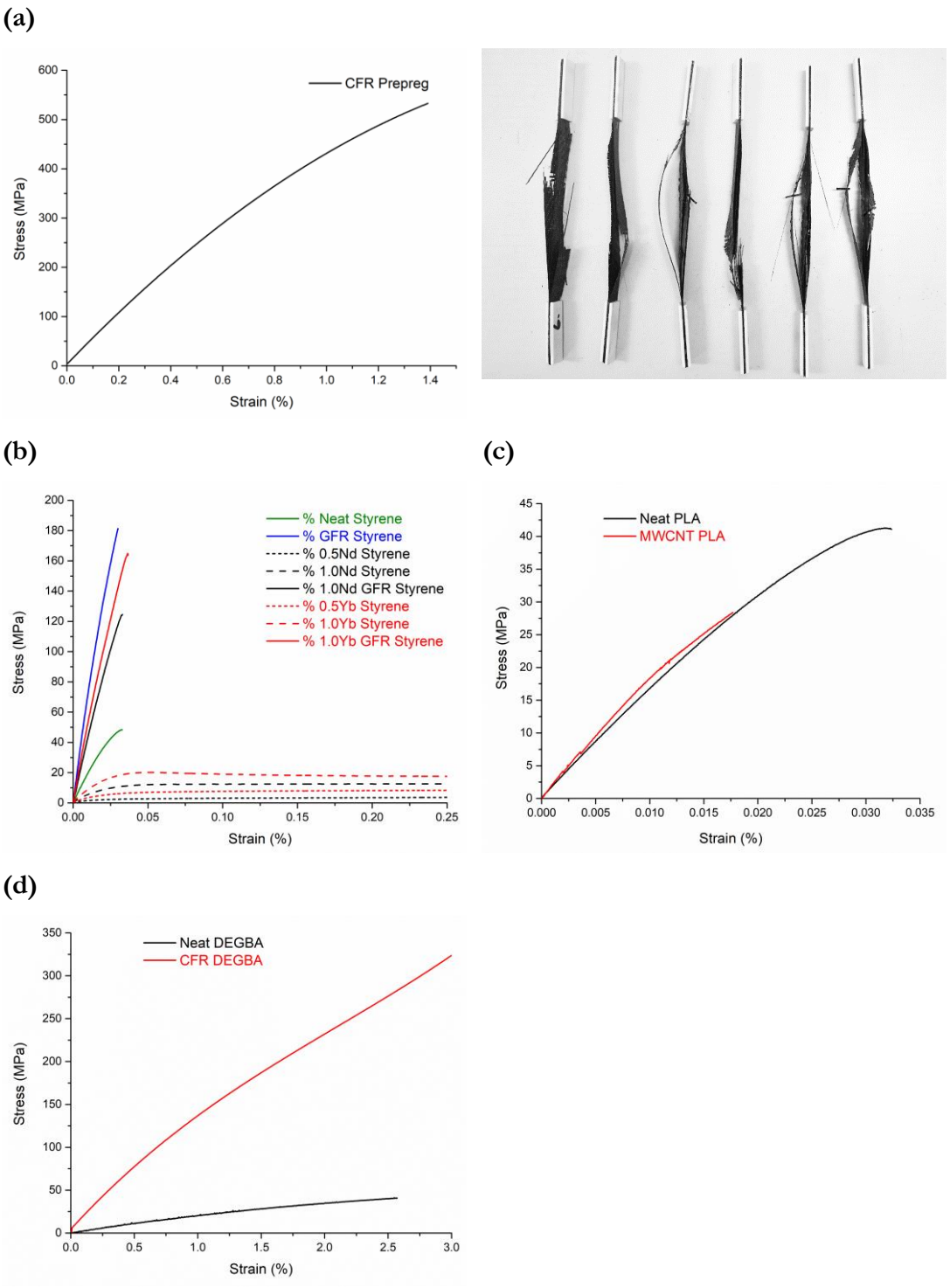

Figure 3.8: Uniaxial tensile properties (a) Carbon fibre/epoxy prepreg SMP (b) Rare earth organic complexes and glass fibre/styrene SMP (c) Carbon nanotube/polylactic acid SMP (d) Carbon fibre/bisphenol A SMP.

the current study with the composite materials developed by NASA for space applications.

As illustrated in Figure 3.8 (a), the calculated tensile strength of the carbon fibre/epoxy prepreg SMP is 547 MPa and the elastic modulus is 52 GPa. Stress-strain behaviour under tensile load showed a nonlinear trend. As has been proven for general composite materials, such nonlinear behaviour can be attributed to the voids between laminae and the progressive failures of fibres due to local bending at void locations [210, 211]. Moreover, as illustrated in Figure 3.8 (a) (right), at the point of tensile failure, a delamination of the material occurred. According to the ASTM standard D 3039/D 3039M-00 [212], this mode of tensile failure can be categorized as "XMV," where the failure is an explosive type, in multiple areas and in various locations.

However, the tensile experiments carried out by Paiva et al. [213], for carbon fabric (0/90) reinforced epoxy composites showed that the specimens demonstrated a lateral type brittle failure. Furthermore, based on the epoxy, the failure location varied, being inside grip, at grip, guage or multiple areas. Importantly, none of the specimens in the experiment by Paiva et al. [213] broke under the "XMV" mode. Possibly the micro level delamination between the layers which were identified during the SEM examinations might have caused local bending. As a result, the identified micro delamination was propagated until the failure of the LASMPC [210, 211].

Inclusion of rare earth organic complexes-based photothermal fillers into styrene-based SMP and GFR styrene SMP affected the mechanical and physical properties of the parent SMP or SMPC material. Figure 3.8 (b) shows the tensile behaviour of the rare earth organic complexes and glass fibre/styrene SMP test specimens. The neat styrene sample showed an ultimate tensile strength (UTS) of 48 MPa. Once reinforced with glass fibres, the UTS increased up to 181 MPa. However, the inclusion of rare earth organic complexes-based particles reduced the UTS of the SMPCs (without fibres). The SMPCs with photothermal fillers demonstrated relatively ductile behaviour and a plastic deformation over 0.25% strain. At any strain level, the stress exhibited by a cross-linked network system is related to the cross-link density, as given by the theory of rubber elasticity. The elastic modulus decreases as the cross-link density decreases [214].

It was noted that the UTS of the SMPCs increased slightly with respect to the increase of photothermal filler materials. The reason for such an increment in the UTS is the increase of the cross-linked density due to the higher levels of ligand TTA and ligand Phen. Furthermore, the SMPCs with $Yb(TTA)_3Phen$ demonstrated a higher UTS compared to the SMPCs with similar mass percentage of $Nd(TTA)_3Phen$. The incorporation of glass

fibres was advantageous to improve the UTS of the SMPCs with rare earth organic complexes-based photothermal fillers. The glass fibre reinforced SMPCs containing 1% of Nd(TTA)3Phen and Yb(TTA)3Phen demonstrated a UTS of 124 and 164 MPa, respectively, which exhibits a significant improvement compared to the SMPCs with only photothermal particles.

Figure 3.8 (c) illustrates the tensile properties of the neat PLA and MWCNT PLA samples. Accordingly, the elastic modulus for neat PLA and MWCNT PLA were 162 GPa and 183 GPa respectively. The UTS of the neat PLA and MWCNT PLA were 41 MPa and 28 MPa, respectively. It has been reported that carbon nanotube reinforcements improve the tensile properties of the composites [144]. However, as shown in Figure 3.6 (b) and (d), the inclusion of MWNCT causes micro level voids to form during the FDM process. The reason for the reduced tensile strength of MWCNT PLA could be the reduced amount of bonding between the layers in the FDM additive manufacturing process.

The tensile stress-strain curves for the neat DEGBA and CFR DEGBA are presented in Figure 3.8 (d). Accordingly, the UTS of the neat DEGBA and CFR DEGBA are 41 MPa and 340 MPa, respectively. The carbon fibre reinforcements increased the UTS to over eight times that of the neat SMP. Interestingly, the elastic modulus showed a significant improvement once reinforced. The elastic modulus of the neat DEGBA and CFR DEGBA were calculated as 2 GPa and 12 GPa, respectively. Accordingly, among the four tested materials, the CFR DEGBA samples showed superior tensile properties.

3.5.2 Compression Properties

Figure 3.9 illustrates the compressive properties of the uniaxial compressive stress-strain behaviour of the four materials. Table 3.4 compares the longitudinal compressive properties of the LASMPC materials used in the current study with the composite materials developed by NASA for space applications.

Compressive failure in polymer composite materials has demonstrated multiple modes of failures. Early investigations attributed composites' compressive failure to elastic instabilities resulting in a fibre buckling mechanism. Subsequent studies have concluded that compressive failure of fibre reinforced composites is caused by plastic microbuckling of the fibres in an idealized inelastic matrix medium. Moreover, fibre kinking, crushing, splitting, delamination and matrix failure can cause a compressive failure [215].

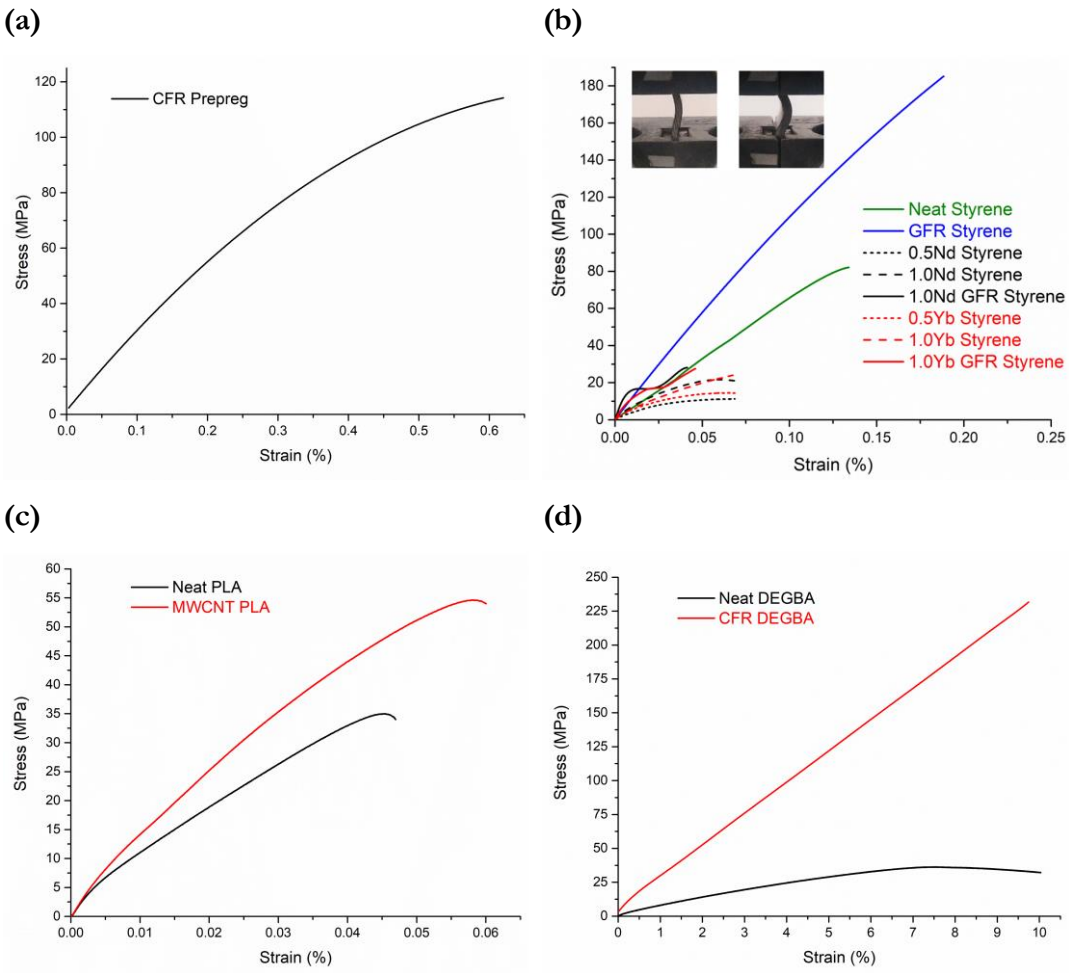

Figure 3.9: Uniaxial compression properties (a) Carbon fibre/epoxy prepreg SMP (b) Rare earth organic complexes and glass fibre/styrene SMP (c) Carbon nanotube/polylactic acid SMP (d) Carbon fibre/bisphenol A SMP.

As shown in Figure 3.9 (a), the compressive strength of the CFR prepreg was 120 MPa. The compressive test curve of the CFR prepreg showed a nonlinear behaviour, just like the tensile curve of the same material. The reason for failure can be attributed to fibre microbuckling due to non-linear response of the matrix material. The micro voids between the laminates as identified during the SEM investigations could cause such behaviour.

Figure 3.9 (b) shows the uniaxial compression test results of the rare earth organic complexes and glass fibre/styrene SMP. Accordingly, the neat styrene and GFR styrene demonstrated compression strengths of 82 and 185 MPa, respectively. Inclusion of rare earth organic complexes-based fillers reduced the compression strength of the SMPCs. Even though the SMPCs with photothermal fillers were reinforced with glass fibres, these

samples did not show a significant improvement in their compressive strength. As illustrated in Figure 3.9 (b) (top left), the buckling behaviour demonstrated by the SMPCs with photothermal fillers (with and without glass fibres) under uniaxial compression loading caused these SMPCs to display reduced compression properties.

Buckling is generally avoided during design modifications. Buckling was a major concern in the design of all slender structural elements due to the resultant capacity reduction associated with large deformations and the resultant catastrophic failure. However, the increasing interest in the design of smart devices and mechanical components has identified buckling and post-buckling responses as a favourable behaviour [216]. The two inspiring features of many buckling phenomena are high rate motion and sudden energy release. These two features make buckling an ideal mechanism for adaptive and smart applications [216]. Therefore, the enhanced buckling behaviour of SMPCs due to the inclusion of rare earth organic complexes-based particulate fillers could be advantageous to develop energy and motion related smart applications activated by light [216].

As shown in Figure 3.9 (c), the inclusion of MWCNT into the PLA SMP matrix improved the compression strength. The compression strengths for the neat PLA and MWCNT PLA are 35 MPa and 55 MPa, respectively. For both samples there was a tendency for shear at ± 45 degrees comparative to the major axis (direction of mechanical loading). This shear mode could cause the compressive failure [217]. According to the failure identification code described in the ASTM D6641 test standard, the failure of the neat PLA and MWCNT PLA were identified as TAT [200]. This failure identification implies that the failure mode, failure area and failure location were transverse shear, at grip and top respectively. The inclusion of MWCNTs might improve the resistant to shear, which resulted the improve of compression strength of MWCNT PLA.

The compression properties of carbon fibre/bisphenol A SMP are shown in Figure 3.9 (d). The compressive strength of neat DEGBA and CFR DEGBA are 36 MPa and 233 MPa, respectively. The neat DEGBA showed a nonlinear matrix failure. The CFR DEGBA showed an almost linear stress-strain curve, that might have failed due to the shear kinking of fibre and damage of the matrix. As per the failure identification code described in the ASTM D6641 test standard, the failure of the CFR DEGBA PLA was identified as KGM [200]. This failure identification implies that the failure mode, failure area and failure location were kink bands, gage and middle respectively.

Table 3.4: Comparison of structural properties of with the composite materials presented for space applications.

Material (Sample ID)	Longitudinal tensile			Longitudinal compressive		
	Ultimate tensile strength (MPa)	Elastic modulus (GPa)	Strain to failure (%)	Ultimate comp. strength (MPa)	Elastic modulus (GPa)	Strain to failure (%)
Current Study						
CFR Prepreg	547	52	1.39	120	29	0.62
Neat Styrene	48	190	0.03	82	65	0.13
GFR Styrene	181	691	0.03	185	110	0.19
0.5Nd Styrene	-	-	<0.25	-	-	-
1.0Nd Styrene	-	-	<0.25	-	-	-
1.0Nd GFR Styrene	124	428	0.03	-	-	-
0.5Yb Styrene	-	-	<0.25	-	-	-
1.0Yb Styrene	-	-	<0.25	-	-	-
1.0Yb GFR Styrene	164	499	0.04	-	-	-
Neat PLA	41	162	0.03	35	157	0.04
MWCNT PLA	28	183	0.02	55	178	0.06
Neat DGEBA	41	2	2.57	32	0.65	10.03
CFR DEGBA	337	12	3.13	232	2.5	9.75
NASA contractor report 187472: Composite materials for space applications [61]						
GRAPHITE/EPOXY: F75/ERLX 1962 (Unidirectional P75/1962, Fibre Volume = 62.5%)	852	319	0.27	437	250	0.20
GRAPHITE/THERMOPLASTIC: (P75/PEEK, $[0°, \pm45°, 90°]_5$, Fibre Volume = 62.2%)	241	92	0.26	147	62	0.32

CARBON/THERMOPLASTIC: (AS4/PES, $[0°, \pm45°, 90°]_5$, Fibre Volume = 53.7%)	554	44	1.35	326	40	1.06
25 V/O DISCONTINUOUS (SiC/Al, 25v/o SiCp/12124-T6)	583	115	1.26	557	128	0.62
GRAPHITE/ALUMINUM: (DWA P100/6061 AI, $[0°]_2$, Fibre Volume = 42.2%)	905	343	0.27	321	332	0.12
GRAPHITE/MAGNESIUM: (P100/AZ91C Mg, $[\pm16°]_5$, Fibre Volume = 30.1%)	422	175	0.002	201	130	0.27
CARBON/GLASS: (HMU/7070 Glass $[0°]_{12,}$ Panel 679, Fibre Volume = 44%)	658	182	0.35	871	147	0.66
CARBON/CARBON (Unidirectional P100/C, Fibre Volume = 52.4)	561	301	0.23	330	272	0.13

3.5.3 Bulk Density

Low density materials drastically change the design parameters of engineering products. Recently most of the metal components were replaced with lightweight composites, mostly in the automotive, aerospace and space sectors, which has significantly contributed to enhancing the fuel efficiency of ground and air vehicles. Table 3.5 quantifies the densities of the test samples. The inclusion of fibre reinforcements and rare earth organic complexes-based photothermal particles has slightly enhanced these samples' density relative to their parent neat SMPs, as anticipated. However, the 4D printed MWCNT PLA samples showed a lower density compared to the neat PLA samples, which contradicted the trend of general observations for the other materials. This could have happened due to enhanced porosity (micro level voids) during the additive manufacturing process, which was confirmed during the SEM investigations. It was reported that the densities of SMPs and SMAs lie between 0.9-1.1 g/cm^3 and 6-8 g/cm^3, respectively [218]. The current study quantified that the densities of LASMPC materials containing fibre reinforcements

and photothermal fillers lie between 1 and 1.5 g/cm^3. The densities of the LASMPCs showed a slight increase compared to the previously reported general SMPs. However, all LASMPCs exhibited significantly lower densities compared to the those of SMAs [218].

3.5.4 Impact Behaviour

The recent progress made in SMP research has been focused on developing SMPC-based components for space engineering applications [27]. However, high energy micrometeoroids and space debris are challenging concerns when selecting lightweight materials for space applications. Therefore, the LASMPCs with improved impact energy absorbance will be a major requirement for structural engineering applications.

Table 3.5 presents the impact energy absorbance of all test samples subjected to a low velocity impact. The inclusions of 0/90 glass fibre into styrene SMP, 0/90 carbon fibre into DEGBA SMP, and MWCNT into PLA SMP increased the impact energy absorbance by 7.86, 2.53 and 1.36 times, respectively, compared to their parent SMP matrix materials.

The damage created through energy absorption might have consisted of several separate and established failures including delamination, matrix cracking and fibre breakage. The increased energy absorbance due to the inclusion of glass and carbon fibres might have resulted due to the energy absorbance attributed to delamination and fibre breakage. Even though the fibre reinforcements could enhance the impact energy absorbance, the samples failed due to the low transverse and interlaminar shear strength associated with laminar construction.

However, the impact behaviour of fibre reinforced LASMPCs can be further improved by incorporating interlaminar reinforcements such as short carbon fibres and CNTs [219, 220]. Also, LASMPCs' light induced self-healing capabilities can be advantageous to heal and recover the damage due to impact [24, 221]. Moreover, the lack of plastic deformation in composites causes irreversible permanent damage due to impact. As was observed during the tensile testing, the incorporation of rare earth organic fillers increased the ductile behaviour and shown a plastic deformation over 0.25% strain. Due to the same reason, the LASMPCs with Nd(TTA)$_3$Phen and Yb(TTA)$_3$Phen displayed improved impact energy absorbance.

Table 3.5: Density, impact energy absorbance, surface roughness and hardness of the test samples.

Material (Sample ID)	Density (g/cm^3)	Impact energy (J)	Surface roughness, Ra (μm)	Hardness (Barcol impressor or Shore C)
CFR Prepreg	1.30	0.54	9.14	56†
Neat Styrene	1.14	0.28	0.32	95.0††
GFR Styrene	1.44	2.20	0.43	97.0††
0.5Nd Styrene	1.20	0.75	0.36	90.0††
1.0Nd Styrene	1.21	0.25	0.37	92.5††
1.0Nd GFR Styrene	1.41	2.40	0.45	93.5††
0.5Yb Styrene	1.21	0.65	0.36	90.5††
1.0Yb Styrene	1.22	0.24	0.37	93.0††
1.0Yb GFR Styrene	1.41	2.50	0.44	94.0††
Neat PLA	1.21	0.17	13.56	42.0††
MWCNT PLA	1.01	0.22	15.60	47.0††
Neat DGEBA	1.19	0.30	0.31	26.0†
CFR DEGBA	1.30	0.76	0.33	58.6†

3.5.5 Surface Roughness and Hardness

Irregularities on a material's surface possibly form nucleation sites for cracks and therefore measurements of surface roughness can be used in the prediction of structural performance [222]. Also, there is a correlation between roughness parameters and tribological behaviour. Rough surfaces wear rapidly and have higher friction coefficients than smooth surfaces [223]. Moreover, surface roughness enhances the adhesion between solid bodies [224]. The surface roughness of LASMPCs is an important factor to be considered.

According to the Beer-Lambert law, the light absorption of a specimen depends on three variables: the extinction coefficient, path length and concentration of the substance [156]. The extinction coefficient, which is also known as absorptivity, depends on the material

and its surface. As the surface roughness increases, the surface reflectance decreases, which enables penetration of more light into the substance. According to the surface roughness values presented in Table 3.5, it can be recognised that the test samples' surface roughness were mainly affected by the manufacturing process.

The samples made by additive manufacturing showed the highest surface roughness. The CFR prepreg samples made by vacuum bagging also demonstrated high roughness, compared to the styrene and DEGBA-based samples made by using glass moulds. The inclusion of rare earth organic complexes-based fillers, MWCNT, glass fibre and carbon fire enhanced the composites' surface roughness, compared to their parent SMP materials. As surface roughness is a plus point for light activation, in future, the light exposed surfaces can be spray coated with wavelength selective photothermal dyes or particles.

From an engineering point of view, hardness is an important factor as the resistance to wear due to friction or erosion depends on the hardness of the material. Table 3.5 presents the hardness test results. The Barcol impressor scale, which is used to determine the hardness of both reinforced and nonreinforced thermoset polymers, was used for the carbon fibre/epoxy prepreg and carbon fibre/bisphenol A (DGEBA) epoxy samples. A Shore durometer, which is used to determine the relative hardness of soft materials (usually plastic or rubber) was used for the rare earth organic complexes and glass fibre/styrene and carbon nanotube/polylactic acid samples. The hardness of the test specimens was measured appropriately by considering the material type and limitations of each measuring type. The inclusion of carbon fibres, glass fibres and carbon MWCNTs enhanced the hardness, compared to their parent SMP materials. The inclusion of rare earth organic particles reduced the hardness, compared to the parent SMP material.

3.6 Thermomechanical Behaviour

3.6.1 Glass Transition Temperature

Below Tg, an SMP material is at a dominant frozen phase and above Tg, an SMP material is at a dominant active phase. At a certain range around Tg, an SMP material demonstrates the combined properties of both phases, where the shape changes occur [225]. The onset point of the storage modulus curve, the peak of the loss modulus curve or the peak of the tan delta curve are often employed to define the glass transition temperature (Tg) [13]. By considering the material parameters defined by Baghani et al., the temperatures Tl, Tg and

Th can be identified where at T=Tl, this is the dominant frozen phase, (b) at T=Tg, this is a combination of both phases and (c) at T=Th, this is the dominant active phase [13, 225]. The temperature region between Tl and Th is the glass transiting region. As a general rule, Tl is taken as =Tg − 20°C and Th is taken as =Tg + 20°C [13].

Figure 3.10 presents the thermomechanical behaviours of the thirteen different samples. The respective Tl, Tg and Th values are presented in Table 3.6. The SMPCs with higher Tg are appropriate for structural engineering applications as shape memory activation will not take place due to the environmental temperature changes.

Compared to CFR prepreg, CFR DEGBA demonstrated a higher Tg. This is explained by the inclusion of carbon fibres into bisphenol A SMP, which enhanced the Tg significantly. Inclusion of rare earth organic complexes reduced the Tg of the SMPCs, which lay between 58 °C and 63 °C. The samples with a lesser amount (0.5%) of photothermal fillers demonstrated lower Tgs. Once the amount of photothermal fillers increased (1.0%), the Tg increased slightly.

Furthermore, $Yb(TTA)_3Phen$-incorporated samples showed a higher Tg than the samples incorporated with the same amount of $Nd(TTA)_3Phen$. Inclusion of glass fibres reduced the Tg of the samples, compared to their parent materials.

The SMPCs incorporated with rare earth organic complexes-based photothermal fillers may require a thermal insulation coating where the NIR light can be transmitted into the material by optical fibres. Figure 3.10 (c) illustrates the storage modulus curves of the rare earth organic complexes and glass fibre/styrene SMP samples. The storage modulus represents the capability of elastic energy storage when a sample was subjected to an elastic deformation. All specimens exhibited a higher storage modulus at lower temperatures and a critically low modulus at higher temperatures. This happened due to the entropy elasticity caused by the micro-Brownian movement in the rubbery phase [13, 15].

The inclusion of glass fibre reinforcements into the SMP matrix demonstrated a significant improvement in storage modules. However, the samples filled with rare earth organic complexes-based photothermal fillers displayed a reduced storage modulus, compared to the parent SMP material. Even though the SMPCs with photothermal fillers were reinforced with glass fibres, no significant improvement in the storage modulus was demonstrated.

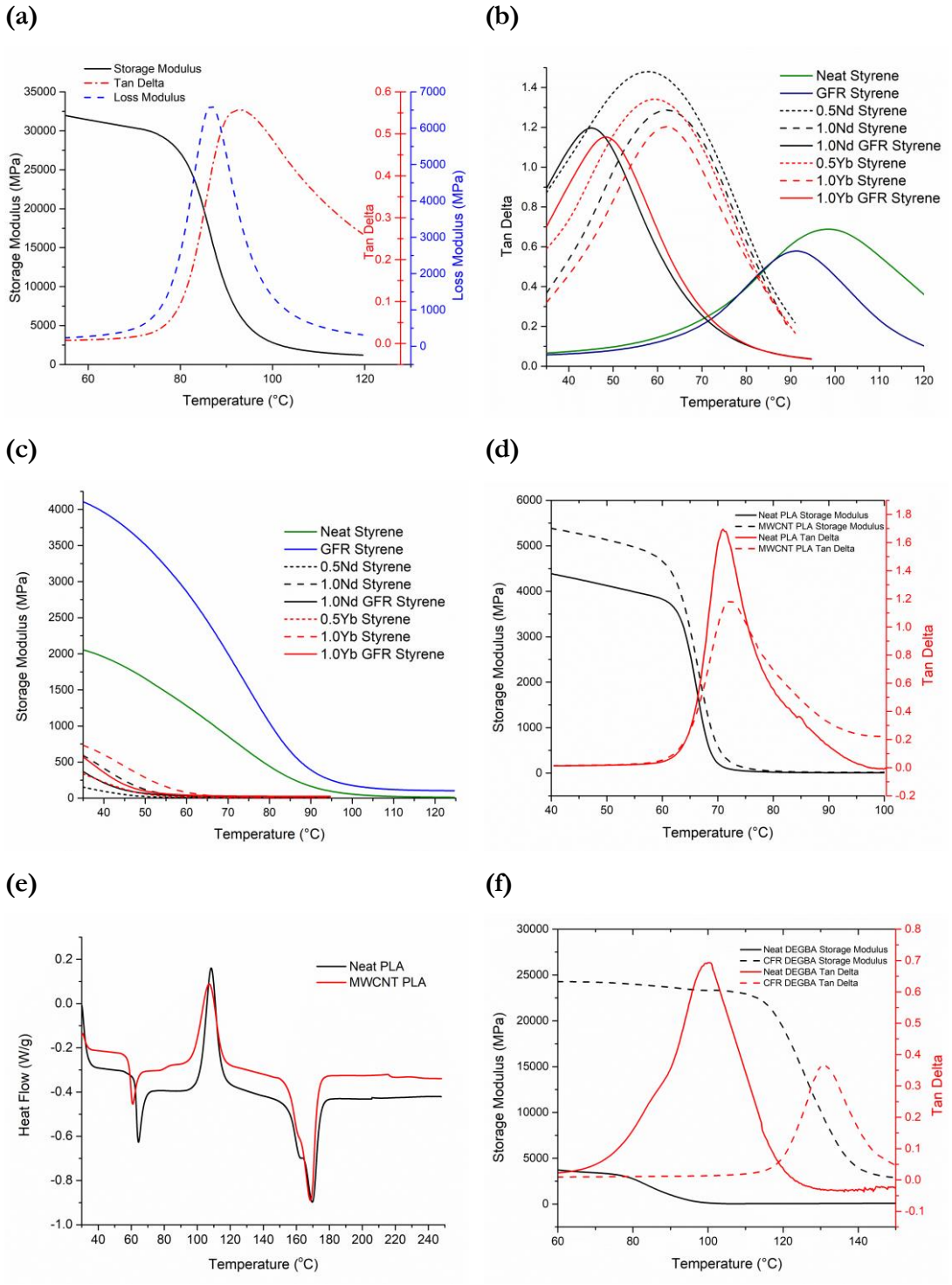

Figure 3.10: Thermomechanical properties of the test samples (a) Storage modulus, loss modulus and Tan delta of the carbon fibre/epoxy prepreg SMP (b) Tan delta of rare earth organic complexes and glass fibre/styrene SMP (c) Storage modulus of rare earth organic complexes and glass fibre/styrene SMP (d) Storage modulus and Tan delta of carbon nanotube/polylactic acid SMP (e) Temperature versus heat flow DSC curve for carbon nanotube/polylactic acid SMP (f) Carbon fibre/bisphenol A SMP.

Table 3.6: Tl, Tg and Th values of the test samples.

Material (Sample ID)	Tl (ºC)	Tg (ºC)	Th (ºC)
CFR Prepreg	60	80†	100
Neat Styrene	81	101††	121
GFR Styrene	72	92††	112
0.5Nd Styrene	38	58††	78
1.0Nd Styrene	43	63††	83
1.0Nd GFR Styrene	25	45††	65
0.5Yb Styrene	39	59††	79
1.0Yb Styrene	43	63††	83
1.0Yb GFR Styrene	28	48††	68
Neat PLA	41	61†	81
MWCNT PLA	43	63†	83
Neat DGEBA	80	100††	120
CFR DEGBA	111	131††	151

† considering storage modulus

†† considering Tan delta

According to the DMA and DSC curves shown in Figure 3.10 (d) and (e), respectively, the inclusion of MWCNT reduced the LASMPC's Tg, compared to its parent neat PLA material. The DSC experiment was only conducted for carbon nanotube/polylactic acid SMP (only thermoplastic SMP was studied here) in order to identify the melting point (Tm), which is important for the FDM additive manufacturing process. In addition, the DSC curve provided the crystallization temperature (Tc), where the atoms or molecules of a material are organized into a structure known as a crystal. Therefore, during the shape programming, SMP materials should be heated to a temperature above Tg but always below Tc. The Tcs for neat PLA and MWCNT PLA can be identified as 108 ˚C and 107 ˚C, respectively. At Tm, a material changes from a solid state to the liquid state. For FDM, the filament should be heated up to Tm at the nozzle. The Tm values for pristine SMP and MWCNT SMPC are 170 ˚C and 169 ˚C, respectively.

3.6.2 Strain Recovery Behaviour

The strain recovery curve obtained from DMA under strain rate mode shows the shape memory characteristics of a SMP material. The thermomechanical cycles of the test samples' stress-free strain recovery process are presented in Figure 3.11. Considering the curves, the respective shape fixity ratios (R_f) and shape recovery ratios (R_r) shown in Table 3.7 can be calculated by using Equations 3.1 and 3.2 which were originally devised by Fejős et al. [226]. Moreover, shape recovery rates (R_{Rate}) were calculated by using Equation 3.3.

$$R_f = \frac{\varepsilon_u}{\varepsilon_m} \times 100\ \% \tag{3.1}$$

$$R_r = \frac{\varepsilon_m - \varepsilon_p}{\varepsilon_m - \varepsilon_0} \times 100\ \% \tag{3.2}$$

$$R_{Rate} = \frac{\varepsilon_m - \varepsilon_p}{T_r - T_i} \tag{3.3}$$

where

ε_0 is the strain of the original shape

ε_m is the strain of the programmed temporary shape

ε_u is the strain of the fixed temporary shape

ε_p is the strain of the recovered shape

T_i is the time at which recovery begins

T_r is the time at which recovery is completed

Figure 3.11 (a) shows the full thermomechanical cycles the stress-free strain recovery process of the carbon fibre/epoxy prepreg SMP. Accordingly, no spring back effect has shown after the shape programming phase because the fixed temporary shape and the required temporary shape is equal. Moreover, it indicates that the strain recovery begins at 62 °C and recovers from 1.5% to 0.12% after the temperature ramp up to 130 °C, followed by a constant temperature for 20 min.

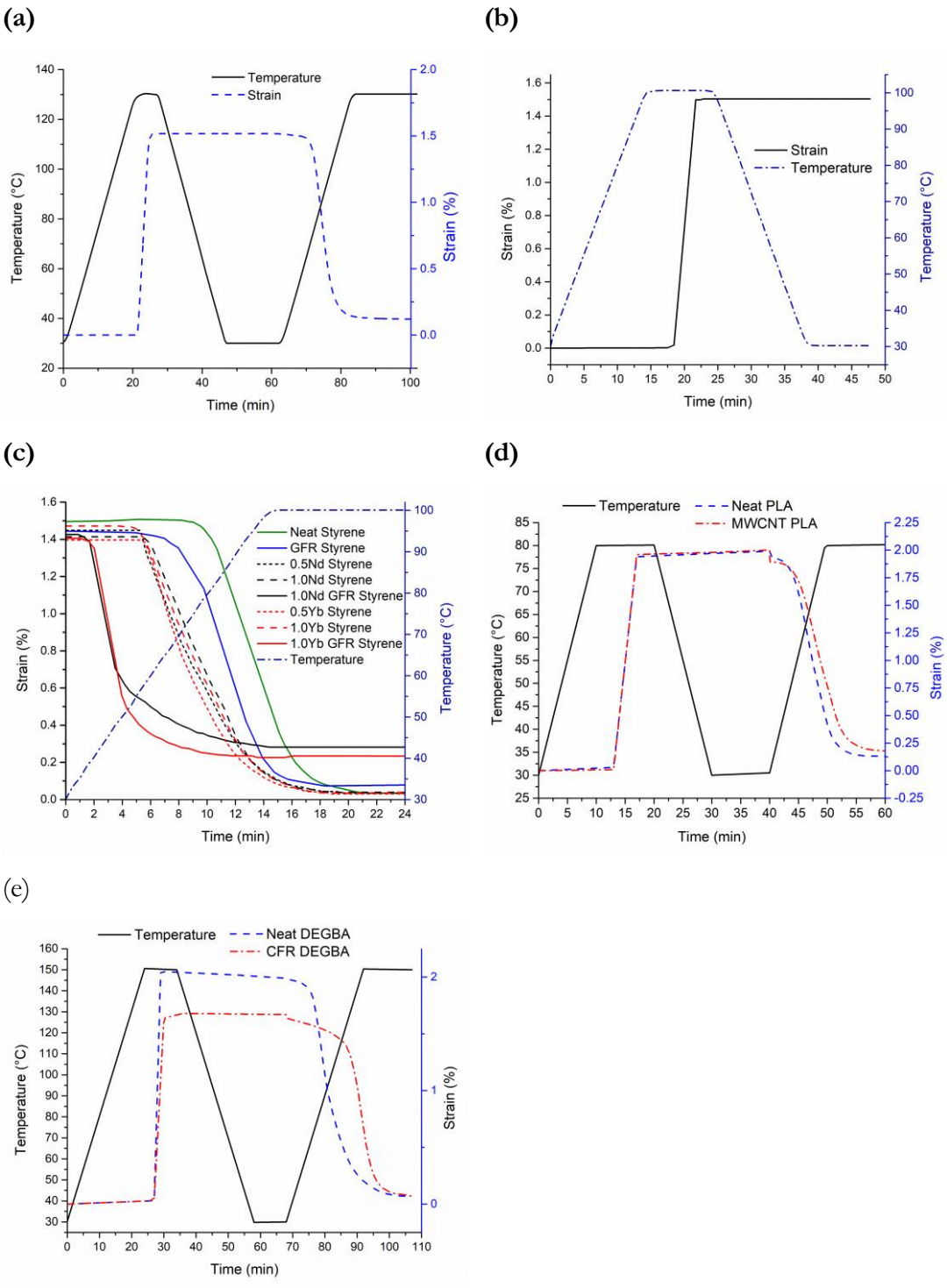

Figure 3.11: Thermomechanical cycles of stress-free strain recovery process (a) Strain programming and recovery of the carbon fibre/epoxy prepreg SMP (b) Strain programming of the rare earth organic complexes and glass fibre/styrene SMP (c) Strain recovery of the rare earth organic complexes and glass fibre/styrene SMP (d) Strain programming and recovery of the carbon nanotube/polylactic acid SMP (e) Strain programming and recovery of the carbon fibre/bisphenol A SMP.

For clear representation, the full shape memory cycle of the rare earth organic complexes and glass fibre/styrene SMP were divided into two parts. Figure 3.11 (b) illustrates the first half of the shape memory cycle, which is shape fixing, common for all test samples. Accordingly, the samples were programmed into a 1.5% strain at 100 °C. In the second half of the shape memory cycle, which is shape recovery, the samples were heated to 100 °C and set isothermal for 10 minutes. Figure 3.11 (c) illustrates the shape recovery behaviours of each test sample. Inclusion of rare earth organic complexes reduced the shape recovery rate compared to the parent material. The SMPCs incorporated with both glass fibres and photothermal fillers demonstrated a fast recovery (~0.23%/min) until a 0.7% strain around their Tg. However, at higher temperatures, those SMPCs showed further recovery at a lower rate. The neat styrene SMP demonstrated an excellent shape fixity while inclusion of photothermal fillers reduced the shape fixity.

Compared to the parent material, the GFR styrene samples showed a lower fixity capability. The reason for this is that the spring back effect is due to the fibre elasticity of the incorporated glass fibres during the removing of applied load [13, 227, 228]. The strain concentration near the fibre ends and fibre elasticity play important roles in LASMPCs' shape recovery properties[228]. The inclusion of rare earth organic complexes had no demonstrated significant effect on the shape recovery ratio. The GFR samples with photothermal fillers displayed a lower shape recovery ratio compared to the SMPCs without fibre reinforcements.

As illustrated in Figure 3.11 (d), the inclusion of MWCNT reduced the shape fixity ratio, shape recovery ratio and shape recovery rate compared to its parent neat PLA material. Preliminary experiments indicated that the shape recovery of the 4D printed neat PLA MWCNT PLA material depended on the thickness of the samples. Based on this preliminary understanding, samples with a 0.8 mm thickness were used for the DMA strain recovery experiments.

Figure 3.11 (e) presents the shape recovery behaviour of the carbon fibre/bisphenol A SMP. Even though the neat DEGBA demonstrated a perfect shape fixity, CFR DEGBA showed a reduction in the shape fixity ratio. Moreover, the CFR DEGBA was only programmed to a 1.6 % strain, even though the DMA was set up to program the samples to a 2 % strain. The inclusion of carbon fibres into the DEGBA SMP might have enhanced the material's flexural strength and recovery stresses significantly. The force applied by the DMA was inadequate to program the sample to the required stain.

Table 3.7: Shape fixity and recovery ratios of the test samples.

Material (Sample ID)	Shape fixity ratio, R_f (%)	Shape recovery ratio, R_r (%)	Shape recovery rate (%/min)
CFR Prepreg	100	86.0	0.07
Neat Styrene	99.7	97.05	0.12
GFR Styrene	96.29	94.52	0.11
0.5Nd Styrene	96.58	97.69	0.1
1.0Nd Styrene	94.27	97.41	0.11
1.0Nd GFR Styrene	95.1	81.21	0.09
0.5Yb Styrene	93.08	97.4	0.1
1.0Yb Styrene	98.08	97.45	0.1
1.0Yb GFR Styrene	93.73	85.03	0.09
Neat PLA	96.72	93.34	0.09
MWCNT PLA	94.5	91.05	0.09
Neat DGEBA	99.49	96.60	0.05
CFR DEGBA	98.20	95.26	0.04

3.7 Summary

In this chapter, deliberations have been provided on the morphology, structural properties and thermomechanical properties of four different types of SMP and LASMPC materials. In addition to the composition of the materials, the measured responses are directly affected by their method of manufacturing. The inclusion of carbon and glass fibres has significantly improved the structural properties of the LASMPC materials, as anticipated. However, the rare earth organic complexes-based photothermal fillers have created negative effects on the structural properties. Carbon-based reinforcements have enhanced the Tg of the materials. Rare earth organic-based photothermal fillers have decreased the Tg and storage modulus significantly. The shape fixity and recovery ratios have been affected by the fibre reinforcements.

LASMPCs only containing rare earth organic complexes are suitable for non-structural applications. The combination of rare earth organic complexes and glass fibres enhances

the material properties so that they are suitable for semi structural and structural applications. MWCNT incorporated PLA can be used to 4D print semi structural and structural components. Interestingly, carbon fibre reinforced LASMPCs are the most suitable candidates for structural engineering applications.

However, the light activation capability of these materials depends on their ability to respond to the photothermal effect. The light absorbance and photothermal effect of the proposed materials need to be thoroughly investigated. The effective light wavelengths and power densities of the irradiated light, to accomplish light activation of each specific LASMPC material type, need to be studied. In view of this, Chapter 4's focus is the photothermal behaviour and light activation of the proposed structural LASMPCs.

Chapter 4

Photothermal Behaviour and Light Activation of LASMPCs

4.1 Introduction

To date various studies have been carried out to introduce different photothermal fillers for LASMPCs, i.e., gold [25, 42, 52], silver [45, 96], titanium [46], graphene [48], carbon black [37], aniline black [36]. However, most of those LASMPC developments were limited to miniature, small scale and biomedical applications. In Chapter 3, the results of examining four types of LASMPC material systems and their structural properties and thermomechanical characteristics have been presented. Chapter 4 provides novel knowledge and scientific understanding on photothermal behaviour and light activation of reinforced LASMPCs with enhanced structural performance.

The light absorbance capabilities of the developed LASMPCs in UV, visible and NIR ranges are demonstrated. In addition to their excellent structural performance and thermomechanical characteristics, carbon fibre reinforced LASMPCs have also shown

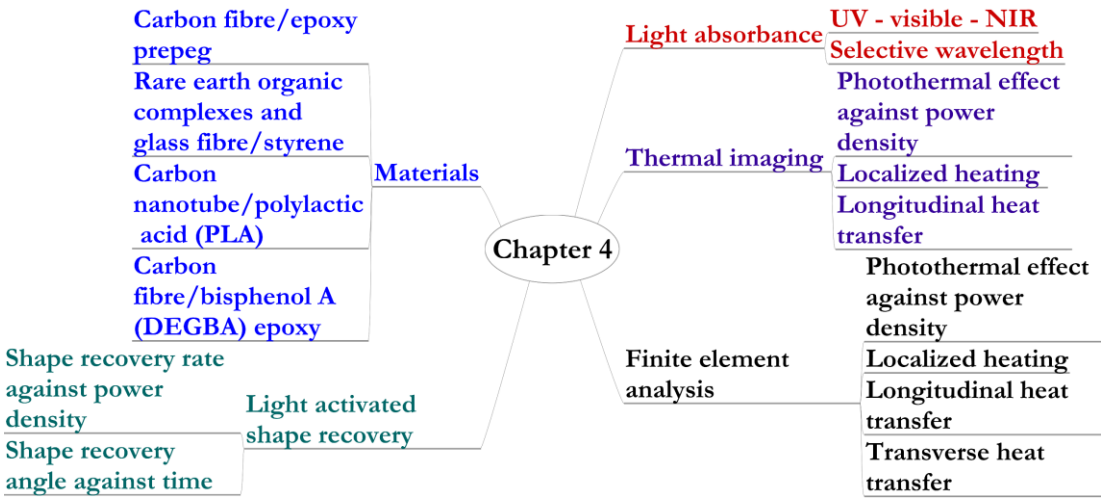

Figure 4.1: Overview of the technical contents of Chapter 4.

higher photothermal performance. Therefore, carbon fibre reinforced LASMPCs have been accepted for further investigations.

The extent of the power density required to control the localized heating and associated shape recovery behaviour is important for developing large scale engineering structures. The experimental and simulation findings on longitudinal heat transfer show a close correlation, which will be beneficial in designing the prospective LASMPC structures and determining the capacity of the required laser irradiation. Extended FEA simulations show transverse heat transfer behaviour, which was difficult to study with the experimental method.

An overview of the technical contents of Chapter 4 is illustrated in Figure 4.1. Significantly, the indispensable findings presented in this chapter enable large scale LASMPC structures to be activated by light energy. The content of this chapter is presented in the publications J3, J4, J5, C1, C2 and C4 as detailed in the appendix A of this thesis.

4.2 Materials and Methods

4.2.1 Material Preparation

In this study, four types of LASMPC materials are presented i) carbon fibre/epoxy prepreg based LASMPC, ii) rare earth organic complexes and glass fibre/styrene-based LASMPC, iii) carbon nanotube/polylactic acid (PLA) based LASMPC and iv) carbon fibre/bisphenol A (DEGBA) epoxy based LASMPC. The material preparation processes of the LASMPCs were different for each material type. The sample preparation methods are described in the Chapter 3, from Sections 3.2.1 to 3.2.4. The prepared samples were cut into standard sizes of test specimens as shown in Table 4.1.

4.2.2 Experimental Methods

The transmittance spectra of the test materials have been obtained by using a Thermo Scientific™ Evolution™ 220 UV-visible spectrophotometer and an Agilent Cary 5000 UV-vis-NIR spectrophotometer. Subsequently, the respective light absorbances were calculated.

Table 4.1: Specification of the photothermal and shape recovery test specimens.

Experiment	Dimensions (mm)	
	Length	Width
Photothermal test	100	100
Light activated shape recovery test	60	10

All light irradiation experiments were conducted in an in-house optical enclosure. The 808 nm (0-20 W) laser source, 980 nm (0-25 W) laser source, lab adjustable power supply units and wavelength dependent collimators were supplied by CivilLaser, China. Different power densities, i.e., 0.01, 0.5, 1.0, 1.5 2.0 and 3.0 W/cm^2 of 808 nm and 980 nm NIR radiation, were irradiated normal to top the surface of the LASMPCs samples. Lab adjustable power supply units were used to control the output power of the lasers. By using the collimators, light was irradiated onto a 10 mm diameter area from a 30 mm distance. For safety concerns, the experiments were observed through a video camera. Figure 4.2 shows the general experimental setup.

By using an FLIR A65 thermal imaging camera, the temperature change due to light absorbance was recorded. Surface properties of the tested materials considering the SEM images and surface roughness test results have been discussed in the Section 3.4.2 and Section 3.5.5 respectively. By using the FLIR ResearchIR software package, the temperature profiles were analysed.

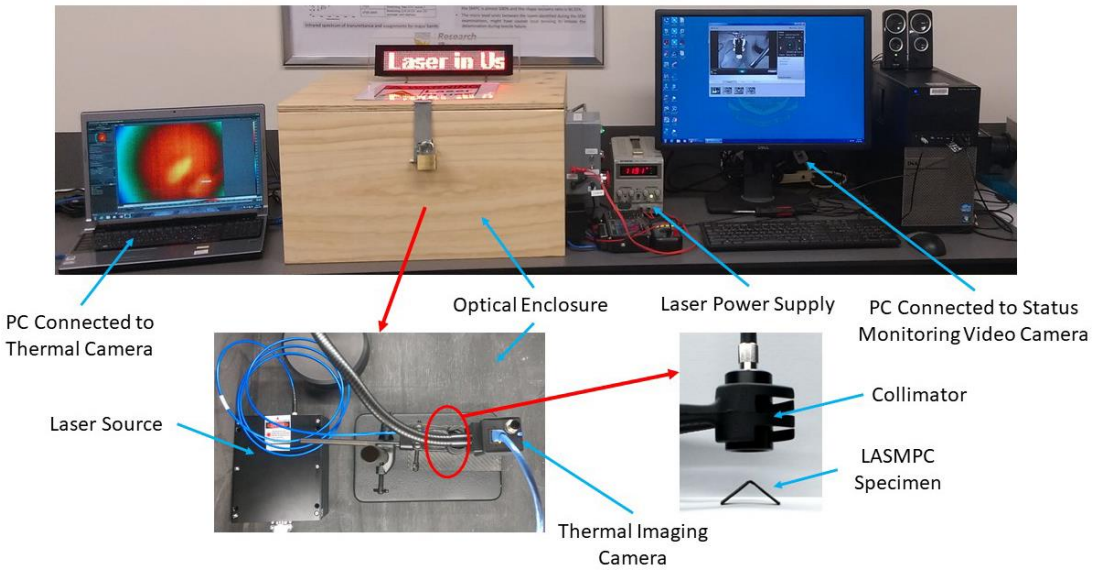

Figure 4.2: Experimental setup of light irradiation onto LASMPCs.

The light activated shape recoveries of the LASMPCs have been investigated experimentally. First the specimens were heated above their Tg by using an oven and programmed into a 90º bend angle, followed by natural cooling up to room temperature to fix the shape. Subsequently the specimens were exposed to adequate power densities of 808 nm NIR radiation and recovery angles were video recorded by using a Nikon D3400 DSLR camera (frame size: 1920 x 1080, frame rate: 60P). Furthermore, the recovery angles were measured using the Gwyddion open source image analysis software package.

4.2.3 Simulation Method

An FEA was carried out to identify the temperature distribution in longitudinal (length wise) and transverse (thickness wise) directions of a carbon fibre/epoxy prepreg based LASMPC specimen (100 x 100 x 1.2 mm^3). The simulation was carried out by using ABAQUS/CAE 2019 software package. Surface heat fluxes with different power densities, i.e., 0.01, 0.5, 1.0, 1.5 and 2.0 W/cm^2 were added onto a 10 mm diameter area on the top surface of a 100 x 100 x 1.2 mm^3 LASMPC specimen. The centre of the heated area was considered as the origin and longitudinal (X direction) and transverse (Z direction) temperature profiles were investigated.

Table 4.2: Orthotropic and temperature dependant material properties of carbon fibre prepreg used for the FEA.

Temperature (°C)	**Density (kg/m^3)**	**Specific heat capacity (J/kg.°C) [229]**	**Thermal conductivity (W/m.°C) [229]**		
			k11	**k22**	**k33**
50	1300	880	7.20	7.20	0.80
100	1300	1040	8.00	8.00	0.86
150	1300	1180	8.70	8.70	0.90
200	1300	1340	9.20	9.20	0.93

The developed model was validated with the experimental findings of CFR prepreg LASMPC. The element type was set as "DC3D4: A 4-node linear heat transfer tetrahedron". Based on the mesh convergence, the element size was set at 1.25 mm. It was assumed that the heat transfer mechanisms from the LASMPCs were due to radiation and convection. For the simulation, the film coefficient was considered to be 30 W/m^2K. Furthermore, hemispherical total emissivity was assumed to be 0.82 [230, 231]. Orthotropic and temperature dependant material properties of carbon fibre prepreg have been assigned as presented in Table 4.2.

4.3 Light Absorbance

The light absorbance ability is one of the most critical factors for LASMPCs' performance. The light absorbance provides an indication of the light wavelengths which can generate the photothermal effect. In order to identify the light absorbance capabilities of the materials, UV-vis-NIR spectroscopy was carried out. Figure 4.3 shows the respective transmittance spectra of the materials from the UV range to the NIR range and Equation 4.1 gives the relation between absorbance (AU) and transmittance (T).

$$AU = 2 - \log_{10} T \tag{4.1}$$

It was revealed that the CFR prepreg had a 0.59 average absorbance throughout the entire wavelength spanning from 200 to 1200 nm. At 808 nm wavelength, the CFR prepreg showed a 0.53 absorbance (AU). As presented in Figure 4.3 (b), both $Nd(TTA)_3Phen$ and $Yb(TTA)_3Phen$ demonstrated absorbance of UV radiation up to 380 nm, visible light from 420 to 490 nm and NIR radiation from 1099 to 1115 nm, which may be attributed to the absorbance of the ligands [159]. The rare earth organic complex of $Yb(TTA)_3Phen$ presented a unique NIR absorbance capability starting at 888 nm and ending at 1063 nm, where the peak was from 940 to 980 nm. The $Nd(TTA)_3Phen$ demonstrated unique absorbance peaks around visible light of 527, 581 and 683 nm, as well as peaks of NIR radiation of 748 and 801 nm. The glass fibres and neat styrene SMP displayed a light absorbance capability in the UV range. However, both glass fibres and neat styrene SMP did not demonstrate a significantly intensive band of light absorbance peaks. Therefore, the addition of $Nd(TTA)_3Phen$ and $Yb(TTA)_3Phen$ into GFR styrene will facilitate a selectively triggered photothermal effect.

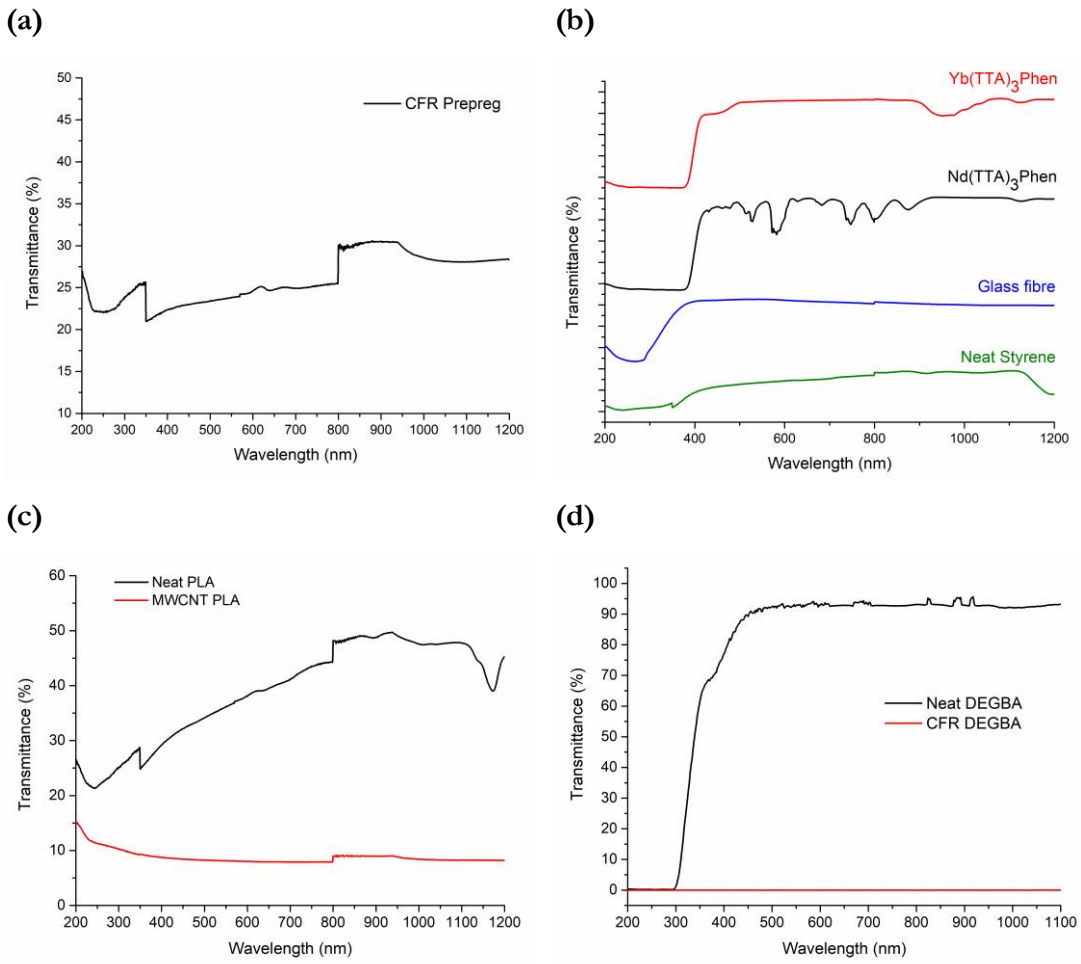

Figure 4.3: UV-Vis-NIR transmittance spectra of the materials (a) Carbon fibre/epoxy prepreg SMP (b) Rare earth organic complexes, glass fibre and styrene SMP (c) Carbon nanotube/polylactic acid SMP (d) Carbon fibre/bisphenol A SMP.

Figure 4.3 (c), shows the UV-Vis-NIR transmittance spectra of the neat PLA and MWCNT PLA SMP materials. At the UV range, the neat PLA showed its highest light absorption (AU = ~0.60). In the visible range, the neat PLA exhibited a decrement in light absorbance with respect to the increase of wavelength (at 400 nm, AU = 0.54 and at 700 nm, AU = 0.39). In the NIR range, the neat PLA showed a low absorbance (AU = ~0.32). However, at a 1172 nm NIR wavelength, neat PLA demonstrated a unique absorbance peak. Compared to the neat PLA, MWCNT PLA displayed greater absorbance throughout the entire tested wavelength range (200 – 1200 nm). In the UV range, MWCNT PLA exhibited an increase in absorbance with respect to the wavelength (at 200 nm, A = 0.82 and at 400 nm, AU = 1.06). In the visible and NIR ranges, MWCNT PLA showed an almost constant light absorbance (AU = ~1.10). As shown in Figure 4.3 (d), the neat DEGBA demonstrated a higher absorbance (AU = ~2.64) up to 298 nm in

the UV range. In the visible and NIR ranges, it displayed a low absorbance (AU = ~0.03). Interestingly, among all the tested materials, the CFR DEGBA demonstrated the highest average absorbance of AU = ~4.74.

In summary, the rare earth organic complexes of $Nd(TTA)_3Phen$ and $Yb(TTA)_3Phen$ respond to UV and selective NIR wavelengths. Carbon-based LASMPCs (carbon fibre and MWCNT) absorb the complete spectrum of light, irrespective of its wavelength. Neat SMPs absorb comparatively more UV light in the spectrum. Compared to UV light, the NIR light spectrum is relatively safer for human bodies and the naked eye [30, 166]. Moreover, UV radiation may result in material degradation and affect the shape memory effect [17]. Therefore, NIR is the most promising range of activation light wavelengths for structural LASMPCs, in that it does not damage the material under intense light irradiation.

4.4 Photothermal Effect

The photothermal effect is a phenomenon which produces thermal energy from electromagnetic radiation [90]. Absorption of electromagnetic radiation causes photoexcitation of the photothermal filler material, which results in a rapid nonequilibrium heating. Once the photothermal fillers are excited with resonant photons, electron–electron scattering results in a rapid increase in the surface temperature of the filler particles. Subsequently, the energy exchange between the electrons and the lattice phonons of the filler material creates an equilibrium. Afterward, the lattice cools down via phonon–phonon coupling, which enables heat dissipation into the surrounding shape memory polymer medium [37, 51]. The photothermal capabilities of the four different material systems were investigated experimentally.

The LASMPCs exposed to light radiation accomplished shape recovery, once heated above their Tg, due to the photothermal effect. The photothermal specimens shown in Table 4.1 were exposed to the 808 nm or 980 nm NIR radiation of a 10 mm diameter circular area. Subsequently, the temperature was recorded by using an FLIR A65 thermal imaging camera. Figure 4.4 (a) describes the coordinates of the recording. The centre of the laser is denoted by "O" and, by considering the centre as the origin XY, Cartesian coordinates are defined. The average temperature of a 3 × 3 pixel area at the origin was

recorded and is presented in Figure 4.4 (b) to (f). It was observed that the temperature at the heating location gradually increased with the increase of power density.

The photothermal behaviour of the CFR prepreg was investigated for five different power densities of 0.01, 0.5, 1.0, 1.5 and 2.0 W/cm^2 of 808 nm NIR radiation, where the samples were subjected to photothermal heating for 120 s. The CFR prepreg was heated over its Tg due to direct exposure to 808 nm near infrared radiation of 1.0 W/cm^2. It was noticed that the origin of the carbon fibre and SMPC specimens were heated up to a particular temperature and remained at a constant temperature throughout the 120 seconds period. This was because of the thermal equilibrium due to the radiation loss of heat from the LASMPC material.

As shown in Figure 4.3 (b), Yb(TTA)$_3$Phen demonstrated a unique absorbance peak from 940 to 980 nm, and Nd(TTA)$_3$Phen had a unique absorbance peak around 801 nm. Accordingly, two NIR laser sources of 808 and 980 nm wavelengths were used to heat the glass fibre reinforced LASMPCs with added Nd(TTA)$_3$Phen and Yb(TTA)$_3$Phen, respectively. Figure 4.4 (c) and (d) illustrate the temperature increment for 300 seconds under three different power densities (1, 2 and 3 W/cm^2) of 808 nm (irradiated to a sample of 1.0Nd GFR Styrene) and 980 nm (irradiated to a sample of 1.0Yb GFR Styrene), respectively. Both samples reached a temperature above Tg, when exposed to a power density of 1 W/cm^2 and the temperature rose with the increase of the power density. Accordingly, the glass fibre reinforced LASMPCs contained rare earth organic complexes-based photothermal fillers were able to activate by selective wavelengths of light. The increment of the power density reduced the time required to reach the Tg. However, due to the slow heat rate, the samples did not show any thermal equilibrium within the first 300 seconds of laser exposure.

The increase of temperature due to the absorbance of 808 nm NIR radiation was investigated for both neat PLA and MWCNT PLA. The samples were exposed to 0.5 W/cm^2 and 1 W/cm^2 laser power and the temperatures were recorded for 60 seconds. These are presented in Figure 4.4 (e). After exposure to 60 seconds of 808 nm laser, the neat PLA reached a temperature of 55 °C under 0.5 W/cm^2 power density and a temperature of 87 °C under 1 W/cm^2 power density. Under similar conditions, MWCNT PLA rose to a temperature of 142 °C under 0.5 W/cm^2 power density and 181 °C under 1 W/cm^2 power density. Both materials can be heated above Tg, by controlling the power density and exposure time. Inclusion of MWCNTs demonstrated an improved

photothermal effect, which enabled heating above the melting temperature (Tm) of the thermoplastic PLA material. However, the temperature values are subject to the specific heat capacity and the mass of the samples.

The neat DEGBA and CFR DEGBA samples were exposed to three power densities: 1.0, 2.0 and 3.0 W/cm^2 of 808 nm NIR radiation. Interestingly, CFR DEGBA showed a significant increase of photothermal heating compared to neat DEGBA exposed to similar power densities. The CFR DEGBA sample exposed to 1 W/cm^2 power density reached its Tg within 59 seconds whereas the neat DEGBA was unable to reach a temperature closer to its Tg after being exposed to 3 W/cm^2 laser power for 60 seconds. The CFR DEGBA exposed to 3 W/cm^2 power density rose to a maximum temperature of 184 ºC in 24 seconds and reached the thermal equilibrium. The reason for this thermal equilibrium is the radiation of electromagnetic waves due to higher energy levels of the electrons.

Table 4.3 compares the photothermal performances of the structural LASMPCs exposed to 1W/cm^2 NIR light. Carbon-based photothermal fillers enabled fast photothermal heating compared to the rare earth organic complexes. Each LASMPC was given a rank depending on the time taken to reach its Tg. Accordingly, MWCNT PLA and CFR Prepreg were ranked as 1 and 2, respectively. Even though the CFR Prepreg obtained rank number two for its photothermal performance, it showed excellent structural properties and thermomechanical characteristics, compared to MWCNT PLA. Therefore, the CFR Prepreg LASMPC was selected for further investigations.

As illustrated in Figure 4.4 (a), once the NIR light was irradiated onto the flat surface of an LACMPC, circular temperature contours can be seen. This could happen due to the similar amount of heat distribution along the X and Y directions. By using the thermal images, heat transfer along the longitudinal direction (along the X axis) was investigated. For this analysis, CFR prepreg material was considered.

Figure 4.5 (a) illustrates the temperature along the X direction after 120 seconds of exposure to 808 nm NIR light, where X zero is the centre of the exposed area (origin). Accordingly, the highest temperature is at the origin and then reduces along the X axis and reaches almost room temperature after 40 mm distance from the origin.

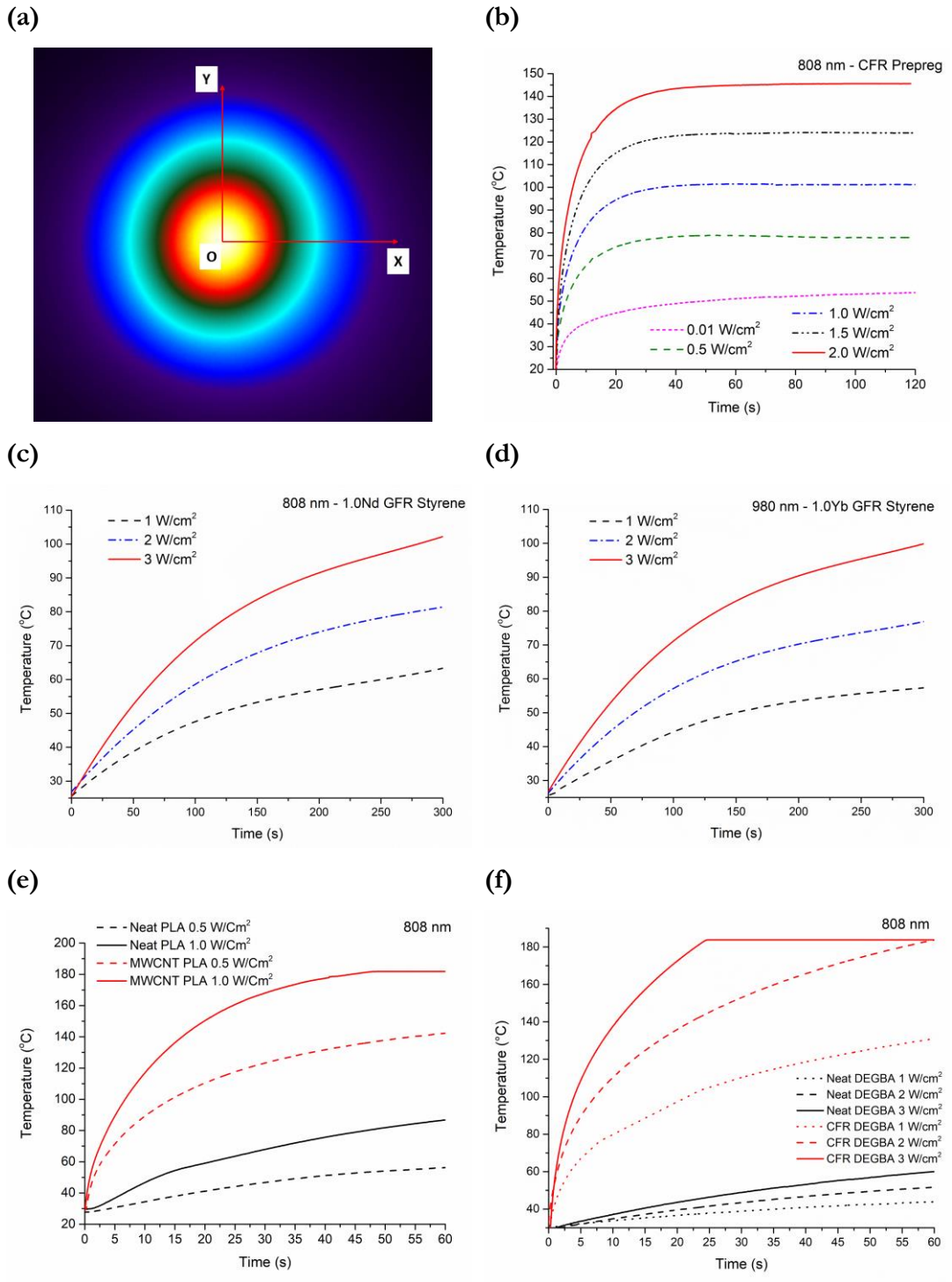

Figure 4.4: Temperature at centre of the laser exposed area over time due to photothermal heating by different power densities of NIR light (a) Cartesian coordinates of the temperature recorded area (b) Carbon fibre/epoxy prepreg SMP exposed to 808 nm NIR light (c) NdTTA$_3$Phen and glass fibre/styrene SMP exposed to 808 nm NIR light (d) YbTTA$_3$Phen and glass fibre/styrene SMP exposed to 980 nm NIR light (e) Carbon nanotube/polylactic acid SMP exposed to 808 nm NIR light (f) Carbon fibre/bisphenol A SMP exposed to 808 nm NIR light.

Table 4.3: Comparison of photothermal performances of the structural LASMPCs exposed to 1W/cm^2 NIR light.

Material (Sample ID)	Exposed light wavelength (nm)	Initial photothermal heat rate (T_{10S}*/10) (°C/seconds)	Time to reach Tg (seconds)	Rank based on the time to reach Tg
CFR Prepreg	808	8.3	9	2
1.0Nd GFR Styrene	808	2.9	82	4
1.0Yb GFR Styrene	980	2.8	128	5
MWCNT PLA	808	11.7	2	1
CFR DEGBA	808	8.0	59	3

* T_{10S}: Temperature (°C) after 10 seconds of 1W/cm^2 NIR exposure

This demonstrates the capability of using NIR light qualitatively and quantitatively for localized activation of LASMPCs. Furthermore, the radius of the area which reaches a temperature above Tg can be controlled by changing the power density of the laser light source. As illustrated in Figure 4.5 (a), when CFR prepreg was exposed to a power density of 1.0, 1.5 and 2.0 W/cm^2, the radius of the area reaching a temperature above Tg increased to 7.5, 10.5 and 12.5 mm, respectively.

Moreover, the localized photothermal heating of a 90º bent CFR prepreg sample due to NIR light was compared with typical hot air heating. The 90º bent specimens were investigated by exposure to NIR radiation of 808 nm wavelength, 2W/cm^2 power density and heated air at 150 ºC, with a 0.5 m^3/min flow rate. Figure 4.5 (b) shows the temperature profiles from the bend location to the free end of the 90º bent samples. In Figure 4.5 (b), 10s NIR and 20s NIR illustrate the localized heating capability of NIR radiation after being exposed for 10 seconds and 20 seconds, respectively. The laser was focused to the bend location where the highest temperature was achieved. However, as illustrated in Figure 4.5 (b), for 20s NIR, the heat flowed to the free end of the specimen with an increase of time.

Comparatively, the carbon fibres have higher thermal conductivity than the polymeric matrices, generally 24.0 W/(m·K) for graphite carbon fibres and 0.17 - 0.79 W/(m·K) for

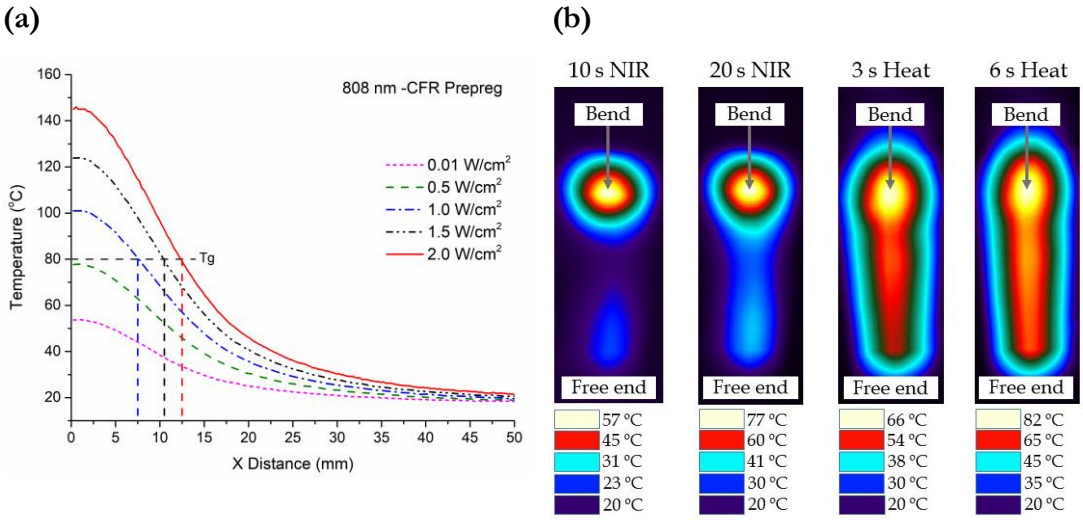

Figure 4.5: Heat transfer behaviour along the surface of CFR prepreg LASMPC (a) Temperature of CFR prepreg along the X axis after being exposed for 120 s of 808 NIR radiation (b) Temperature profiles from the bend location to free end of 90º bent samples (left to right: i) after 10 s exposure to NIR radiation ii) after 20 s exposure to NIR radiation iii) after 3 s exposure to heated air iv) after 6 s exposer to heated air).

epoxy matrices [229]. Therefore, the presence of carbon fibres caused an increase in the temperature throughout the specimens, even though the NIR radiation accomplished localized heating. Figure 4.5 (b), 3s Heat and 6s Heat illustrate the temperature profiles from the bend location to the free end of the CFR prepreg specimens, after being exposed to heated air for 3 seconds and 6 seconds respectively. As per the illustrations, the heated air increased the temperature of the entire surface. However, heating of the free end was non-effective in this case. If the power of the laser is increased, the recovery rate due to NIR radiation will be increased. Therefore, the laser, which requires significantly less power than the heated air, will be the bespoke stimulus for light activated SMPs and its reinforced composites.

In summary, the carbon-based photothermal fillers (carbon fibre and MWCNT) demonstrate higher photothermal performance compared to selectively triggered rare earth organic complexes-based photothermal fillers. The increase of power density enhances the rate of photothermal heating. With irradiation time, these LASMPCs' temperatures reach a maximum and remain constant as the materials reach their equilibrium between energy supply and energy loss.

Moreover, radiation is the most appropriate manner of LASMPC activation in space applications, which are supposed to be operated in a vacuum. In comparison with heat,

light enables the triggering of SMPs in a remote, localized and non-contact manner, independent from the environmental conditions. The use of light to remotely trigger molecular processes inside LASMPCs is advantageous since light can travel a long distance. Moreover, spatially controlled activation is possible as the light beam (often a laser) can be delivered to selected areas. Also, light triggered processes can be halted and resumed on demand by turning them on and off or by controlling the power of the excitation light [232].

4.5 Simulation on Heat Transfer in LASMPCs

A finite element simulation was carried out for carbon fibre prepreg SMP in order to investigate the heat distribution in the material due to photothermal heating. To gain insight into heat transfer in LASMPCs, a detailed finite element analysis on heat transfer was conducted by using the commercial FEA software ABAQUS/CAE 2019. Section 4.2.3 describes the simulation method and the FEA model in detail. Figure 4.6 (a) shows the mesh convergence result. The results show a steady behaviour when the element size becomes lower than 2 mm. Based on the mesh convergence result, a 1.25 mm element size was selected for the FEA simulation.

Figure 4.6 (b) illustrates the top surface and through thickness temperature contours from FEA. The top surface temperature contours shown in Figure 4.6 (b) obtained from the FEA simulation demonstrate circular patterns the same as the experimental results shown in Figure 4.4 (a), obtained by the thermal imaging camera. However, there was a difficulty in measuring the through thickness temperature profiles of a thin specimen (1.2 mm thickness) by using the experimental setup. Advantageously the simulation results provided the necessary understanding on through thickness heat flow, essential for studying the LASMPC activation.

The temperature increase at the centre of the heated area obtained from the simulation is shown in Figure 4.6 (c) and the respective experimental result is presented in Figure 4.4 (b). Just as the experimental findings, the simulation results demonstrated a thermal equilibrium between the energy supply and the energy loss.

Table 4.4 displays the correlation between the experimental and simulation results. Relative to the experimental results, the simulation results exhibit a slight increase ($<$ +1°C) in the temperatures after the material was heated for 120 seconds.

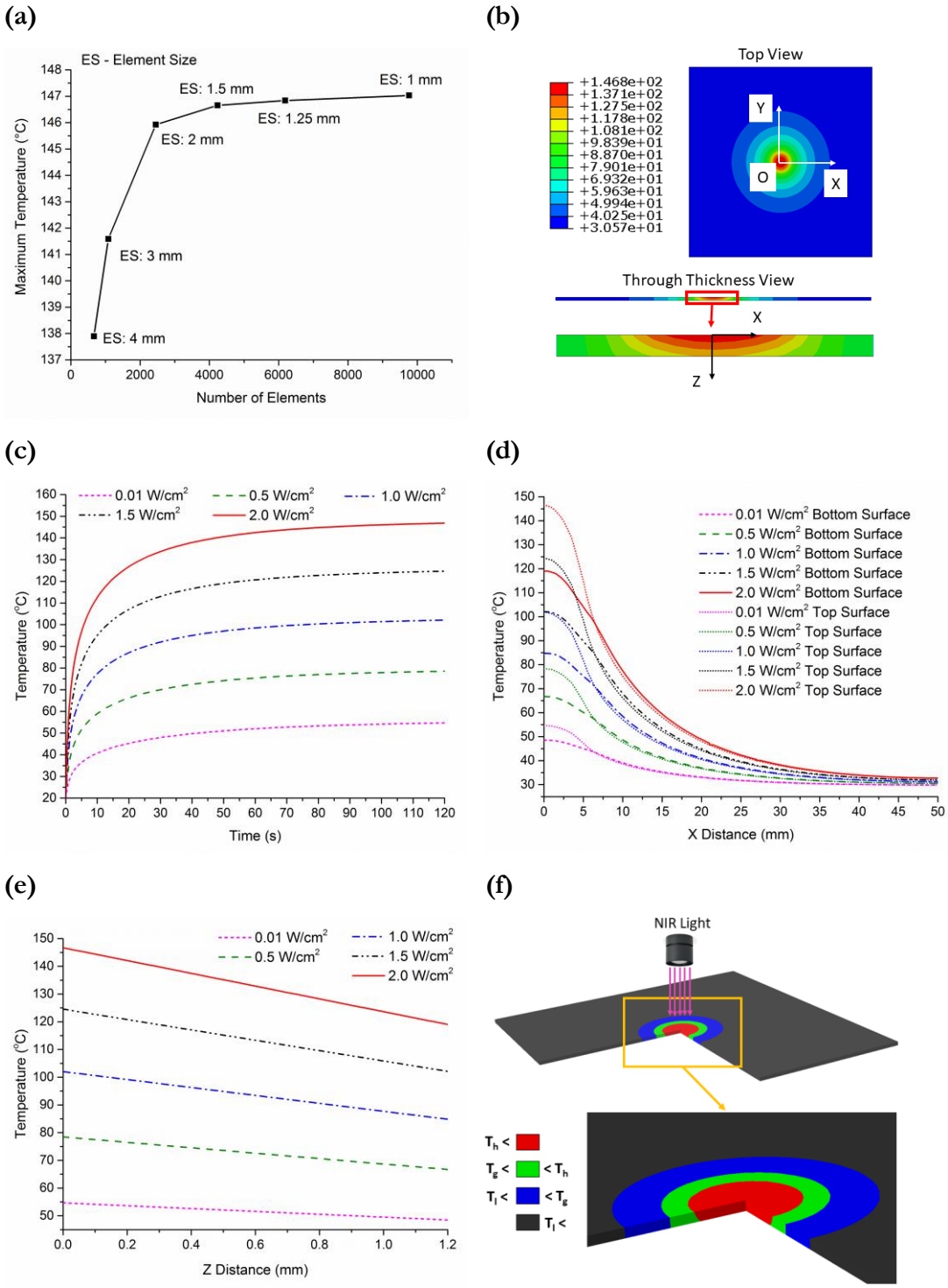

Figure 4.6: Finite element analysis on heat transfer of CFR prepreg (a) Mesh convergence (b) Temperature contours due to 2 W/cm^2 power density (c) Temperature at centre of the heated area over time due to different power densities (d) Temperature of bottom surface along the X axis compared to top surface after being heated for 120 s (e) Through thickness temperature along the Z axis after being heated for 120 s (f) 3D temperature profile due to photothermal heating.

Table 4.4: Correlation between experimental and simulation results.

Power density (W/cm^2)	Temperature at the centre of the top surface, after exposure to 120 seconds of NIR radiation (°C)		Initial photothermal heat rate (T_{10S}*/10) (°C/seconds)	
	Exp†	**Sim‡**	**Exp†**	**Sim‡**
0.01	53.71	54.71	4.0	4.0
0.5	77.93	78.53	6.6	5.9
1.0	101.23	102.11	8.3	7.7
1.5	123.93	124.67	10.0	9.5
2.0	145.74	146.72	11.8	11.3

T_{10S}*: Temperature (°C) after 10 seconds of NIR exposure

Exp†: Experimental result

Sim‡: Simulation result

The difference between the experimental and simulation results on the initial photothermal heat rate was < 0.8 °C/seconds. These minor errors might have been caused due to the total hemispherical emissivity. It has been proved that the ratio of absorptivity (α) to the total hemispherical emissivity (ε) controls the thermal equilibrium [233]. For the simulation, the hemispherical total emissivity was considered to be 0.82 [230, 231]. Moreover, the error values vary with respect to the temperature because the defined material properties were temperature dependant.

Figure 4.6 (d) illustrates the FEA results of the bottom surface temperature compared to the top surface temperature along the X axis. At the centre of the laser exposed area, the top and bottom surface temperatures showed a significant difference. However, along the X axis, the top surface's temperature dropped rapidly than the bottom surface's temperature. As a result, at a particular X coordinate, the top and bottom surface temperatures overlapped. The distance from the centre to the point where the top and bottom surface temperatures overlapped, increased with the irradiated power density.

Figure 4.6 (e) illustrates the through thickness temperature along the Z axis (at the centre of the laser exposed area). The gradient of the through thickness temperature has

increased with respect to the increase of the supplied power density. Just as with the experimental observations, the simulation also proved the localized heating capability of the photothermal effect. The temperature at the laser exposed area showed higher values and dropped rapidly along the distance outwards from this laser exposed area.

Figure 4.6 (f), illustrates a 3D view of the photothermal heating behaviour of a LASMPC upon exposure to an NIR laser beam. Four different temperature contours were drawn to illustrate the regions, i.e., above Th, Tg to Th, Tl to Tg and below Tl. Closer to the centre, the contours were conical and away from the centre, the contours were cylindrical.

4.6 Light Activated Shape Recovery of LASMPCs

The light activated shape recovery performances of carbon fibre and carbon nanotube reinforced LASMPCs were studied experimentally because of their superlative structural performances and photothermal effect, beneficial for engineering applications as discussed in Sections 3.5 and 4.4. Herein, 90° bent specimens were exposed to 808 nm near infrared radiation and the recovery angles were measured over time. Figure 4.7 (a) illustrates the light activated shape recovery steps of the carbon fibre prepreg SMP, showing the initial stage with 90° bend, two intermediate recovery stages and the final stage showing almost full recovery. Furthermore, by means of image processing, the recovery angles of the carbon fibre prepreg SMP specimens exposed to five different power densities (0.01, 0.5, 1.0, 1.5, 2.0 W/cm^2) were measured for 21 seconds with 3 second gaps. These are presented in Figure 4.7 (b).

Accordingly, when exposed to 2.0 W/cm^2 power density, the carbon fibre prepreg SMP specimen started the shape recovery soon after exposure. The time taken to start the shape recovery of the specimens exposed to 1.5, 1.0 and 0.5 W/cm^2 NIR radiation increased with respect to the decrease of power density. The reason for this is the difference in heating rate and time taken to transfer the heat into the bottom layers of the LASMPC.

The CFR Prepreg specimens exposed to 2.0, 1.5, and 1.0 W/cm^2 fully recovered after being exposed to 12, 18 and 21 seconds, respectively, which verifies that the recovery rate depends on the power density. The increment of the power density increases the recovery rate.

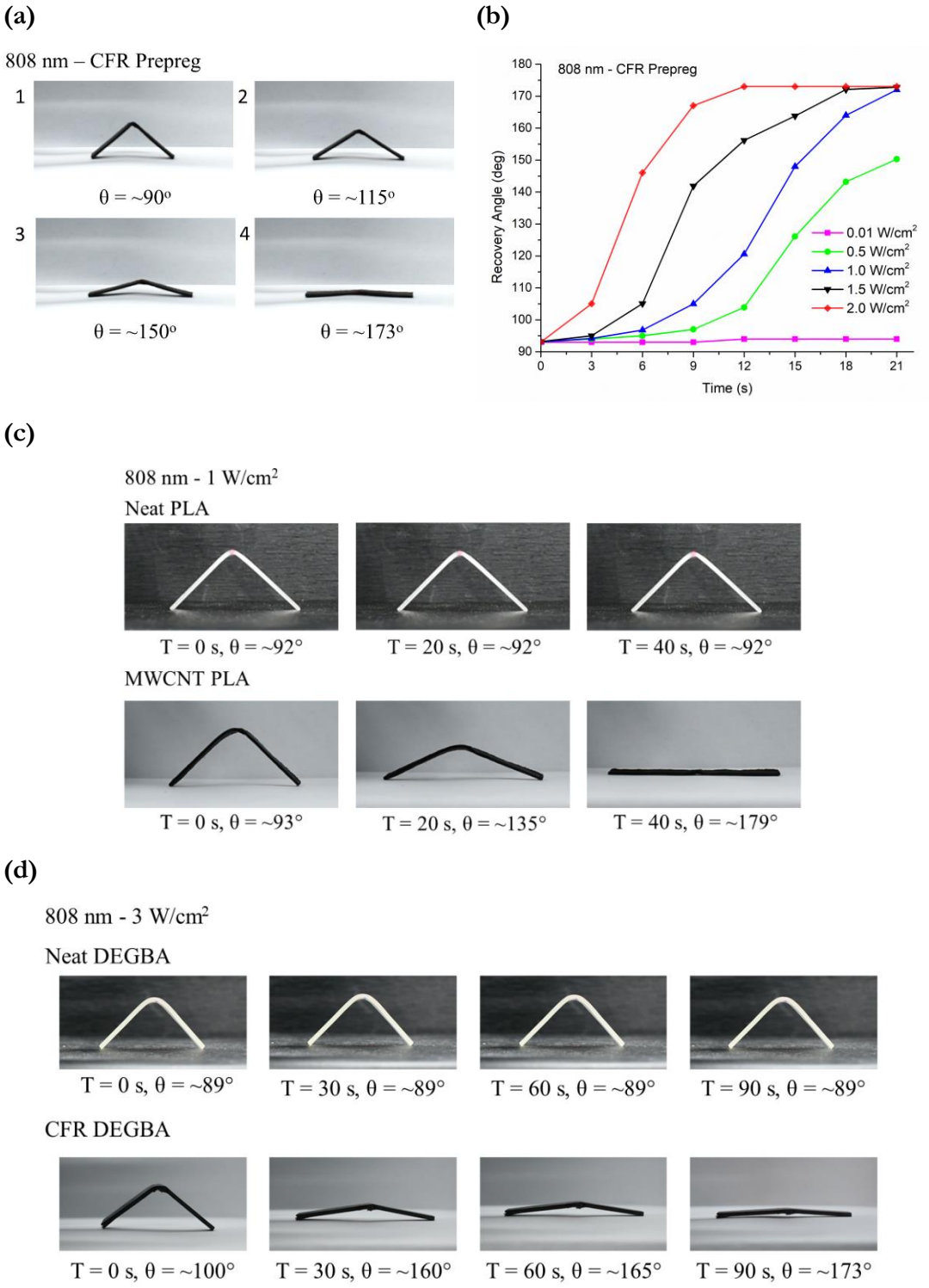

Figure 4.7: 808 nm light activated shape recovery steps of LASMPCs (a) Light activated shape recovery behaviour of CFR prepreg SMP (b) Shape recovery angles versus time for CFR prepreg SMP exposed to five different power densities (c) Shape recovery angles versus time for carbon nanotube/polylactic acid SMP exposed 1 W/cm^2 power density (d) Shape recovery angles versus time for carbon fibre/bisphenol A SMP exposed 3 W/cm^2 power density.

The specimen exposed to 0.5 W/cm^2 reached a 150° recovery angle in 21 seconds. It was noticed that the sample exposed to 0.5 W/cm^2 fully recovered after being exposed to 78 seconds of continued laser radiation. According to Figure 4.4 (b), the specimen exposed to 0.5 W/cm^2 heated up to 78 °C, reached the transition region (T_l-T_h) and was then able to accomplish a shape recovery [13, 225]. As illustrated in Figure 4.4 (b), the specimen exposed to 0.01 W/cm^2 only heated up to 54 °C, which is less than T_l. Therefore, the specimen exposed to 0.01 W/cm^2 did not show any shape recovery behaviour.

The carbon nanotube/polylactic acid SMP specimens were exposed to NIR radiation of 808 nm wavelength with 1 W/cm^2 power density. Respective shape recovery angles were measured, and these are presented in Figure 4.7 (c). Even though the specimens were programmed to a 90° angle, the neat PLA and MWCNT PLA specimens were fixed to 92° and 93° angles, respectively. The neat PLA specimen exposed to NIR radiation did not demonstrate any shape recovery within 40 seconds. However, the MWCNT PLA specimen almost fully recovered within 40 seconds due to the NIR light absorbance.

The carbon fibre/bisphenol A SMP specimens exposed to 3 W/cm^2 power density also showed similar light activated shape recovery behaviours. As illustrated in Figure 4.7 (d), the CFR DEGBA specimen was fixed into a 100° angle although it was programmed in to a 90° angle. After being exposed to 90 seconds of NIR radiation, neat DEGBA did not show any shape recovery behaviour. However, CFR DEGBA recovered up to a 173° angle within 90 seconds, where the original shape was a flat 180°.

According to the UV-vis-NIR spectroscopy results shown in Figure 4.3 (a), (c) and (d), carbon fibre and carbon nanotube filled LASMPCs absorb light irrespective to the exposed wavelength. Accordingly, it is anticipated that the carbon fibre and carbon nanotube incorporated LASMPCs demonstrate similar light activated shape recovery behaviours upon exposure to any of the light wavelengths. However, as presented in Figure 4.7 (b), it is anticipated that the shape recovery ratio and shape recovery rate will depend on the power density of the exposed light.

4.7 Summary

This chapter has presented the investigations concerning the light absorbance and photothermal behaviour of LASMPCs intended for structural engineering applications.

MWCNT PLA LASMPC demonstrated an excellent photothermal capability followed by CFR Prepreg, CFR DEGBA, 1.0Nd GFR Styrene and 1.0Yb GFR Styrene. Glass fibre reinforced LASMPCs containing rare earth organic complexes facilitate selectively triggered the photothermal effect.

Due to its improved structural performance, thermomechanical characteristics and photothermal performance, carbon fibre reinforced prepreg LASMPC was studied comprehensively and isolated for further research. It was found that the increase of power density enhances the rate of photothermal heating and rate of light activated shape recovery. Experimental and simulation results have proven the localized heating capability of LASMPCs due to light irradiation.

The findings on longitudinal and transverse heat transfer will be advantageous to design LASMPC structures. However, it is essential to further understand the behaviour of the carbon fibre reinforced LASMPC materials in the long run within robust operational environments. In addition, there is a necessity to develop an innovative method of light irradiation appropriate for LASMPC structures. Accordingly, an innovative technique of remote activation of LASMPCs via optical fibres is demonstrated in Chapter 5. In addition, Chapter 5 presents the advanced light activation methodologies and case studies of prospective space engineering applications made of reinforced LASMPCs.

Chapter 5

Remote Activation of LASMPCs and Perspective on Space Applications

5.1 Introduction

In Chapters 3 and 4 of this thesis, comprehensively deliberations were presented on the structural, thermomechanical and photothermal behaviour of LASMPC materials. This chapter provides advanced actuation techniques for LASMPC materials and conceptual demonstrations of structural engineering applications.

In general, stimulation is carried out by direct exposure of the LASMPC components to light. However, this limits the use of LASMPC materials to a few specific engineering applications. The recent advances in fibre optic technologies have facilitated the remote activation of light sensitive materials and equipment. Embedded optical fibres have been identified as the best way to remotely activate light activated SMP components [32, 56, 165]. The existing optical fibre light dispersion techniques demonstrate a joule heating of

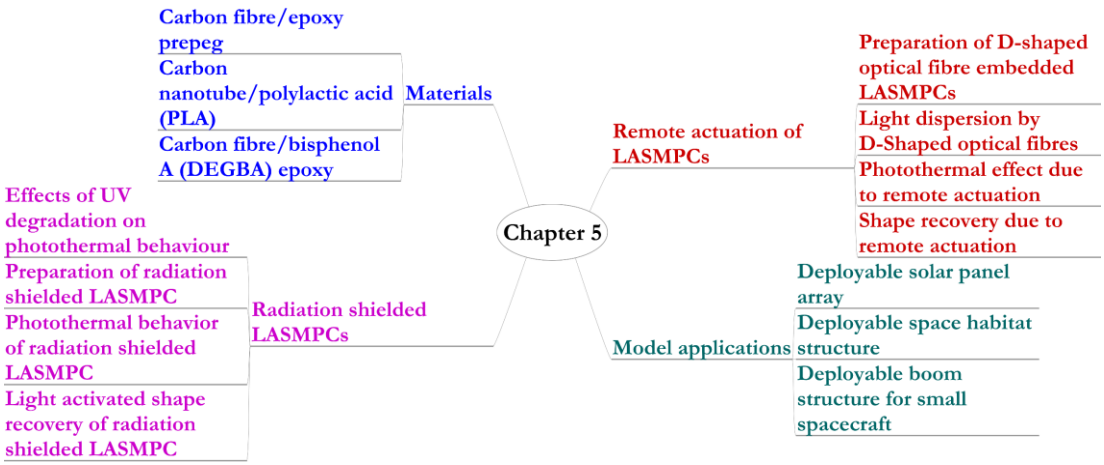

Figure 5.1: Overview of the technical contents of Chapter 5.

a significantly small area of SMP, which limits the scale of applications to miniature component levels.

This chapter presents the capability of innovative D-shaped optical fibres to send and disperse NIR light into an LASMPC, which can generate the adequate photothermal effect necessary for the shape recovery process of relatively large samples. Embedding of a D-shaped optical fibre in an LASMPC creates a single unit smart actuator which can be remotely activated by light. Remotely controllable smart actuators can be located at any difficult to reach positions and controlled safely. This would be a breakthrough technology for biomedical, aerospace and many other challenging engineering applications.

This study is focused on the structural LASMPCs primarily intended for space engineering applications that will be subjected to extreme levels of radiation [16, 17, 19]. Interestingly, in this chapter, LASMPCs shielded from radiation are discussed. One benefit of the shielding of LASMPCs in this way is it may reduce the degradation they may otherwise have due to environmental radiation [16, 17, 19]. Moreover, such shielding can block sunlight and thus impede the unanticipated shape recovery of LASMPC components as they need to be activated on demand.

Ultimately the suitability of the developed LASMPC materials for space engineering applications is demonstrated by using three different scaled working models, namely, a deployable solar panel array, a deployable space habitat structure and a deployable boom structure for small spacecraft.

Figure *5.1* briefly illustrates the flow of the technical content of this chapter. The content of this chapter is presented in the publications J2, J4, J5, C1 and C3 as detailed in the appendix A of this thesis.

5.2 Materials

This chapter presents the remote activation of carbon fibre/epoxy prepreg LASMPC material. Carbon fibre/bisphenol A (DEGBA) epoxy SMP is used to study the effects of UV radiation on photothermal behaviour. A few scaled models of structural engineering applications of LASMPCs are demonstrated by using carbon fibre/epoxy prepreg and carbon nanotube/polylactic acid LASMPC materials. The preparation processes of the LASMPCs have been detailed in Sections 3.2.1, 3.2.3 and 3.2.4.

5.2.1 Preparation of Optical Fibre Coupled LASMPC

Optical fibre embedded LASMPC specimens were prepared to investigate their remote stimulation using NIR light. Unpolished bare optical fibres and side polished D-shaped optical fibres were embedded into carbon fibre/epoxy prepreg based LASMPC samples. The optical fibre patch codes (TECS-clad multimode, step index) with a 400 μm core diameter, 2 m length and a SMA type connector were manufactured by Thorlabs Inc. and supplied by Lastek Pty. Ltd., Australia. The jacket, protective tube and buffer of the optical fibre were removed by a mechanical stripper. A custom made file with diamond lapping polishing sheets on its surface was used to side polish the optical fibre into a D shape for a 20 mm span from the fibre tip, as illustrated in Figure 5.5. The diamond lapping polishing sheets with 6 μm grit were produced by Thorlabs Inc. and supplied by Lastek Pty. Ltd., Australia. The polishing process partially removed the technology enhanced clad silica (TECS) hard polymer cladding and the silica core for a 20 mm length from the tip of the fibre. For complete scientific understanding, both D-shaped polished and unpolished fibres were embedded in carbon fibre prepreg LASMPCs. These polished and unpolished fibres were placed in between layers 2 and 3 of the four-layer LASMPC specimens (30 x 30 x 1.2 mm^3). The prepreg sheets, along with the optical fibre, were cured as per the procedure described in Section 3.2.1.

5.2.2 Preparation of Radiation Shielded LASMPC

A radiation shielded LASMPC was prepared by covering the carbon fibre/epoxy prepreg LASMPC sheets with a metalized polyamide polymer laminated glass cloth. The protective cloth "DEI Reflect-A-GOLD™ – Heat Reflective Tape (2"x 15') was supplied by TAS Autosport, Australia. It was a tape together with high temperature pressure sensitive adhesive to use in environments with extreme temperature swings. According to the manufacturer, the tape withstands temperatures up to 427 °C, resists UV degradation for long term performance, is 0.1651 mm thick and the adhesive is protected by a release liner rated to withstand up to 163 °C. The carbon fibre/epoxy prepreg LASMPC specimens were prepared as described in Section 3.2.1.1. Subsequently the specimens were covered by using the tape as showed in Figure 5.2. Due to the practical difficulties in shape programming, the test specimens for light activated shape recovery experiments were first programmed into a 90° bend angle and then shielded.

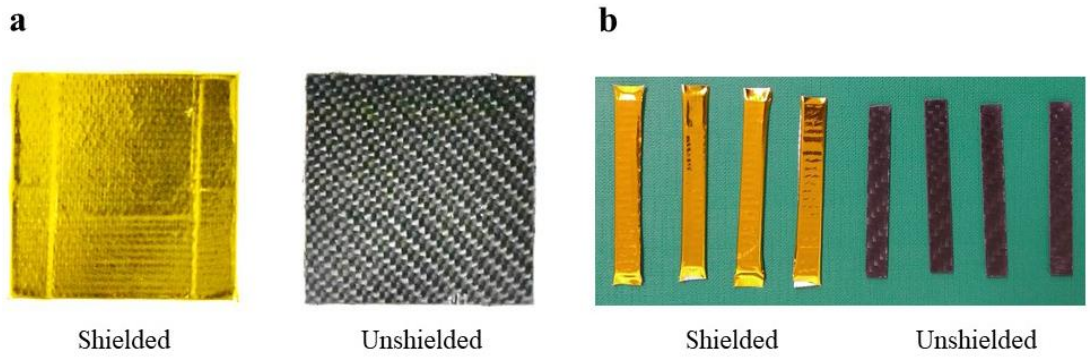

Figure 5.2: Radiation shielded and unshielded LASMPC specimens (a) 100 x 100 x 1.2 mm^3 specimens for photothermal heating experiment (b) 60 x 8 x 1.2 mm^3 specimens for light activated shape recovery experiment.

5.2.3 Preparation of Model LASMPC Applications

In order to demonstrate the applicability of the proposed LASMPCs, a few scaled models were developed. As illustrated in Figure 5.3 (a), a model of a deployable solar panel array was fabricated by using four Sanyo amorphous solar cell photovoltaic solar panels (58.1 × 48.6 × 1.3 mm) supplied by RS Components, Australia. These solar panels were coupled and held by carbon fibre/epoxy prepreg LASMPC made structural members (50 × 10 × 1.2 mm).

Figure 5.3 (c), presents a model of a cube shaped deployable structure that was fabricated by using 12 carbon fibre/epoxy prepreg LASMPC strips with a 6 mm width and 1.2 mm thickness. The strips were cut into 65 mm lengths and joined together using Selleys Ultra Repair temperature resistant adhesive. Moreover, by following the same 4D printing manufacturing procedure presented in, Section 3.2.3, deployable boom structure models were fabricated. Figure 5.3 (c) shows the 3D CAD model of the fabricated boom structures. Note that all dimensions in Figure 5.3 are in millimetres.

5.3 Experimental and Simulation Methods

5.3.1 Evaluation of Optical Fibre Coupled LASMPC

The quality of the optical fibre polishing process was studied by using a Jeol benchtop scanning electron microscope (JCM-6000 SEM). The samples were gold coated before the SEM investigations. Moreover, a laser torch was connected to the SMA type

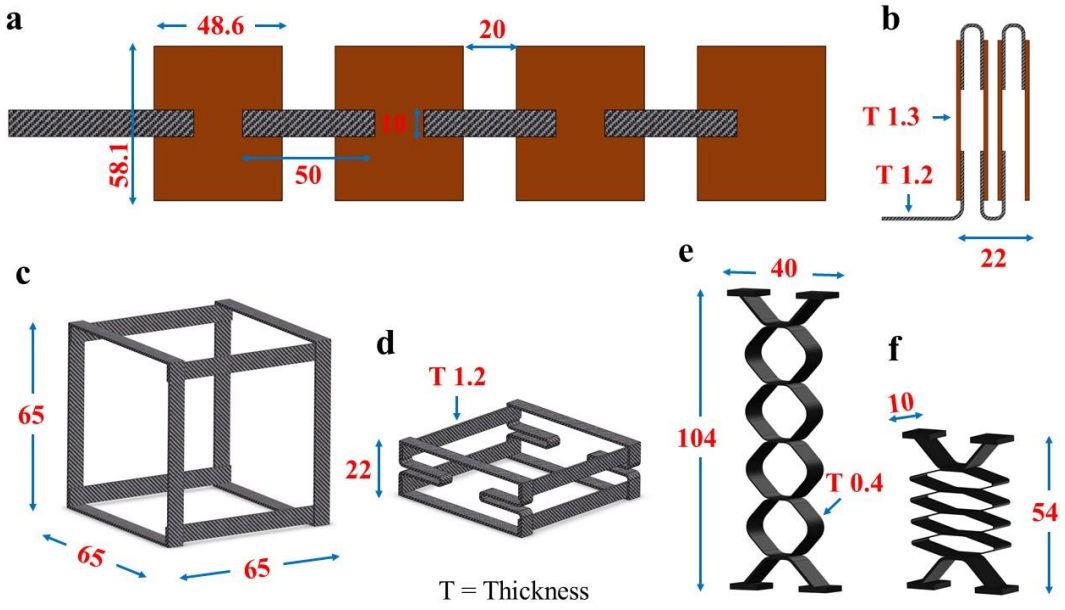

Figure 5.3: Computer aided drawings of the model LASMPC applications (all dimensions are in millimetres) (a) Original shape (bottom view) of the deployable solar panel array (b) Programmed shape (side view) of the deployable solar panel array (c) Original shape of the deployable space habitat structure (d) Programmed shape of the deployable space habitat structure (e) Original shape of the deployable boom structure (f) Programmed shape of the deployable boom structure.

connector and red light dispersion from the polished and unpolished fibres was captured by a Nikon D3400 DSLR camera (frame size: 1920 x 1080, frame rate: 60P).

In order to study the photothermal and shape recovery behaviours of the LASMPC samples (30 x 30 x 1 mm^3), an 808 nm NIR laser source was connected to the SMA connector and light was sent into the material. The 808 nm, 20 W laser source and a lab adjustable power supply were supplied by CivilLaser, China. The laser source and the LASMPC samples were placed inside the same tailor made optical encloser showed in Chapter 4 (Figure 2). The optical fibre coupled LASMPC connected to the laser source is shown in Figure 5.4 (a). The power of the NIR radiation was controlled by the lab adjustable power supply. The respective temperature variations were captured by an FLIR A65 thermal imaging camera. The LASMPC sample was programmed into a 90° bend along the embedded fibre line. The light activated shape recovery behaviour due to 808 nm 1.5 W NIR radiation was video captured by a Nikon D3400 DSLR camera (frame size: 1920 x 1080, frame rate: 60P) and the respective shape fixing and recovery angles were determined by means of image processing.

Moreover, FEA was carried out to simulate the temperature distribution in the longitudinal (length wise) and transverse (thickness wise) directions of a 30 x 30 x 1 mm^3 LASMPC specimens coupled to optical fibres. The ABAQUS/CAE 2019 software package was used for the simulation and the simulation procedure and the model have been described in Section 4.2.3 of this thesis. Both unpolished and D-shaped polished cases were simulated. Based on the light dispersion of two different approaches unpolished and D-shaped polished, a power of 0.5 W was assigned in each case.

5.3.2 Evaluation of the Effects of UV Radiation

Neat DEGBA and CFR DEGBA specimens (100 x 100 x 2 mm^3) were exposed to 1000 hrs of UV radiation. SUNTEST XLS equipment from ATLAS Material Testing Solutions was used to provide the UV light irradiance. The irradiated UV wavelength was in the range of 325 to 400 nm. The intensity of the UV radiation inside the chamber was 750 W/cm^2. Samples were evenly distributed inside the chamber at equal distance from the UV source to ensure similar exposure. The chamber was equipped with a 2.2 kVA air-cooled Xenon-lamp, and the exposure was done in an ambient atmosphere where the temperature was varied between 22 and 24 °C, with a relative humidity between 30 and 50%. Subsequently, the photothermal behaviour of the UV exposed and unexposed samples were tested according to the procedure described in Section 4.2.2.

5.3.3 Evaluation of the Radiation Shielded LASMPC

The photothermal effect of the shielded carbon fibre/epoxy prepreg LASMPC was compared with the unshielded LASMPC. Accordingly, 808 nm 2 W/cm^2 NIR radiation was irradiated onto a flat surface of the specimen (100 x 100 x 1.2 mm^3) and the temperature increase of the opposite surface was recorded by an FLIR A65 thermal imaging camera. The experimental setup is shown in Figure 5.4 (b). In the case of the shielded LASMPC, only the laser irradiated surface was protected with the metalized polyamide polymer laminated glass cloth, and its temperature monitored opposite surface was retained uncovered. Moreover, 808 nm 2 W/cm^2 NIR radiation was irradiated onto a fully shielded LASMPC specimen (60 x 8 x 1.2 mm^3) and the respective shape recovery behaviour was video recorded. With the aid of image processing, the shape recovery rate was measured. The respective experimental procedure has been described in Section 4.2.2.

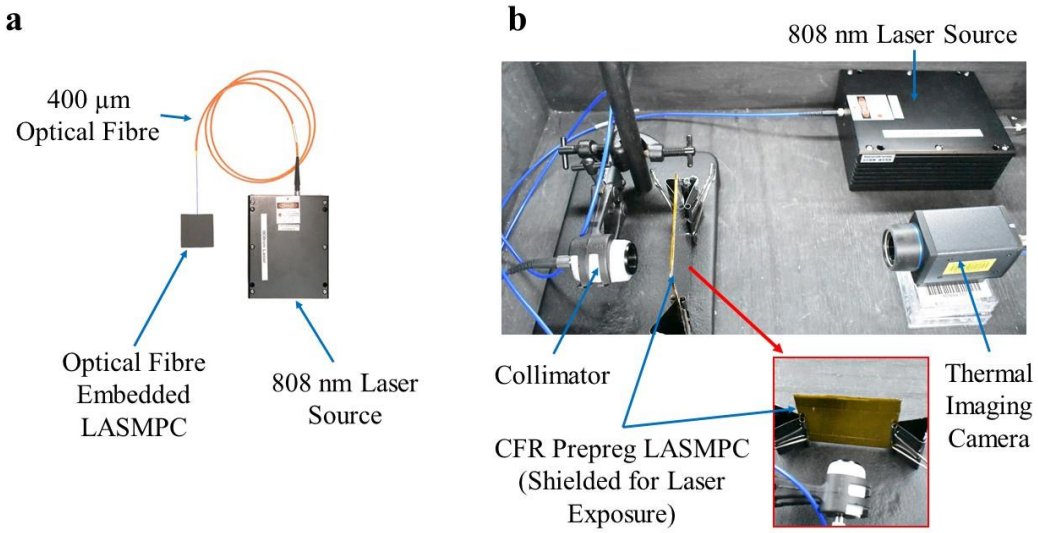

Figure 5.4: Experimental setups (a) Optical fibre coupled LASMPC connected to the laser source (b) Photothermal test setup for radiation shielded LASMPC.

5.3.4 Evaluation of the Scaled Models

Initially, the scaled models made of LASMPCs, namely, i) deployable solar panel array, ii) deployable space habitat structure and iii) deployable boom structure, described in Section 5.2.3, were programmed into the compact shapes shown in Figure 5.3 (b), (d) and (f), respectively. The deployable solar panel array was recovered into its fully expanded shape through four steps of localized NIR irradiation onto each bend location (under 808 nm, 2 W/cm^2 exposure). The deployable space habitat structure was kept in an oven at 130 ºC under 80 kPa vacuum and shape recovery was video recorded. In the same way, the shape recovery behaviour of the deployable boom structure was investigated at 80 °C under 80 kPa vacuum conditions. It was assumed that the deployable space habitat structure and the deployable boom structure could absorb sunlight in space and the entire structure would be heated homogenously, as happened in the vacuum oven.

5.4 Remote Actuation of LASMPCs

The ability of D-shaped optical fibres to remotely control the shape memory actuation of LASMPCs was proved. Figure 5.5 shows the proposed technique of remotely controlling

SMP actuation via D-shaped optical fibres. The performance of the D-shaped polished fibres was compared with that of the unpolished bare fibres.

5.4.1 Performance of D-shaped Optical Fibres

The quality of the polishing process was investigated through SEM. Light dispersion capabilities of the fibres were studied by means of red light dispersion. Photothermal capabilities were studied by means of joule heating of the LASMPC due to NIR light. D-shaped polished and unpolished fibres were compared in each case. The results are presented in Figure 5.6. As shown in Figure 5.6 (a) the unpolished fibre had a 425 μm diameter, including the hard polymer cladding (the fibre core diameter was 400 μm). The TECS cladding and the silica core were partially removed by using 6 μm grit diamond lapping polishing sheets. As shown in Figure 5.6 (b), the width of the formed polished silica core surface was measured as 310 μm. The removed silica core material turned into dust particles and the removed cladding material turned into continuous chips during the polishing process. However, cleaning with wet wipes removed all debris resulting from the polishing of the fibre.

Once the red laser light was sent through the unpolished fibre, the light was dispersed into a concentrated spot at the fibre tip, whereas the polished D-shaped fibre dispersed

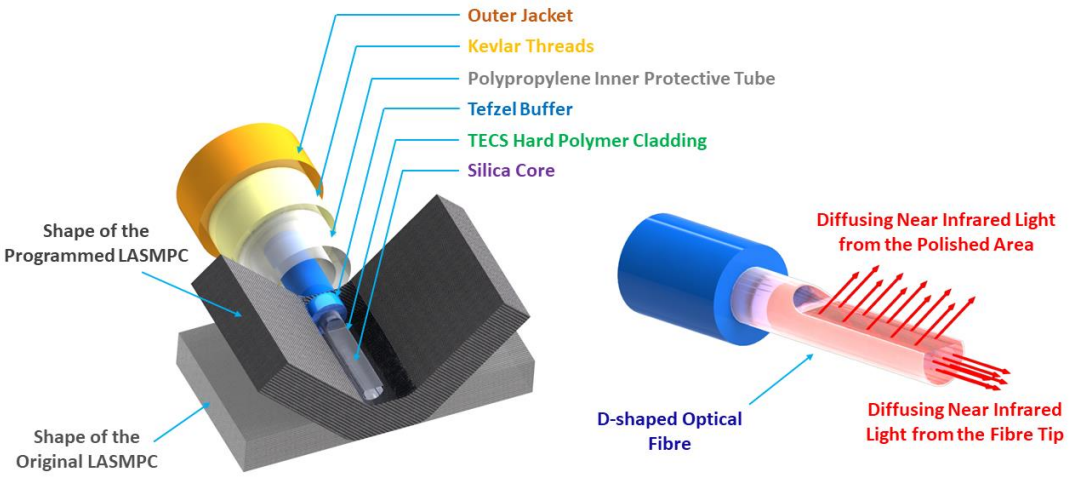

Figure 5.5: The proposed technique of remote controlled SMP actuation via D-shaped optical fibres. Design of the optical fibre embedded carbon fibre reinforced LASMPC and the anticipated light dispersion behaviour.

the red light through the polished area, as shown in Figure 5.6 (c) and (d), respectively. As illustrated in Figure 5.6 (e), 808 nm, 0.5 W NIR radiation was dispersed into the LASMPC through an unpolished fibre, which generated a maximum temperature of 153 °C at the fibre tip where the temperature contours are shown as circular. As illustrated in Figure 5.6 (f), the same amount of radiation generated nearly elliptical temperature contours and a maximum temperature of 117 °C along the D-shaped fibre line, which can activate a larger portion of the LASMPC.

As illustrated in Figure 5.7, the top view temperature profiles obtained from the FEA also demonstrated similar temperature contours. In addition, the through thickness temperature along the optical fibre was simulated for both unpolished and D-shaped polished fibres, as presented in Figure 5.7 (a) and (b), respectively. It has been reported that a relatively long time is needed for an LASMPC to reach its Tg as the thickness of the specimen increases, which allows a slower shape recovery behaviour [37]. One of the reasons for such behaviour is the rise in heat capacity as the volume of the sample increases. Moreover, with the increase of thickness, the thermal conduction in the transverse direction becomes slower.

According to the Beer–Lambert law, the light absorption of a specimen depends on three variables: extinction coefficient, path length and concentration of the substance. Usually light is irradiated onto the LASMPCs in a transverse direction and therefore the path length increases with the thickness of the sample [37]. Eventually, the increase of path length towards the light incident direction will enhance the photothermal effect.

The D-shaped optical fibres can disperse light into the LASMPC specimens either in longitudinal or transverse directions, as per the orientation of the fibre placement in the LASMPC. In this work, the D-shaped optical fibres were oriented in such a way that the light was dispersed upward. The simulation showed that the temperature increase due to photothermal heating was higher towards the light incident direction. Accordingly, the top half of the LASMPC reached higher temperatures compared to the bottom half. However, the heat transfers in the longitudinal and transverse directions allow the LASMPCs to reach its Tg.

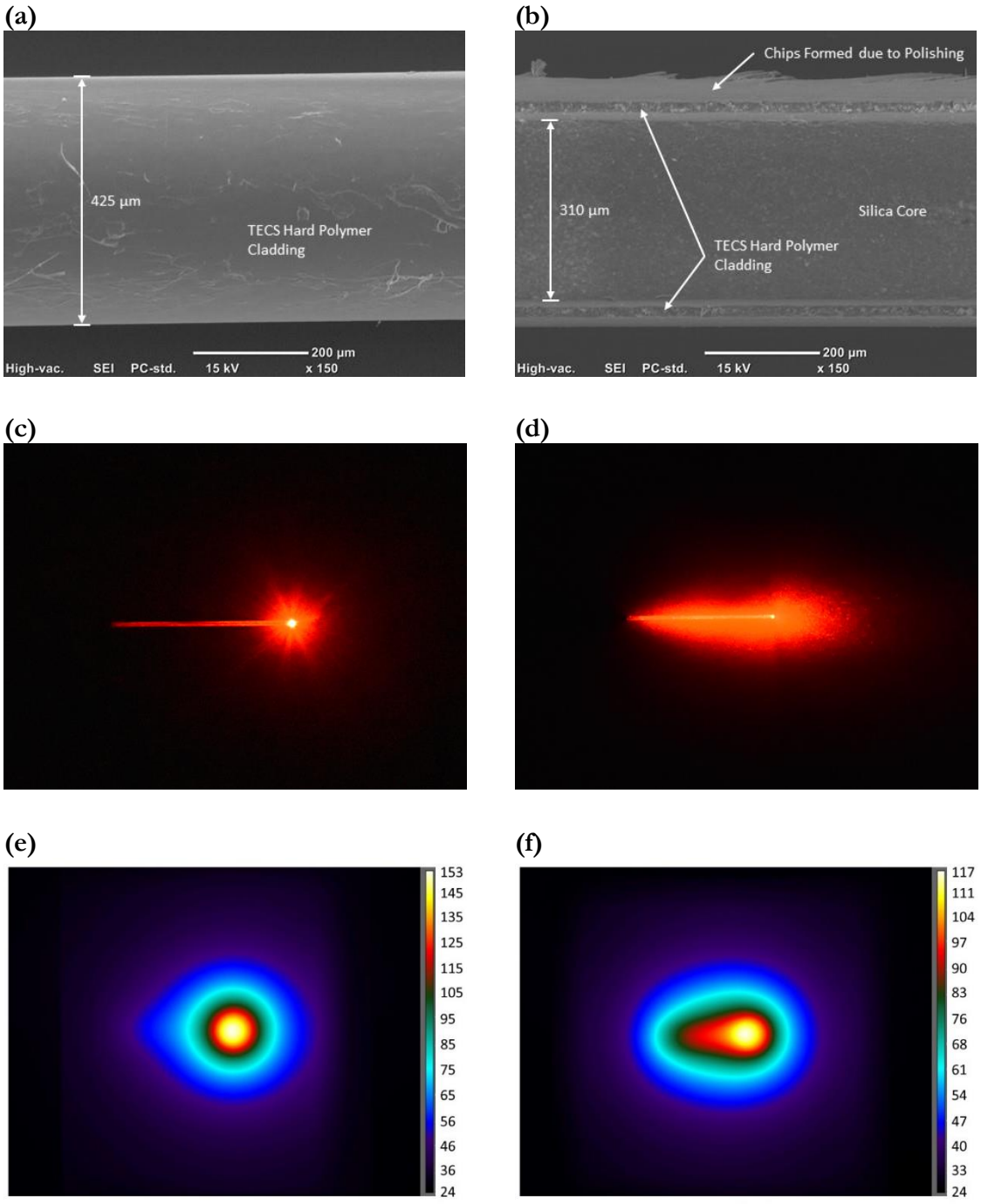

Figure 5.6: Comparison between unpolished and D-shaped side polished fibres. (a) SEM of unpolished fibre (b) SEM of D-shaped polished fibre (c) Red light dispersion by a 20 mm span of an unpolished bare fibre. (d) Red light dispersion by a 20 mm span of a D-shaped polished fibre. (e) Photothermal heating behaviour due to 300 seconds exposure of 0.5 W, 808 nm NIR radiation by an unpolished fibre embedded LASMPC (f) Photothermal heating behaviour due to 300 seconds exposure of 0.5 W, 808 nm NIR radiation by a D-shaped polished fibre embedded LASMPC.

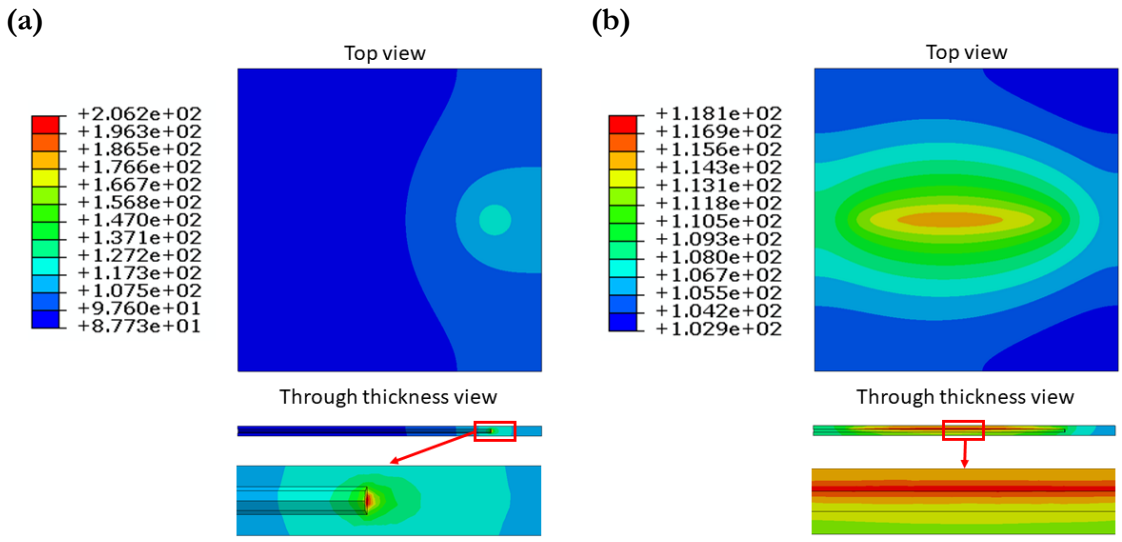

Figure 5.7: Temperature (°C) profiles obtained from the finite element analysis on longitudinal and transverse directions due to photothermal heating for 300 seconds. (a) Unpolished fibre (b) D-shaped polished fibre.

5.4.2 Remote Actuation via D-Shaped Optical Fibres

As showed in Figure 5.5, the D-shaped fibre was embedded into the LASMPC in such a way that the polished surface remained parallel to the top surface of the LASMPC. It was anticipated that most of the NIR light sent through the fibre would disperse outwards through the polished area and the rest of the light would disperse through the fibre tip. Accordingly, the LASMPC could be programmed into a 90° bend along the line of the optical fibre as this did not damage the optical fibre during the shape programming. When the NIR light was sent through the optical fibre, the light was dispersed through the D-shaped area into the programmed LASMPC to generate the adequate photothermal heat for shape recovery.

It is proved that the light transmitted through an embedded D-shaped optical fibre can facilitate the shape recovery of a 30 x 30 x 1.2 mm^3 LASMPC. The LASMPC sample was programmed into a 90° bend along the embedded fibre line. Due to the spring back effect, the shape was not fixed at the 90° bend angle, but the sprung back sample was fixed to a 103° bend angle.

Figure 5.8 (a) illustrates the sequence of the shape recovery when the programmed sample received 1.5 W of 808 nm NIR radiation through the embedded D-shaped optical fibre. Within the first 120 seconds, the LASMPC sample showed a fast recovery. At 180

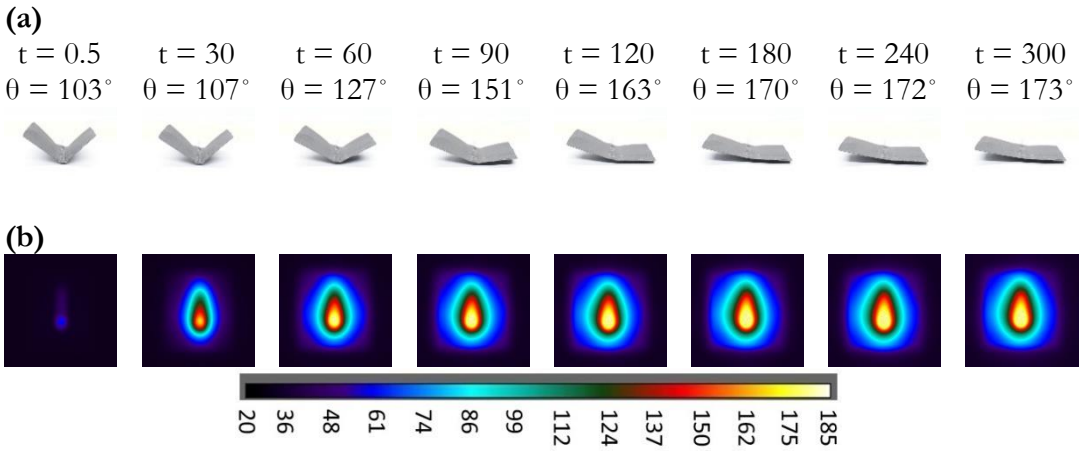

Figure 5.8: Sequence of the LASMPC shape recovery trigged by a 400 μm embedded D-shaped side polished optical fibre. 30 x 30 x 1.2 mm^3 sample exposed to 1.5 W of 808 nm NIR radiation. (a) Front view image captures respective recovery angles against exposure time. (b) Top view thermographic captures respective photothermal behaviour against time.

seconds, the sample reached 173°. However, the original shape was a flat, i.e., 180° angle. The sequence of the photothermal behaviour is shown in Figure 5.8 (b). Subsequent thermographic investigations showed that the D-shaped fibres were capable of transmitting the required amount of radiation to perform a shape recovery.

Figure 5.9 provides the temperature along the axis of the embedded fibre. It was revealed that, with the exposure to 1.5 W of 808 nm NIR radiation, the LASMPC begins to heat along the polished fibre length from 5 mm to 25 mm. In the first 60 seconds the temperature showed a rapid increase and thereafter a progressive increase to a maximum of 180 °C. At 180 °C, the material reached thermal equilibrium. After 60 seconds, the entire bent length of the LASMPC sample reached a temperature above 60 °C, which is the lower limit of the glass transition region (T_l), presented in Table 3.5 of this thesis. At 300 seconds, the entire bent length of the LASMPC sample reached its Tg which is 76 °C.

As described in Chapter 3, the glassy to rubbery phase transition of the LASMPC occurs while the temperature increases from 60 to 100 °C. At this stage, the recovery stresses generated in the LASMPC were adequate to achieve shape recovery. Based on the angle measurements, shape fixity and recovery ratios were calculated as 85.6 % and 92.2 %, respectively [226, 234]. Though the carbon fibre/epoxy prepreg SMP demonstrated an excellent shape fixity ratio, a slight drop in shape fixity was observed. The effects of the

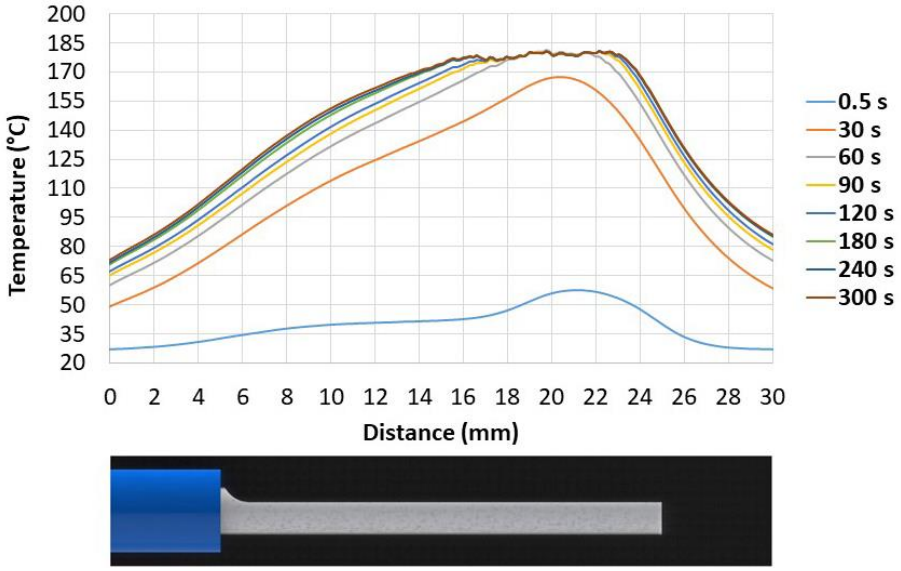

Figure 5.9: Temperature increment with time and respective cross-section along the embedded D-shaped optical fibre. 0 - 5 mm Tefzel buffer, 5 - 25 mm D-shaped bare fibre and 25 - 30 mm without optical fibre.

embedded optical fibre that aligned with the shape programming line may have caused this discrepancy.

5.5 Radiation Shielded LASMPCs

5.5.1 Effects of UV Degradation on Photothermal Behaviour

Exposure to UV radiation affects the shape fixity, shape recovery, storage modulus, Tg and mechanical properties of SMPs [17-19]. Figure 5.10 presents the effects of UV radiation on the photothermal behaviour of carbon fibre/bisphenol A (DEGBA) epoxy based LASMPC. Neat DEGBA and CFR DEGBA samples exposed to 1000 hours of UV radiation were tested and compared with the samples unexposed to UV. The neat samples were used in order to identify the unique UV radiation effects on polymer matrix materials.

As shown in Figure 5.10 (a), the UV exposed neat DEGBA samples showed a higher photothermal efficiency than the samples unexposed to UV. The reason for such behaviour might be the change of the chemical structure due photochemical degradation [235]. The UV degradation of polymers causes the colour changes of the samples [17, 18]. As usual the UV exposed neat DEGBA specimens turned yellow, while the unexposed samples remained transparent.

Accordingly, the UV exposed neat DEGBA samples might have shown a higher photothermal efficiency as the UV degradation enhanced the light absorbance in the visible and NIR regions [18]. Moreover, the photothermal efficiency of the UV degraded neat DEGBA samples increased with respect to the irradiated power density of the NIR light. For example, after 60 seconds of photothermal heating, the temperature differences between the UV exposed and unexposed samples were measured as 3, 5 and 9 °C for the specimens subjected to 1, 2 and 3 W/cm^2 power densities of NIR radiation, respectively.

Figure 5.10 (b) shows the photothermal behaviour of CFR DEGBA. The yellowing of CFR DEDBA samples exposed to UV was not as clear as that of the neat DEGBA because of its black colour carbon fibre reinforcements. In the case of CFR DEGBA, the primary light absorbing material was carbon fibres. Because of this, Figure 5.10 (b) illustrates no significant difference between the UV exposed and unexposed samples. This indicates that UV degradation did not show any significant effect on the photothermal behaviour of CFR DEGBA as that of yellowed neat DEGBA. However, the LASMPCs materials having higher photothermal efficiency need to be protected from UV degradation, as it affects mechanical properties and shape memory characteristics [17-19].

5.5.2 Performance of the Radiation Shielded LASMPC

The LASMPC structures intended for space engineering applications will be exposed to excessive amounts of radiation. LASMPC materials are designed to absorb light energy to generate the heat required for shape recovery. Certain LASMPC applications are designed to be activated upon exposure to sunlight in space. However, due to radiation in space, LASMPC materials can be subjected to excessive amounts of heating. Such heating can activate the shape recovery process in an unexpected manner, whereas the shape recovery is required to occur only on demand. In contrast, in shaded space environments, LASMPCs can lose their heat due to radiation from the material to dark space. Therefore, heating of LASMPCs by an external light source could be difficult.

Shielding of LASMPCs from radiation will reduce these limitations. In general, the current use of multilayer insulations accomplish two basic requirements: i) reflect solar radiation back into space and keep the instruments cool enough to operate while in sunlight; ii) maintain internal temperatures at a reasonable level and protect the instruments from the

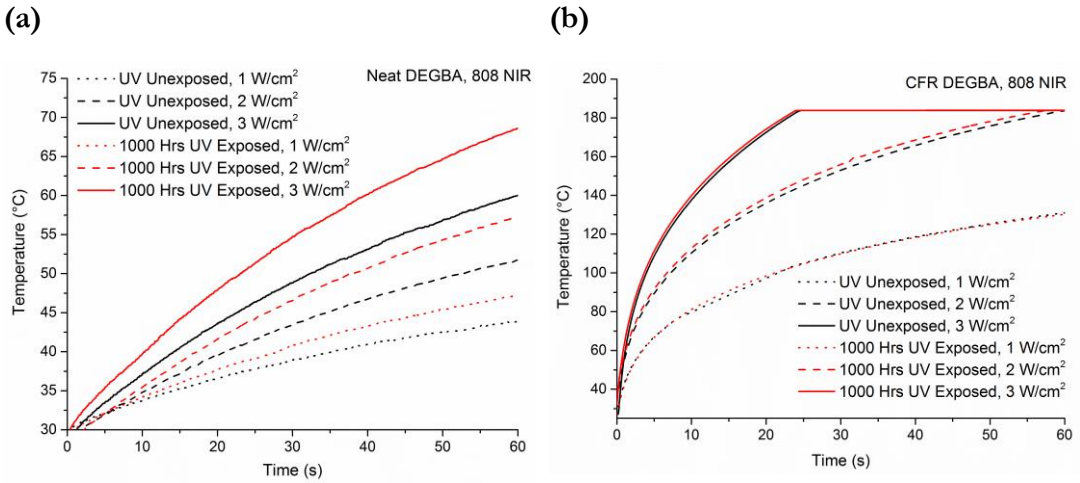

Figure 5.10: Photothermal behaviour due to 1, 2 and 3 W/cm^2 power density, 808 nm NIR light. Comparison between 1000 hrs UV exposed specimens and UV unexposed specimens (a) Neat DEGBA (b) CFR DEGBA.

extreme cold when the spacecraft moves through dark space (shaded locations) [236-238]. This study explicates the necessity of radiation protection for LASMPCs and the shape memory behaviour of shielded LASMPCs that are design for space applications. The admissible experimentation was conducted in a controlled terrestrial atmosphere.

Figure 5.11 presents a comparison between the shielded and unshielded CFR prepreg LASMPC concerning their photothermal and light activated shape recovery behaviour. Figure 5.11 (a) and (b) illustrate the temperature profiles at the centre and along the X axis of the samples due to photothermal heating by 808 nm 2 W/cm^2 NIR radiation, respectively. The temperature was measured on the opposite surface of the laser exposed surface. Accordingly, the measured temperature increase was due to the heat transfer in the transverse direction (through thickness).

As a result there was a few seconds of delay to the increase in temperature shown in Figure 5.11 (a) (the laser was switched on at 0 seconds). The centre temperature of the unshielded CFR prepreg LASMPC reached its lower limit of glass transition region (60 °C) within 8 seconds. However, the shielded LASMPC only reached a temperature of 53 °C after being exposed to 60 seconds of NIR radiation. As shown in Figure 5.11 (b), after being exposed to 60 seconds of NIR radiation, the temperature of the centre (X = 0) reached the uppermost value and gradually decreased along the X axis. Up to 21 mm distance from the centre, the unshielded LASMPC showed a higher temperature than the

shielded one. Above 21 mm distance from the centre both specimens were at room temperature (~25 °C).

As described in Chapter 4, carbon fibres absorb light in the entire range of wavelength from UV to NIR. Therefore, the light activated shape recovery of carbon fibre reinforced LASMPCs primarily depends on the power density of the irradiated light. The mean solar irradiance at the planets of Mercury, Venus, Earth, Mars and Jupiter are predicted as 0.91164, 0.2611, 0.13661, 0.05886 and 0.00505 W/cm^2, respectively [239]. Mercury receives the most intense solar radiation than any other planets in our solar system. The intensity of the irradiated light onto the LASMPCs (2 W/cm^2) is more than twice the intensity of the light that Mercury receives (0.91164 W/cm^2).

Figure 5.11 (c) shows the shape recovery behaviour of 90° bent LASMPC specimens. The unshielded specimen almost fully recovered within 12 seconds of 808 nm 2 W/cm^2 NIR

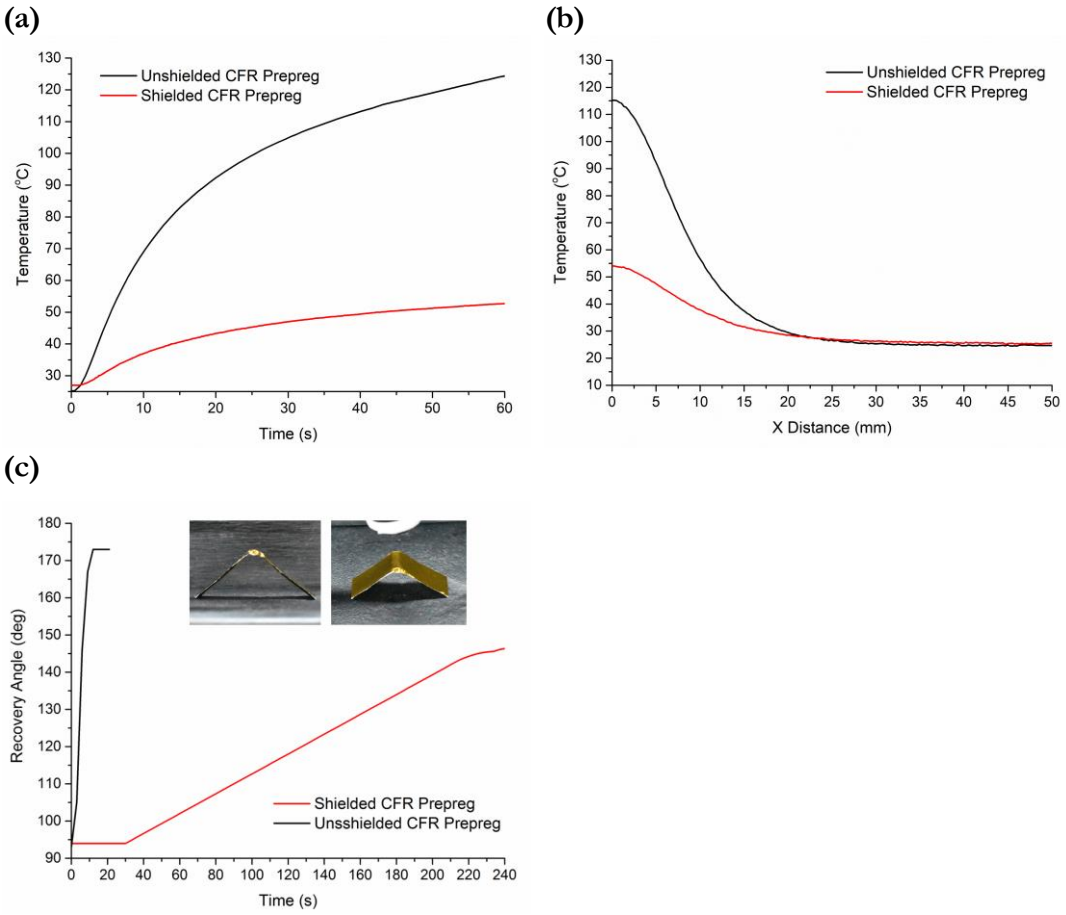

Figure 5.11: Photothermal behaviour and light activated shape recovery behaviour due to 808 nm 2 W/cm^2 NIR radiation. Comparison between shielded and unshielded CFR prepreg LASMPC (a) Temperature at the centre (b) Temperature along X axis after being exposed to 60 seconds of NIR radiation (c) Light activated shape recovery.

light irradiance. With the same NIR irradiance, the shielded LASMPC did not show any shape recovery behaviour until 30 seconds. After 30 seconds of NIR irradiance, the shielded LASMPC displayed a slow recovery and at 240 seconds it recovered to a 146° angle.

This indicates that the flexible shielding material (metalized polyamide polymer laminated glass cloth) did not constrain the shape recovery movements of the LASMPC. However, it did block the radiation to some extent. Accordingly, the shielding of LASMPCs may reduce their degradation due to UV [17-19] and Gamma (γ) [16] radiation. Moreover, this shielding may reduce instances of LASMPCs' random and unpredicted shape recovery where the shape recovery needs to be remotely controllable. As described in Section 5.3, optical fibres have the ability to deliver the light into the shielded LASMPCs, in order to accomplish the required shape recovery on demand. In future, the multilayer insulations currently used on spacecrafts have to be tested for LASMPC deployable structures.

5.6 Scaled Model LASMPC Applications

LASMPCs have the ability to be used in microscale to large scale applications for industries as varied as biomedicine, aerospace and space engineering. This section presents the applicability of the proposed LASMPCs for space engineering applications. They are required to endure uniquely harsh environments and maintain their structural permanence. These are the most challenging concerns when selecting lightweight smart materials for space applications.

Moreover, the advancement of deployable structures which can be compressed and expanded in their shapes becomes important as it reduces the room occupied in spacecraft and makes the best use of the structures' volumes when in space. Deployable devices fabricated by using shape memory composites are able to undergo large deformations, which have been developed to make large structures fit into small volumes. Compared to other energy storing structures, the SMPC made structures demonstrate less complexity, high strength and lightness in weight, which are advantageous for space engineering applications. Moreover, LASMPC made structures can demonstrate controlled, sequential and remote actuations.

Herein three model space applications of LASMPCs are presented: a scaled deployable solar panel array model, a scaled deployable space habitat structure model and a scaled

deployable boom structure model for small spacecraft. The functionalities of these scaled models were studied based on experimentation in a controlled atmosphere. These types of LASMPC structures can be compressed and packed in a spacecraft, transported to an outer space location and ultimately deployed into their expanded shape by using the stimulus of light.

5.6.1 Scaled Deployable Solar Panel Array Model

Deployable solar panel arrays are extensively applicable for satellites [240, 241]. Figure 5.12 illustrates a model of a deployable solar panel array made out of LASMPC, which can be used in a satellite. Figure 5.12 (a) shows the sectional view of the initial compacted shape and the areas subjected to NIR radiation (808 nm, 2 W/cm^2) during the four steps of localized activation. The anticipated shape recovery behaviour of each step is shown by the arrows. The compacted and programmed shape of the deployable solar panel array is illustrated in Figure 5.12 (b). Successively, Figure 5.12 (c), (d) and (e) present the appearance of the partially recovered solar panel array after activation step 1, 2 and 3, respectively. In each case, the number of solar panels in use is different and it increases corresponding to the activation steps.

The final and fully expanded solar panel array with all four solar panels in use is presented in Figure 5.12 (f). For each step image processing was carried out and the recovery angle-

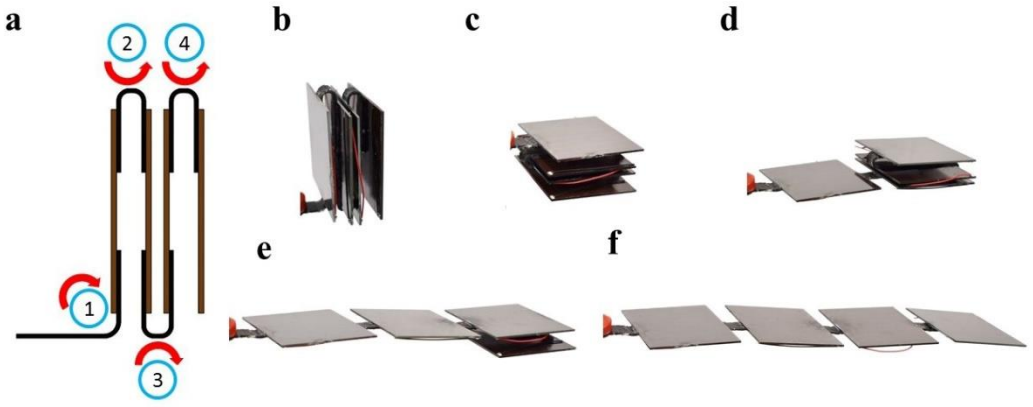

Figure 5.12: Shape recovery sequence of the model of deployable solar panel array for a satellite (a) Steps of NIR irradiation and respective shape recovery behaviours (b) Initial compacted shape (c) View after recovery step 1, one solar panel in use (d) View after recovery step 2, two solar panels in use (e) View after recovery step 3, three solar panels in use (f) Fully recovered view after step 4, four solar panels in use.

based shape recovery ratios of the steps 1 to 4 were determined as 97.4 %, 96.1 %, 96.4 %, 96.5 % respectively. The full deployment process accomplished approximately a 1:10 increase in length comparative to the programmed shape of the solar panel array. The localized photothermal heating capability of the light stimulus, discussed in Chapter 4, has enabled the sequential and controlled activation of the solar panel array. Use of remote actuation via optical fibres, described in Section 5.3, can further advance the deployment functionalities of the proposed solar panel array.

5.6.2 Scaled Deployable Space Habitat Structure Model

Figure 5.13 illustrates the recovery steps of a model of a deployable structure considered for a space habitat. The shape of the structure was recovered, after continuing radiation for 18 min at 130 ºC in 80 kPa vacuum. The recovery time is reasonably high compared to that of the 90º bended experiments presented in Chapter 4. The reason for such a delay could be the internal stress of the structural members. The 90º bended experiments were carried out under stress free strain recovery conditions, since one end of the specimens stayed free. In the deployable structure, both ends of the columns were jointed to beams. Furthermore, the weight of the top four beams was supported by columns. However, in space, gravity may be zero or it may change depending on a structure's proximity to planets.

The average length (L), width (W) and height (H) of the structure, before and after the recovery process were measured. Although the expected programmed shape presented in Figure 5.3 (d) was 22 mm in height, the height of the actual programmed shape was 24 mm. Also, the height of the recovered shape was 1 mm less than the original shape presented in Figure 5.3 (c). The reason for this is the slight curvatures measured in the four columns of the recovered shape. Accordingly, the enclosed volume (L x W x H) of the original shape, programmed shape and recovered shape were 0.274625 m^3, 0.1014 m^3 and 0.2704 m^3, respectively. The volume compression ratio during shape programming was 2.7 : 1 and the volume expansion ratio during the shape recovery was 1 : 2.66.

Figure 5.13 (a) to (g) illustrate the recovery sequence of the deployable structure in seven steps. It was observed that columns did not recover uniformly. This is the reason for the buckled shape appearing from 6 min to 15 min. The internal stress developed in each column affected its recovery rate.

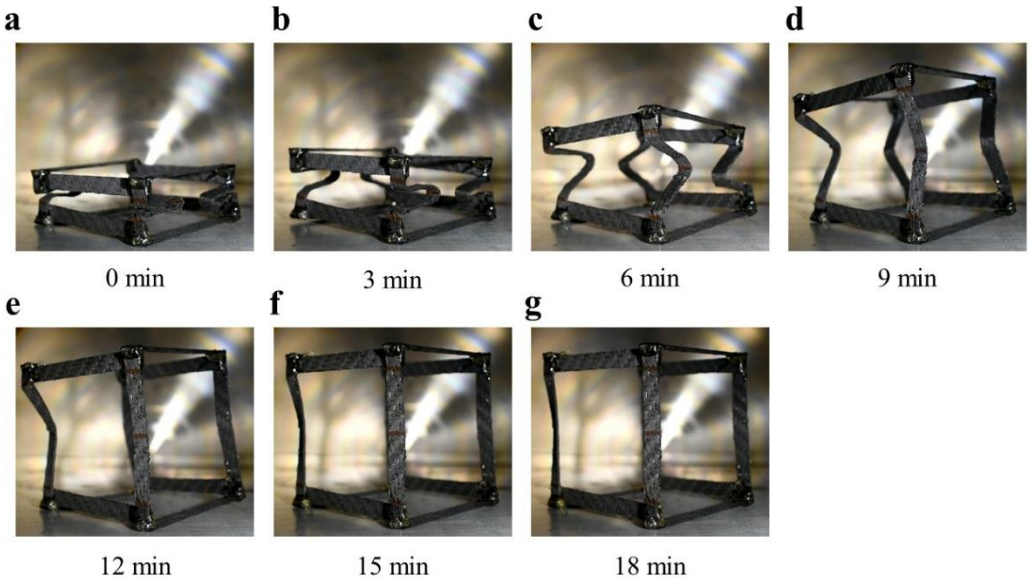

Figure 5.13: Shape recovery sequence of the deployable space habitat structure at 130 ºC in 80 kPa vacuum (a) Initial programmed shape (b - f) Shape recovery steps (g) Fully recovered shape.

It is assumed that each bend was equally exposed to radiation as it was in an enclosed vacuum oven. However, in reality each bend location might not have heated equally. However, the recovery behaviour presented by the model structure is advantageous for deployable space habitats. Currently there are several deployable mechanisms used for everyday use and advanced engineering applications, i.e., scissor-hinged, sliding, umbrella, hinged collapsible, inflatable, pneumatic, folded and telescopic [242-244]. Moreover, the concept of deployable space habitats has been proved with working prototypes [245].

The importance of using LASMPC materials for space habitats is that the deployable structures can be fabricated as a single unit. Space habitats are designed to deploy once, not repeatedly like some other deployable applications. There are no moving joints and assembly components in the LASMPC made structures. Space travellers do not need to engage with any assembling or construction work in space, which will save their time and energy. Furthermore, travellers do not need to take any tools or equipment for construction works.

Through the presence of light radiation in the space, the LASMPC materials will be activated on their own once exposed to the surroundings. However, once deployed, the whole structure should be covered with a light reflective material (fabric / foil), which

makes an enclosed living space for space travellers. Moreover, this will protect the structure from long term radiation effects.

5.6.3 Scaled Deployable Boom Structure Model

Four-dimensional (4D) printing is the convergence of three-dimensional (3D) printing with an emerging additive manufacturing technology for smart materials. 4D printing refers to the capability of changing the shape, property, or functionality of a 3D printed structure under a particular external stimulus. Figure 5.14 shows deployable boom structures (neat PLA and MWCNT PLA) fabricated by 4D printing additive manufacturing technology.

Compared to thermosets, the thermoplastics are capable of recycling, self-healing, impact resistance, and precision manufacturing. Injection moulding and 3D printing techniques were researched for the fabrication of SMP thermoplastics. Advantageously, 3D printing enables small quantities of customized static structures to be produced at a relatively low cost and with less lead time.

The proposed model of a deployable boom structure is intended for small spacecraft. Compared to large space systems, the small systems offer fast development time, low cost, the possibility of large swarm missions and more scientific return on investment [246]. The National Aeronautics and Space Administration (NASA) has developed lightweight deployable composite booms for small spacecraft missions [247, 248]. The proposed LASMPC made boom structure enables custom made self-actuating features in response to light.

The shape fixity and recovery behaviours of the proposed deployable boom structure model were investigated. For both fixing and recovery, the boom structure models made of neat PLA and MWCNT PLA were heated up to 80 °C in the oven. Shape programming was accomplished by applying a compression load along the longitudinal direction of the heated booms. Shape recovery was accomplished under stress free conditions at 80 MPa vacuum.

In Chapter 4, Figure 4.4 (e) showed that both neat PLA and MWCNT PLA heated above Tg once exposed to a NIR radiation of 1 W/cm^2. Due to the radiation in the vacuum oven, both boom structure models made out of neat PLA and MWCNT PLA materials were recovered. However, the boom structure made from MWCNT PLA demonstrated

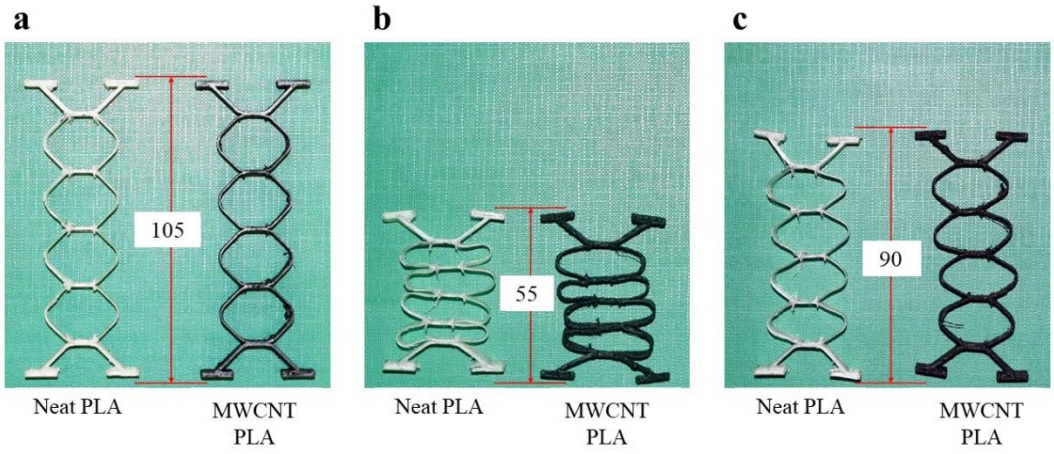

Figure 5.14: Shape memory behaviour of the 4D printed boom structures (all dimensions are in millimetres) (a) Original shape (b) Programmed shape (c) Recovered shape.

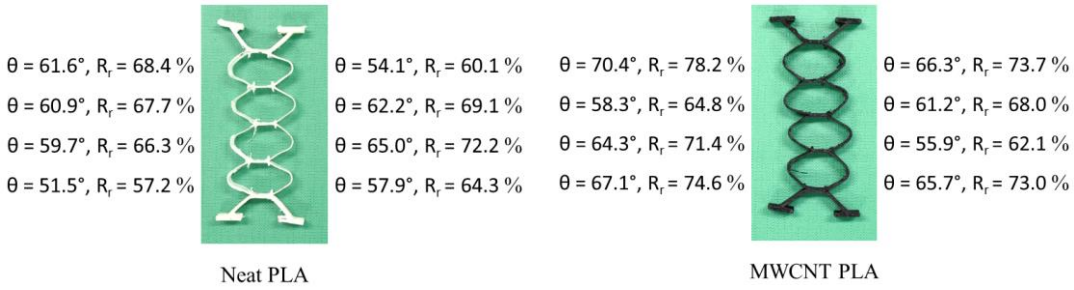

Figure 5.15: Shape recovery angle and recovery ratio of each boom segment.

a fast recovery. The original, programmed and recovered lengths of the model boom structures were approximately 105 mm, 55 mm and 90 mm, respectively. By considering the lengthwise shape changes, the shape recovery ratio of the fabricated model boom structure was calculated as ~86 %. Moreover, recovery angle (θ) based shape recovery ratios (R_r) of each boom segment were calculated and presented in Figure 5.15.

The programmed and recovered shapes demonstrated inadequate dimensional stability. The reason for such behaviour is the uneven stresses applied during the shape programming due to the load applied by hand. Use of custom designed tools and unidirectional load will assist accurate shape programming.

Compared to the obtained mechanical properties for MWCNT reinforced LASMPC, the carbon fibre reinforced LASMPCs demonstrate the greater strength required for space applications. At present, few commercially available 3D printers are capable of continuous

fibre reinforced 3D printing. With further developments to 3D printing technology and SMP materials, continuous fibre reinforced 4D printing will be practicable in the future.

5.7 Summary

In this chapter, details have been provided of the applicability of the structurally performing, light-triggered shape memory materials presented in Chapters 3 and 4, for large scale engineering applications. Moreover, advanced techniques of remote actuation and radiation protection for LASMPC applications have been presented. It was proved that the embedding of a D-shaped optical fibre enables the light dispersion into LASMPC materials, which can generate the adequate photothermal effect required for shape memory actuation of relatively large LASMPC samples. A D-shaped optical fibre enables dispersion of light through the polished area along the fibre rather than dispersion through the tip of the fibre.

Furthermore, shielding an LASMPC with a radiation protection material will reduce the polymer degradation in environments with a higher amount of radiation. Also, radiation shielding can block sunlight and retain the temporary shape until the shape recovery is required on demand through a controllable light source. Such shielding can also protect the radiation heat loss from an LASMPC in shaded or dark space environments.

A combination of optical fibre coupled and radiation shielded LASMPCs will further advance actuators for future space applications. Three scaled application models of LASMPCs have been presented: a deployable solar panel array, a deployable space habitat structure and a deployable boom structure for small spacecraft. However, further research can improve these innovative concepts for various other applications in space exploration. The next chapter presents the conclusions to the current research and suggestion for future work.

Chapter 6

Conclusions and Future Research

This chapter highlights the innovative scientific outcomes and contributions made by the author of this thesis towards the advancement of science and engineering. The current study has successfully addressed the four objectives set out in Section 1.3 of this thesis. The observations and firsthand experiences gained through this project have been discussed and summarized appropriately in Chapters 3 to 5. This chapter point out the important facts of the summaries presented in chapter 3 to 5. The breakthrough findings resulted from this study are compiled in order to demonstrate the conclusive achievements of this study. At the outset, the key innovative scientific outcomes of this study are indicated step by step followed by the conclusions to this research. For further investigations, the author has endorsed recommendations for future directions.

The scientific outcomes of this study contributed to a book chapter, a review journal article, four research journal articles and four conference proceedings, as detailed in Appendix A of this thesis. Moreover, Appendix B details the associated awards won by the author of this thesis, at prestigious international events and conferences.

6.1 Key Outcomes of the Study

1. A material development framework for structural LASMPCs:

The structural LASMPC materials comprise three core components: the SMP matrix, reinforcement and photothermal filler. The impeccable combination of these three components is subjected to the intended application, engineering design parameters and predetermined manufacturing method, which ranges from classic hand layup to cutting edge robot assisted composite or additive manufacturing. It was showed that both thermosets and thermoplastics are suitable as SMP matrices for structural LASMPCs. The current study admitted four representative composite material systems and three apt manufacturing methods to establish an LASMPC development

framework. Across the board, scientific understanding and new knowledge have been engendered through a comprehensive experimental progression. The instigated material development framework guided material selection, preparation procedures designed to ensure the human and environmental safety and characterization strategies that enhance and underpin the anticipated shape memory functions, structural performance, a high level of safety and cost-effectiveness.

2. Empirical investigation on the effects of reinforcement and photothermal fillers:

The inclusion of reinforcements improved the inherently weak mechanical properties of the pristine SMPs. Carbon fire and MWCNT reinforcements increased both structural properties and photothermal effect. The rare earth based photothermal fillers improved the light absorbance capabilities but affected the shape memory characteristics, thermal conductivity and structural performance of the LASMPCs. Due to this reason the effects of the fibre reinforcements and photothermal fillers on the performances of LASMPCs were systemically studied and explicated during this study. It was revealed that the performance of the LASMPCs varied with respect to the weight fraction of the fibre reinforcement and photothermal fillers.

3. Failure mode analysis and defect identification of LASMPCs:

The FTIR findings revealed that the inclusion of filler materials alters the chemical bonds of the LASMPCs (relative to their parent materials), which affected the shape memory characteristics of the pristine SMPs. The microscopic investigations on the surface and cross-sections discovered micro level manufacturing defects occurred due to the three different LASMPC manufacturing methods used in this study. The failure modes under tension and compression showed direct relationship to those preidentified manufacturing defects. Failure mechanisms of the LAMPCSs were identified as delamination, plastic microbuckling, and shear kinking. Moreover, the uneven surface texture and high surface roughness of the materials improved the light abortion capabilities.

4. Light activation methodologies for structural LASMPCs:

Inimitable approaches and mechanisms are indispensable to deliver light radiation to activate LASMPC structures. This study revealed that the material level enhancements on light absorbance empower the shape recovery of massive LASMPC structures appearing in scattered low intensity light, serving as sunlight. In different circumstances, an intense laser beam emitting a certain wavelength of light can trigger relatively low light absorbing structural LASMPC materials that act only in response to a selective light wavelength of NIR radiation. Furthermore, focusing a laser beam onto designated locations of a LASMPC structure according to a predetermined sequence can deploy the structure in a step by step manner. The up-to-the-minute innovative finding on embedded D-shaped optical fibre in an LACMPC component is a breakthrough for the light activation of smart LASMPCs structures. The D-shaped optical fibres succeeded in dispersing light into the LASMPC structures, which eliminated the barrier to remote actuation of smart LASMPC structures.

5. Tailored experimental procedures for LASMPC research:

Chapter 4 and 5 present customised experimental setups to evaluate the photothermal effect and light activated shape memory behaviour of LASMPCs. These in-house experimental apparatuses were designed and fabricated by considering the Australia New Zealand standards for human, environment and equipment safety. Therefore, the LASMPC experiments comprised of powerful lasers, vacuumed and high temperature environmental conditions. Interestingly, the apparatuses enabled the anticipated accurate experimentations.

6. A simulation approach for photothermal LASMPCs:

The SMP materials' time-dependent viscoelastic behaviour-based finite elements simulations are incapable on their own in fully describing the light activated SME of composite materials. The current study presents a rigorous photothermal FEA procedure that is integrated into the prevailing high end FEA packages. The add on feature provides an accurate simulation of three dimensional photothermal heating of LASMPCs and fills the long awaited requirement of an FEA tool for LASMPC component design. The established FEA model is capable of accommodating all

modes of light diffusion such as scattered low intensity light, focussed laser beams and light delivery through fibre optics.

7. Design and development of deployable structures:

Three deployable structure models were developed by using laminating and 3D printing methods. These models consisted of LASMPC structural members and non-structural components such as solar panels. Apt composite joining method were used for the assembly. The facts such as anticipated volume change, uniform light irradiation for even stimulation and dimensional stability during the deployment were studied by using these miniature models. The presented techniques and practises can be adapted for actual size deployable structures.

8. An insight to apply LASMPCs for space engineering:

The inherent advantages of light make it the foremost stimulus for space engineering applications. The improvements to their structural properties and cutting edge remote activation methodologies have justified LASMPCs' aptness for space engineering applications. Additionally, the current study has introduced the use of flexible radiation shields to prevent degradation due to UV light and eliminate unanticipated shape recoveries due to space radiation. Using scaled models, the concept of light triggered deployable space structures has been conceptually demonstrated. The deployable structures made of structural LASMPCs indisputably reduce the occupied volume in the spacecraft during travel and permit the best use of the deployed volume in space.

6.2 Conclusions

Most researchers who have developed LASMPC systems for micro scale, miniature and biomedical applications have not given any attention to LASMPCs for structural and large scale engineering applications. In this study four type of representative structural LASMPC systems have been developed: i) carbon fibre/epoxy prepreg based LASMPC ii) rare earth organic complexes and glass fibre/styrene based LASMPC iii) carbon nanotube/polylactic acid (PLA) based LASMPC iv) carbon fibre/bisphenol A (DEGBA)

epoxy based LASMPC. These materials underwent a comprehensive experimental analysis to build up vital scientific understanding on their structural performance and light activated shape memory behaviours.

It was revealed that the inclusion of carbon fibres significantly enhances LASMPCs' structural properties and photothermal heating performances. The carbon fibre reinforced samples have shown not only superlative mechanical properties but also above 98% shape fixity and the anticipated full recovery. Furthermore, glass transition temperatures ranging from 80 to 130 °C make them admissible for environments with extreme temperatures. At an any given light wavelength from UV to NIR (200 – 1200 nm), the carbon fibre LASMPCs proved to have a higher light absorbance, which makes them capable of actuating under scattered low intensity light. As carbon fibres act as both a reinforcement and a photothermal filler, large structures made of CFR LASMPCs are cost effective.

In contrast, the LASMPCs containing rare earth organic complexes of $Nd(TTA)_3Phen$ and $Yb(TTA)_3Phen$ selectively respond to high power lasers (>1 W/cm^2) of 808 nm and 980 nm, respectively. The glass fibre reinforcements succeeded in enhancing the structural properties, without affecting the light absorbance of these selectively triggered LASMPCs. Hence the GFR LASMPCs containing rare earth organic complexes-based fillers are competent to facilitate the on demand selective wavelength actuation of semi-structural and structural components. In comparison to the few types of selective wavelength photothermal fillers researched to date such as gold NPs, NSs and NRs, the rare earth organic complexes are a cost effective solution for the production of large scale structures.

The inclusion of MWCNTs into PLA SMP has placed 3D printing technology at another level of made-to-order product manufacturing, where the 4D printed components undergo shape changes upon exposure to the light stimulus. MWCNT filled LASMPCs showed the best photothermal heating as the samples reached their glass transition within 2 seconds upon exposure to 1 W/cm^2 NIR radiation. It is evidently proving that additive manufacturing is capable of producing complex geometries with less lead times. Therefore, MAWCNT PLA is not a material whose use is limited to shape changing structures but also suitable for load bearing components with complex geometries such as locking mechanisms and hinges that undertake shape changes as a result of a light stimulus.

It has been proved that the embedding of a side polished D-shaped optical fibre into an LASMPC enables remote actuation capabilities. The D-shaped fibre was capable of heating the LASMPC material along the embedded fibre, which activated a larger portion of the LASMPC component. The embedded fibre was not damaged or fragmented during the shape programming and recovery processes. The proposed method is appropriate not only for high Tg photothermal LASMPCs but also for low Tg photothermal LASMPCs and non-heating photo responsive SMPs. Due to this breakthrough technology, the actuators located at difficult to reach positions can be controlled easily with light energy.

It has also been shown that exposure to 1000 hours of UV radiation turned pristine SMPs a yellow colour, which increased their light absorbance and photothermal effect. However, this enhancement is insignificant for LACMPCs, because the photothermal filler acts as the primary light absorber. Shielding of LASMPCs by using a metalized polyamide polymer laminated glass cloth will reduce the polymer degradation in environments with a higher amount of radiation. It has been demonstrated that the use of a flexible shielding material does not constrain the shape recovery movements of the LASMPC components but blocks the interfering environmental radiation that affects the material.

Three scaled model space applications of LASMPCs have been demonstrated: a deployable solar panel array model, a deployable space habitat structure model and a deployable boom structure model for small spacecraft. The solar panel array was subjected to localized photothermal heating, which enabled sequential activation in four recovery steps. The deployable space habitat structure showed a 2.7:1 volume compression ratio during shape programming and a 1:2.66 volume expansion ratio during the shape recovery. The revolutionary 4D printing technology facilitated the fabrication of the deployable boom structure model. The lengthwise shape recovery ratio of this fabricated boom structure model was approximately 86 %. These findings have established the foundation of future manufacturing of LASMPC components for space habitats, spacecraft and satellites.

The successful completion of the current study has significantly contributed to the scientific knowledge base by founding a material development framework for high performance structural LASMPCs while retaining superlative shape memory and photothermal effects. This new knowledge and understanding of structural LASMPC material systems will open up windows of opportunity for the scientific and engineering

communities to provide innovative solutions to realize the sophisticated large scale engineering demands in aerospace and space applications and beyond. Moreover, proved remote actuation and radiation shielding has increased the opportunities for using structural LASMPCs for advanced space engineering applications. In due course, the deployable LASMPC structures will shape future space missions and facilitate more scientific return on investment.

6.3 Future Directions and Recommendations

In this study, major attention was given to deployable space structures. However, LASMPCs' potential has been shown for a wider range of engineering applications. As such, the consideration of LASMPCs in more engineering applications is warranted. Also, explorations of other reinforcements such as basalt, kevlar, polybenzoxazole and various natural fibres are also warranted to improve properties such as impact and fire resistance. Various metallic and organic photothermal fillers that are currently limited to photothermal therapies and solar thermal systems can be introduced for LASMPC systems. For the safety of commercial LASMPC components, necessary measures should be taken to eliminate delamination and internal voids by extending failure analysis research of LASMPC materials. This thesis provides an exclusive material framework for imminent LASMPC developments. However, there is space for further research on the optimisation of structural, thermomechanical and photothermal properties. Further, structural LASMPCs with multi and reversible shape memory effects should be investigated for repeatable applications.

Advanced real time monitoring techniques should be developed to determine in situ strain and temperature changes of the sophisticated LASMPC components during their operation. Embedment of distributed optical fire sensors into SMPCs will be an innovative technique to quantify the thermomechanical behaviours of the large SMPC components.

Hypothetically, the double D-shaped optical fibres could disperse light in two opposite directions, which may speed up the shape recovery process. Moreover, multi D-shaped fibres will be beneficial to heat different locations of the LASMPC by using a single optical fibre. An array of optical fibres or a multicore optical fibre embedded into LASMPCs could distribute optical power to multiple locations from a single laser source.

LASMPCs should be further tested against gamma radiation, plasma, atomic oxygen and thermal cycling in order to improve their long term performance in a space environment. Dispersing light into radiation shielded LASMPCs by using embedded optical fibres will advance LASMPC activation on demand. Investigations into the long term behaviour of LASMPCs in harsh operational environments are warranted. In future LASMPC structures can possibly be tested under space conditions at the international space station or during deep space missions. Further research on structural LASMPCs is recommended, aimed at breakthrough technological advancements for future space missions.

References

1. Dietsch, B. and T. Tong, A review - Features and benefits of shape memory polymers (SMPs). Journal of Advanced Materials, 2007. 39(2): p. 3-12.
2. Leng, J., et al., Shape-memory polymers and their composites: Stimulus methods and applications. Progress in Materials Science, 2011. 56(7): p. 1077-1135.
3. Wang, W., et al., Recent developments in shape memory polymer nanocomposites: Actuation methods and mechanisms. Coordination Chemistry Reviews, 2016. 320-321: p. 38-52.
4. Sun, L., et al., Stimulus-responsive shape memory materials: A review. Materials & Design, 2012. 33: p. 577-640.
5. Ratna, D. and J. Karger-Kocsis, Recent advances in shape memory polymers and composites: A review. Journal of Materials Science, 2008. 43(1): p. 254-269.
6. Liu, Y., et al., Review of electro-active shape-memory polymer composite. Composites Science and Technology, 2009. 69(13): p. 2064-2068.
7. Li, H., et al., The reinforcement efficiency of carbon nanotubes/shape memory polymer nanocomposites. Composites Part B: Engineering, 2013. 44(1): p. 508-516.
8. Keramati, M., et al., Dispersion of Graphene Nanoplatelets in Polylactic Acid with the Aid of a Zwitterionic Surfactant: Evaluation of the Shape Memory Behavior. Polymer-Plastics Technology and Engineering, 2016. 55(10): p. 1039-1047.
9. Dong, Y., et al., Novel vapor-grown carbon nanofiber/epoxy shape memory nanocomposites prepared via latex technology. Materials Letters, 2014. 132: p. 206-209.
10. Dong, Y. and Q.-Q. Ni, Effect of vapor-grown carbon nanofibers and in situ hydrolyzed silica on the mechanical and shape memory properties of water-borne epoxy composites. Polymer Composites, 2015. 36(9): p. 1712-1720.
11. Guo, J., et al., Effects of short carbon fibres and nanoparticles on mechanical, thermal and shape memory properties of SMP hybrid nanocomposites. Composites Part B: Engineering, 2016. 90: p. 152-159.
12. Leng, J., et al., Electroactivate shape-memory polymer filled with nanocarbon particles and short carbon fibers. Applied Physics Letters, 2007. 91(14): p. 144105.

13. Al Azzawi, W., et al., Quantitative and qualitative analyses of mechanical behavior and dimensional stability of styrene-based shape memory composites. Journal of Intelligent Material Systems and Structures, 2017. 28(20): p. 3115-3126.
14. Lan, X., et al., Fiber reinforced shape-memory polymer composite and its application in a deployable hinge. Smart Materials and Structures, 2009. 18(2): p. 024002.
15. Ohki, T., et al., Mechanical and shape memory behavior of composites with shape memory polymer. Composites Part A: Applied Science and Manufacturing, 2004. 35(9): p. 1065-1073.
16. Leng, J., et al., Effect of the γ-radiation on the properties of epoxy-based shape memory polymers. Journal of Intelligent Material Systems and Structures, 2014. 25(10): p. 1256-1263.
17. Al Azzawi, W., et al., Investigation of ultraviolet radiation effects on thermomechanical properties and shape memory behaviour of styrene-based shape memory polymers and its composite. Composites Science and Technology, 2018. 165: p. 266-273.
18. Xie, F., et al., Effects of accelerated aging on thermal, mechanical and shape memory properties of cyanate-based shape memory polymer: I vacuum ultraviolet radiation. Polymer Degradation and Stability, 2017. 138: p. 91-97.
19. Jang, J.H., et al., Long-term properties of carbon fiber-reinforced shape memory epoxy/polymer composites exposed to vacuum and ultraviolet radiation. Smart Materials and Structures, 2019. 28(11): p. 115013.
20. Zhao, W., et al., Shape memory polymers and their composites in biomedical applications. Materials Science and Engineering: C, 2019. 97: p. 864-883.
21. Small, I.V.W., et al., Biomedical applications of thermally activated shape memory polymers. Journal of Materials Chemistry, 2010. 20(17): p. 3356-3366.
22. Zhang, W., et al., Shape memory behavior and recovery force of 4D printed textile functional composites. Composites Science and Technology, 2018. 160: p. 224-230.
23. Ji, F., et al., Smart polymer fibers with shape memory effect. Smart Materials and Structures, 2006. 15(6): p. 1547-1554.

24. Nji, J. and G. Li, A self-healing 3D woven fabric reinforced shape memory polymer composite for impact mitigation. Smart Materials and Structures, 2010. 19(3): p. 035007.
25. Zhang, H. and Y. Zhao, Polymers with Dual Light-Triggered Functions of Shape Memory and Healing Using Gold Nanoparticles. ACS Applied Materials & Interfaces, 2013. 5(24): p. 13069-13075.
26. Li, F., et al., Progress of shape memory polymers and their composites in aerospace applications. Smart Materials and Structures, 2019. 28(10): p. 103003.
27. Liu, Y., et al., Shape memory polymers and their composites in aerospace applications: a review. Smart Materials and Structures, 2014. 23(2): p. 023001.
28. Lendlein, A., et al., Light-induced shape-memory polymers. Nature, 2005. 434(7035): p. 879-882.
29. Li, Y., et al., Photoresponsive Liquid Crystalline Epoxy Networks with Shape Memory Behavior and Dynamic Ester Bonds. ACS Applied Materials & Interfaces, 2016. 8(24): p. 15750-15757.
30. Fang, L., et al., Shape-memory polymer composites selectively triggered by near-infrared light of two certain wavelengths and their applications at macro-/microscale. Composites Science and Technology, 2017. 138: p. 106-116.
31. ISO, 20473:2007 Optics and photonics - Spectral bands. 2015: International Organization for Standardization.
32. Small Iv, W., et al., Laser-activated shape memory polymer intravascular thrombectomy device. Optics Express, 2005. 13(20): p. 8204-8213.
33. Maitland, D.J., et al., Photothermal properties of shape memory polymer micro-actuators for treating stroke. Lasers in Surgery and Medicine, 2002. 30(1): p. 1-11.
34. Maitland, D.J., et al., Prototype laser-activated shape memory polymer foam device for embolic treatment of aneurysms. Journal of Biomedical Optics, 2007. 12(3): p. 1-3, 3.
35. Small, W., et al., Shape Memory Polymer Stent With Expandable Foam: A New Concept for Endovascular Embolization of Fusiform Aneurysms. IEEE Transactions on Biomedical Engineering, 2007. 54(6): p. 1157-1160.
36. Fang, L., et al., Near-Infrared Light Triggered Soft Actuators in Aqueous Media Prepared from Shape-Memory Polymer Composites. Macromolecular Materials and Engineering, 2016. 301(9): p. 1111-1120.

37. Liu, Y., et al., An investigation on laser-triggered shape memory behaviors of hydro-epoxy/carbon black composites. Smart Materials and Structures, 2018. 27(9): p. 095008.
38. Zhao, Y. and T. Ikeda, Smart Light-Responsive Materials: Azobenzene-Containing Polymers and Liquid Crystals. 2008: John Wiley & Sons, Inc.
39. Hada, M., et al., Ultrafast isomerization-induced cooperative motions to higher molecular orientation in smectic liquid-crystalline azobenzene molecules. Nature Communications, 2019. 10(1): p. 4159.
40. Filipcsei, G., et al., Swelling degree and shape change of photo- and thermo-response of spirobenzopyran-functionalized porous pNIPAAm hydrogels. Journal of Molecular Liquids, 2014. 189: p. 63-67.
41. Jeon, S.-J., et al., Shape-Morphing Materials from Stimuli-Responsive Hydrogel Hybrids. Accounts of Chemical Research, 2017. 50(2): p. 161-169.
42. Zhang, H., et al., Light Polarization-Controlled Shape-Memory Polymer/Gold Nanorod Composite. Macromolecular Rapid Communications, 2013. 34(19): p. 1575-1579.
43. Zheng, Y., et al., Light-induced shape recovery of deformed shape memory polymer micropillar arrays with gold nanorods. RSC Advances, 2015. 5(39): p. 30495-30499.
44. Yi, D.H., et al., The synergistic effect of the combined thin multi-walled carbon nanotubes and reduced graphene oxides on photothermally actuated shape memory polyurethane composites. Journal of Colloid and Interface Science, 2014. 432: p. 128-134.
45. Yenpech, N., et al., Laser-triggered shape memory based on thermoplastic and thermoset matrices with silver nanoparticles. Polymer, 2019. 182: p. 121792.
46. Ishii, S., et al., Hybridizing Poly(ε-caprolactone) and Plasmonic Titanium Nitride Nanoparticles for Broadband Photoresponsive Shape Memory Films. ACS Applied Materials & Interfaces, 2016. 8(8): p. 5634-5640.
47. Ahir, S.V. and E.M. Terentjev, Photomechanical actuation in polymer–nanotube composites. Nature Materials, 2005. 4(6): p. 491-495.
48. Loomis, J., et al., Graphene/elastomer composite-based photo-thermal nanopositioners. Scientific Reports, 2013. 3(1): p. 1900.

49. Zhang, Y., et al., Near-infrared light-induced shape memory, self-healable and anti-bacterial elastomers prepared by incorporation of a diketopyrrolopyrrole-based conjugated polymer. Materials Chemistry Frontiers, 2019. 3(5): p. 836-841.
50. Qian, W., et al., Photothermal-Triggered Shape Memory Polymer Prepared by Cross-Linking Porphyrin-Loaded Micellar Particles. Materials (Basel, Switzerland), 2019. 12(3): p. 496.
51. Webb, J.A. and R. Bardhan, Emerging advances in nanomedicine with engineered gold nanostructures. Nanoscale, 2014. 6(5): p. 2502-2530.
52. Mishra, S.R. and J.B. Tracy, Sequential Actuation of Shape-Memory Polymers through Wavelength-Selective Photothermal Heating of Gold Nanospheres and Nanorods. ACS Applied Nano Materials, 2018. 1(7): p. 3063-3067.
53. Yu, L., et al., Multi-shape-memory effects in a wavelength-selective multicomposite. Journal of Materials Chemistry A, 2015. 3(26): p. 13953-13961.
54. Li, W., et al., Light-actuated reversible shape memory effect of a polymer composite. Composites Part A: Applied Science and Manufacturing, 2018. 110: p. 70-75.
55. Beblo, R.V. and L.M. Weiland, Light Activated Shape Memory Polymer Characterization. Journal of Applied Mechanics, 2008. 76(1).
56. Zhang, D., et al., Infrared laser-activated shape memory polymer. SPIE Smart Structures and Materials + Nondestructive Evaluation and Health Monitoring. Vol. 6932. 2008: SPIE.
57. Sodhi, J.S. and I.J. Rao, Modeling the mechanics of light activated shape memory polymers. International Journal of Engineering Science, 2010. 48(11): p. 1576-1589.
58. Beblo, R.V. and L.M. Weiland, Demonstration of a multiscale modeling technique: prediction of the stress–strain response of light activated shape memory polymers. Smart Materials and Structures, 2010. 19(9): p. 094012.
59. Long, K.N., et al., Photomechanics of light-activated polymers. Journal of the Mechanics and Physics of Solids, 2009. 57(7): p. 1103-1121.
60. Finckenor, M.M. and K.K.D. Groh, A Researcher's Guide to: Space Environmental Effects, in ISS Researcher's Guide Series, D. Steele, Editor. 2016: NASA ISS Program Science Office.
61. Rawal, S.P., et al., Composite materials for space applications - NASA Contractor Report 1874722. 1990, Martin Marietta Astronautics Group: NASA.

62. MSFC, Design and Manufacturing Guideline for Aerospace Composites - Lesson Number 682. 1999: NASA.
63. Zhao, Q., et al., Recent progress in shape memory polymer: New behavior, enabling materials, and mechanistic understanding. Progress in Polymer Science, 2015. 49-50: p. 79-120.
64. Zhou, B., et al., A glass transition model for shape memory polymer and its composite. International Journal of Modern Physics B, 2009. 23(06n07): p. 1248-1253.
65. Baghani, M., et al., An analytical solution for shape-memory-polymer Euler–Bernoulli beams under bending. International Journal of Mechanical Sciences, 2014. 84: p. 84-90.
66. Behl, M. and A. Lendlein, Shape-memory polymers. Materials Today, 2007. 10(4): p. 20-28.
67. Hager, M.D., et al., Shape memory polymers: Past, present and future developments. Progress in Polymer Science, 2015. 49-50: p. 3-33.
68. Pretsch, T., Review on the Functional Determinants and Durability of Shape Memory Polymers. Polymers, 2010. 2(3): p. 120-158.
69. Voit, W., et al., High-Strain Shape-Memory Polymers. Advanced Functional Materials, 2010. 20(1): p. 162-171.
70. Lendlein, A. and S. Kelch, Shape-Memory Polymers. Angewandte Chemie International Edition, 2002. 41(12): p. 2034-2057.
71. Sharma, K. and G. Srinivas, Flying smart: Smart materials used in aviation industry. Materials Today: Proceedings, 2019.
72. Li, F., et al., Mechanical analysis of a tip-loaded deployable truss based on shape memory polymer composite. Composite Structures, 2020. 242: p. 112196.
73. Ivens, J., et al., Shape recovery in a thermoset shape memory polymer and its fabric-reinforced composites. Express Polymer Letters, 2011. 5: p. 254-261.
74. Gall, K., et al., Carbon Fiber Reinforced Shape Memory Polymer Composites. Journal of Intelligent Material Systems and Structures, 2000. 11(11): p. 877-886.
75. Xie, H., et al., Reinforcement of shape-memory poly(ethylene-co-vinyl acetate) by carbon fibre to access robust recovery capability under resistant condition. Composites Science and Technology, 2018. 157: p. 202-208.
76. Xu, T., et al., Effects of ultraviolet radiation on morphology and thermo-mechanical properties of shape memory polymer based syntactic foam.

Composites Part A: Applied Science and Manufacturing, 2011. 42(10): p. 1525-1533.

77. Wong, T.-t., et al., Degradation of nano-ZnO particles filled styrene-based and epoxy-based SMPs under UVA exposure. Composite Structures, 2015. 132: p. 1056-1064.

78. Tandon, G.P., et al., Durability Assessment of Styrene- and Epoxy-based Shape-memory Polymer Resins. Journal of Intelligent Material Systems and Structures, 2009. 20(17): p. 2127-2143.

79. Kong, D. and X. Xiao, High Cycle-life Shape Memory Polymer at High Temperature. Scientific Reports, 2016. 6(1): p. 33610.

80. Yamada, M., et al., Photomobile Polymer Materials: Towards Light-Driven Plastic Motors. Angewandte Chemie International Edition, 2008. 47(27): p. 4986-4988.

81. Watanabe, S., et al., Two-wavelength infrared responsive hydrogel actuators containing rare-earth photothermal conversion particles. Scientific Reports, 2018. 8(1): p. 13528.

82. Yu, Y., et al., Directed bending of a polymer film by light. Nature, 2003. 425(6954): p. 145-145.

83. Li, C., et al., Synthesis of a Photoresponsive Liquid-Crystalline Polymer Containing Azobenzene. Macromolecular Rapid Communications, 2009. 30(22): p. 1928-1935.

84. Iqbal, D. and M.H. Samiullah, Photo-Responsive Shape-Memory and Shape-Changing Liquid-Crystal Polymer Networks. Materials (Basel, Switzerland), 2013. 6(1): p. 116-142.

85. Qin, C., et al., A supramolecular assembly of cross-linked azobenzene/polymers for a high-performance light-driven actuator. Journal of Materials Chemistry A, 2015. 3(32): p. 16453-16460.

86. Wang, X., Photoresponsive Liquid Crystal Elastomers, in Azo Polymers: Synthesis, Functions and Applications. 2017, Springer Berlin Heidelberg: Berlin, Heidelberg. p. 197-228.

87. Tomatsu, I., et al., Photoresponsive hydrogels for biomedical applications. Advanced Drug Delivery Reviews, 2011. 63(14): p. 1257-1266.

88. Sugiura, S., et al., On-demand microfluidic control by micropatterned light irradiation of a photoresponsive hydrogel sheet. Lab on a Chip, 2009. 9(2): p. 196-198.
89. Alfimov, M.V., et al., Photoswitchable molecular receptors. Journal of Photochemistry and Photobiology A: Chemistry, 2003. 158(2): p. 183-198.
90. Shou, Q., et al., Near-infrared light-responsive shape-memory poly(ε-caprolactone) films that actuate in physiological temperature range. Polymer Journal, 2014. 46(8): p. 492-498.
91. Vaia, R., Remote-controlled actuators. Nature Materials, 2005. 4(6): p. 429-430.
92. Lashgari, S., et al., Shape memory nanocomposite of poly(L-lactic acid)/graphene nanoplatelets triggered by infrared light and thermal heating. Express Polymer Letters, 2016. 10: p. 349-359.
93. Lu, H., et al., Significantly improving infrared light-induced shape recovery behavior of shape memory polymeric nanocomposite via a synergistic effect of carbon nanotube and boron nitride. Composites Part B: Engineering, 2014. 62: p. 256-261.
94. Wang, J., et al., High-Performance Photothermal Conversion of Narrow-Bandgap Ti2O3 Nanoparticles. Advanced Materials, 2017. 29(3): p. 1603730.
95. Jiang, R., et al., Mass-Based Photothermal Comparison Among Gold Nanocrystals, PbS Nanocrystals, Organic Dyes, and Carbon Black. The Journal of Physical Chemistry C, 2013. 117(17): p. 8909-8915.
96. Toncheva, A., et al., Fast IR-Actuated Shape-Memory Polymers Using in Situ Silver Nanoparticle-Grafted Cellulose Nanocrystals. ACS Applied Materials & Interfaces, 2018. 10(35): p. 29933-29942.
97. Rentería-Tapia, V., et al., Silver Nanoparticles Dispersed on Silica Glass for Applications as Photothermal Selective Material. Energy Procedia, 2014. 57: p. 2241-2248.
98. Boca, S.C., et al., Chitosan-coated triangular silver nanoparticles as a novel class of biocompatible, highly effective photothermal transducers for in vitro cancer cell therapy. Cancer Letters, 2011. 311(2): p. 131-140.
99. Manikandan, M., et al., Platinum nanoparticles for the photothermal treatment of Neuro 2A cancer cells. Biomaterials, 2013. 34(23): p. 5833-5842.
100. Ou, G., et al., Photothermal therapy by using titanium oxide nanoparticles. Nano Research, 2016. 9(5): p. 1236-1243.

101. Ren, W., et al., A Near Infrared Light Triggered Hydrogenated Black TiO2 for Cancer Photothermal Therapy. Advanced Healthcare Materials, 2015. 4(10): p. 1526-1536.
102. He, W., et al., Plasmonic titanium nitride nanoparticles for in vivo photoacoustic tomography imaging and photothermal cancer therapy. Biomaterials, 2017. 132: p. 37-47.
103. Ishii, S., et al., Titanium Nitride Nanoparticles as Plasmonic Solar Heat Transducers. The Journal of Physical Chemistry C, 2016. 120(4): p. 2343-2348.
104. Ktifa, S., et al., Photothermal investigation Study of ZnO thin films: effects of Zn and O polar substrate. Applied Physics A, 2014. 114(2): p. 559-563.
105. Fang, J. and Y. Xuan, Investigation of optical absorption and photothermal conversion characteristics of binary CuO/ZnO nanofluids. RSC Advances, 2017. 7(88): p. 56023-56033.
106. Vimala, K., et al., Synergistic effect of chemo-photothermal for breast cancer therapy using folic acid (FA) modified zinc oxide nanosheet. Journal of Colloid and Interface Science, 2017. 488: p. 92-108.
107. Neelgund, G.M. and A. Oki, Cobalt Phthalocyanine-Sensitized Graphene–ZnO Composite: An Efficient Near-Infrared-Active Photothermal Agent. ACS Omega, 2019. 4(3): p. 5696-5704.
108. Xu, B., et al., Synthesis of novel microencapsulated phase change materials with copper and copper oxide for solar energy storage and photo-thermal conversion. Solar Energy Materials and Solar Cells, 2018. 179: p. 87-94.
109. Wang, S., et al., Plasmonic Copper Sulfide Nanocrystals Exhibiting Near-Infrared Photothermal and Photodynamic Therapeutic Effects. ACS Nano, 2015. 9(2): p. 1788-1800.
110. Feng, W., et al., In vitro and in vivo toxicity studies of copper sulfide nanoplates for potential photothermal applications. Nanomedicine: Nanotechnology, Biology and Medicine, 2015. 11(4): p. 901-912.
111. Sotiriou, G.A., et al., Photothermal Killing of Cancer Cells by the Controlled Plasmonic Coupling of Silica-Coated Au/Fe2O3 Nanoaggregates. Advanced Functional Materials, 2014. 24(19): p. 2818-2827.
112. Larsen, G.K., et al., Multifunctional Fe2O3–Au Nanoparticles with Different Shapes: Enhanced Catalysis, Photothermal Effects, and Magnetic Recyclability. The Journal of Physical Chemistry C, 2016. 120(28): p. 15162-15172.

113. Rubio-Ruiz, B., et al., High-Precision Photothermal Ablation Using Biocompatible Palladium Nanoparticles and Laser Scanning Microscopy. ACS Applied Materials & Interfaces, 2018. 10(4): p. 3341-3348.
114. Huang, X., et al., Freestanding palladium nanosheets with plasmonic and catalytic properties. Nature Nanotechnology, 2011. 6(1): p. 28-32.
115. Chou, S.S., et al., Chemically Exfoliated MoS2 as Near-Infrared Photothermal Agents. Angewandte Chemie International Edition, 2013. 52(15): p. 4160-4164.
116. Yin, W., et al., High-Throughput Synthesis of Single-Layer MoS2 Nanosheets as a Near-Infrared Photothermal-Triggered Drug Delivery for Effective Cancer Therapy. ACS Nano, 2014. 8(7): p. 6922-6933.
117. Cheng, L., et al., PEGylated WS2 Nanosheets as a Multifunctional Theranostic Agent for in vivo Dual-Modal CT/Photoacoustic Imaging Guided Photothermal Therapy. Advanced Materials, 2014. 26(12): p. 1886-1893.
118. Zhou, Y., et al., Rapid Near-Infrared Light Responsive Shape Memory Polymer Hybrids and Novel Chiral Actuators Based on Photothermal W18O49 Nanowires. Advanced Functional Materials, 2019. 29(33): p. 1901202.
119. Bai, Y., et al., Fabrication of remote controllable devices with multistage responsiveness based on a NIR light-induced shape memory ionomer containing various bridge ions. Journal of Materials Chemistry A, 2019. 7(36): p. 20723-20732.
120. Zheng, X., et al., Indocyanine Green-Containing Nanostructure as Near Infrared Dual-Functional Targeting Probes for Optical Imaging and Photothermal Therapy. Molecular Pharmaceutics, 2011. 8(2): p. 447-456.
121. Yu, J., et al., Self-Assembly Synthesis, Tumor Cell Targeting, and Photothermal Capabilities of Antibody-Coated Indocyanine Green Nanocapsules. Journal of the American Chemical Society, 2010. 132(6): p. 1929-1938.
122. Chen, M., et al., Polypyrrole nanoparticles for high-performance in vivo near-infrared photothermal cancer therapy. Chemical Communications, 2012. 48(71): p. 8934-8936.
123. Zha, Z., et al., Uniform Polypyrrole Nanoparticles with High Photothermal Conversion Efficiency for Photothermal Ablation of Cancer Cells. Advanced Materials, 2013. 25(5): p. 777-782.

124. Liu, T.W., et al., Porphyrins for Imaging, Photodynamic Therapy, and Photothermal Therapy, in Cancer Theranostics, X. Chen and S. Wong, Editors. 2014, Academic Press: Oxford. p. 229-254.
125. Fang, L., et al., Self-Healing Epoxy Coatings via Focused Sunlight Based on Photothermal Effect. Macromolecular Materials and Engineering, 2017. 302(9): p. 1700059.
126. Shao, Q., et al., Mussel-inspired immobilization of BN nanosheets onto poly(p-phenylene benzobisoxazole) fibers: Multifunctional interface for photothermal self-healing. Applied Surface Science, 2018. 440: p. 1159-1165.
127. Lambert, T.N., et al., Water-Soluble Germanium(0) Nanocrystals: Cell Recognition and Near-Infrared Photothermal Conversion Properties. Small, 2007. 3(4): p. 691-699.
128. Sun, W., et al., Size-Tunable Photothermal Germanium Nanocrystals. Angewandte Chemie International Edition, 2017. 56(22): p. 6329-6334.
129. Ishii, S., et al., Resonant Optical Absorption and Photothermal Process in High Refractive Index Germanium Nanoparticles. Advanced Optical Materials, 2017. 5(5): p. 1600902.
130. Meng, Z.-Y., et al., Effect of different dimensional carbon nanoparticles on the shape memory behavior of thermotropic liquid crystalline polymer. Composites Science and Technology, 2017. 138: p. 8-14.
131. Yang, K., et al., Graphene in Mice: Ultrahigh In Vivo Tumor Uptake and Efficient Photothermal Therapy. Nano Letters, 2010. 10(9): p. 3318-3323.
132. Han, D., et al., Thermal properties of carbon black aqueous nanofluids for solar absorption. Nanoscale Research Letters, 2011. 6(1): p. 457.
133. Leng, J., et al., Infrared light-active shape memory polymer filled with nanocarbon particles. Journal of Applied Polymer Science, 2009. 114(4): p. 2455-2460.
134. Moon, H.K., et al., In Vivo Near-Infrared Mediated Tumor Destruction by Photothermal Effect of Carbon Nanotubes. ACS Nano, 2009. 3(11): p. 3707-3713.
135. Sun, L., et al., Fluorinated carbon fiber as a novel nanocarrier for cancer chemo-photothermal therapy. Journal of Materials Chemistry B, 2017. 5(30): p. 6128-6137.

136. Zhang, H., et al., Optically triggered and spatially controllable shape-memory polymer–gold nanoparticle composite materials. Journal of Materials Chemistry, 2012. 22(3): p. 845-849.
137. Xiao, Z., et al., Shape Matters: A Gold Nanoparticle Enabled Shape Memory Polymer Triggered by Laser Irradiation. Particle & Particle Systems Characterization, 2013. 30(4): p. 338-345.
138. Zhang, H., et al., Light-Controlled Complex Deformation and Motion of Shape-Memory Polymers Using a Temperature Gradient. ACS Macro Letters, 2014. 3(9): p. 940-943.
139. Leonardi, A.B., et al., Remote activation by green-light irradiation of shape memory epoxies containing gold nanoparticles. European Polymer Journal, 2015. 71: p. 451-460.
140. Wang, L., et al., Silver-coordination polymer network combining antibacterial action and shape memory capabilities. RSC Advances, 2014. 4(61): p. 32276-32282.
141. Choudhury, B., et al., Defect generation, d-d transition, and band gap reduction in Cu-doped TiO2 nanoparticles. International Nano Letters, 2013. 3(1): p. 25.
142. Cho, J.W., et al., Electroactive Shape-Memory Polyurethane Composites Incorporating Carbon Nanotubes. Macromolecular Rapid Communications, 2005. 26(5): p. 412-416.
143. Zhou, G., et al., Fast Triggering of Shape Memory Polymers using an Embedded Carbon Nanotube Sponge Network. Scientific Reports, 2016. 6(1): p. 24148.
144. Ni, Q.-Q., et al., Shape memory effect and mechanical properties of carbon nanotube/shape memory polymer nanocomposites. Composite Structures, 2007. 81(2): p. 176-184.
145. Zhang, X., et al., Optically- and Thermally-Responsive Programmable Materials Based on Carbon Nanotube-Hydrogel Polymer Composites. Nano Letters, 2011. 11(8): p. 3239-3244.
146. Li, D. and R.B. Kaner, Graphene-Based Materials. Science, 2008. 320(5880): p. 1170-1171.
147. Tang, Z., et al., Incorporation of graphene into polyester/carbon nanofibers composites for better multi-stimuli responsive shape memory performances. Carbon, 2013. 64: p. 487-498.

148. Lee, S.-H., et al., 3D Networked Graphene-Ferromagnetic Hybrids for Fast Shape Memory Polymers with Enhanced Mechanical Stiffness and Thermal Conductivity. Small, 2014. 10(19): p. 3880-3886.
149. Yoonessi, M., et al., Graphene Polyimide Nanocomposites; Thermal, Mechanical, and High-Temperature Shape Memory Effects. ACS Nano, 2012. 6(9): p. 7644-7655.
150. Yu, L. and H. Yu, Light-Powered Tumbler Movement of Graphene Oxide/Polymer Nanocomposites. ACS Applied Materials & Interfaces, 2015. 7(6): p. 3834-3839.
151. Yi, D.H., et al., Mechanical and photothermal shape memory properties of in-situ polymerized hyperbranched polyurethane composites with functionalized graphene. Fibers and Polymers, 2015. 16(8): p. 1766-1771.
152. Yang, Z., et al., Dual-Triggered and Thermally Reconfigurable Shape Memory Graphene-Vitrimer Composites. ACS Applied Materials & Interfaces, 2016. 8(33): p. 21691-21699.
153. Wang, E., et al., Light-Controlled Graphene-Elastin Composite Hydrogel Actuators. Nano Letters, 2013. 13(6): p. 2826-2830.
154. Zhu, C.-H., et al., Photothermally Sensitive Poly(N-isopropylacrylamide)/Graphene Oxide Nanocomposite Hydrogels as Remote Light-Controlled Liquid Microvalves. Advanced Functional Materials, 2012. 22(19): p. 4017-4022.
155. Garcia Rosales, C.A., et al., 3D printing of shape memory polymer (SMP)/carbon black (CB) nanocomposites with electro-responsive toughness enhancement. Materials Research Express, 2018. 5(6): p. 065704.
156. Swinehart, D.F., The Beer-Lambert Law. Journal of Chemical Education, 1962. 39(7): p. 333.
157. Huang, C. and Z. Bian, Introduction, in Rare Earth Coordination Chemistry: Fundamentals and Applications. 2011, John Wiley & Sons: Singapore. p. 1-39.
158. Shahi, P.K., et al., Revelation of the Technological Versatility of the Eu(TTA)3Phen Complex by Demonstrating Energy Harvesting, Ultraviolet Light Detection, Temperature Sensing, and Laser Applications. ACS Applied Materials & Interfaces, 2015. 7(33): p. 18231-18239.

159. Shahalizad, A., et al., Near infrared electroluminescence from Nd(TTA)3phen in solution-processed small molecule organic light-emitting diodes. Organic Electronics, 2017. 44: p. 50-58.
160. Fang, T., et al., Preparation and assembly of five photoresponsive polymers to achieve complex light-induced shape deformations. Materials & Design, 2018. 144: p. 129-139.
161. Wang, H., et al., Light-induced rare earth organic complex/shape-memory polymer composites with high strength and luminescence based on hydrogen bonding. Composites Part A: Applied Science and Manufacturing, 2019. 125: p. 105525.
162. Bhat, N.V., et al., Simultaneous polymerization and crystallization of aniline. Synthetic Metals, 2002. 130(2): p. 185-192.
163. White, T.J., et al., A high frequency photodriven polymer oscillator. Soft Matter, 2008. 4(9): p. 1796-1798.
164. van Oosten, C.L., et al., Printed artificial cilia from liquid-crystal network actuators modularly driven by light. Nature Materials, 2009. 8(8): p. 677-682.
165. Baer, G.M., et al., Fabrication and in vitro deployment of a laser-activated shape memory polymer vascular stent. Biomedical engineering online, 2007. 6: p. 43-43.
166. Fang, L., et al., Precise stimulation of near-infrared light responsive shape-memory polymer composites using upconversion particles with photothermal capability. Composites Science and Technology, 2017. 152: p. 190-197.
167. Leng, J., et al., Study on the activation of styrene-based shape memory polymer by medium-infrared laser light. Applied Physics Letters, 2010. 96(11): p. 111905.
168. Liu, Y., et al., Sequential self-folding of polymer sheets. Science Advances, 2017. 3(3): p. e1602417.
169. Hu, J., et al., Recent advances in shape–memory polymers: Structure, mechanism, functionality, modeling and applications. Progress in Polymer Science, 2012. 37(12): p. 1720-1763.
170. Wang, K. and X.X. Zhu, Two-Way Reversible Shape Memory Polymers Containing Polydopamine Nanospheres: Light Actuation, Robotic Locomotion, and Artificial Muscles. ACS Biomaterials Science & Engineering, 2018. 4(8): p. 3099-3106.

171. Westbrook, K.K., et al., Two-way reversible shape memory effects in a free-standing polymer composite. Smart Materials and Structures, 2011. 20(6): p. 065010.
172. Behl, M., et al., Reversible Bidirectional Shape-Memory Polymers. Advanced Materials, 2013. 25(32): p. 4466-4469.
173. Behl, M. and A. Lendlein, Triple-shape polymers. Journal of Materials Chemistry, 2010. 20(17): p. 3335-3345.
174. Luo, X. and P.T. Mather, Triple-Shape Polymeric Composites (TSPCs). Advanced Functional Materials, 2010. 20(16): p. 2649-2656.
175. Xie, T., Tunable polymer multi-shape memory effect. Nature, 2010. 464(7286): p. 267-270.
176. Zhao, Q., et al., Shape-memory polymers with multiple transitions: complex actively moving polymers. Soft Matter, 2013. 9(6): p. 1744-1755.
177. Chung, T., et al., Two-Way Reversible Shape Memory in a Semicrystalline Network. Macromolecules, 2008. 41(1): p. 184-192.
178. Bothe, M. and T. Pretsch, Two-Way Shape Changes of a Shape-Memory Poly(ester urethane). Macromolecular Chemistry and Physics, 2012. 213(22): p. 2378-2385.
179. Taya, M., et al., Design of two-way reversible bending actuator based on a shape memory alloy/shape memory polymer composite. Smart Materials and Structures, 2013. 22(10): p. 105003.
180. Terao, F., et al., Light-Driven Molecular-Crystal Actuators: Rapid and Reversible Bending of Rodlike Mixed Crystals of Diarylethene Derivatives. Angewandte Chemie International Edition, 2012. 51(4): p. 901-904.
181. Yang, Q., et al., Artificial muscles made of chiral two-way shape memory polymer fibers. Applied Physics Letters, 2016. 109(18): p. 183701.
182. Fan, J. and G. Li, High performance and tunable artificial muscle based on two-way shape memory polymer. RSC Advances, 2017. 7(2): p. 1127-1136.
183. Yu, K., et al., Design and analysis of morphing wing based on SMP composite. SPIE Smart Structures and Materials + Nondestructive Evaluation and Health Monitoring. Vol. 7290. 2009: SPIE.
184. Perkins, D., et al., Morphing Wing Structures for Loitering Air Vehicles, in 45th AIAA/ASME/ASCE/AHS/ASC Structures, Structural Dynamics & Materials Conference.

185. Yuan, Z., et al., Modeling the response of light-activated shape memory polymers. Mathematics and Mechanics of Solids, 2017. 22(5): p. 1116-1143.
186. Sodhi, J.S., et al., Inhomogeneous deformations of Light Activated Shape Memory Polymers. International Journal of Engineering Science, 2015. 89: p. 1-17.
187. Beblo, R. and L.M. Weiland. Multiscale Modeling of Light Activated Shape Memory Polymer. in ASME 2008 Conference on Smart Materials, Adaptive Structures and Intelligent Systems. 2008.
188. Rajagopal, K.R., Multiple Configurations in Continuum Mechanics. Reports of the Institute for Computational and Applied Mechanics, 1995. 6.
189. Rao, I.J. Constitutive modeling of crystallizable shape memory polymers. in Proceedings of SPE-ANTEC. 2002.
190. Scott, T.F., et al., Photoinduced Plasticity in Cross-Linked Polymers. Science, 2005. 308(5728): p. 1615.
191. Hinkle, J., et al., Design and Materials Study on Secondary Structures in Deployable Planetary and Space Habitats, in 52nd AIAA/ASME/ASCE/AHS/ASC Structures, Structural Dynamics and Materials Conference.
192. Li, F., et al., Preliminary design and analysis of a cubic deployable support structure based on shape memory polymer composite. International Journal of Smart and Nano Materials, 2016. 7(2): p. 106-118.
193. Sun, J., et al., Mechanical properties of shape memory polymer composites enhanced by elastic fibers and their application in variable stiffness morphing skins. Journal of Intelligent Material Systems and Structures, 2014. 26(15): p. 2020-2027.
194. Keller, P., et al., Development of Elastic Memory Composite Stiffeners for a Flexible Precision Reflector, in 47th AIAA/ASME/ASCE/AHS/ASC Structures, Structural Dynamics, and Materials Conference.
195. Chen, Q., et al., Design and Testing of a Space Deployable Mechanism, in 4th AIAA Spacecraft Structures Conference.
196. Kohlmeyer, R.R. and J. Chen, Wavelength-Selective, IR Light-Driven Hinges Based on Liquid Crystalline Elastomer Composites. Angewandte Chemie International Edition, 2013. 52(35): p. 9234-9237.

197. Guo, Q., et al., Entanglement-Based Thermoplastic Shape Memory Polymeric Particles with Photothermal Actuation for Biomedical Applications. ACS Applied Materials & Interfaces, 2018. 10(16): p. 13333-13341.
198. Zhi, Y., et al., Quasi-linear viscoelastic modeling of light-activated shape memory polymers. Journal of Intelligent Material Systems and Structures, 2017. 28(18): p. 2500-2515.
199. ISO 527-5:2009, in Plastics - Determination of tensile properties - Part 5: Test conditions for unidirectional fibre-reinforced plastic composites. 2009-07, International Organization for Standardization.
200. ASTM D6641 / D6641M-16e1, in Standard Test Method for Compressive Properties of Polymer Matrix Composite Materials Using a Combined Loading Compression (CLC) Test Fixture. 2016, ASTM International, West Conshohocken, PA.
201. ASTM D2583 - 13a, in Standard Test Method for Indentation Hardness of Rigid Plastics by Means of a Barcol Impressor. 2013, ASTM International, West Conshohocken, PA.
202. ASTM D2240 - 15e1, in Standard Test Method for Rubber Property—Durometer Hardness. 2015, ASTM International, West Conshohocken, PA.
203. González, M.G., et al., Applications of FTIR on epoxy resins-identification, monitoring the curing process, phase separation and water uptake, in Infrared Spectroscopy-Materials Science, Engineering and Technology. 2012, InTech. p. 261-284.
204. Guignot, C., et al., Degradation of segmented poly (etherurethane) Tecoflex® induced by electron beam irradiation: characterization and evaluation. Nuclear Instruments and Methods in Physics Research Section B: Beam Interactions with Materials and Atoms, 2001. 185(1): p. 100-107.
205. Noda, I., et al., Group Frequency Assignments for Major Infrared Bands Observed in Common Synthetic Polymers, in Physical Properties of Polymers Handbook, J.E. Mark, Editor. 2007, Springer New York: New York, NY. p. 395-406.
206. Jung, M.R., et al., Validation of ATR FT-IR to identify polymers of plastic marine debris, including those ingested by marine organisms. Marine Pollution Bulletin, 2018. 127: p. 704-716.

207. Zhao, S., et al., Preparation and Fluorescent Property of Eu(TTA)3Phen Incorporated in Polycarbonate Resin. Polymer Journal, 2006. 38(6): p. 523-526.
208. Yuniarto, K., et al., Infrared and Raman studies on polylactide acid and polyethylene glycol-400 blend. AIP Conference Proceedings, 2016. 1725(1): p. 020101.
209. Cherdoud-Chihani, A., et al., Study of crosslinking acid copolymer/DGEBA systems by FTIR. Journal of Applied Polymer Science, 2003. 87(13): p. 2033-2051.
210. Kakei, A.A., et al., Use of an elasto-plastic model and strain measurements of embedded fibre Bragg grating sensors to detect Mode I delamination crack propagation in woven cloth (0/90) composite materials. Structural Health Monitoring, 2018. 17(2): p. 363-378.
211. Kakei, A.A.G., et al., Development of fracture and damage modeling concepts for composite materials, in Structural health monitoring technologies and next-generation smart composite structures. 2016, CRC Press. p. 339–364.
212. ASTM D3039/D 3039M, in Standard test method for tensile properties of polymer matrix composite materials. 2008, ASTM International, West Conshohocken, PA.
213. Paiva, J.M.F.d., et al., Comparison of tensile strength of different carbon fabric reinforced epoxy composites. Materials Research, 2006. 9: p. 83-90.
214. Mukherjee, D.P., et al., Effect of Hydrophobic Elastin Ligands on the Stress-Strain Properties of Elastin Fibers. Connective Tissue Research, 1976. 4(3): p. 177-179.
215. Nair, S.N., et al., Failure Behavior of Unidirectional Composites under Compression Loading: Effect of Fiber Waviness. Materials (Basel, Switzerland), 2017. 10(8): p. 909.
216. Hu, N. and R. Burgueño, Buckling-induced smart applications: recent advances and trends. Smart Materials and Structures, 2015. 24(6): p. 063001.
217. Argüello-Bastos, J.D., et al., Study of mechanical properties under compression failure in reinforced composite materials produced by additive manufacturing. Journal of Physics: Conference Series, 2018. 1126: p. 012005.
218. Liu, C., et al., Review of progress in shape-memory polymers. Journal of Materials Chemistry, 2007. 17(16): p. 1543-1558.

219. Kostopoulos, V., et al., Impact and after-impact properties of carbon fibre reinforced composites enhanced with multi-wall carbon nanotubes. Composites Science and Technology, 2010. 70(4): p. 553-563.
220. Walker, L., et al., Improving impact resistance of carbon-fibre composites through interlaminar reinforcement. Composites Part A: Applied Science and Manufacturing, 2002. 33(6): p. 893-902.
221. Dong, Y., et al., Shape memory, self-healing property, and NIR photothermal effect of epoxy resin coating with polydopamine@polypyrrole nanoparticles. Progress in Organic Coatings, 2019. 136: p. 105232.
222. Proudhon, H., et al., A fretting crack initiation prediction taking into account the surface roughness and the crack nucleation process volume. International Journal of Fatigue, 2005. 27(5): p. 569-579.
223. Sedlaček, M., et al., Correlation between standard roughness parameters skewness and kurtosis and tribological behaviour of contact surfaces. Tribology International, 2012. 48: p. 102-112.
224. Peressadko, A.G., et al., Influence of Surface Roughness on Adhesion between Elastic Bodies. Physical Review Letters, 2005. 95(12): p. 124301.
225. Baghani, M., et al., A constitutive model for shape memory polymers with application to torsion of prismatic bars. Journal of Intelligent Material Systems and Structures, 2012. 23(2): p. 107-116.
226. Fejős, M., et al., Shape memory characteristics of woven glass fibre fabric reinforced epoxy composite in flexure. Journal of Reinforced Plastics and Composites, 2012. 31(22): p. 1532-1537.
227. Murugan, M.S., et al., Actuation of shape memory polymer composites triggered by electrical resistive heating. Journal of Intelligent Material Systems and Structures, 2017. 28(17): p. 2363-2371.
228. Nishikawa, M., et al., Effect of fiber arrangement on shape fixity and shape recovery in thermally activated shape memory polymer-based composites. Composites Part A: Applied Science and Manufacturing, 2012. 43(1): p. 165-173.
229. Joven, R., et al. Thermal Properties of Carbon Fiber-Epoxy Composites with Different Fabric Weaves. in 44th ISTC SAMPE International Symposium Proceedings. 2012. Charleston SC.
230. Hubbard, J.A., et al., Carbon fiber composite characterization in adverse thermal environments. 2011, Sandia National Laboratories.

231. Adibekyan, A., et al., Review of PTB Measurements on Emissivity, Reflectivity and Transmissivity of Semitransparent Fiber-Reinforced Plastic Composites. International Journal of Thermophysics, 2019. 40(4): p. 36.
232. Habault, D., et al., Light-triggered self-healing and shape-memory polymers. Chemical Society Reviews, 2013. 42(17): p. 7244-7256.
233. Balat-Pichelin, M., et al., Emissivity measurements on carbon–carbon composites at high temperature under high vacuum. Applied Surface Science, 2006. 253(2): p. 778-783.
234. Azzawi, W.A., et al., Implementation of a finite element analysis procedure for structural analysis of shape memory behaviour of fibre reinforced shape memory polymer composites. Smart Materials and Structures, 2017. 26(12): p. 125002.
235. Nagai, N., et al., Infrared analysis of depth profiles in UV-photochemical degradation of polymers. Polymer Degradation and Stability, 2005. 88(2): p. 224-233.
236. Kang, C.-S., Multilayer Insulation for Spacecraft Applications, in COSPAR Colloquia Series, F.-B. Hsiao, Editor. 1999, Pergamon. p. 175-179.
237. Finckenor, M.M. and D. Dooling, Multilayer Insulation Material Guidelines. 1999, NASA.
238. Medina, D.F., Solar Radiation and Spacecraft Shielding, in Handbook of Cosmic Hazards and Planetary Defense, J.N. Pelton and F. Allahdadi, Editors. 2015, Springer International Publishing: Cham. p. 295-314.
239. C.B.Honsberg and S.G.Bowden. Photovoltaics Education Website. 2019 02/04/2020]; Available from: www.pveducation.org.
240. Santoni, F., et al., An innovative deployable solar panel system for Cubesats. Acta Astronautica, 2014. 95: p. 210-217.
241. Kuang, J., et al., Nonlinear dynamics of a satellite with deployable solar panel arrays. International Journal of Non-Linear Mechanics, 2004. 39(7): p. 1161-1179.
242. Puig, L., et al., A review on large deployable structures for astrophysics missions. Acta Astronautica, 2010. 67(1): p. 12-26.
243. Fenci, G.E. and N.G. Currie, Deployable structures classification: A review. International Journal of Space Structures, 2017. 32(2): p. 112-130.

244. Pellegrino, S., Deployable Structures. International Centre for Mechanical Sciences. 2014: Springer, Vienna.
245. Hinkle, J., et al., Design and Materials Study on Secondary Structures in Deployable Planetary and Space Habitats, in 52nd AIAA/ASME/ASCE/AHS/ASC Structures, Structural Dynamics and Materials Conference. 2011.
246. Fernandez, J.M. Advanced Deployable Shell-Based Composite Booms for Small Satellite Structural Applications Including Solar Sails. in 4th International Symposium on Solar Sailing. 2017. Kyoto; Japan.
247. Belvin, W.K., et al., Advanced Deployable Structural Systems for Small Satellites, in NATO CSO STO Specialist Meeting AVT-257 /RSM-041 on Best Practices for Risk Reduction for Overall Space Systems. 2016: Zaragoza; Spain.
248. Fernandez, J.M., et al. NASA's Advanced Solar Sail Propulsion System for Low-Cost Deep Space Exploration and Science Missions that Use High Performance Rollable Composite Booms. in 4th International Symposium on Solar Sailing. 2017. Kyoto; Japan.

Appendix A: List of Publications

Book Chapters

B1 - Wessam Al Azzawi, **Madhubhashitha Herath**, Jayantha Epaarachchi, Modeling, analysis, and testing of viscoelastic properties of shape memory polymer composites and a brief review of their space engineering applications, Creep and Fatigue in Polymer Matrix Composites 2nd Edition, 2019, pp. 465-495.

Journal Articles

J1 - **Madhubhashitha Herath**, Jayantha Epaarachchi, Mainul Islam, Liang Fang, Jinsong Leng, Light Activated Shape Memory Polymers and Composites: A Review, European Polymer Journal, 2020, 136, p. 109912.

J2 - **Madhubhashitha Herath**, Jayantha Epaarachchi, Mainul Islam, Fenghua Zhang, Jinsong Leng, Liang Fang, Cheng Yan, Gang Ding Peng, Wolfgang Schade, Remote actuation of light activated shape memory polymers via D-shaped optical fibres, Smart Materials and Structures, 2020, 29(4), pp. 1-9.

J3 - **Madhubhashitha Herath**, Jayantha Epaarachchi, Mainul Islam, Cheng Yan, Fenghua Zhang, Jinsong Leng, Effects of selectively triggered photothermal particles on shape memory polymer composites: An investigation on structural performance, thermomechanical characteristics and photothermal behavior, Journal of Intelligent Material Systems and Structures, 2019, 30(20), pp. 3124-3135.

J4 - **Madhubhashitha Herath**, Jayantha Epaarachchi, Mainul Islam, Jinsong Leng, Carbon Fibre Reinforced Shape Memory Polymer Composites for Deployable Space Habitats, Engineer - Journal of the Institution of Engineers, Sri Lanka, 2019, 52(1), pp. 1-9.

J5 - **Madhubhashitha Herath**, Jayantha Epaarachchi, Mainul Islam, Wessam Al Azzawi, Jinsong Leng, Fenghua Zhang, Structural performance and photothermal recovery of carbon fibre reinforced shape memory polymer, Composites Science and Technology, 2018, 167, pp. 206-214.

Conference Proceedings

C1 - **Madhubhashitha Herath**, Jayantha Epaarachchi, Mainul Islam, Fenghua Zhang, Jinsong Leng, 4D Printed Shape Memory Polymer Composite Structures for Deployable Small Spacecrafts, ASME Conference on Smart Materials Adaptive Structures and Intelligent Systems, Louisville KY, USA, 2019.

C2 - **Madhubhashitha Herath**, Jayantha Epaarachchi, Mainul Islam, Liang Fang, Fenghua Zhang, Jinsong Leng, Performance of Rare Earth Organic Complexes Based Light Activated Shape Memory Polymer Composites, 22nd International Conference on Composite Materials, Melbourne, Australia, 2019.

C3 - **Madhubhashitha Herath**, Jayantha Epaarachchi, Mainul Islam, Jinsong Leng, Near Infrared Light Activated Shape Memory Polymer Composite for Space Applications, 11th Asian-Australasian Conference on Composite Materials, Cairns, Australia, 2018.

C4 - **Madhubhashitha Herath**, Wessam Al Azzawi, Jayantha Epaarachchi, Mainul Islam, Scott Robertson, Jinsong Leng, Fenghua Zhang, Thermomechanical Behaviour and Shape Memory Characteristic of Carbon Fibre Reinforced Epoxy, International Conference on Nanoscience and Nanotechnology, Wollongong, Australia, 2018.

Appendix B: Associated Awards

- **Madhubhashitha Herath**, Young Researcher Award at 11th Asian-Australasian Conference on Composite Materials – 2018.

- **Madhubhashitha Herath**, Best Student Paper Finalist at ASME Conference on Smart Materials, Adaptive Structures and Intelligent Systems – 2019.

- **Madhubhashitha Herath**, Pitchfest Finalist at Australian International Airshow and Aerospace & Defense Exposition – 2019.

- **Madhubhashitha Herath**, Best Poster Runner Up at Open Day Center for Future Materials USQ – 2020.

- **Madhubhashitha Herath**, Best Poster Runner Up at Open Day Center for Future Materials USQ – 2018.